Design and development of dissipative anchoring system for seismic strengthening of heritage structures

Thesis submitted to University College London for the degree of

Doctor of Philosophy

by

Victor Melatti

Department of Civil Environmental & Geomatic Engineering

UCL

July 2021

I, Victor Melatti, confirm that the work presented in this thesis is my own. Where information has been derived from other sources, I confirm that this has been indicated in the thesis.

Abstract

The scope of this research is to develop the next generation of dissipating grouted anchoring system for the seismic strengthening of historical masonry structures.

Historic masonry buildings often experience out-of-plane failure due to the lack of effective connection between perpendicular walls. The insertion of steel elements at corner connections is commonly applied in rehabilitation practice to control this collapse mode and locally increase the strength and stiffness of the structure. Nonetheless, they are unable to dissipate the seismic forces rather than through cracking and yielding of the steel elements, as they present limited dissipative and ductility capacity.

To this purpose, the proposed system integrates a friction-based dissipative device with stainless-steel anchors grouted within the thickness of walls. The system provides 1) effective connections between panels and reduced intrusiveness, 2) energy dissipation capacity and additional ductility.

The proposed framework addresses the assessment and refinement of the dissipative system by means of experimental and numerical activities and provides a displacement-based design tool for its implementation to heritage buildings.

The first goal of this research is the refinement of a patented prototype of friction-based device to improve its short-term performance as well as deliver a reliable and robust long-term behaviour. This task is performed according to a test-analyse-redesign procedure that can be used to improve the durability and stability of a typical friction-based device. The performance of the innovative system is then investigated by experimental tests performed on specimens reproducing a strengthened masonry connection.

To address the technical gap in design codes, the second aim of this research is to propose a design method for the implementation of the dissipative system within the framework of the displacement-based design. The design procedure is applied to a case-study structure and the performance of the building strengthened by the innovative anchoring system is determined by non-linear dynamic analysis. Performance's comparisons between different strengthening solutions are drawn, emphasizing that the additional ductility capacity reduces the seismic demand, thus resulting in a less invasive intervention in compliance with the requirements of current codes.

Impact statement

This work presents a dissipative anchoring system that can be used to improve the seismic response of heritage buildings. This study has an impact on a social, industrial, and academic level.

With respect to the former, public and private organizations may implement a design scheme that makes use of the dissipative system to provide a cost-effective, adaptable, and reliable seismic upgrade of historic masonry buildings, which are particularly vulnerable to seismic events and for which modern strengthening solutions are hardy implemented. A second output of this work is the proposal of a design procedure to optimize the implementation of anchoring system, according to the modern principles of performance-based design. Although scientific literature and guidelines fosters the development of such analysis methods, strengthening systems are commonly designed according to capacity-based methods. Medium and long-term impact will grow significantly as the research, development, and exploitation of the system is promoted.

From the industrial point of view, CINTEC International, partner and co-owner of the system's patent, aims not just at the commercialisation of the dissipative system, but at the provision of a bespoke design and installation service through their network of specifically trained seismic engineers and contractors. This business model has been successfully developed by Cintec over the last thirty years and has cemented its international reputation and position in the marketplace.

Finally, this research addresses major intellectual challenges within the field of conservation and earthquake engineering, going beyond the state-of-the-art of passive control system for heritage structures. The results presented in Chapters 4 and 6 have been published in two journal papers, respectively Melatti and D'Ayala (2020), *Methodology for the assessment and refinement of friction-based dissipative devices* and Melatti and D'Ayala (2021), *Displacement-based design procedure of grouted anchoring systems for the seismic upgrade of heritage buildings*.

Acknowledgements

First and foremost, I would like to thank my principal supervisor, Professor Dina D'Ayala for her guidance and unwearied support, it has been a true privilege to work with her throughout my PhD studies. Being an exceptional academic, scientist, and engineer, she inspired me to constantly challenge my knowledge to become a better researcher, expand my horizons and skills. Her support never failed me, and I consider her a dear friend.

I would also like to thank my second supervisor, Dr. Philippe Duffour, who also influenced my growth as a researcher. I consider myself very lucky for having the opportunity to work with such amazing teachers and persons like Dina and Philippe.

I would like to thank Dr. Wendel Sebastian, who I worked with for the past 9 months and whose support and guidance were greatly appreciated.

I would like to thank Luca Giacomelli who helped me with the Python coding for Chapter 6.

I would like to thank Peter James and Dennis Lee, Managing Director and Project Manager at Cintec International, for funding this research project and providing continuous technical and economic support. Finally, I would like to thank the technical staff at UCL for manufacturing the prototypes and helping with the experimental programme.

I am very grateful to my office mates and dear friends Giulia, Vale, Kosta, David, Loan and Takhmina for their personal support, chats, and laugh we had together. Their friendship made the last four years the best ones of my life. I would like to thank all the students, faculty and staff associated with EPICentre and all the people I met during the presentations, coffee breaks, lunches, and parties we had together.

Special thanks to Luca and Tommi, friends and brilliant engineers that motivated me to never give up on my goals; Eleonora, Carla, Maki, and Dafne and for their lightness and spirit; Fabio, Simona, Luca Pan, Roberta, Nicola and Kim, old and new London friends.

This list would not be complete without thanking Chiara for being by my side, supporting, and motivating me to finish my thesis. She helped me to keep a healthy balance between work and social life, which was equally fundamental. Finally, I would like to express my deep gratitude to my family for their constant support and encouragement to embark on this journey. In particular, my parents, Annamaria and Claudio, have thought me the importance of perseverance and studying which are key to progress and succeed in life.

A special thought goes to my hometown, L'Aquila, devastated by an earthquake on April 30th 2009, and to the 309 people that died that night. This dissertation is dedicated to them.

My hope is that - one day - tragedies like this may never repeat and that the results of my work can be a step towards that future.

Contents

List of Figures

List of tables

1 Introduction

1.1 Motivation

UNESCO, through its Cultural Heritage Division, defines the cultural heritage as “the entire corpus of material signs handed on by the past to each culture and, therefore, to the whole of humankind” (UNESCO 1989). The preservation of cultural heritage represents a corner-stone of any cultural policy, as its recognizable features give people a connection to certain social values, beliefs and customs. Together with cultural traditions, works of art, entire territories and unique landscapes, monuments and historic buildings represent an essential part of the cultural heritage. The survival of historic buildings is threatened by phenomena that occur over a long period, such as pollution or atmospheric agents, and by natural hazards, like earthquakes, that can reduce buildings to ruins within few seconds. In the latter case, designing innovative systems able to enhance the resilience of these specific structures to seismic events is a fundamental aspect of Conservation Engineering. This particular branch of the civil engineering deals with managing the well-being of a building, minimising alteration and extending its life for future generations (D’Ayala and Forsyth 2008). Despite the constant efforts of national and international organizations, the issue of securing the entire built heritage is far from being solved, due to the extent and variety of the heritage itself. The need for effective strengthening systems is compelling as the damage observed after strong earthquakes have shown that historical structures are particularly vulnerable to seismic events. In countries such as Italy, which has the largest number of cultural sites listed in the World Heritage Site List, or New Zealand, which rightly prides itself for its seismic design codes and preparedness, large number of heritage buildings were equally damaged beyond repair during the seismic sequence of the 2016 Central Italy earthquake (6.2 magnitude) and the 2011 Christchurch earthquake in New Zealand, (6.3 magnitude).

Drawing on these observations, the research of efficient structural solutions for the prevention of seismic-related damage and protection of human lives is a priority in the Conservation Engineering’s agenda. While many solutions able to improve the global response of new or recently built structures to seismic action are available, only few options have the potential of being implemented in historic buildings. The choice is limited by the conservation principles,

enshrined in international documents as the ICOMOS/ISCARSAH Recommendations (2021) and national guidelines, such as the Italian DPCM 2011(D.P.C.M, 2011), which states that the benefits of possible upgrade interventions in terms of seismic performance must be weighed against the impact on the original aesthetic and structural authenticity of the building. Given these limitations, the implementation of prevention measures must be tailored to the type of buildings and materials.

In the last decades, the behaviour of historic masonry buildings under seismic excitation has been largely investigated (D'Ayala and Speranza 2003; Giresini et al. 2015; Abrams et al. 2017; AlShawa et al. 2019), highlighting that these buildings often display an out-of-plane failure mechanism, as shown in Figure 1-1.

Figure 1-1 Out-of-plane detachment of façade from the lateral walls after a) and b) L'Aquila (2009), c) Christchurch (NZ) (2011), d) Central Italy (2015) earthquakes.

This collapse mode is mostly due to the lack of effective connection between perpendicular walls and several technical solutions for the improvement of structural connections have been designed for the seismic protection of heritage assets. For instance, the insertion of steel elements at corner connections is a traditional and commonly used retrofit techniques and the improvement deriving from the insertion of metallic ties to control the out-of-plane collapse mechanism is commonly accepted and applied in rehabilitation practice (Paganoni and D'Ayala 2014, Candela et al. 2016, Muñoz et al. 2018). Typically, these anchorage systems are inserted at the connection of two perpendicular panels, thus restoring the box-like behaviour of the building, as shown in Figure 1.2.

a) b)

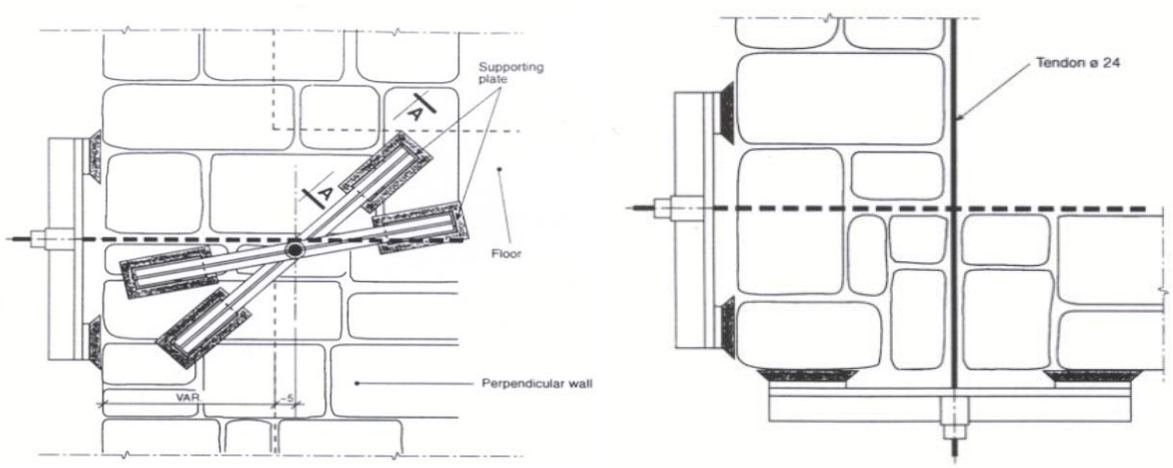

Figure 1-2 View of anchorage system: a) front view, b) horizontal section (Source FEMA 547)

The insertion of metallic cross ties can prevent the collapse of the structure, but the structure remains unable to dissipate the seismic forces rather than through cracking. This may not always be the optimal solution in applications to heritage structures, which have a high cultural value and precious finishing.

Therefore, in the last decades alternative systems have been researched to provide energy dissipation capacity to heritage structures, in line with the modern principle of performance-based design (D'Ayala 2014). This approach requires that the structure meets certain measurable and predictable *performance objective*, namely the acceptable level of damage selected for a specified earthquake intensity level. The selected performance objectives will depend on the intended use and importance of the structure, with safety-critical buildings required to remain *operational* (light damage, most operations can resume immediately) after a severe earthquake event.

In contrast with traditional prescribed building codes, which mandate specific construction practices, such approach encourages design solutions that can be beneficial for different seismic action levels, such as the use of energy dissipation devices that shift the response of the structure from the elastic-only range to an elasto-plastic one (EN 1998-3 2005).

Laboratory testing of connection between adjacent walls have been performed to assess the benefits of strength-only and energy dissipation systems, but the examples of experimental procedures devised for this purpose either are not standardised (Indirli and Castellano 2008) and therefore hardly repeatable, or only applied to reduced scale elements or portion of structures (Paganoni and D'Ayala 2014; G. Maddaloni et al. 2016). Moreover, the design codes are vague when it comes to define the assessment and design procedures to be followed when implementing innovative strengthening system in historic structures (FEMA 356, 2000) (EN 1998-1). Therefore, international agreed guidelines for their retrofit are still lacking and the choice of the strengthening system is left to the experience of the individual engineer without the reassuring support of comprehensive experimental data.

To address the lack of modern strengthening systems for the seismic protection of heritage structures, this thesis proposes an innovative dissipating anchoring system able to improve the global response of historic structures to seismic events. The system comprises a friction-based device, available in two models, able to provide energy dissipation capacity and ductility. The implementation of the dissipative system is proposed according to a novel performance-based design procedure, which exploits the provided ductility to reduce the seismic demand. Both the dissipative system and the design procedure have been developed specifically for heritage structures to address the existing gap in terms of retrofitting systems and design methods between the improvements obtained for the new structures and for the existing ones, especially historic buildings.

1.2 Aim and objectives of research

The scope of this research is to develop the next generation of Dissipative Grouted Anchoring System (D-GAS) which integrates friction-based dissipative device with grouted stainless-steel anchors. The proposed system draws on the results of a collaborative project between Prof D'Ayala and Cintec International, to develop new methods for the protection of cultural heritage. Within this partnership, two devices, a "hysteretic device" and a "frictional device" as

referenced in Paganoni (2015), able to dissipate earthquake-generated forces, were designed, extensively tested and finally patented (James et al. 2014). The frictional device showed better results in terms of energy dissipation capacity and versatility than the hysteretic device, but its performance was not consistent throughout the experimental campaign, limiting its practical application.

Therefore, the first goal of this research is the refinement of the patented prototype of friction-based device and the assessment of the performance of the D-GAS as connected to masonry walls.

To these purposes, a validation framework is developed. Although applied to a specific dissipative system, the proposed framework is of generic value: it proposes a design-make-test-analyse-redesign procedure that can be used to improve the stability and durability of the single components of the system, as well as testing its global performance in a pilot implementation. For industrial manufacturing, the procedure is iterated until the prototype presents a stable and reliable behaviour according to the European guidelines for the validation of dissipative devices (EN 15129 2006).

Throughout this process, the design and refinement of the D-GAS is carried out trying to adhere as much as possible to the current performance-based design framework to ease the formulation of design procedures compatible with modern design principles. In pursuing this approach, the current gap between design procedure concerning the strengthening of structural connections for new-built and heritage structures becomes apparent: current regulations (EN 1998-1:2004 2004; CMIT 2009) do not provide clear prescriptions leaving the end users with the only support of qualitative indications.

Therefore, the second main objective of this thesis is to provide a design procedure for the implementation of the anchoring systems in historic masonry structures built in seismic areas. The process draws on several relevant experimental studies available in literature, and on experimental results and an analysis framework for out-of-plane failure assessment of walls, both developed by the author within this study.

The analysis framework can be performed for increasing level of numerical complexity, starting from a static two-dimensional analysis up to a dynamic tri-dimensional one. It should be noted that the accuracy and the level of uncertainty will directly depend on the level of complexity that the analyst will choose to pursue in conducting the vulnerability assessment.

Although the validation process of the dissipative system is conceived as flexible and can be enlarged through further testing and analysis, this thesis aim is to identify the relevant specific features that can influence the system's design and provide a reliable example towards the development of more efficient structural solutions and more comprehensive design codes.

1.3 Content of the Thesis

Besides this first introductory chapter, and a chapter of conclusions and suggestions for future work, this thesis consists of 6 chapters laid out as follows:

Chapter 2 contains a review of literature research work relevant to retrofitting of masonry structures by means of traditional and innovative systems. Special importance is given to methods comprising steel cross ties and friction-based dissipative devices, as they are the main components of the retrofitting system proposed in this project. The types of requirements that should control the development of new products and rule their design are discussed also with reference to the principles of modern conservation philosophy.

In light of this review, Chapter 3 presents the research methodology developed to validate the D-GAS and the procedural steps for its design and implementation to historical buildings. To this purpose a validation process is developed: it consists of a series of activities carried out through experimental tests and numerical simulations to assess and refine the performance of the system and develop a design strategy able to exploit its load and displacement capacity.

Chapter 4 and Chapter 5 present the bulk of the work done on the assessment of the innovative system. The work consists of experimental and numerical computational activities aimed to characterize the properties of the dissipative device in an isolated configuration and of the device as connected to a set of steel bars embedded in a masonry panel. In particular:

Chapter 4 presents the main features of the innovative friction-based device, its constituent elements, and its function. Four different prototypes are presented, and the results of laboratory tests performed on each device are reported, also discussing the reasons for the technical choices made during the concept design phases. Secondly, numerical models of the prototypes were developed using the commercial software Abaqus, aiming to improve the design of the devices. The validation process led to the refinement of two models that present a performance within the code's requirements for short- and long-term stability and durability.

In Chapter 5 the performance of the whole assembly is investigated: firstly, a set of monotonic pull-out tests are performed on the system connected to a single masonry panel, inferring the influence of the device's activation on the capacity and failure modes of traditional grouted anchoring system. Then the D-GAS is implemented in a T-shaped connection between masonry walls to prove that the insertion of the device allows controlling the rocking motion between the two panels, avoiding the pull-out failure of the grouted elements. Numerical models of the testing set-up are implemented and the modelling techniques that best reproduce the experimental evidence will be used in Chapter 6 to numerically validate the implementation of a set of D-GAS on a case-study structure.

In Chapter 6 a design method for the implementation of the dissipative system within the framework of the displacement-based design is proposed. This aims at addressing the technical gap in design codes, which are vague when it comes to define the assessment and design procedures to be followed when implementing innovative strengthening system in historic structures. The design procedure is applied to a case-study structure and the performance of the building strengthened by the innovative anchoring system is determined by non-linear dynamic analysis. Performance's comparisons between different strengthening solutions are drawn, emphasizing that the additional ductility capacity reduces the seismic demand, thus resulting in a less invasive intervention in compliance with the requirements of current codes.

Chapter 7, the final chapter, contains the conclusions of the present research project, its novelty and the main achievements, the further challenges, and the possible improvements of the research.

2 Literature review of techniques for the seismic strengthening of heritage structures

2.1 Introduction

The performance of structural components and their relative interaction determine the performance of a structure in case of a seismic event. International codes for the seismic design of buildings, such as the Eurocode 8, stress the importance of connection between vertical and horizontal elements to ensure that the building acts together in resisting the horizontal seismic action (EN 1998:2005, section 4.2.1.5). The code provisions are motivated by the fact that well-designed connection allow the floor systems and the roof to transmit the inertia seismic forces to the vertical structural members according to their relative stiffness (Tomaževič 1999, D.P.C.M. 2011).

Regarding masonry structures, international guidelines provide provisions to ensure effective connections between orthogonal walls in addition to those between walls and floors. Well-designed connectors ensure the box-like behaviour of the building transferring the seismic forces originating in other portions of the building to the load-bearing elements. However, these provisions are stated in qualitative terms compared to the level of detailing provided for different building typologies. For instance, the Annexes of Eurocode 8 (part 3) provides specific information for the assessment of reinforced concrete buildings in their present state and for their seismic upgrading, when necessary (EN 1998-3 2005, Annex A): the contribution of FRP jacketing to the shear capacity of a rectangular section is explicitly provided, for instance.

This lack of specific guidance in current provisions has resulted in the existing gap between code's recommendations and today's rehabilitation/retrofitting practice and in the large number of failures that are still observed on heritage buildings in the aftermaths of major seismic events, even in countries at the forefront of earthquake protection like New Zealand and Italy, as evidenced by the Christchurch (2011) and the Central Italy (2015) earthquakes.

To verify the existence of this gap in knowledge and investigate its extent, a review of the systems available to improve structural connections of unreinforced masonry buildings is

presented in this Chapter. These are grouped according to the main parameter controlling they design, namely the strength or the ductility that they provide.

In section 2.2, a general overview of the role of structural connections in masonry buildings is provided, focusing on the damage they develop when undergoing seismic events or during experimental tests.

In section 2.3, strength-only systems in use today for masonry structures are reviewed. The reviewed systems can improve the in-plane strength of masonry panels; however, the fact that most of these techniques focus at strengthening single structural elements rather than the connections between elements in historic building suggests that further work should be carried out specifically on the strengthening of connections in historic building. Moreover, all these techniques pertain to the category of capacity designed systems and present drawbacks connected to high stiffness in respect to the existing parent materials that put them in contrast with the current trend in seismic engineering design.

Therefore, in paragraph 2.4 a review of systems that enhance the energy dissipation and ductility capacity of structural connections of heritage structures is presented. As the innovative anchoring system proposed in this thesis aims at improving the connections among perpendicular walls, special importance is given to systems that aim to exploit the relative motion of adjacent walls. These are critically discussed to highlight what are the main challenges of implementing dissipative systems to heritage structure, for instance their compatibility with the conservation principles of minimal intervention, and to identify the main parameters that control their design. The results of this review will contribute to define the tasks and activities of the validation methodology presented in Chapter 3.

2.2 Role of structural connections in heritage structures

Unreinforced masonry buildings present a high vulnerability to earthquakes as observed in field inspection following seismic events (Wilkinson et al. 2013; Moon et al. 2014; Derakhshan et al. 2014; Putrino and D'Ayala 2018). This evidence is also confirmed by shaking table tests on scaled and full size masonry models where the total collapse of the building is observed due to wall separation under a relatively moderate earthquake motion (Tomaževič et al. 1996; Benedetti et al. 1998; Magenes et al. 2010; Mendes et al. 2014; Maddaloni et al. 2018). Conversely, when well-built quoins are present, the overturning mechanism of the façade is

restrained, but it can eventually develop, for higher excitations, involving part of the side walls. Such mechanisms also depend on the quality of the masonry, on the layout of openings and perpendicular load-bearing walls and floor structure (D'Ayala and Speranza 2003).

In-plane and out-of-plane mechanism of masonry walls can be predicted by analytical models that take in account building geometry, materials, and connections to surrounding elements. D'Ayala and Speranza (2003), having an extensive database of on-site observations collected in the aftermath of several seismic events, derived the minimum value of lateral acceleration which will cause the overturning or in-plane failure of a building, and quantified the reduction in vulnerability associated with strengthening implementations. De Felice and Giannini (2001) also developed an analytical model to predict the seismic resistance of a façade with respect to out-of-plane collapse and the response is investigated applying both static horizontal forces and acceleration impulse.

Both methods pertain to the force-based design as they assume that the loading forces causing the overturning of the façade can be computed from the peak ground accelerations and the elastic period of the structure. This is a legitimate approach if the unreinforced masonry is perceived to possess very limited ductility capacity and allows modelling the effect of the seismic action by considering concentrated lateral forces where concentration of mass exists.

Conversely, in the last decade experimental tests have shown that masonry structures often possess a post-cracking capacity under dynamic loading which would allow for a shift of design philosophy from force-based design to displacement-based design (Doherty et al. 2002). Al Shawa et al. (2012) conducted a series of experimental shaking table tests on a wall restrained by two orthogonal panels and loaded out of its plane, showing that it can be set into motion without necessary collapsing. Numerical and analytical nonlinear dynamic model have been derived to represent the rocking of masonry façade, using monolithic (Prajapati et al. 2015) or two-rigid-body model (Sorrentino 2008), validated according to experimental observations (Shi 2016), as shown in Figure 2-1.

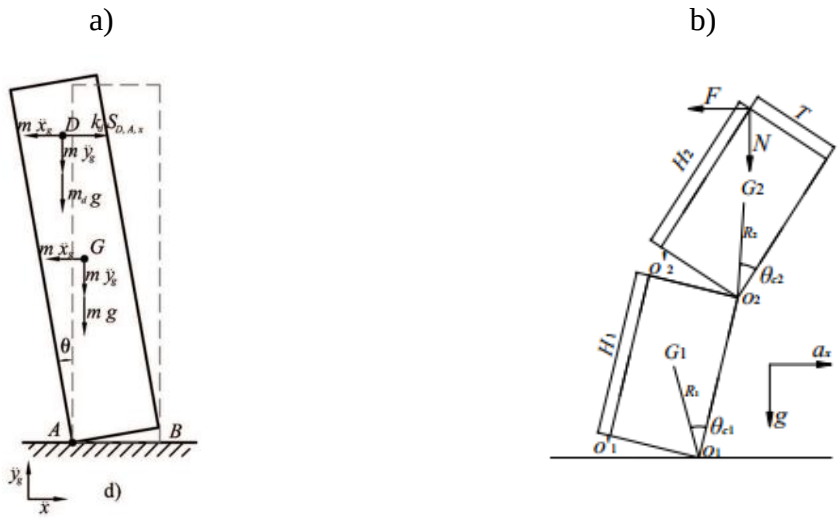

Figure 2-1: Parameters describing the model of a rigid body and its rocking motion a) monolithic approach b) two-rigid-body model (credits for the images to Prajapati et al. 2015 and Shi 2016)

The conservative approach neglecting this "reserve capacity" may result in a too conservative seismic assessment of historic buildings, and in turn to an invasive strengthening design and in prohibitive economic penalty (Doherty et al. 2002).

Nonetheless, the development of strengthening procedures in line with the modern philosophy of seismic engineering hardly follows and traditional reinforcement systems are still largely used. This can be explained considering that any structural intervention aimed to improve the global response of a historic building to seismic load needs to comply with the principle of minimum intervention of Conservation Engineering, presented in the ICOMOS/ISCARSAH Recommendations for the Analysis and Restoration of Architectural Heritage (ICOMOS/ISCARSAH 2021). This principle is defined as an intervention that optimally combines compliance with adequate structural requirements with the maximum possible protection of the heritage values.

Traditional strengthening systems, which evolved through decades of experience and testing, often present an intrinsic physical and mechanical affinity with the original masonry. Hydraulic lime-based mortars or grouts for repair or injection are examples of this compatibility, as they present properties which are similar to those of the masonry components.

Conversely, innovative techniques can introduce undesirable side-effects due to incompatibility between original materials and technique. For instance, Portland cement may introduce soluble salts that, after penetrating original mortars or stone, may experience expansive recrystallization and cause cracking or pulverization (Chemical incompatibility). Other techniques can give rise to physical incompatibility: waterproof materials to inject or repoint an existing and porous

ancient one may disrupt the natural humidity exchange between the existing material with the environment, which may cause internal pressures and may foster chemical and physical problems.

Together with principle of compatibility, the following criteria are listed in the latest version of ICOMOS guidelines, currently under review and available as draft (ICOMOS/ISCARSAH 2021) to facilitate the design of minimum interventions:

- ***Durability***: Insufficient durability of the new material induce its expansion, cracking or debonding which may in turn damage the original one. Iron and steel corrosion, for instance, has been a source of massive damage in restored heritage structures. Moreover, the safety of the structure can be compromised by the loss of the efficiency of the strengthening.
- ***Invasiveness.*** Non-invasive repair or strengthening techniques should be preferred to more invasive alternatives. For obvious reasons, they will contribute to preserve the material integrity of the existing structure.
- ***Removability***. Whenever possible, the measures adopted should be removable so that they may be removed and replaced with more suitable measures if required. As a general principle, no intervention should compromise its future replacement. The replacement may be motivated by insufficient effectivity or by new technological developments. Removability implies that the dismantlement of the intervention will only generate limited and repairable deterioration on the original construction.
- ***Controllability***. It must be possible to control the intervention during its execution. Measures that are impossible to control should not be allowed. Whenever possible, monitoring should be used to control the adequate performance of the structure during the execution of the intervention. It is also desirable to use monitoring to control the performance of the repaired or strengthened structure during a certain period of time following the intervention, as a way to assess its effectiveness.
- ***Obtrusiveness:*** Obtrusiveness refers to the quality of being undesirably noticeable, meaning that "replacements of missing parts must integrate harmoniously with the whole" (ICOMOS 2003).
- ***Sustainability.*** Sustainable materials and technologies characterized by low environmental impact during their life cycle (manufacturing, transportation, placement or removal) should be preferred.

A second reason for the popularity of traditional techniques among conservation engineers is that they are often preliminary to other strengthening interventions. For instance, before proceeding to seismic upgrade with dampers it is common practice to improve the masonry substratum by means of cementitious-based injections (Indirli et al. 2001). A third reason is that innovative systems able to add ductility capacity to the structural elements are methodically

regulated in case of application to new constructions, while code prescriptions (EN 1998-3:2005 2005) are mainly qualitative regarding the retrofit of heritage structures (Paganoni and D'Ayala 2014).

As a result, strength-only systems are still widely applied, despite experimental studies performed on masonry structures reinforced by strength-only systems show that collateral effects may rise, for instance due to mechanical incompatibility: combining materials or structural members with very different stiffness may result in damage to the more fragile one (which is normally the ancient material). Benedetti et al. (1998), for instance, observe this effect using reinforced concrete bands at floor level to improve masonry structural connections: it was found that this technique is not effective in redistributing the horizontal load if the quality of the masonry is poor and shear failure of the masonry might occur, as shown in Figure 2-2.

Figure 2-2. Shear failure of masonry structure reinforced by means of concrete bands (Benedetti, Carydis, and Pezzoli 1998)

The effects of incompatibility of strengthening systems with the historic substratum has also been observed in historic city centres experiencing major seismic events. Strengthening systems, such as reinforced concrete ring beams, represent an increase in mass and a sudden change in stiffness along the height of the walls, inducing increased inertial forces that frequently determine the ultimate collapse of the structure undergoing seismic loading (Dina D'Ayala and Paganoni 2011; Maddaloni 2016), as shown in Figure 2-3.

Figure 2-3 Failure due to excessive weight of RC roof structure built on poor quality masonry walls (credits to Maddaloni 2016).

Far better performance is observed for strengthening systems that restore the box-like behaviour of buildings without increasing the overall mass. Tomazevic et al. (1996) for example, tested different strengthening configurations showing that masonry models reinforced by means of steel ties did not display wall separation and disintegration under seismic-like ground motion. Similar conclusions were drawn by Mendes et al. (2014), testing a Portuguese building typology made by limestone and lime mortar and strengthened by steel elements connecting the timber joists and the masonry walls. Improvements in seismic performance of masonry structures by means of repair/strengthening solutions that do not involve increment in the overall mass of the structure (such as injections and helical steel bars) were also obtained by Maddaloni et al. (2018).

On the other hand, steel ties, especially if pretensioned, can leads to localized high stiffness that caused severe crack to the masonry, even if the total collapse was prevented, or to the pull-out failure at the head of the anchorage due to the different deformability of metal and masonry.

The use of ductile systems recommended by international codes (EN 1998:2005) has the potential of overcoming these issues, thus achieving the objective of protecting culturally valuable finishes and preserving life and safety. Nevertheless, high-ductility systems are seldom applied to heritage structures and often remain within the domain of scientific research, without much guidance being provided to end users for real case studies (Paganoni 2015).

In light of these considerations, the extent of the discrepancy between technological development and construction practice feasibility in the field of the seismic protection of heritage structures will be investigated in the remain of the chapter.

However, a full review of the strength-only system is outside the scope of this thesis, which rather proposes a passive control system to enhance the ductility and energy dissipation capacity

of masonry connections. Therefore capacity-based systems are briefly discussed to ascertain the efficiency of these solutions and their compliance with conservation principles presented in this section. A more detailed review of strength-only techniques can be found in several reports, such as the documents produced within the framework of the Niker Project (available at www.niker.eu, 2010 and 2012).

2.3 Strength-only systems for retrofitting and upgrading of masonry connection

Unreinforced masonry buildings tend to pose a great seismic risk to human life because they are not capable of dissipating energy through large inelastic deformation during earthquakes, while maintaining their integrity (Mazzolani 2001). The overall behaviour of masonry constructions depends, in the first place, on the strength of the single wall, which is determined by the quality of the employed materials. Secondly, the mutual interaction between the building constituents, namely the effective connections between adjacent horizontal/vertical elements, governs the way the structure will respond to external loading, such as a seismic event. Therefore, a large variety of systems has been developed in the last centuries to improve the structural behaviour of a heritage building, enhancing the strength of each structural component or the connections among components.

Traditional techniques, such as local dismantling and reconstruction (also known as scuci-cuci) and structural repointing, consist in the removal of parts where major deterioration has occurred and substitution with new material reproducing the mechanical properties of the original one. Thus, they are normally compatible to the original parts due to use of materials with similar properties. Moreover, the compatibility and durability in the long term have been proven through an experience of centuries. They are partially reversable and non-obtrusive, while the invasiveness depends on the extent of the intervention. It should be noted that these techniques tend to restore the original structural performance, without providing a significant improvement in seismic response. In the extreme case, namely if the building displays severe decay or damage, whole structural members can be replaced; however, this technique is generally avoided as it might modify the seismic response of the building. In general repair is preferred to substitution, which is often an incompatible, irreversible, invasive, and obtrusive intervention. A complete list of traditional techniques available for heritage structures is

provided in Table 2-1, along with their adherence to the conservation principles according to the classification provided within the framework of the FP7 NIKER project (NIKER 2012).

Where traditional techniques prove inadequate, the consolidation of a monument can be achieved using any modern technique for conservation engineering that have shown its efficacy through by scientific data and proved by experience. These are based on the use of innovative materials which in some case show severe compatibility problems (as in the case of Portland cement or epoxy resins) when used to restore or strengthen brick or stone masonry structures. The success of a retrofit by injection, for instance, depends on the injection technique adopted and on its physical/chemical compatibility with the masonry to be retrofitted. Grout and lime-based mortar have been used as injection material, restoring or even improving the load-bearing capacity of the original wall (ElGawady, Lestuzzi, and Badoux 2004). Considering the beneficial effects of this retrofitting technique and the fact that it does not alter the aesthetic features of historic assets, nowadays injections are considered as a non-invasive technique and are largely used strengthening technique for this building typology (EN 1998-3 2005).

A variety of surface treatments have also been proposed with the purpose of increasing the strength and stiffness of structural members. Reinforced concrete or mortar jacketing (Borri et al. 2011), reinforced plasters, FRP laminates or sheets (Gostič 2012) have been proposed. However, their applicability is restricted due to the high level of intrusiveness and obtrusiveness, and little reversibility as removing the added material normally causes the peeling off of the brick or stone surface. A comprehensive list of modern techniques available for heritage structures is provided in Table 2-1 and additional details can be found in the provided references.

Table 2-1 classification of traditional and modern strengthening techniques

	Criteria for minimum intervention				
Traditional techniques	Compatibility	Removability	Durability	Invasiveness	Obtrusiveness
Local dismantling and reconstruction	YES	PARTIAL	YES	YES	NO
Structural repointing	YES	PARTIAL	YES	YES	NO
Tying	YES	YES	YES	NO	NO
Intramural Tying	CONDITIONAL	YES	YES	NO	NO
Fastening	YES	YES	NO	NO	NO
Confinement of piers by stiff rings	YES	YES	YES	NO	PARTIALLY
Substitution of structural member	NO	NO	YES	YES	NO
Modern techniques					
Grout injections of cracks	CONDITIONAL	NO	YES	NO	NO
External reinforcement	CONDITIONAL	NO	YES	MODERATE	YES
Internal reinforcement	CONDITIONAL	NO	CONDITIONAL	YES	NO
Reinforced injections (stitching)	NO	NO	NO	YES	YES
Jacketing	NO	CONDITIONAL	YES	NO	YES
Desmantling and reassembling	YES	NO	YES	YES	YES
Secondary structures	NO	NO	YES	NO	YES

Focusing on the improvement of structural connections, several systems have been designed to connect adjacent structural elements and have a significant positive effect on the seismic performance of masonry structure. However only few techniques are applicable to building with architectural or heritage value. Some systems, such as RC ring beam or steel hoops, have crucial drawbacks if applied to historic masonry due to mechanical compatibility, as commented in section 2.2. To resolve this problem a masonry ring beam made of its existing elemens (bricks or stones) kept together by a composite net embedded into the mortar bed joints was proposed by Sisti et al. (2016). Despite its compatibility, the disadvntages of this technique are its invasive and destructive nature, as it requires the demolition of a upper portion of the walls, which are then reconstructed embedding composite materials.

Overall, it appears that the principles of minimal intervention of ICOMOS/ISCARSAH chart should be weighed up on a case-by-case basis, depending on the material and immaterial value they represent, and the effectiveness of innovative strengthening/repair techniques should be verified by experimental testing. Examples of such laboratory activities have been reported by Maddaloni et al. (2018).

Anchoring system, which provides wall-to-wall and wall-to-floor connections and improve the integrity of the structure are commented in detail in the next section. The reason for this is twofold: firstly the use of this technique was known since the Byzantine times (St Sophia in Istanbul 5th century) (Mainstone 1969), continued through the Gothic architecture and it is today widely popular as anti-seismic system. Secondly, metallic ties are an essential part of the dissipative system proposed in this thesis. Therefore, a deeper overview of anchors is essential to comprehend the design of the proposed innovative dissipative anchoring system.

2.3.1 Anchoring system

Good performance is observed for strengthening systems that restore the box-like behaviour of buildings by means of anchors installed at the intersection of perpendicular sets of walls (Contrafatto 2014). This retrofitting system does not increase the overall mass of the structure and does not interfere with the original layout (Giresini et al. 2018). A variety of metal elements are usually involved in the anchoring system, normally steel or stainless steel elements (stirrups, longitudinal or shear reinforcement bars, threaded rods) and more recently ties rods made out of composite materials have been proposed in research for their superior mechanical and chemical properties (G. Maddaloni et al. 2016; Ceroni and Di Ludovico 2020). These metals have a good compatibility with the masonry substrate and high durability as they are not affected by corrosion.

The two most common anchor types in use are through-bolt connection and adhesive anchors (FEMA 547/2006 2006). The first relies on plates on the exterior façade of the masonry walls to transfer the tension of the bars to the resisting structural elements (walls or floors). The ties can be high tensioned, but greater anchoring devices are required, namely larger end-elements, and excessive tension could induce high local stiffness, damaging the masonry at the anchoring level in case of a seismic event.

Adhesive anchors rely on the chemical properties of the adhesive material for their grip to the parent material. For applications to masonry substrates, adhesive anchors are typically installed through injection: a viscous material is pumped into the hole drilled for the anchor and the volume of injected material fills the voids. Both resins and cementitious grouts are typically used, with the latter displaying a larger material compatibility with the masonry substrate.

Special mesh sleeves can be wrapped around the bar to help controlling the amount of injected material. For instance, CINTEC International, industrial partner of this research activity, provides the installation of masonry anchoring systems supplying a permeable fabric sleeve (known as “socket”) into which a high-strength grout is pumped. The flexible sleeve restrains the grout flow and expands to up to twice its previous diameter, moulding itself into the shapes and spaces within the wall. This type of anchor is particularly suitable for use with hollow or perforated masonry units and in voided masonry generally, including rubble stonework. This system provides a chemical bonding between the grout and the steel rod and a chemical/mechanical bonding between the inflated sleeve and the parent material.

The knowledge concerning the behaviour of anchors in masonry is still not exhaustive, as the experimental research in this field is limited (Gigla and Wenzel 2000; Arifovic and Neilsen 2006; Paganoni and D'Ayala 2014; Moreira et al. 2014; Silveri et al. 2016; Ceroni, Cuzzilla, and Pecce 2016; Ceroni and Di Ludovico 2020) compared to the availability of scientific studies on anchors injected in concrete elements.

Most of the tests performed on anchors in masonry aim at evaluating the bond capacity and ultimate strength capacity of the anchors for the numerous parameters that can influence the behaviour of anchors, such as type of masonry substrates, anchor's material, surface and length of embedment, anchor's diameter etc. To this purpose, pull-out tests on single masonry panel are performed and empirical formulations are obtained to predict the maximum load capacity. A complete review of the experimental pull-out tests available in the literature on grouted anchors is presented in Chapter 5, with reference to the testing activity carried out by the author to validate the behaviour of the innovative anchoring system connected to a masonry wall.

Despite the numerous testing activities carried out to assess the load capacity of anchorages, the effectiveness of grouted anchors to connect two adjacent walls is rarely experimentally pursued. Therefore, it is not surprising that field observations made after recent earthquakes have revealed that poorly designed anchoring systems can cause of local failure of reinforced masonry buildings (Wilkinson et al. 2013; Putrino and D'Ayala 2018). Pull-out tests on adhesive anchor connections conducted in existing buildings damaged by the 2011 New Zealand earthquake have highlighted that the adhesive type, the strength of the masonry materials the anchor depth and anchor rod diameter play an important role in determining the capacity of this anchoring typology (Dizhur, Schultz, and Ingham 2016; Derakhshan et al. 2014). In particular, it was found that longer embedment length and higher masonry compressive strength increase the maximum pull-out load of anchors, while a reduction of capacity was found increasing the rod diameter from 16 mm to 20mm. This is due to the larger diameter hole which determines a reduction of the brick cross-sectional area, which in turn causes the split of the brick.

Notwithstanding the number of technical solutions available for the improvement of structural connections by means of metallic anchors, the experimental testing of such connections is rarely performed, leaving the end users to comply with the code requirements with the only support of qualitative indications.

Nevertheless, a few experimental campaigns have been devoted to the assessment of structural connections, both in unreinforced and strengthened configurations. In these activities, scaled mock-ups have been tested by shaking table tests to determine the beneficial influence of anchoring solutions. Where time or financial constrains would not allow the tests on mock-ups, the strengthening solutions were assessed on subassemblies including two or more walls. These generally consist of a masonry panel loaded in the out-of-plane direction and, in some cases, two side wall returns, which are either fully connected to the front wall or detached so as to simulate pre-existing damage. However, materials, geometry of the front and wing walls, and strengthening systems greatly vary from author to author. Al Shawa (2011) for instance, performed a set of shaking table tests on three C-shaped brick walls strengthened by different techniques, including steel ties (Figure 2-4a). Indirli and Castellano (2008) carried out a set of shaking table tests on brick walls simulating a portion of a church façade connecting it to a stiff steel frame representing the rest of the structure, as shown in Figure 2-4b; different strengthening elements were used at the interface between the two.

a) b)

Figure 2-4 Masonry mock-ups used in the shaking table tests a) Al Shawa (2011), b) Indirli and Castellano (2008)

Recently few attempts have been made to quantify the beneficial effects of anchoring systems on wall connections. An experimental program was carried out by Paganoni and D'Ayala on the T-shaped masonry connection shown in Figure 2-5 a, strengthened with stainless steel anchors (Paganoni and D'Ayala 2014). Two experimental campaigns on masonry corner connections strengthened by metallic grouted anchors were conducted, proving that the testing set up, shown in Figure 2-5a was suitable to identify the most recurring failure modes. The main performance thresholds, such as first damage, maximum load, and maximum displacement before loss of capacity were determined. The quantitative data aim at informing the design of grouted ties for the strengthening for structural connections of heritage structures.

Similarly, Maddaloni et al. (2016) performed experimental tests under monotonic or cyclic horizontal displacements on T-shaped wall (shown in Figure 2-5 b) in three different configurations: as-built, repaired, and strengthened by a grouted anchors made by hollow CFRP pultruded carbon tubes wrapped with a stainless-steel fabric. The experimental results show that the proposed innovative strengthening technique may be a sound alternative to traditional steel-based connections and may be a suitable system in the case of historical buildings.

a) b)

Figure 2-5 Experimental set-up for almost-static tests of masonry connections strengthened by anchoring systems a) Paganoni and D'Ayala (2014), b) G. Maddaloni et al. (2016)

All the above-mentioned techniques have proved to significantly increase the strength and/or stiffness of the resisting structural elements allowing the structure to resist the earthquake-induced forces while remaining in the elastic range. Some of them can also provide a certain level of ductility to the structure, further improving the performance of the building. However, they present drawbacks, such as high local stiffness or mechanical incompatibility in respect to the existing material and in general are not in line with the current trend in seismic engineering design which foster the use of system able to provide ductility and energy dissipation capacity to heritage buildings.

A review of such systems is presented in the next section. This section has also highlighted that experimental testing is crucial to understand structural connections, which in turn determine the response of historic buildings to seismic excitations. For this reason, the ultimate validation step of the proposed dissipative anchoring system will involve the testing of the complete assembly implemented in a T-shaped connection of walls. The set-up, presented in Chapter 5, will draw on the ones proposed by Paganoni and D'Ayala (2014) and Maddaloni et al. (2016) aiming at providing a benchmark for future test of strengthened connections.

2.4 Passive control systems in current engineering practice

In contrast to capacity base design, the evolution of seismic structural design led to the understanding that well-designed structures can deform inelastically to the deformations imposed by the seismic actions without loss of strength (Calvi et al. 2008). This approach allows to reduce the intensity of the expected inertia forces induced by the ground motion by an R factor, proportional to the available ductility capacity of the structural system (EN 1998:2005-1). The inelastic deformation implies that a certain level of damage is allowed, but not collapse.

Accordingly, international guidelines have defined a set of limit states to define the performance requirements of structures with respect to a design seismic action, and performance-based design procedures have been proposed to optimize the structure for multiple seismic action levels. These procedures encourage the use of systems, such as damping and base isolation devices, to allow for a considerable level of control on the structural performance.

Drawing on these considerations, several passive control systems have been developed either to decrease the seismic demand by means of seismic isolation or to increase of the dissipative capacity of the structure through the enhancement of its ductility or the use of additional dissipative devices. While many solutions are available for new or recently built structures, only few options have the potential of being implemented in historic masonry buildings. Such choices are limited by the conservation principles previously introduced.

In this section, the available options for the improvement of the seismic capacity of existing masonry structures, without involving an increase of elastic energy, are reviewed.

The innovative anchoring system proposed in this work dissipates energy through friction and falls into the category of passive control systems as its activation is triggered by the magnitude of seismic energy imparted to the system. Therefore, particular emphasis is given to passive control systems tailored for the use on historic masonry structures which agree with the present architectural limitations of ICOMOS.

2.4.1 Base isolation systems

Base isolation concept was coined by engineers and scientists as early as the 1920’s (Patil et al. 2012), but practical applications of this concept became reality within the last 40 years with the development of multilayer elastomeric bearings (Naeim et al. 1999). The principle in base isolation technique consists of essentially decouple the structure from earthquake ground

motions by providing separate isolation devices between the base of the structure and its foundation (Clemente, De Stefano, and Zago 2012).

Base isolation systems have been adopted as an innovative retrofitting strategy for the enhancement of the seismic performance of some monumental building. Several countries, such as the USA, New Zealand, Japan and Italy have adopted this solution. In the USA, examples of this implementation are Ninth Circuit U.S. Court of Appeals building located in San Francisco, which suffered damage during the 1989 Loma Prieta earthquake (A. S. . Mokha et al. 1996) and the Utah state Capital Building (USA) (Johnson 2005). In both cases the use of strength-only approach was deemed unacceptable, as the increased stiffness would cause higher levels of horizontal forces leading to damages to the ornamentation and other precious features of the building. The implementation effectively achieved life safety criteria and minimized damage but the installation presents a highly invasive nature that required the complete removal and replacement of the existing footing and foundation (Johnson 2005). In New Zealand following the Christchurch earthquake of 2011, it was found that base isolation systems allowed mid-rise (in general isolation systems are not feasible in taller building) unstrengthened masonry (stone or bricks) buildings to prevent major damages and protected the safety of occupants (Zahrai and Yazdani 2014). In Italy and Japan seismic isolation systems have been implemented on buildings catalogued as of historical interest such as the *Archivio di Stato* (D'Amato, Gigliotti, and Laguardia 2019), which dates back to 1930, and the National Museum of Western Art in Tokyo designed by Le Corbusier in 1958 (Nakamura and Okada 2019).

De Luca et al. (2001) conducted laboratory seismic testing of a full-scale model representing part of the façade of the S. Vincente de Fora monastery in Lisbon. The model retrofitted with base isolation system displayed an improved behaviour compared to the response obtained for the fixed-base model. Depending on the earthquake input and on the rubber isolators, the masonry part above the isolators experienced displacements from 2.8 up to 24 times smaller than the ones registered in the fixed-base test model. Accordingly the forces are reduced up to 15 times and no cracking in the masonry elements of the specimens have been observed following the base isolation test (De Luca et al. 2001). Despite the good laboratory results on the effectiveness of this technique, the implementation of an isolation scheme is often economically demanding, as new foundations need to be excavated and a system of piles which temporarily bears the loads needs to be casted.

Recently, this type of intervention has been proposed for the seismic rehabilitation of Palazzo Margherita in L'Aquila, whose structure suffered damages during the 2009 L'Aquila earthquake

(Clemente and De Stefano 2011). This solution was deemed the most feasible based on the results obtained from a microzoning analysis carried out after the seismic event and allowed to obtain, in principle, a good structural result without compromising the architectural characteristic of the superstructure, which dates back to the sixteenth century. However, in a later stage of the design process, this solution was not implemented due to high irregularity of the foundation, and a combination of strength-only techniques were preferred, such as the Reticulatus, internal FRP jacketing and metallic anchors (details available here https://www.iesingegneria.eu/project-single.php?project=25).

Although isolation systems have been successfully implemented in some historic buildings, the major limitation is the topology and strength of the existing foundations. In order to be implementable, the foundations need to be well defined and recognisable, as for the case of the above-mentioned buildings which were built in the past century. However, the large majority of heritage structures have irregular and weak foundations, as they were built centuries ago (Palazzo Margherita in L'Aquila dates back to 1294) so that the isolation systems are seldom a viable option, without substantial geotechnical expensive work.

2.4.2 Damping devices

Passive energy dissipation systems utilize a wide range of materials and technologies to enhance the damping, stiffness and strength characteristics of structures. Compared with the isolation systems presented in the previous section, energy dissipation systems can be applied in a broader context and the construction cost are substantially lower than for base isolation (Pall et al. 2004). According to the performance-based classification scheme (e.g. FEMA 1997), passive energy dissipation systems are categorized depending on the way the dissipation is achieved, namely by the conversion of kinetic energy to heat or by the transferring of energy among vibrating modal shapes, i.e. shifting the energy to higher modes of vibration (Constantinou et al. 1998).

The first mechanism incorporates both **hysteretic devices** that dissipate energy with no significant rate dependence, and **viscoelastic devices** that exhibit considerable rate (or frequency) dependence. Included in the former group are devices that operate on principles such as yielding of metals and frictional sliding, while the latter group consists of devices involving deformation of viscoelastic solids or fluids (Soong et al. 2002).

The second mechanism, pertaining to the transfer of energy between modes, is utilized in dynamic vibration absorbers. In these systems, supplemental oscillators are introduced, to

transfer some of the structural vibrational energy from the primary structural members to the absorbers. Although they have been proposed for seismic design, the primary applications to date have been for alleviation of vibrations due to wind loading (Petrini, Giaralis, and Wang 2020)

In case of heritage structures, several researchers explored the concept of embedding multiple oscillating units of significant mass into the ground around structures to filter out incoming seismic waves within a certain frequency band in which resonant structural frequencies lie (Woods 1968; Palermo et al. 2016).

In this manner, these metamaterial-like structures act as shields/barriers for seismic waves of significant structural damage potential. Nevertheless, the abovementioned approaches for non-invasive seismic protection of structures address only surface seismic waves and cannot control structural response due to body seismic waves, which may be significant especially in near-fault conditions. To this end, an alternative approach, termed vibrating barrier (ViBa), was proposed by Cacciola and Tombari (2015), to dissipate seismic kinetic energy rather than reflecting or refracting the various types of seismic waves. Specifically, ViBa comprises a free-to-vibrate mass encased in a rigid containment buried in the ground and connected to the walls of the containment through linear springs and dampers.

To date, several studies on the efficiency of the ViBa have been carried out to investigated the potential of ViBa for the seismic protection of heritage buildings: Shadlou et al. (2019) applied ViBa to control the seismic response of the Zoser Pyramid demonstrating by finite element analysis that this technology can reduce the Von Mises stresses by 40% especially in those areas where the damages caused by the 1992 Cairo Earthquake have been observed.

Nevertheless, the effectiveness of ViBa in containing structural seismic response demands is positively correlated to the inertial property, namely on the ViBa mass, which may result in significant excavation and construction cost. To address this major limitation, an inerter can be incorporated, thus called IViBa, to act as an inertial/mass amplifier. Although never applied to heritage buildings, this technology has the potential to reduce the motion of an adjacent seismically excited structure with contained excavation costs (Cacciola, Giaralis, and Tombari 2020).

Viscous dampers

Viscoelastic energy dissipation systems include devices consisting of viscoelastic solid materials and devices operating by deformation of viscoelastic fluids. They exhibit stiffness and damping coefficients that are frequency dependent and damping forces proportional to velocity (Constantinou et al. 1998). Their typical force-displacement loops are illustrated in Figure 2-6.

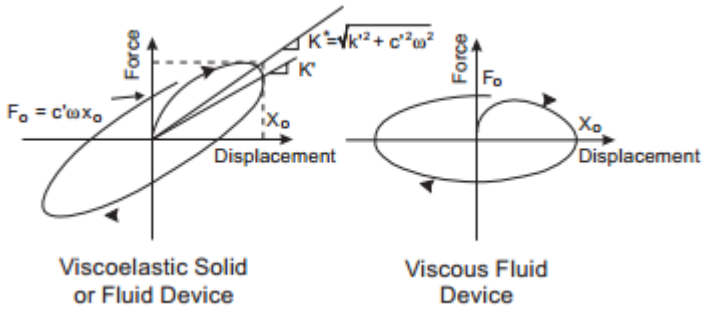

Figure 2-6 Idealized Force-Displacement Loops of Viscoelastic Energy Dissipation Devices (from Constantinou et al. 1998)

They consist of a hollow cylinder filled with fluid, often silicone based, and a piston. As the piston moves, the fluid is forced to flow through orifices either around or through the piston head. The resulting difference in pressure across the piston head can produce very large forces that resist the relative motion of the damper; input energy is dissipated in the form of heat due to friction between the piston head and fluid particles flowing at high velocity (Soong et al. 2002). Conversely, since these devices are velocity-dependent, slow movements, such as thermal expansions, can occur without producing high reaction forces. Viscous dissipative dampers have been employed for the seismic upgrading of heritage structures. In the early 1990's, the applicability of these dampers was tested in Italy for the seismic rehabilitation of buildings of special cultural and historic interest (Mazzolani 2001). The first two applications of viscous dissipative dampers to cultural heritage building were the church of St Giovanni Battista in Carife in 1990 and the new library of the University of Naples in 1996. In both cases, oleo-dynamic devices were used to couple the new roof structure to a reinforced concrete ring beam cast on top of the masonry walls, thus ensuring a better redistribution of the horizontal loads among different walls (Mazzolani 2001). Following the experience of Carife and Naples, few years later, in 1999, the St Francesco Church at Assisi, damaged by the Umbria earthquake in 1997, was consolidated and restored with the combined use of oleo-dynamic devices and shape memory alloys devices (Indirli et al. 2008). This strengthening solution will be discussed more in detail with reference to shape memory alloys materials.

Recently, Giresini et al. (2021) developed an innovative anti-seismic device called LICORD, able to control the out-of-plane motion of masonry walls. The system consists of a set of viscous shock absorbers connected to the extremity of traditional tie-rods, aiming at combining traditional and innovative system, as proposed by D'Ayala and Paganoni (2014). The system was experimentally tested as connected to a masonry wall undergoing free rocking motion from an initial displaced position. The system proved to reduce the oscillations amplitude, especially adjusting the damping factor of the absorbers to optimize the response, which reduces the number of impacts of the wall and avoids the brittle failure of the tie. However, the design of the LICOND system appears quite invasive as illustrated in Figure 2-7 and its performance was assessed with respect to a set of forces which are significantly smaller than the ones expected during a seismic action. As stated by the authors, despite the initial promising results, further testing will be required to validate the system.

Figure 2-7 masonry wall equipped with LICORD system, credits to Giresini et al. (2021)

Hysteretic systems

Examples of hysteretic systems include devices based on yielding of metals or through sliding friction. Typical force-displacement loops of hysteretic energy dissipation systems are shown in Figure 2-8. Hysteretic systems are often called displacement-dependent, as their behaviour involve algebraic relations between force and displacement (FEMA 1997).

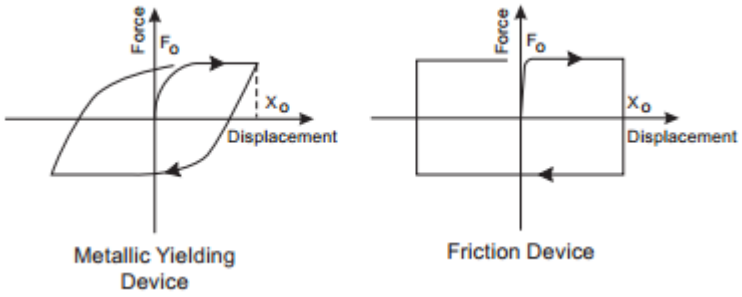

Figure 2-8 Idealized Force-displacement Loops Hysteretic Energy Dissipation Devices (from Constantinou et al. 1998)

Added Damping and Stiffness (ADAS) dampers, and Buckling-Restrained Brace (BRBs), are examples of yielding devices. The first consisting of a series of steel plates connected to the floor level which achieve energy dissipation by plasticly deforming under seismic loading, thus preventing the primary structural elements, usually the beams, from deforming inelastically. Such metallic devices find a number of application for retrofit both existing and new structures (Soong and Spencer (2002), Vasdravellis et al. (2014), Mohsenian and Mortezaei (2019), Baiguera et al. (2019)) having proved to be not substantially influenced by temperature and having a stable hysteretic behaviour

Buckling-restrained brace (BRBs)feature an external case enclosing a metallic core (the yielding component) surrounded by a a filler material, often mortar. The case allows for the BRB to develop a stable yielding behaviour both in tension and in compression avoiding buckling, as demonstrated in many experimental campaigns (e.g. Di Sarno and Manfredi, 2012).

A system for retrofitting masonry structures based on a hysteretic behaviour was proposed by D'Ayala and Paganoni (2014). The proposed dissipative anchoring system comprises a device designed to have variable cross-sectional area and lower yielding strength than the one of the threaded bars to which the device is connected. This means that, for a given level of axial force acting on the assembly, different sections feature different stress levels, but only the dissipative element undergoes yielding, as proved by extensive laboratory activities. The device underwent on site validation by installation in the Oratory of S.Giuseppe dei Minimi in L'Aquila, which reported serious damages as result of the seismic event of the April 2009. One wall of this historic building presented evident out-of-plane damage, which is the typology of damage mechanism that the dissipative anchoring device mainly aims to prevent and control. The system was able to deliver a performance similar to that of the standard anchors, but with the non-negligible advantage of preventing damage at the anchor heads (Paganoni 2015).

Compared to shape memory alloys devices, a steel-yielding device has the advantage of being less expensive and easier to design given the constitutive law of steel is well known by professionals.

The DIS-CAM (DISsipative Active Confinement of Masonry) system is also based on the post-elastic behaviour of steel. This was proposed by (Dolce et al. 2009) for the seismic upgrading of the drum supporting the dome of the S. Nicolò's church in Catania (Italy). The system consists of angle steel plates welded in correspondence to the corner of the openings, connected by net of steel ribbons. During a seismic event, the dissipative capacity is provided by rocking behaviour of the masonry panels, which stress the steel elements over their elastic limit. A net of steel ribbons limits the allowable rocking motion of the panels to prevent the ultimate failure of the structure. The system was applied on scaled models representing the shape and materials of the real dome and experimentally tested by shaking table for increasing intensity of natural earthquake records. Compared to other strength-only solutions, the dissipating capacity of the dissipative elements allowed the dome to resist higher seismic accelerations without damage. The CAM system was recently used to establish a connection between two flat FRP reinforcements applied on the two sides of a masonry wall (Ferretti 2020). This system proved to increase the in-plane and out-of-plane strength, as the pre-tensioning of the CAM strap determines a more rigid connection between the FRP strips. Moreover, the steel straps of the CAM can yield providing ductility to the wall, thus compensating for the brittle behaviour of the FRP. However, the system, illustrated in Figure 2-9, appears quite invasive, several holes need to be drilled to secure the CAM system and round angles need to be implemented to avoid stress concentrations at the edges.

Figure 2-9 Strap/strip technique developed by (Ferretti 2020)

Among the yielding dissipative dampers, Shape Memory Alloys (SMAs) have received considerable interest from the research community of earthquake engineering because they exhibit self-centring capability on the material level. SMAs are classified as high-performance metallic materials that can undergo large strains and still recover their original shape. SMA dampers are frequently classified as hysteretic for their negligible rate dependency. However, experimental tests have demonstrated that Nichel-Titanium Alloy can present a significant influence on the mechanical behaviour, altering the hysteresis loops and the transformation stresses (I. Schmidt 2004). Conversely, other alloys, such as Cu-based alloys, show no significant influence on the shape of the hysteresis curve and energy dissipation capacity as reported in the finding of Araya, Marivil, and Cristóbal (2008). This unique feature of SMAs is due to the reversible transformations between two phases, namely, Austenite and Martensite.

Recent studies have extended the use of SMAs to seismic resilience design because their excellent super elasticity with a recoverable strain (up to 8%) offers simple realization of self-centring capability. Moreover, SMAs possess high resistance to fatigue and corrosion (similar to stainless steel). Examples of super elastic SMA-based self-centring devices or structural members utilized in civil structures include SMA braces (S. Zhu et al. 2014), SMA base isolators (Casciati et al. 2007), SMA dampers (Li et al. 2014), and reinforced concrete members with reinforcing superelastic SMA bars (Shahverdi et al. 2016). Wang and Zhu (2018) also explored the cyclic behaviour of SMA bars under tension-compression loading, managing to prevent the compression-induced buckling by adding a buckling restrain device around the dog boned-shaped SMA sample.

In 1999, Shape Memory Alloys Devices (SMADs) were used to consolidate three historical masonry building, which were damaged by the Umbria-Marche (Italy) earthquake in 1997, namely the St Francesco Church at Assisi, San Feliciano cathedral in Foligno and San Serafino Church in Montegranaro, as reported by Mazzolani (2001). Thanks to their special thermo-mechanical properties, the SMADs, used in series with horizontal steel ties allow for controlled displacement of the masonry wall under low-intensity earthquake and can increase their stiffness under extraordinary horizontal actions to prevent the ultimate failure of the structure(Indirli and Castellano 2008). The strengthening intervention carried out at S. Francesco Church aimed to contain the pounding action between the tympanum and the concrete roof beam (inserted in the 1960’s) that had also caused the collapse of the transept vault. The beneficial effect of the introduction of the SMA devices is twofold: under service load and low intensity horizontal actions (wind, small-intensity earthquakes), the SMAD is

rigid, and no displacement is allowed, similarly to a traditional steel anchor. In contrast, under higher intensity horizontal actions (stronger earthquakes) the SMAD stiffness lessens, allowing for “controlled displacements” that permit the masonry to dissipate part of the energy transmitted by the earthquake, mainly thanks to the formation of micro cracks in the brick walls, taking care to avoid dangerous macro cracks. Moreover, due to the reduced stiffness of the SMADs lower forces are transmitted to the historic building, which should be able to sustain the seismic load of a high intensity earthquake (Bonci et al. 2000). The strengthening intervention carried out with these devices are largely depending on the case study, with load capacity and maximum allowable displacement ranging from 17 to 52 KN and between ±8 to ±25 mm (Indirli and Castellano 2008). The implementation of the system is illustrated in Figure 2-10.

Figure 2-10. Photographs of the SMA device insertion for the Assisi Basilica tympanum (IT) (Indirli and Castellano 2008);

The same innovative materials have been used in the retrofitting of the bell tower of St George Church in Trignano (Reggio Emilia). Here, pre-tensioned ties in SMA were anchored on the foundation and the structure was able to survive with minor damages a successive seismic event in 2000 (Casciati and Faravelli, 2009). Pre-tensioning of the SMA ties is essential to achieve energy dissipation under low intensity earthquakes or the ties are most likely to remain in the linear elastic range during the seismic event (S. Zhu et al. 2014). Dolce et al. (1999) proposed the implementation of two separate groups of SMA elements to achieve re-centring of the structural system and energy dissipation capacities in a structure. The devices are made of two moving parts (tubes) designed to display relative motion during seismic action between their extremities, which are connected to moving parts of the structural systems. The re-centring objective is achieved by means of two studs inserted transversely in the tubes which are pre-stressed to provide a supplemental re-centring force.

In general,, the cost of these materials is high but not prohibitive and are competitive with the cost of other seismic retrofitting system, such as isolation system based on high damping rubber bearings (Dolce at al. 1999). On the other hand, the use of SMA-based devices needs specialized knowledge of the super-elastic properties of SMAs and the related supplemental re-centring capabilities, thus the costs related to the design of structures with this passive control system can be demanding.

In contrast, friction-based dampers dissipate energy by converting kinetic energy into heat by friction. The formula describing the friction resistance at the instant of imminent sliding or during sliding itself is obtain as:

$$F_{fric} = n \, \mu \, F_{perp} \tag{2.1}$$

This law, referred as "Coloumb's Law of Friction", states that the frictional force (F_{fric}) generated at the interfaces between the sliding element and a number of surfaces (n) is proportional to the perpendicular force (F_{perp}) exerted on the sliding element by means of a friction coefficient (μ) (Constantinou et al. 1998).

A first examination of the effects of frictional damping on the response of building structures was conducted by Mayes et al. in 1975, but it was Keightley in 1977 to study the applicability of frictional dampers on multi-storey buildings. Subsequently, Pall et al. (1980) continued the development of passive frictional dampers to improve the seismic response of structures. In analogy to the automobiles' brake system, Pall outlined the objective of friction dampers which is "to slow down the motion of vibrating buildings by braking rather than breaking" (Pall et al. 1982).

One of the main advantages of friction devices is the rectangular shape of hysteresis loops that dissipate a large amount of energy. As such, friction devices have many applications and are thoroughly studied (A. Pall and Marsh 1982; Ciampi et al. 1995; Mualla and Belev 2002; Soong and Spencer 2002; Rojas et al. 2005; Christopoulos et al. 2008; Freddi et al. 2017; Latour et al. 2018). Currently, available devices differ for functioning principle and typology of material used as friction interface.

For bolted-slotted dampers, for instance, the slip load at which the device starts its relative movement is controlled by the pressure applied by bolts on a series of metallic profiles. One example of such devices is the Pall Friction Damper, which has been applied for new

construction and for retrofit of existing buildings (Avtar Pall and Pall 2004) on more than 250 major buildings across U.S.A, Canada, Mexico and Philippines.

A simple design for Slotted Bolted Connection was proposed by Latour et al. (2018) and Nastri et al. (2019) to improve the behaviour of beam-to-column connections under seismic action. Latour proposed the integration of beam-to-column joints by means of a removable friction damper located at the beam flange level, as shown in Figure 2-11a. The friction pad is designed to activate under severe seismic loading conditions to protect the primary connection components from damage. Friction based devices can also be implemented at the column base connection with the goal of overcoming the shortcomings of conventional column bases. In terms of strength, column bases are typically designed as full-strength so that plastic hinges are developed at the bottom end of the column, inducing non-repairable damages. In this sense, Freddi et al. (2017) presented a rocking damage-free steel column base (Figure 2-11b), which uses post-tensioned high-strength steel bars to control rocking behaviour and friction devices to dissipate seismic energy. The friction device consists of two steel plates bolted to the base plate and two plates of brass material interface. Under seismic load the rocking of the column base results in relative sliding of the steel and brass elements and, thus, in energy dissipation due to friction.

a) b)

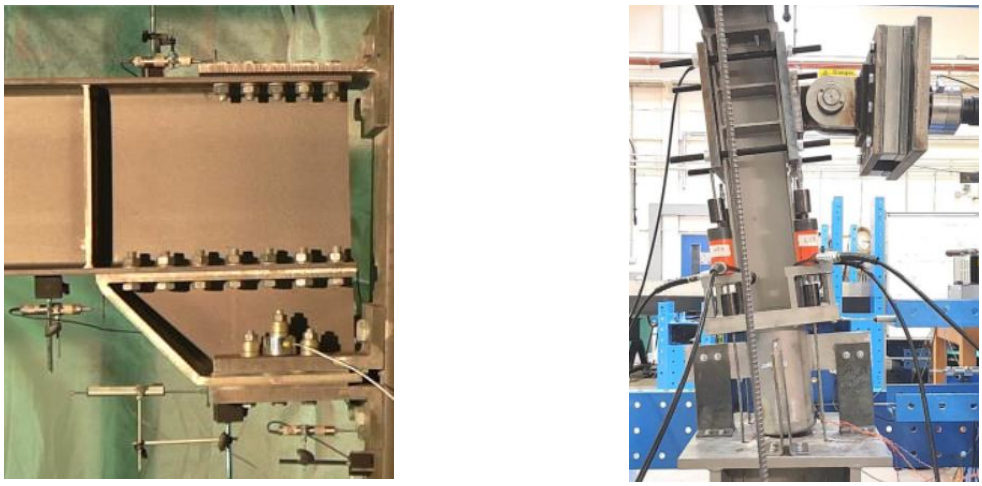

Figure 2-11 Friction-based devices located at the a) beam flange level (Latour et al. 2018) , b) column base (Freddi et al. 2017)

A second category of friction-based devices is represented by the uniaxial friction devices. They are composed by an assembly where the compressive force developed by a spring acts on wedges and provokes a normal force on the internal surface of a cylinder, which controls the sliding motion (Aiken et al. 1993). The device developed by Surimoto Metal Industries Ltd.

and the friction damper manufactured by Fluor Daniel, Inc. are two examples of uniaxial friction devices. They have a similar design, but the damper produced by Fluor Daniel can be adjusted to the desired slippage force and can generate self-centering loops, thus avoiding the presence of residual deformation (Nims et al. 1993).

Christopoulos et al. (2008) proposed a similar design for a bracing system able to eliminating residual deformations. The system consists of two bracing members and a energy dissipation system which activates when the braces undergo large axial deformation. The recentering capability is provided by tensioning element by providing sufficient pretension to overcome the force required to activate the energy dissipation mechanisms. An illustrative sketch in Figure 2-12 describes the funtioning and design of the system.

a) b)

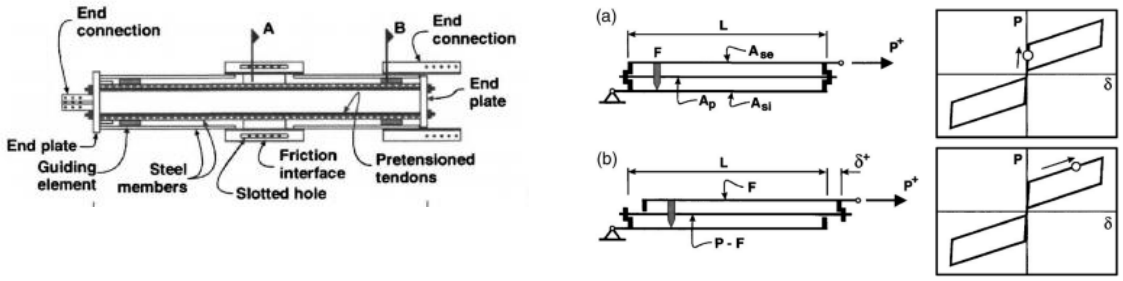

Figure 2-12 a) Design of self-centering system proposed by Christopoulos et al. (2008), b) mechanics and hysteretic response

It is clear from Equation 2.1 that in order to predict the slippage load of a friction-based device, an accurate knowledge of the clamping force (F_{perp}) and of the friction coefficient (μ) are required. In general, the clamping force can be easily controlled applying one of the tightening procedures proposed by EN 1090-2 (i.e. torque method, combined method, direct Tension Indicator TDI). Experimental analysis regarding the accuracy of the tightening procedures proposed by EN 1090-2 have assessed the time-related loss in bolt pretension, to ensure that a minimum level of prestressing is kept over the full life of a structure, i.e. at least 50 years (Antimo et al. 2017). Extrapolating the short-term data, it was found a 50% loss in bolt pre-tensioning within first 18 hours after the loading procedure, as shown in Figure 2-13 (Ferrante Cavallaro et al. 2018). Disc springs and flat washers can be used to maintain the initial pre-load as shown in Figure 2-13). However, disc springs do not behave inelastically, but are able to push the bolt and restore the preload force initially applied only if loaded within their elastic capacity. Therefore, for higher values of bolt loading conical washer should be applied as they proved to reduce the preloading loss. As reported by D'Antimo et al. (2020) a loss of about 8%

over a period of 50 years can be estimated if a combination of Belleville flat washers is used, extrapolating the recorded loss over a period of five months.

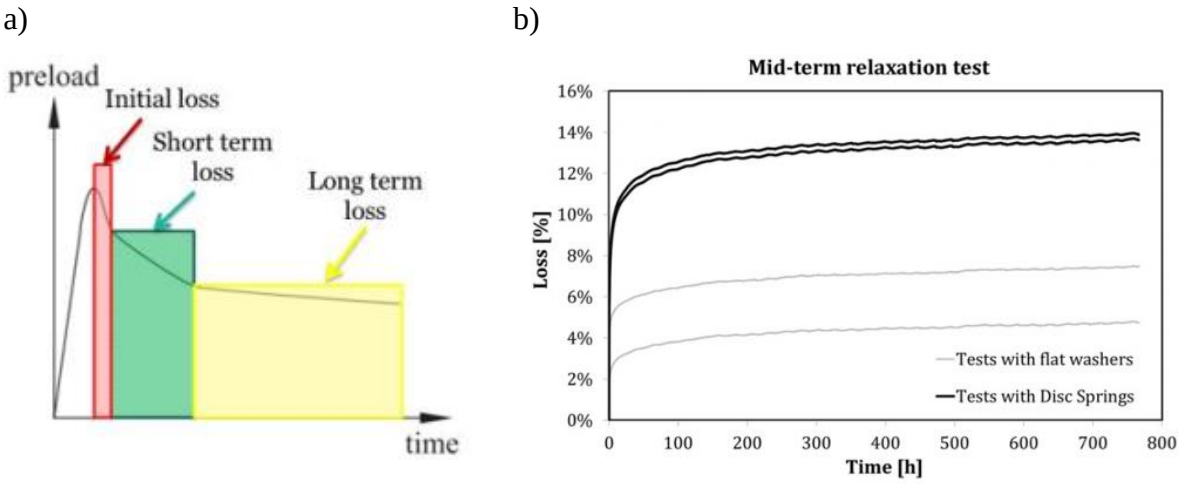

Figure 2-13: a) Loss of preload over time b) Medium-term relaxation tests results of pretension loss in bolt connection (Ferrante Cavallaro et al. 2018).

The second parameter that determines the slip force is the friction coefficient (μ), which depends on the type of materials employed to realise the dissipative interface of the damper and can be difficult to predict because of its dependence on several micro and macroscopic factors (hardness, shear resistance, roughness, superficial finishing of the interface materials). Therefore, experimental tests need to be performed on the chosen material to characterize its frictional properties and correctly dimension the friction-based device

Among the different materials that can be used for friction-based dissipative devices, some of them are preferred over others, either for their good performance or their low cost. In general, a high value of coefficient of friction is desired for a friction damper in order to reduce the size of the device and the bolt preload (Latour 2014). Latour (2014) studied six different interfaces under cyclic load, namely steel–steel interface, brass–steel interface, sprayed aluminium– steel interface and three interfaces adopting different types of friction rubber-based materials, obtaining the friction properties of the coupled frictional interfaces. For the steel materials, it was found that the steel-on-steel interface exhibited a high value of friction coefficient (μ =0.4) but a most unstable behaviour, softening rapidly after a hardening behaviour. Conversely, brass on steel interface exhibited a lower friction coefficient (μ =0.2), but with a stable and hardening behaviour. Thermally sprayed aluminium on steel interface exhibited the highest friction coefficient (μ =0.6), and a stable behaviour, with small degradation. The results of three types of rubber materials sliding on steel showed that rubber materials produce low friction resistance

(μ =0.15) but produce stable force-displacement loops with low material degradation. Drawing on these results, a friction-based device made of steel plates coated with sprayed aluminium was implemented in a beam-to-column joint (Latour et al. 2018), achieving stable hysteresis loops over 50 cycles of load, even if a significant difference (about 20% of variation) between static and dynamic friction coefficient was identified.

Despite the abundance of friction-based devices available, very few friction dampers have been designed and tested for historic masonry structures.

D'Ayala & Paganoni (2014) developed, in collaboration with Cintec International, a friction-based dissipative device specifically designed for reducing the damages induced by seismic events on historic masonry structures. The device is connected in series with metallic steel ties and the assembly is inserted at the corner connection between two adjacent walls (Figure 2-14), typically along the corner connection between the façade and the side walls of a church.

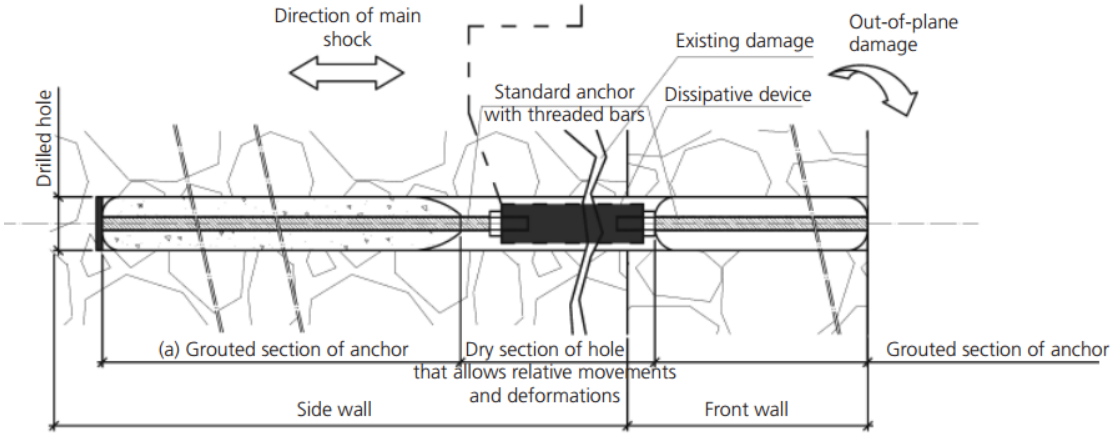

Figure 2-14 Set-up of dissipative anchor device coupled with standard grouted anchor and installed at damaged corner connection (D'Ayala and Paganoni 2015)

For low intensity excitations (wind load, low intensity earthquakes) the system behaves rigidly, not allowing any relative displacement between the connected elements. For high intensity excitations (strong earthquakes), a controlled displacement is allowed up to 20 mm by means of a pin inserted in the device. The device underwent computational and experimental validation, and presents repeatable hysteresis cycles, while the connection to the rest of the anchor remain elastic, thus ensuring ease of replacement in the aftermaths of a seismic event, as required by BS EN 15129:2009 (BSI 2009). Nevertheless, the slip load recorded throughout the experimental testing is not consistent due to mechanical locking and presence of metallic dust within the assembly produced by the progressive wearing of the frictional surfaces. This issue might lead to difficulties when dimensioning the device (Paganoni and D'Ayala 2010).

An energy dissipation device based on friction was developed for masonry structures by Totoev (2015), but it is limited to mortar-less walls made of Semi-Interlocking Masonry (SIM). Compared to traditional masonry walls, SIM infill panels act as energy dissipation devices, as they dissipate earthquake energy through friction between bricks, while the out-of-plane relative movement is hindered. This system proves that friction-based systems significantly improve the energy dissipation capacity, but the SIM dissipative device is not suitable for historical buildings, where the mortar is typically the bonding agent between blocks and the relative motion between courses would represent a source for local and global structural failure.

A solution for single nave churches was proposed by Preti et al. (2019), where energy dissipation is obtained by installing friction-based devices at the corners of the roof diaphragm, enabling the deformation of the structure under lateral loads. Tests on a full-scale 2x2m portion of such "dissipative diaphragm" shows that the use of friction dampers reduced the shear demand transferred to the facade in comparison to a stiffer roof. The average maximum drift demand for such flexible diaphragm, 0.6% as reported by the authors, is well within the range of the undamaged transversal response of masonry arches, measured in other experimental campaigns (Bolis et al. 2017; Alshawa et al. 2012). Nonetheless, for churches with vaulted ceilings or in presence of precious finishing such as frescos and bas-reliefs, such maximum drift may be unacceptable: stiffer roof diaphragm would be required to limit the maximum drift within acceptable values, which from experimental tests can be set at about 0.15–0.2% (Preti et al. 2019). Nonetheless, increasing the stiffness of such "dissipative diaphragm" is not recommended, as it would inhibit the self-centring capabilities of the system, leaving remarkable residual deformations.

2.5 Conclusions

Structural connections are crucial to understand, predict and control the response of buildings to seismic excitation. Damages and failure of historic structures during main earthquakes are often related to discontinuous or low-quality connections among structural elements. This structural weakness can be due to several reasons, such as the poor quality of original constructive techniques, the deterioration due to weathering and previous seismic events, the architectural modifications that are frequently carried out on monumental and residential buildings.

On-site observations find correspondence with analytical models able to correlate the mechanical properties, geometry and boundary conditions of masonry panels to observed damage modes, thus ascertaining the link between connections and seismic-induced damage. In particular, insufficient, weak connections are the primary cause of one of the most recurring failure mechanisms, namely the out-of-plane damage and overturning of masonry panels. This failure mode constitutes a risk for safety and human lives, and secondly seriously endanger unique heritage assets.

Accordingly, current design codes recommend the strengthening of connections in heritage buildings with the purpose of improving the overall structural response.

Reviewing the consolidation interventions for buildings with monumental features, it can be concluded that strength-only techniques are still widely applied in practice because some of them, like metallic cross ties, have been proven to restore the connection between adjacent elements without significantly increasing the overall mass. Nevertheless, even these systems are not exempt from drawbacks, such as pull-out failures, as the large number of failures in the aftermaths of recent seismic events have highlighted. This clearly shows that gaps still exist in the regulations regarding the design of seismic strengthening for structural connections, and this might have serious repercussions on buildings' performance.

Lack of standardisation also affect the development of innovative strengthening systems that can provide a higher level of ductility to the building rather than enhance its capacity only. Reviewing the variety of systems available, it is clear that the concept of energy dissipation and ductility can be applied to heritage structures; on the other hand, it is also clear that this is seldom done in practice. Mandara and Mazzolani's STUs and Fip's SMADs have been applied in practice to historical masonry structures, while, to the author's knowledge, other systems are still at the stage of experimental validation or have never been applied in practice. It is the case of the rocking-damper system DIS-CAM that was not implemented on a structure.

Therefore, besides notable exceptions, dissipative systems remain within the domain of scientific research, without much guidance being provided to end users who wish to implement such systems in real projects.

In the attempt of tackling such technical gap, an innovative passive control system specifically tailored for the seismic strengthening of heritage structures is developed.

In this system, the energy dissipation capacity relies on the presence of a friction-based device which exploits and controls the rocking behaviour that monumental structures often exhibit

during earthquakes. As highlighted in the review, friction-based devices offer a flexible design, as the mechanical parts and the slippage force can be designed for the load associated to the target displacement. Moreover, they can be dimensioned to have an activation threshold lower than the buckling critical load and the permitted displacement can be determined by the insertion of an internal pin that blocks the relative displacement of the device's parts. In terms of level of supplied damping, the energy dissipated per cycle by a friction device is larger than that dissipated in a yielding cycle for the same amplitude and load peak (M. C. Constantinou, Soong, and Dargush 1998). Devices made out of Shape Memory Alloys (SMADs) have the ability to dissipate a significant amount of energy with a negligible degradation and permanent deformation. In a typical usage, the strain range is about 6-8%, which provides them with very high-energy dissipation per unit mass of material. Nonetheless, SMADs are costly: on the market, a kilogram of Nitilon alloy bar is roughly £150, against approximately £30 for stainless steel grade 304 bar. Furthermore, physical behaviour of these alloys is complex to model and few specific software can be used for numerical analysis involving SMAs. These two issues cannot be overlooked when attempting to develop a strengthening system that should be both readily available and such that conservation-engineering professionals feel comfortable using it.

The initial prototype of friction-based device, developed and patented within a joint research project (FP7-NIKER), is the starting point for the present research. Its principal features have been presented within this chapter and are available in detail in two publications (D'Ayala and Paganoni 2014; Paganoni 2015).

In the next Chapter, it is described the validation methodology that led to the development of the next generation of dissipative anchoring system and the design method for its implementation.

This aims at tackling the lack of standardisation that still exist in the testing procedure of seismic system for strengthening masonry connections and the lack of practical tools for the implementation of such system in compliance with the principles of modern design.

3 Research methodology: validation and design procedure of dissipative anchoring system

3.1 Introduction

The increasing knowledge and awareness of the effect of structural connections on the seismic behaviour of heritage buildings, has led to the improvement of traditional systems and, most importantly, to the development of innovative techniques that rely on ductility and energy dissipation. A variety of these innovative systems have been tested and successfully implemented in several case studies, as discussed in Chapter 2.

Nonetheless, the clear-cut shift from force-based to displacement-based design that has characterized new structures has not affected to the same extent the research and the implementation of strengthening systems for heritage buildings.

As discussed in Chapter 2, the lack of guidance on the design of strengthening solution for masonry connections, elevated costs of the system's materials, and the difficulty of modelling their coupling with masonry structures led to the limited application of dissipative devices to heritage buildings. In fact, the main goal of the development of a dissipative device should not be the creation of something completely new, but rather the improvement of an existing strengthening techniques, which is already widely applied, familiar to the professionals operating in the field of conservation engineering, cost-effective and in line with the current conservation practice.

A successful example of this philosophy is represented by the grouted anchoring system proposed by D'Ayala and Paganoni (2014) and patented in joint partnership with Cintec International (James et al. 2011). The system, already discussed in Chapter 2, comprises an advanced anchoring technology, which is worldwide applied by professionals for conservation work, and a friction-based dissipative device, which provides large energy dissipation capacity and a flexible design.

The friction device prototype showed good results in terms of energy dissipation capacity and versatility. Nonetheless, the performance of the device was not consistent throughout the

experimental campaign, limiting its practical application (D'Ayala and Paganoni 2014). Nonetheless, the goal set for that research project was not explore all possible testing scenarios but rather provide a set of guidelines for the development of strengthening systems for historical connections. In this regard, their goal was fulfilled as their work clearly inspired the experimental tests performed in this research and by other authors (Maddaloni et al. 2016).

The promising results of the first prototype of friction-based dissipative device led to the research reported in this thesis, which aims at manufacturing the new generation of reliable dissipative anchoring system and define a design procedure for its implementation in line with the modern design codes.

To achieve these goals, a generic validation procedure applicable to dissipative devices is proposed. The procedure is developed to meet the code's requirements on the application of anti-seismic devices to heritage structures and it is demonstrated through the development and application of the D-GAS. Then a displacement-based design procedure is presented to verify that the performance of a heritage structure can significantly improve as a result of the dissipative anchor's implementation. In Section 3.2 a brief overview of the D-GAS is provided to present the principle underlying the functioning of the system. The methodology that guides the validation process of the D-GAS is outlined in section 3.3.

3.2 Properties of the dissipative grouted anchoring system

A Dissipative Grouted Anchoring System (D-GAS) comprises a friction-base device connected in series to a Grouted Anchoring System (GAS). The friction-based device, such as the one developed and patented by James et al. (2011) is shown in Figure 3-1a. Such device, designed to increase the performance of grouted tie anchors in the non-linear range, is connected to stainless-steel profiles (Figure 3-1b) that are encased in a fabric sleeve filled with grout. The assembly is then installed in holes core-drilled in the structure to connect orthogonal walls or walls to stiff diaphragms (Figure 3-1c). When the grout is injected in the flexible sleeves, they expand, thus moulding into the shape and space within the wall, providing mechanical and chemical bonding.

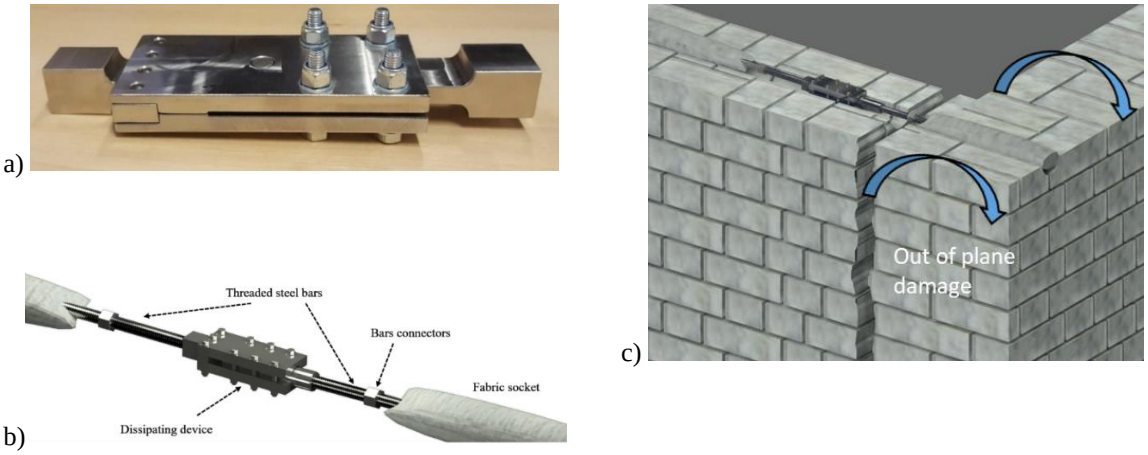

Figure 3-1 a) Patented design of the dissipative device, b) Insertion of the device at the connection between perpendicular walls

A Dissipative Grouted Anchoring System (D-GAS) can be schematically modelled as in Figure 3-2a by a system of springs representing the grouted anchors and the device. The strength of the grouted ties, $F_{bond,side}$ and $F_{bond,front}$, is determined once the shear strength developed between the grout and the parent material, and the embedment length L_t are known, assuming that the bond capacity is the weakest link in the system. Conversely, the device's strength F_{fric} is equal to the friction resistance the device is designed to provide. The system is adjusted to have F_{fric} at the bottom of the anchor strength hierarchy, so that, during an earthquake (Figure 3-2b), the detachment of the façade from the side walls activates the device and prevents the bonding failure of the anchors. Therefore, the device is tuned to activate for a slippage load equal to the estimated bonding resistance of the portion of wall which the anchors controls, and smaller than the bond that the two grouted steel elements can provide, namely $F_{bond,side}$ and $F_{bond,front}$. With reference to Figure 3-2b, the design check is expressed by Eq. 3.1 :

$$F_{fric} < \min\left(F_{bond,side}, F_{bond,front}\right) \tag{3.1}$$

The sliding motion is bounded to a maximum displacement by a fix pin and should not exceed the maximum displacement capacity that the wall can display. The latter is the displacement Δ_u corresponding to a state of Significant Damage (SD) of the system, according to the assessment procedure proposed by Dolšek and Fajfar (2008) and the N2 method (EN 1998-1:2004 2004). Knowing the values of F_{fric} and Δ_u it is possible to determine all the parameters that controls the device's performance: the effective damping is obtained from the slip capacity of the device and can be used to quantify the energy dissipative capacity of the device. In Chapter 4, the damping will be used as controlling target to quantify the stability of the device. On the other

hand, the displacement capacity Δ_u will be used to determine the ductility capacity of the device, whereby a displacement-based design procedure will be implemented in Chapter 6.

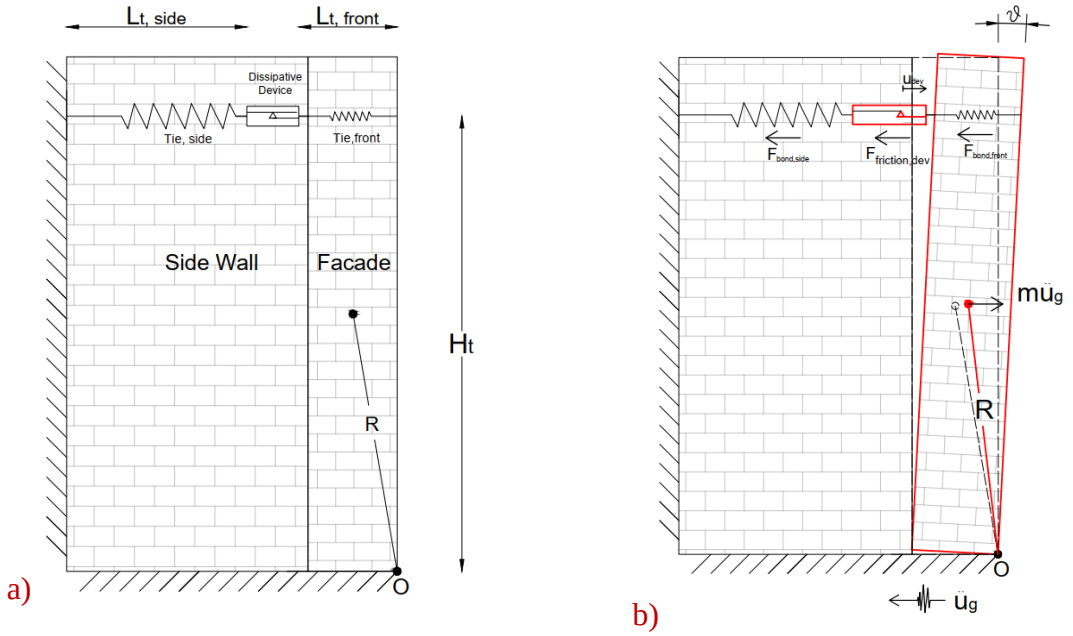

Figure 3-2 a) Corner connection strengthened by dissipative anchoring system (James et al. 2011): a) resting position of the wall, b) tilted configuration of the wall due to base acceleration and activation of the device.

The dissipative anchoring system can be installed along the wall height, so that the energy dissipation can take place even for small rotations of the rocking motion. It is suitable both for connections that have already experienced a crack as a result of a seismic event or for undamaged weak connections. In the latter case, a structural analysis is required to determine the optimal location where the devices should be placed, namely where a vertical/diagonal crack is likely to happen.

3.3 Validation methodology

A validation methodology for the development and use of dissipative devices in line with the modern design codes, can be articulated in three main tasks. These are here presented with reference to the innovative system proposed in this thesis, namely the D-GAS.

- Task 1: Assessment and Refinement of Friction-based dissipative devices (experimental and numerical);

- Task 2: Performance of Dissipative Grouted Anchoring System as connected to masonry walls (experimental and numerical);
- Task 3: Design procedure for the implementation of the D-GAS within the framework of Performance-based design.

The relationship between these tasks is represented in the flowchart of Figure 3-3.

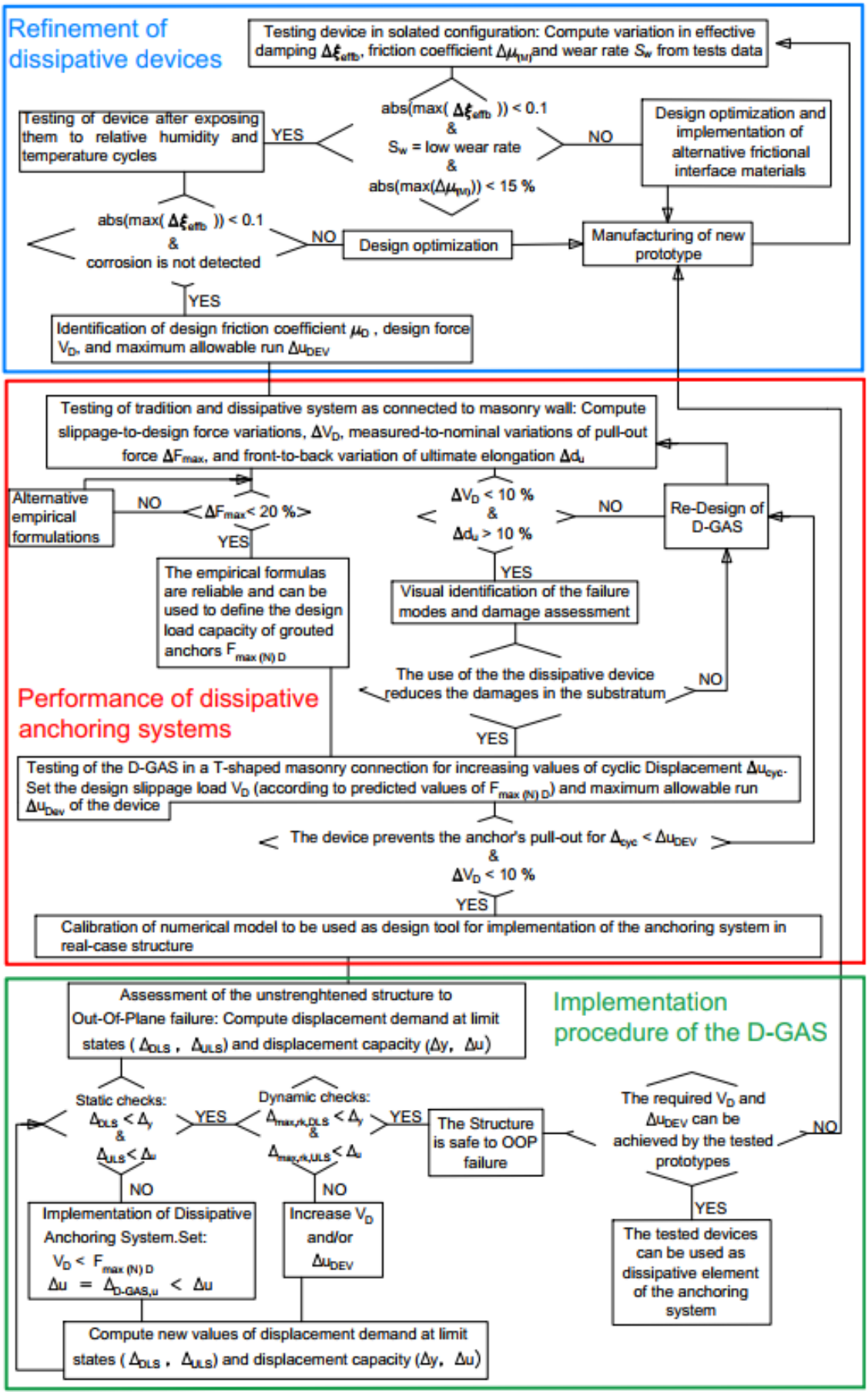

Figure 3-3 Methodology for refinement, assessment, and design implementation of dissipative anchoring system

Each stage is carried out through a combination of experimental and numerical activities, which represent the two crucial validation steps that researchers and producers follow to assess the performance of current and innovative techniques for structural strengthening, and to tune products' performance to code requirements or ad-hoc specifications.

Prescriptions that specifically addresses the experimental validation of anti-seismic devices for the strengthening of heritage buildings are currently missing. Thus, the approach followed herein is to integrate existing guidelines with the technical literature available on similar case studies. The testing protocol adopted in for this research follows an increasing level of complexity: the device is firstly assessed in the isolated configuration to pursue its full characterization and a refinement process is carried out to meet the code's performance requirements. Secondly, the revised prototype is connected to a metallic tie grouted in a masonry panel to assess the damage of masonry panels as a consequence of monotonic pull-out loading. Finally, cyclic tests on subassembly of a T-shaped masonry connection are carried out to supplement the outcome of pull-out tests.

The three testing sessions are performed with the ultimate objective of fully assessing the performance of the D-GAS, as well as of identifying a set of parameters useful for the development of a design procedure for its implementation in a structure. The testing methodologies developed for each testing session have a general value and are commented in detail to provide an example on how to methodically assess strengthening systems for heritage structures in case prescriptions are missing from current codes.

It should be noted that the experimental validation by means of dynamic tests on a full structure is missing from this thesis. In fact, a European-funded research project was proposed to carry out pseudo-dynamic tests of a large subassembly strengthened by the D-GAS at the JRC laboratories. Unfortunately, the project was not selected, and alternative dynamic tests could not be performed due to time and financial constraints.

However, missing experimental information is compensated by the results of computational activities carried out by the author.

Computational activities are a recurring validation step in this thesis, as they offer the possibility of performing parametric analysis and vary a large number of boundary conditions, materials and inputs.

Computational modelling of a whole structure implies the ability of correctly simulating the response of the strengthening system and its interaction with the construction materials and its

structural elements. Therefore, Finite Element Models (FEMs) are developed in Abaqus, proceeding from lower to higher level of complexity, namely considering at first only the dissipative device and then progressively incorporating more and more elements of the connection and of the structure, in line with the methodology followed during the experimental assessment.

Experimental work is generally the preparatory step to all the models, as it provides the source for material properties and input data and allows validating the modelling hypnotises and techniques. As the models grew in complexity, the experimental results are also used to identify the satisfactory level of approximation, whereby the behaviour of the system is correctly simulated, but the computational burden is kept within limits.

After being calibrated, models are able to provide additional information regarding phenomena that cannot be measured during experimental tests, such as the overall distribution of strains in the system during cycles of loads.

Ultimately, the modelling techniques that best achieve a good compromise between accuracy and expediency are collated to simulate the dynamic response of a case study structure in need of seismic upgrade and prove that the D-GAS is suitable for the strengthening of heritage structures.

Additionally, this model will be used to validate a simplified approach developed in this research to assess the vulnerability of a masonry building to out-of-plane failure and identify the optimal anchoring solution that prevents it. Differently from the Abaqus model, this approach, developed in Python, neglects the detailed geometry and material properties of the façade to significantly reduce the computational burden of the analysis and rapidly perform a multi-level performance design in line with the modern design philosophy.

The three stages of the validation process that led to the refinement of the D-GAS are firstly outlined in the following and then analysed by discussing their outcomes Chapter 4, 5, and 6.

3.3.1 Assessment and refinement of friction-based dissipative devices

The dissipative device proposed by D'Ayala and Paganoni (2014) and introduced in the previous section is designed to be readily available, affordable, and straightforward to control and design. Nonetheless, following extensive testing, the performance of the friction-based prototype - referenced as SteSq as it features a square-shaped slider and stainless steel as material of the frictional interface - is considered unsatisfactory as the resistance to motion

increases with the number of cycles (D'Ayala and Paganoni 2014). Therefore, the iterative strategy summarized in the blue box of Figure 3-3 is developed to investigate the stability and durability of the device over a short-term and a long-term assessment framework. The results of this procedure shall inform the design, refinement and production of new prototypes.

The first task (Short-term Assessment) explores the stability of the device's performance by determining the variation of the viscous damping ξ_{effb} over several load cycles. Additionally, the changes in frictional properties of parts in contact due to progressive wear S_w of surfaces are quantified by the variation of the coefficient of friction $\Delta\mu_M$.

The characterisation of the devices in the isolated configuration is carried out according to the procedures and limits described by EN 15129 (2006), despite the fact that neither EN 15129 nor Eurocode 8 specifically addresses the issue of dissipative systems for the strengthening of heritage buildings. The EN 15129 regulates the validation process needed for the production and sale of anti-seismic devices, the latter provides qualitative indications for their applications in structures. Nonetheless, the assessment and refinement procedure aims at ensuring repeatability of tests through several sets of prototypes and different loading conditions, thus the use of codified experimental procedures is of capital importance.

If the parameter $\Delta\xi_{effb}$ is above the target tolerance of variation, the prototype is redesigned, "virtually" testing the different solutions through detailed finite element models. As previously outlined,

The optimised prototypes are manufactured according to the design modifications that have the potential of improving the device's behaviour and tested again for short-term stability.

Finally, the prototypes that satisfy the requirements for the short-term assessment undergo a process of durability characterization. A device might be non-operational for years before an earthquake strikes and its expected response might be affected by several factors. This type of tests is rarely investigated in literature, even though these devices often comprise different metals or high-tech materials that might be affected by aggressive environmental conditions. This lack of knowledge is partially due to the insufficient guidance of EN 15129: while stating that the effects of ageing should be evaluated by repeating the cyclic loading tests in different exposure conditions, it remains vague on the details, especially for displacement-dependant devices that do not carry vertical loads. Given this lack of guidance, the ranges for the environmental variables could be derived from the weathering conditions expected for masonry walls in an earthquake-prone region in relatively extreme climatic conditions.

The devices are exposed to temperature and humidity cycles and then tested with the same protocol used in the "short-term assessment" to determine any loss in performance stability and signs of corrosion due to environmental exposure.

In Chapter 4 the assessment and refinement methodology is applied to the SteSq device, resulting, after several iteration, in the manufacturing of the next generation of dissipative devices. These devices present a stable behaviour, with an effective damping within the EN 15129 performance requirement, which allows for a univocal value of the design friction coefficient μ_D, activation slippage load V_D, and slippage capacity $\Delta_{D_{GAS},u}$. These parameters will feed into the subsequent validation tasks and into the design procedures, as reported in the sections below.

3.3.2 Performance of Dissipative Grouted Anchoring System installed in masonry walls

The tests performed on the friction device in the isolated configuration, are not sufficient to fully identify the behaviour of the dissipative anchoring system.

When strengthening intervention are carried out on historic building, the masonry substrate generally represents the weak link due to its low mechanical properties. Therefore, experimental tests should be performed to assess the performance of the strengthening technology as embedded in the masonry suberate and an adequate term of comparison should be used to quantify the performance's improvement.

As the dissipative devices aim at tackling the drawbacks typical of standard steel anchors, the extent of this improvement can be quantified only when the performance of standard and dissipative anchors is tested in similar conditions. Furthermore, testing standard grouted anchors alongside to the innovative system, allows for checking that the chosen experimental procedures are suitable. The behaviour of historical materials is complex and common mechanisms of failure of standard anchors are known from the literature; if the testing set-up can recreate those, the validity of the assumptions used in the laboratory environment is also substantiated.

Accordingly, pull-out tests are carried out to analyse the behaviour of a connection between two vertical elements, i.e. walls, strengthened by steel anchors. The main focus is on the performance of the connection element, namely the anchor, as stand-alone (GAS) and coupled

with the dissipative devices (D-GAS). Then the level of damage of the masonry panels is ascertained as consequence of the horizontal loading applied.

The tests on the D-GAS draw on the results of the refinement methodology: the new generation of devices is implemented in the dissipative system and the desired design force V_D is provided according to the set of equations obtained from the short-term assessment of the device. The variation between design and measured values is checked against the tolerances provided by the EN 15129 (2006), thus verifying the compliance of the device to the pertinent code when the complete assembly is tested.

The data obtained for the pull-out tests of the GAS are used to enrich the literature on the performance of this anchoring technology. A database is constructed to summarize the values of the mean parameters defining the performance of grouted anchors. Specifically, the maximum pull-out load, displacement capacity and failure modes for each experimental campaign are reported and normalised to determine values of generic validity for design purposes.

The values of maximum load capacity measured for the testing activity reported in this thesis and the ones collected from previous studies are compared to the expected values predicted by the analytical formulas available in the literature. Where large variations between measured and analytical values of maximum pull-out force ΔF_{max} are computed, alterative empirical formulas are proposed.

Pull-out tests offer the advantage that only one element of connection, i.e. only one of the two walls, has to be built; this simplifies the test set-up, the loading apparatus and measuring equipment. Accordingly, they are suitable for the first assessment of the devices in presence of a substratum. Nonetheless, these tests' set-up doesn't reproduce a full corner connection, thus it can only partially represent the overall response of a strengthened masonry subsystem. Moreover, pull-out tests are carried out in monotonic load regime, this clearly being a considerable simplification in respect to the load input experienced by a structure during an earthquake.

Hence, cyclic tests on subassembly of T-shaped masonry connection are carried out to supplement the outcome of pull-out tests. No code prescription exists for similar tests, which are therefore devised drawing on the experience acquired during the pull-out campaign and on the technical literature.

This testing session is performed with the objective of fully assessing the performance of the dissipative anchoring system when fully grouted in a masonry connection and identifying a set of parameters useful for the development of the design procedure. Drawing on the results of the previous tests, a design load hierarchy is set, namely tuning the slippage load of the device to be smaller than the pull-out capacity of the anchors. For increasing values of cyclic imposed displacement, the fundamental assumptions at the base of the D-GAS functioning is verified, i.e. that the detachment of the front wall from the side walls triggers the activation of the device while preventing the bonding failure of the anchors.

It is worth highlighting that this validation step has been only partially concluded as the spread of Covid-19 during Spring 2020 forced the experimental activity to stop. The tests were resumed during Spring 2021 upon re-opening of the laboratories but due to access restrictions, only the results of the tests performed on one of the T-shaped connections have been included in this thesis. Nonetheless, the complete report of these tests will be available in future journal publications.

Finally, the experimental set-ups are reproduced in a numerical model using the FEM software Abaqus. The numerical model developed for the dissipative device is implemented in a model which includes the masonry panel and ad-hoc elements to define their mutual interaction.

Simulating single parts of the anchor assembly and its interaction with the parent material gives a better understanding of the laws governing the anchor behaviour; these laws can be then implemented in a larger, more complex model (presented in Chapter 6), where mesh and geometry need to be simplified to avoid an excessive computational burden. The FEM model will be crucial for the validation of the developed design procedure described in Chapter 6 and outlined in the next section. As already discussed, non-linear modelling of the structure is an essential step in the seismic assessment of historic structures and in the design/optimisation of the upgrade intervention.

3.3.3 Performance-based design of D-GAS

Upon completion of the experimental validation process, it is possible to collate all results in a design procedure and prove by computational analysis that devices are suitable for the strengthening of heritage structures in seismic prone areas. The design procedures for traditional anchoring systems typically follows a Force-Based (FB) approach due to the limited

ductility capacity that this strengthening system possess. For acceleration demands corresponding to high magnitude earthquakes, this may lead to over-dimensioned ties and anchoring plates, and unfeasible designs, especially for historic buildings where minimum intervention criteria may limit the number and sizing of the intervention (Paganoni and D'Ayala 2014).

Conversely, Displacement-Based (DB) methods could be formulated to prevent Out-Of-Plane (OOP) failures when the strengthening system provide a well-defined displacement capacity. Current regulations, such as the N2 method procedure proposed in the Eurocode 8 (EN 1998-1:2004 2004), allow to adequately reduce the seismic demand depending on the ductility that these systems provide, thus reducing intrusiveness of the strengthening interventions. Nonetheless, clear procedures for the design of systems able to prevent the OOP failure of historic buildings, are missing, besides qualitative indications (EN 1998-1:2004 2004; CMIT 2009).

Therefore, a DB design procedure for grouted anchoring systems in historic masonry structures is presented in Chapter 6, drawing on the N2 method procedure proposed in the Eurocode 8 (EN 1998-1:2004 2004).

Firstly, a non-linear model is implemented considering the front wall as a rigid block and evaluating its lateral force capacity in its original configuration. A set of threshold displacements corresponding to the progression from linear to nonlinear behaviour of the system (Δ_y and Δ_u) is identified, neglecting the restraining action provided by the side wall in terms of traction and friction resistance to the OOP motion. Then the performance point coordinates are computed for the Damage and Ultimate limit state (Δ_{DLS} and Δ_{ULS}), and the required ductility compared with the system's available ductility. If the displacement demand exceeds the capacity, two strengthening configurations are proposed to prevent the OOP failure, namely grouted anchors with and without the friction-base dissipative device.

The contribution of the anchors is included in the model by an idealised non-linear constitutive law, underpinned by the database and the load-strain curves obtained from the pull-out review and analysis. The presence of the dissipative device is included by limiting the tensile capacity of the anchor to the design sliding threshold of the device V_D and by increasing the ultimate displacement capacity to account for the full capacity of the system $\Delta_{D-GAS,u}$.

Depending on the type and sizing of the strengthened configuration assumed, the displacement capacity of the wall and the inelastic seismic demand vary, and the design solution is not unique.

Therefore, a dynamic analysis is proposed as a final step of the design procedure to validate the vulnerability assessment of walls prone to overturning and determine the optimal solution to strengthen them. Having computed the evolution of the system throughout the seismic event, the optimal solution is determined for the design that minimizes the sizing of the intervention and maximize the energy dissipated by the anchoring system with respect to the seismic energy imparted to the wall.

This design procedure is developed as a Python program, and it is exemplified with respect to a case-study structure. The program provides a rapid tool to assess and design a strengthening solution based on the ductility of the system rather than on a force-based approach. To validate this tool, the obtained design solution is verified performing a dynamic analysis of the same case-study structure in Abaqus: a detailed numerical model is implemented using the modelling techniques identified in the previous computational activities. The Abaqus model presents a high computational cost and high level of detailing, as the structure's geometry is fully reproduced, and the traction and friction capacity of the masonry connection is included. This suggests that the two numerical techniques can be complementary to one another, the first as a preliminary design tool, the second as a tool for refinement and validation.

In the next three Chapters, the procedural steps illustrated in Figure 3-3 are applied to the proposed D-GAS to prove that the methodology can be used to assess and refine the performance of an innovative anchoring system for heritage structures. Upon validation with sensitivity analysis, for different strong motion and different geometries and materials, the Python procedure can become a standalone designer tool, to determine the feasibility of the intervention. The sensitivity analysis is not included in the present study, but it is one of the future developments.

4 Design optimization of friction-based dissipative devices

4.1 Introduction

The first validation step of the innovative anchoring system consists of improving the dissipative device to meet the code's performance requirements. To this purpose, in this Chapter the validation programme proposed in Chapter 3 is applied to the first prototype of friction device developed by D'Ayala and Cintec, namely the SteSq device. The programme consists of several tasks (Melatti and D'Ayala 2020), mutually linked as illustrated by the flowchart of Figure 4-1.

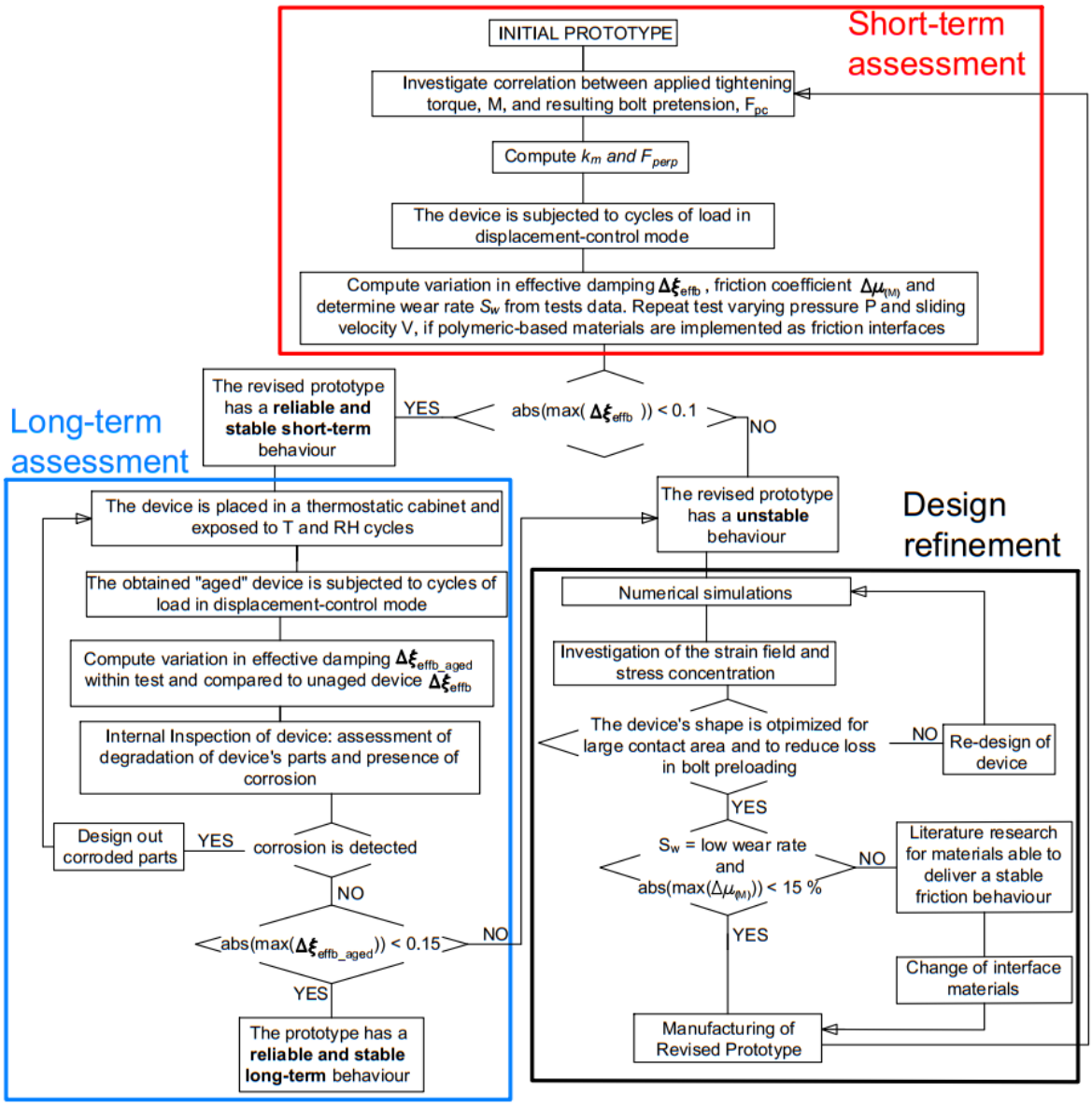

Figure 4-1: Methodology for the assessment and refinement of friction-based dissipative devices.

First, the SteSq device is subjected to cyclic testing to investigate its short-term response to several loading input (Section 4.2) and changes in frictional properties of parts in contact due to progressive wear.

In general, wear of sliding surfaces can be caused by many *mechanisms* such as adhesion, abrasion, oxidation, delamination, melting, and more (Lim and Ashby 1987). It follows that the wear rate Sw is a function of many factors: the normal force, F_{perp} acting across the sliding surfaces, their relative velocity, v, their initial temperature, T_0, and the thermal, mechanical and chemical properties of the materials which meet at the surface. For each of the mechanisms, Sw_i can be defined as:

$$Sw_i = f\left\{F_{perp}, v, T_0, \text{th.}, \text{mech.}, \text{ch. properties}\right\} \tag{4.1}$$

Among these, the one affecting the SteSq prototype is mainly the effect of plasticity-dominated wear, consisting in the removal of slivers of metal from one or both surfaces (M. Latour, Piluso, and Rizzano 2014). If two plates of the same material are in contact, as in the case of steel-on-steel plates, severe wear with high wear rate is often registered: this process makes the contact surfaces rougher than the original state and a hardening behaviour of the friction coefficient is recorded. In contrast, if two different materials are experiencing sliding in dry friction conditions, mild wear with a low wear rate will be recorded on the surface with lower elastic modulus E. The removal of material from contact surfaces results in thinner plates and a reduction of the clamping force, determining a softening behaviour of the slip load. In both cases, the hysteretic behaviour of the damper is greatly affected by the wear and extensive laboratory tests need to be performed to design solutions able to minimize this material loss during dynamic loading.

In the proposed methodology, two activities are set out for the assessment of the short-term behaviour of the device: first, the empirical correlation between the applied tightening torque M, and the tension transferred to the bolts F_{pc} is determined. A parameter k_m is computed to investigate the influence of the device's geometry and the type of nut on the bolts tightening load. Secondly, the variability of the dissipative capacity of the device under external cyclic loading for different tightening load is investigated. The values of slip force is recorded for each cycle, and the effective viscous damping $\xi_{effb}$is computed according to EN 15129 (EN 15129

2006) provisions. The amplitude of the variation of ξ_{effb} throughout the test determines the stability of the device.

According to the EN 15129's requirements (EN 15129 2006) for displacement-dependent devices, devices shall undergo 20 cycle reversals with a variation of the effective viscous damping $\Delta\xi_{effb}$ not greater than ±10% of the value recorded at the third cycle. At the end of each testing session, a visual inspection of the device determines the wear rate Sw due to the friction of components in contact. Depending on the friction materials involved, the factors of Eq. (4-1) that affect Sw are experimentally determined.

Then, a numerical model is developed to replicate the testing set up and investigate the stress-strain field. This task, referred as design refinement and detailed in Section 4.3, complements the results of the short-term assessment to determine the new design of the design. This testing-analysis-redesign process is iterated until a stable and reliable short-term behaviour is achieved, according to the code's limits, leading to the manufacturing of the new generation of friction devices, presented in Section 4.4.

Under the same testing protocols, the short-term performance of the new generation of devices is reported in Section 4.5.

Finally, in Section 4.6 the long-term response of the new generation of devices is reported, having exposed the devices to adverse environmental conditions. For bolted slotted devices, the loss of initial bolt preload is the main cause of instability over time. Immediately after tightening, the bolt experiences an initial loss which is mainly associated with the installation process, and increases with the magnitude of the applied preload, especially if the bolt is tightened beyond its yield limit (Heistermann 2014). Beyond this, a mid-term loss occurs continuously during its operational life, the loss-rate becoming stable over time. (D'Antimo et al. 2020) identified a direct correlation between the loss of preloading and the service loading conditions highlighting that the use of a conical disk springs reduces the loss of preload over time. High temperature may also influence the bolt preload. Test conducted on bolts grade 8.8 showed that temperatures above 300° C activate creep and relaxation phenomena reducing the yield strength of the steel, which produces a proportional load relaxation in the fastener (Kodur, Kand, and Khaliq 2012). Nonetheless the service operability of dissipative devices never reaches such range of temperatures in typical civil applications, as studies on frictional dampers have confirmed (Lee et al. 2016).

Another source of possible long-term instability for friction-based dissipative devices is the oxidation of the elements composing the device due to environmental conditions. Stainless steel, an alloy of iron, chrome and carbon, is typically used as principal material in such devices, as it presents good mechanical strength, and better resistance to environmental corrosion than iron steel (The European Stainless Steel Development Association 2009). The chromium ions react with oxygen forming a protective stable film which acts as a barrier for additional corrosion. Nonetheless, friction devices might include other metals in combinations with stainless steel. For instance, brass and aluminium are typically used as friction shims to improve the stability of the hysteresis loops, while different steel alloys might be used for the fasteners to achieve higher strength. In certain circumstances, such mixed-material design can lead to galvanic corrosion in one of the partner materials. This phenomenon takes place when two metals in contact have different corrosion potential in presence of an electrolyte. Contrary to widespread belief, the difference in potential in an electrochemical cell alone is not a good indicator of the actual risk of galvanic corrosion (The European Stainless Steel Development Association, ESSDA 2009). The decisive factor is the difference in potential observed under real operating conditions. As the proposed device is intended to be inserted within the thickness of historical masonry walls, the corrosion process can be simulated by exposing the prototype to the environmental conditions typically observed in the masonry fabric of historical walls. As reported by D'Ayala and Aktas (2016) and Aktas et al. (2017), monitoring the relative humidity (RH) within the wall thickness, typical ranges are between 65% and 70% when the outside temperature and RH vary between 10°C and 20°C and 40% to 90% respectively. For outdoor temperature between 0°C and 10°C, the in-wall RH reaches values of about 85-95%, meaning that the walls are subject to prolonged saturation in vapor phase and therefore are highly likely to contain liquid water. These conditions might trigger galvanic corrosion in the anodal element. Moreover, rainwater has a specific conductivity three orders of magnitude greater than pure water, causing an acceleration of the oxidation process (ESSDA 2009). For these reasons, the risk of galvanic corrosion is explored in the long-term durability task. The devices are exposed to temperature and humidity cycles that simulate the environmental conditions of a real-case installation to explore the resistance of the prototypes to corrosion. After conditioning, the devices are tested with the same protocol used in the "short-term assessment" to determine any loss in performance stability due to environmental exposure. The maximum variation of effective damping after the aging process (referred to as $\Delta\xi_{effb\_aged}$) shall be within ±15% as indicated by EN 15129 (2006).

The experimental and numerical activities are presented and commented giving relevance to the test set-up, to the relevant parameters governing the devices' behaviour and the acceptable threshold values available in the literature to verify the stable and reliable behaviour for anti-seismic devices.

4.2 Short-term assessment – Characterisation of dissipative behaviour

The short-term assessment aims to identify and quantify all the parameters that control the performance of the SteSq prototype. The reported results refer to the SteSq device tested in isolated configuration: the prototype is disconnected from the threaded bars that complete the dissipative system and 150mm-long threaded bars are screwed at both ends to allow the insertion of the device in the testing apparatus. The EN 15129 (2006) and EN 1090-2 (2008) are used for defining the testing protocols, as they provide guidance for performance acceptance of seismic dissipative systems and tightening operations of bolted unions.

4.2.1 Quantification of k_m for the specific device assembly

The first task of the laboratory activity is to determine the clamping force F_{pc} transferred to the fasteners during the tightening operation of the bolts. For the SteSq device, the torque method is applied by tightening the fasteners to a reference value of torque. The EN 1090-2 provides an empirical correlation between the reference tightening torque M and the resulting nominal preload in the bolt $F_{pc\,(N)}$:

$$M = k_m \, d \, F_{pc\,(N)} \tag{4.2}$$

where d is the nominal diameter of the bolt and K_m is assumed equal to 0.2 for non-lubricated bolt conditions. Eq. (4.2) provides an approximation of the transferred preload as it is estimated that only about 10% of the tightening torque results in useful bolt tensioning. The remaining 90% is lost due to various forms of friction that occur during the tightening process (Green-Warren 2018). In addition, the preload in the bolt can be inconsistent from fastener to fastener and depends on the type of nuts used. For these reasons, Eq. (4.2) is not applicable to all situations and testing of actual fastener components is recommended to quantify k_m for all critical-use applications (Mahmoud, Rodriguez Lopez, and A. Riveros 2016).

Since the parameter k_m includes all the factors affecting the relationship between applied bolt torque and resulting bolt tension, including number and layout of bolts and geometry of the objects to fasten, appropriate values were determined experimentally. The torque was applied in increasing steps of 5Nm to sets of four bolts by means of a dynamometric torque wrench. Each set is composed of four bolts (class 8.8) with nominal diameter of 8mm, these being the fasteners used to apply the perpendicular load to the dissipative device.

The variation of the pretension transmitted throughout the test was recorded by two donut load cells installed below the head of two bolts. In this way, the bolt pretension F_{pc} and the tightening torque M are unequivocally determined for each increment in torque. Two geometries were considered (see Figure 4-2). Initially the pretension is recorded for bolts that go through a single plate (Figure 4-2a) to determine the variation of transmitted bolt pretension when two different types of nuts are considered, namely locking and normal nuts. Lock nuts are used to reduce the loss in bolt preloading that all bolted connection experience with time. A nylon ring is inserted inside the normal steel nut, imparting higher friction grip between the mating threads, thus increasing the friction force resisting the loosening effect (Saha et al. 2007).

In a second test the bolts are tightened to the dissipative device to determine the variation of bolt load due to the deformability of the plates forming the device during tightening (Figure 4-2b). When the pre-tension is applied to deviating surfaces, a bending moment will be induced due to the inclination on one or both surfaces. As a result, the combined presence of axial force and bending moment may cause a higher stress levels under the bolt head (Söderlund 2017). Both locking and normal nuts are tested also for the second set of tests.

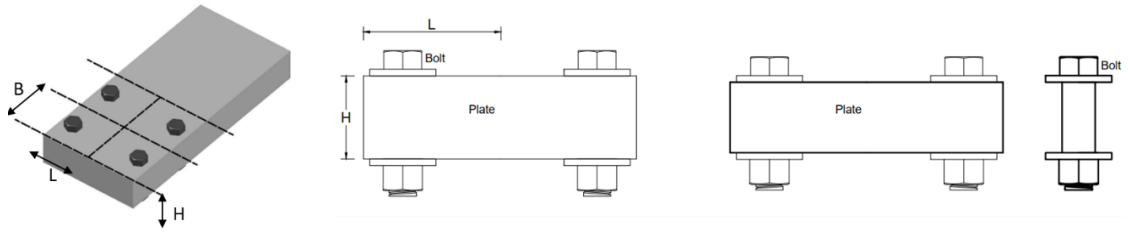

a)

b)

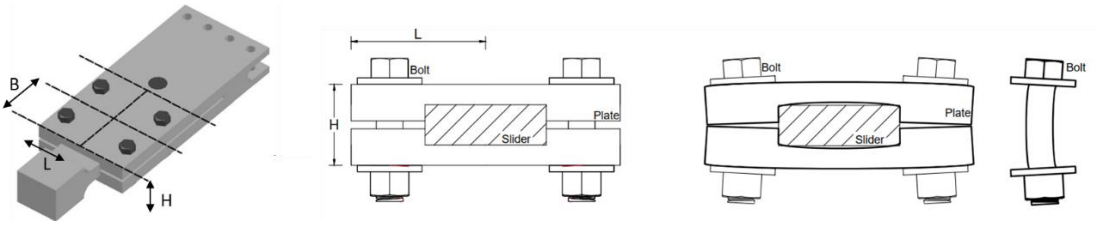

Figure 4-2. Tested joint geometries: a) Single Plate (SP) geometry, b) SteSq Device (D) geometry. Undeformed and deformed shape of plates and bolts during tightening.

The predicted ultimate applicable tightening torque M_u is computed from Eq. (4.3) as the torque required to achieve the proof load F_{pl}, equal to 70% of the nominal bolt strength, f_{ub} :

$$M_u = k_m\, d\, F_{pl} = \; k_m\, d\, (0.7\, f_{ub} A_s) = \; 30 \text{ Nm} \tag{4.3}$$

where A_s is the nominal stress area of the bolt and K_m is equal to 0.2. Figure 4-3 shows the values of the bolt load recorded for each geometry and type of nut, where the points represent the mean value of the set of bolts.

It was found that the mean values deviate from the nominal values obtained by applying Eq. (4.3), which are also shown in Figure 4-3 as reference. For the single plate (SP) configuration, a linear correlation between the applied tightening torque and the recorded bolt preload is obtained, as shown in Figure 4-3a. Moreover, both Figure 4-3a and Figure 4-3b show that the use of lock nuts causes a reduction of bolt load in the range of 10-15% with respect to normal nuts. This is because during the tightening process the lock nuts exhibit higher friction with the threads so that a smaller portion of the torque is transmitted to the bolt's stem as pretension. Regarding the tests carried out on the device configuration, Figure 4-3b highlights that the geometry determines a loss in the bolt preload for increasing values of torque.

A simple analytical model can be implemented to consider the behaviour of the device and compute the loss of bolt preload. With reference to Figure 4-4a, a beam-model of the upper plate is created, following the middle-surface of the plate.

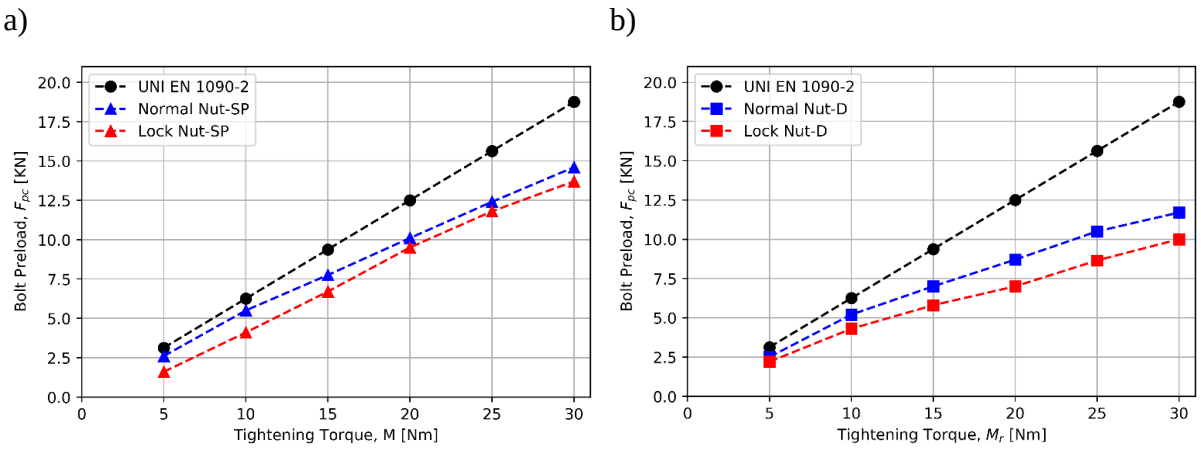

Figure 4-3. Bolt pretension when normal nuts and lock nuts are employed on a) single plate geometry (SP) and b) device geometry (D).

The element ABCD represents half of the upper plate, the vertical spring at point A represents the response of the bolt along its longitudinal axis, while the horizontal spring at A and the spring at point C represent the axial stiffness of the slider in the horizonal and vertical direction, respectively.

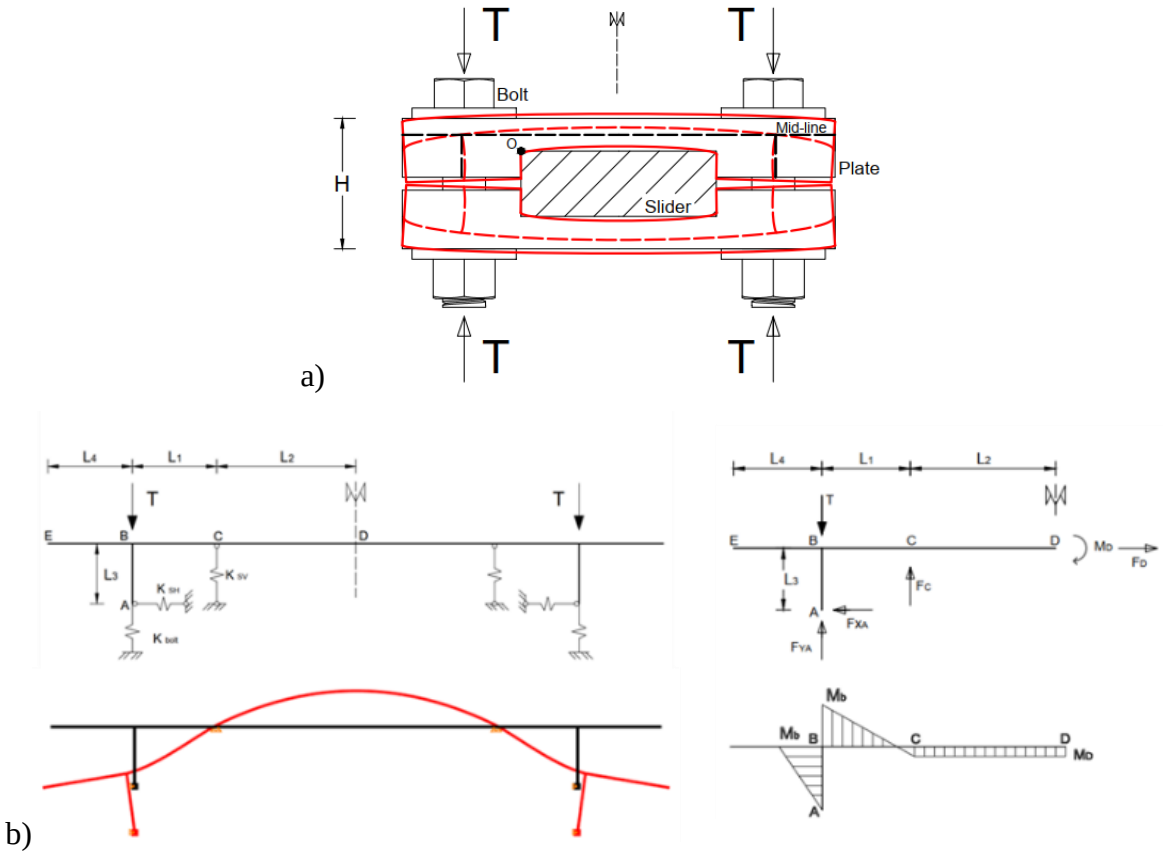

Figure 4-4. a) Cross section of SteSq device, mid-line of clamping plate (dotted line) b) Numerical model of the clamping plate, deformed shape, free body diagram and diagram of bending moment

An increasing vertical force is applied at point B to study the deformation of the model during the tightening. Figure 4-4b illustrates the obtained free body diagram and the diagrams of bending moment which increases linearly along element AB and it is maximum at point B.

The forces acting on the bolt can be derived from element AB and are reported in Figure 4-5a. With reference to Figure 4-5 the resulting tensile stress is the combination of the axial load and the bending moment, and it is maximum under the head of the bolt (section A-A) where the contribution of the bending moment is maximum. The shear stresses are negligible compared to the tensile stress generated by the combined presence of axial force and bending moment under the bolt head. For values of bolt preload greater than 7.5 KN, the bending moment causes the tensile stress to exceed the yielding limit, causing localized plasticity. Assuming a perfectly plastic behaviour of the bolt's material beyond the yielding point, a portion of traction force is lost with respect to an elastic model.

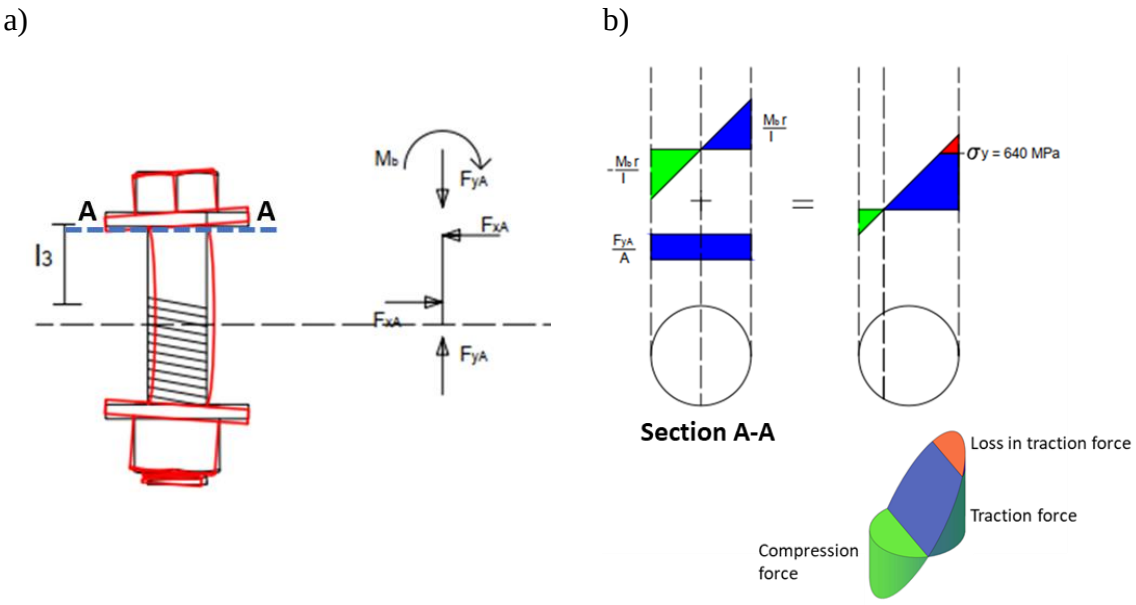

Figure 4-5. a) Forces acting on the bolt's shank, b) Tensile stress under the bolt's head

The non-linear evolution of the analytical model is compared with the experimental values recorded for the device configuration in Figure 4-6a. In general, the correspondence between the numerical model and the experimental trend is well captured. Initially, the numerical model displays a liner trend, confirming that the bolts remain in their elastic phase for torque reference values up to 15 Nm. According to BS EN 1090-2, this value can be considered as maximum permissible value of torque for the device, as it induces a tensile stress equal to 90% of the

yielding limit (EN 1090-2:2008 2008). For larger values of torque, the model displays a non-linear behaviour reflecting the loss in bolt preload due to the local yielding at the bolt's head, The loss is well captured by the numerical model which assumes a bilinear constitutive law, shown in Figure 4-6b, obtained from the values of nominal ultimate stress and deformation for bolt class 8.8 (Rockside Export 2019).

a) b)

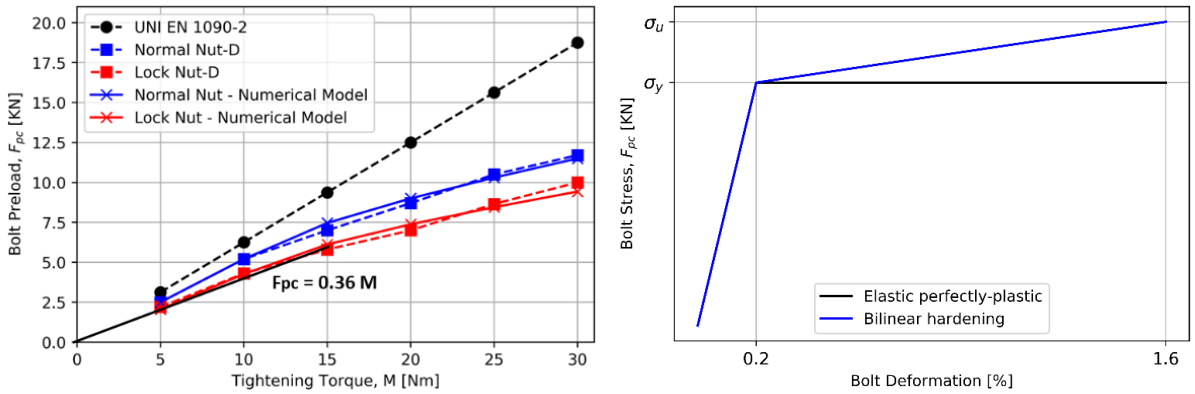

Figure 4-6. Correspondence between numerical model and experimental evidence: a) perfectly plastic behaviour of steel, b) bilinear behaviour of steel

To keep consistency with the linear formulation of Eq. (4.2), the linear regression over the measurement on lock nuts, shown in Figure 4-6a, is used to obtain an empirical equation relating the applied torque - up to the maximum permissible value of torque (15Nm) - to the nominal bolt pretension:

$$F_{pc\,(N)} = 0.36\,M \tag{4.4}$$

Comparing Eq. (4.4) to Eq. (4.2) and considering that the nominal diameter of the bolts is 8 mm:

$$F_{pc\,(N)} = \frac{M}{k_m d} = \frac{M}{k_m 8} = 0.36\,M \tag{4.5}$$

Which allows to compute the specific value of k_m applicable to the device as:

$$k_m = 0.35 \tag{4.6}$$

Once the bolt preloading F_{pc} is determined for each value of tightening torque, the nominal value of perpendicular force $F_{\text{perp (N)}}$ applied to the sliding surfaces is determined as:

$$F_{\text{perp (N)}} = m\, F_{pc\,(N)} \tag{4.7}$$

where m is the number of tightened bolts.

4.2.2 Assessing the stability of the effective viscous damping

The objective of the second testing activity is to evaluate the performance of the device under cyclic loading. The test layout consists in connecting the SteSq prototype to a universal testing machine, which imposes a relative motion to the slider according to a sinusoidal displacement history. Before the motion is initiated, the bolts gripping the assembly are tightened to a reference value of torque, which determines a nominal value of perpendicular force $F_{\text{perp (N)}}$ according to Eq. (4.4) and Eq. (4.7). Several tests are performed on the same device, in sequence, for values of tightening torque increasing by 5Nm up to the value of maximum allowable torque as determined in the previous Section. Each test consists of 20 cycles of sinusoidal displacement to a maximum amplitude of ± 5mm.The value of pretension of two bolts, $F_{pc\,1}$ and $F_{pc\,2}$, is monitored throughout the duration of the test. The measured variation of applied load $F_{\text{perp (M)}}$ is computed as:

$$F_{\text{perp (M)}} = m\, F_{pc\,(M)} = m\, \frac{F_{pc1} + F_{pc2}}{n_{lc}} \tag{4.8}$$

where m is the number of tightened bolts and n_{lc} is the number of load cells. During the tightening operations the accuracy β of the measured value of perpendicular force, $F_{\text{perp (M)}}$ is computed as:

$$\beta = F_{perp\,(M)}/F_{perp\,(N)} \tag{4.9}$$

Among the tightening methods proposed by EN1090-2 (combined, torque, tension control), the torque method shall be capable of achieving ±95% reliability (Ferrante Cavallaro et al. 2018), thus a tolerance of 5% between nominal and measured force is allowed (see Table 4-1).

Besides the pressure cells, the testing apparatus also comprises two Linear Variable Differential Transformers (LVDTs) to measure the displacement d_r of the slider relative to the fixed sleeve of the device and two strain gauges to measure local strains where the greater deformations are expected, namely near the bolts and the locking end, as shown in Figure 4-7.

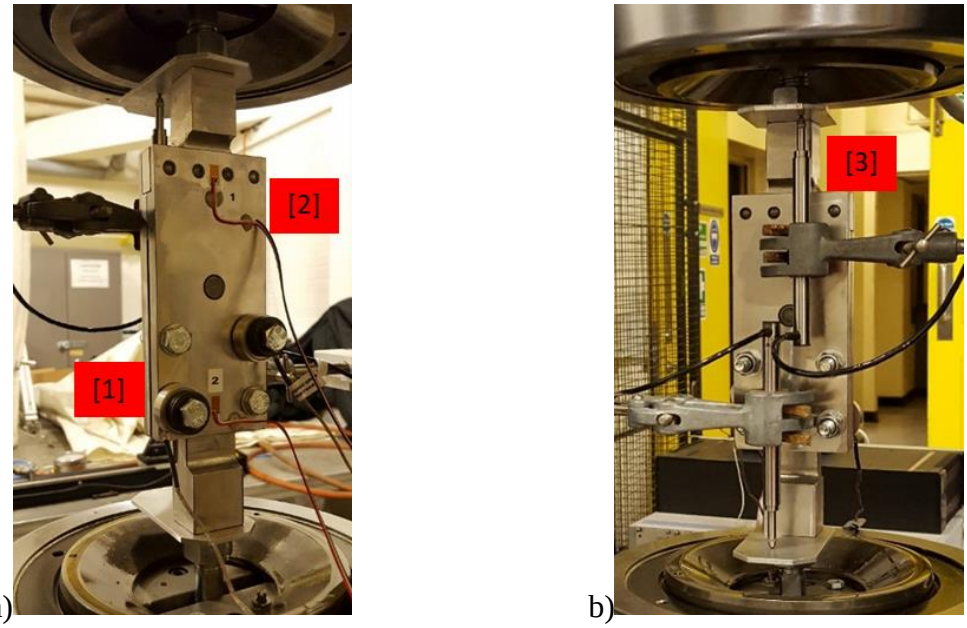

Figure 4-7. Testing apparatus: [1] load cells, [2] strain gauges, [3] LVDTs

EN 15129 (2006) is taken as reference for this testing activity, as it provides the testing requirements for the verification of consistency of seismic devices' performance. According to the guidelines, the sinusoidal displacement history is defined as follows:

$$d_r(\mathrm{t}) = d_0 \sin(2\pi f_0 t) \tag{4.10}$$

where d_0 is the peak stroke (set at ±5mm), f_0 is the loading frequency (set at 0.1 Hz) and t is the time in seconds. The slippage force $F_{\mathrm{slip\ (M)}}$ that determines the relative motion of the slider is measured by a load cell in series to the device

In a standard Coulomb friction equation, the ratio between $F_{\mathrm{perp\ (M)}}$ and $F_{\mathrm{slip\ (M)}}$ is expressed through the coefficient of friction, μ, which is a property typical of the materials that come into contact under the action of the perpendicular force. In this case though, the measured friction coefficient μ_M represent an "apparent" friction coefficient because, due to the peculiarity of the device assembly, the ratio between $F_{\mathrm{perp\ (M)}}$ and $F_{\mathrm{slip\ (M)}}$ is influenced by several factors. As the test-set up does not allow quantifying separately the influence of each parameter, μ_M is calculated as average over each cycle on the basis of the recorded values of $F_{\mathrm{perp\ (M)}}$ and $F_{\mathrm{slip\ (M)}}$ as:

$$\mu_M = \frac{F_{\text{slip (M)}}}{n\, F_{perp\,(M)}} \tag{4.11}$$

Then a design value of friction coefficient μ_D is obtained as the mean value of μ_M recorded during over 20 cycles of load and the design force of the device is determined as follows:

$$V_D = \mu_D\, n\, F_{\text{perp (N)}} \tag{4.12}$$

In Eq. (4.12) the number of friction surfaces *n* is one of the three parameters that determines the value of friction coefficient. In their simplest design, bolted-slotted devices present two plates clamped on friction pads by pre-stressed bolts. Given their geometry only the upper and lower surfaces of the friction pad are pre-stressed and involved in the sliding motion. Therefore, the number of friction surfaces is equal to 2 (n = 2), as reported by several authors (Grigorian, Yang, and Popoc 1993; Avtar Pall and Pall 2004; Lee et al. 2016).

On the other hand, the geometry of the SteSq device makes the external plates bend around the slider element when the bolts are tightened. Thus, the lateral surfaces are acted upon by a positive pressure and contribute to the resistance to sliding exerted through friction, together with the upper and lower surfaces (see Figure 4-12 for a representation of the lateral contact pressure on the slider). Therefore, to compute the value of friction coefficient four contact surfaces (n = 4) are considered in Eq. (4.12).

According to EN 15129 the hysteretic capacity of the device can be computed considering the effective viscous damping for each cycle:

$$\xi_{effb} = \frac{W(d_b)}{2\pi V_D d_b} = \frac{4\, F_{\text{slip (M)}} d_b}{2\pi V_D d_b} = \frac{4\, F_{\text{slip (M)}}}{2\pi V_D} \tag{4.13}$$

where $W(d_b)$ is the energy dissipated by the device during each cycle, with maximum displacement equal to d_b, and V_D is the design force of the device. To assure a stable behaviour under cyclic loading, EN 15129 limits the effective damping variation in a series of load cycles relevant to the same displacement as follows:

$$\Delta\xi_{effb} = \frac{\left|\xi_{effb,i} - \xi_{effb,3}\right|}{\xi_{effb,3}} < 0.1 \tag{4.14}$$

where subscripts 3 and i relate to quantities at the 3^{rd} and i^{th} load cycle of an experimental test, with $i \geq 3$.

Results are presented in terms of load displacement history for each increment of torque applied to the bolt. The load-displacement loops shown in Figure 4-8a have a regular rectangular shape as expected for a friction-based sliding device, but a change in slippage load is noticeable between successive cycles due to progressive wear of surfaces in contact. The presence of debris particles lost by the worn-out surfaces in contact remains within the assembly, thus creating additional resistance to slide. As a result, $F_{perp\ (M)}$ increases from the initial imposed value. For the case of 15 Nm, the measured perpendicular force displays the larger variation, initially increasing by 6% in 11 cycles and then decreasing by 10%, due to loss in bolt preloading, as shown in Figure 4-8b, where $F_{perp\ (M)}$ is normalized with respect to the nominal value $F_{perp\ (N)}$. The value of β for the first cycle, as computed from Eq. (4.9), is above the target of 95% for 5 and 10 Nm and just below the threshold (β = 93.3%) for 15 Nm, possibly due to the instantaneous loss of pre-loading between the tightening phase and the application of the cyclic loading protocol.

a) b)

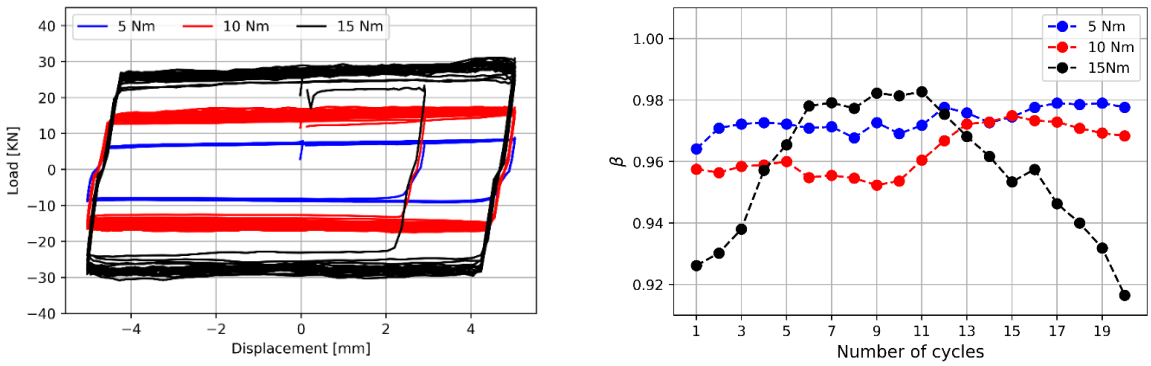

Figure 4-8. Test results for nominal bolt torque of 5,10 and 15 Nm over 20 cycles of load: a) load displacement loops, b) maximum values of $F_{\text{perp (M)}}$ in each cycle, normalized to the nominal value $F_{\text{perp (N)}}$.

The repeated rubbing of the plates also produces surface roughness, thus increasing friction. The initial value of friction $\mu_{0\ (M)}$ is computed with respect to the first cycle of load, for each value of torque imposed. The increase in $\mu_{(M)}$ with respect to the initial value is shown in Figure 4-9a, for each value of torque imposed, while the μ_D value and $max(\mu_{(M)})$ values are reported in Table 4-1. The maximum variation of $\mu_{(M)}$ from μ_D over 20 cycles is obtained for M = 10 Nm ($max(\Delta\mu_{(M)}) = 15\%$), while the absolute maximum value of friction coefficient, $\mu_{max} = 0.39$, is obtained for a nominal torque of 15Nm after 57 cycles of load.

a) b)

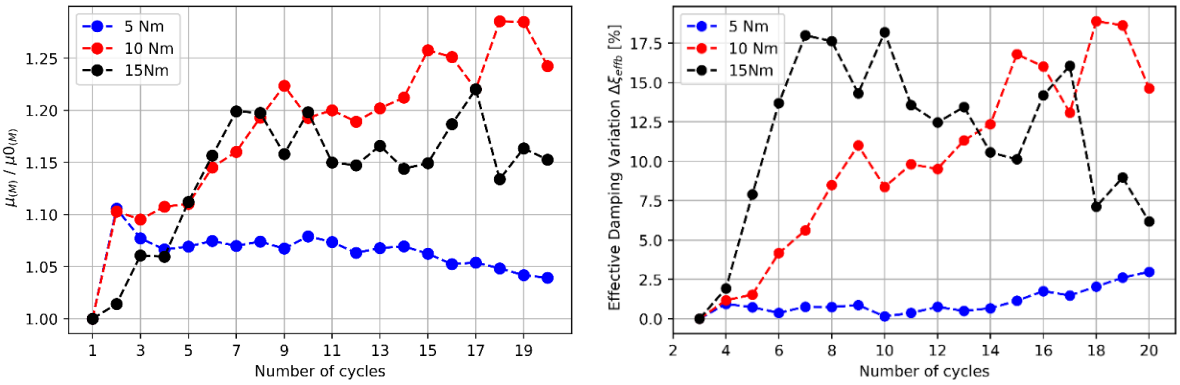

Figure 4-9. a) Variation of friction coefficient $\mu_{(M)}$ with number of cycles, and b) of effective damping.

The variation of effective damping (see Figure 4-9b) is calculated according to Eq. (4.14). The combined effect of additional pressure and interlocking phenomenon due to surface roughness determines that subsequent tests require a greater slippage force to overcome the additional mechanical resistance. Moreover, the range of values of sliding force widens with increasing values of initial tightening torque. According to EN 15129, the absolute variation of effective damping over the series of cyclic testing, should not differ by more than 10% from the value of effective damping recorded at the 3rd cycle. As showed in Figure 4-9b, for M equal to 10 and 15 Nm,

$$abs(\max(\Delta\xi_{effb}) > 0.18 \tag{4.15}$$

while for M = 5Nm it is below the threshold value. Nonetheless, the slippage force recorded at 5 Nm would determine a small contribution in terms of dissipated energy, making the device unfit for a seismic upgrade.

Table 4-1 Results of test activity on SteSq prototype

Variable	Symbol	Reference torque values		
		5 [Nm]	10 [Nm]	15 [Nm]
Nominal bolt preload	$F_{pc\,(N)}$	1.79	3.57	5.36
Measured bolt preload	$F_{pc\,(M)}$	1.75	3.45	5
Nominal perpendicular force	$F_{perp\,(N)}$	7.14	14.3	21.4
Measured perpendicular force	$F_{perp\,(M)}$	7	13.8	20
Accuracy of initial F_{perp}	β	98%	96.60%	93.33%
Initial friction coefficient	$\mu_{0\,(M)}$	0.26	0.26	0.32
Max friction coefficient	$\mu_{max\,(M)}$	0.288	0.34	0.392
Design friction coefficient	μ_D	0.28	0.31	0.36
Max variability of $\mu_{(M)}$	$\max(\Delta\mu_{(M)})$	7%	15%	11%
Design force	V_D	8	17.7	30.9
Slippage Force at 3rd cycle	$F_{sl,3}$	7.87	16	26.3
Max Slippage Force	$F_{sl\,(max)}$	8.00	19.00	31.10
Min Slippage Force	$F_{sl\,(min)}$	7.24	14.5	24.4
Effective Damping at 3rd cycle	$\xi_{effb,3}$	0.624	0.56	0.52
Max variability of Eff. Damping	$\max(\Delta\xi_{effb})$	2.97%	18.80%	18.18%

The visual inspections conducted on the dissipative devices after 60 cycles confirms that both the horizontal and vertical faces of the slider exhibited evidence of resistance through friction, as shown by the severe signs of wear (see Figure 4-10), also confirming that the number of surfaces involved in the action is 4. Nonetheless, the abrasion is visible in proximity of the edges of the frictional plates while no signs of wear are present in their central portion. This means that the geometry of the sample produces a non-homogenous distribution of pressure over the frictional plates, which appear to be only partially in contact as already highlighted in Section 4.1. The reduced contact area leads to high-stress concentration, which explains the excessive wear and tear, the resulting increase in apparent friction coefficient μ_M and the variations of the hysteretic loops among loading cycles. The depth of the abrasion marks was measured to a maximum value of 1.5 mm. Given the abrasion depth and the computed maximum variation of $\mu_{(M)}$, the wear rate S_w is deemed “severe with high wear rate”.

a) b)

Figure 4-10: Superficial wearing of the frictional device: a) the assembly; b) particular of the slider

4.3 Design optimisation

The testing activities highlights several shortfalls for prototype SteSq. During the tightening operations, its geometry induces high tensile stress under the bolts' head, leading to localized plasticity for reference values of torque greater than 15 Nm. This leads to preload-loss directly after tightening and to a non-linear correlation between applied torque and effective bolt preload. To avoid this, the maximum allowable torque is halved compared to a configuration where the plates remain flat during tightening, thus drastically reducing the maximum friction resistance the device can produce.

The vibrations induced during cyclic loading did not cause significant bolt loosening, as the bolt preload variation is within a ±10% threshold. Conversely, the friction coefficient displayed a hardening behaviour, significantly increasing from the recorded initial value. As expected in the case of steel-on-steel friction (Lim and Ashby 1987), severe wear with high wear rate is registered, and the removal of slivers from both surfaces determines surface roughness. This effect is worsened by larger pressure acting on the plates and three design values of friction coefficients μ_D are obtained, namely 0.28, 0.31 and 0.37 for 5, 10 and 15 Nm of reference torque respectively. Consequently, the slippage load shows an increasing trend over 20 cycles of load, and the variability of effective damping is greater than the recommended value in EN 15129.

According to the proposed methodology, the SteSq prototype failed the reliability condition for the short-term assessment, therefore different design solutions are analysed to improve its behaviour according to the tests' results.

4.3.1 Numerical model of SteSq

A 3D numerical model of the SteSq prototype is developed using ABAQUS software (Dassault Systems 2019) to allow for a detailed representation of all prototype's parts to investigate the strain field produced during testing.

The numerical model comprises three parts, representing the slider, the clamping plates, and the tightening bolts (Figure 4-11). Three-dimensional volume elements (C3D8R) are used for the mesh since a complete and accurate three-dimensional stress/strain distribution is critical to interpret the phenomena observed during the tests. Boundary conditions are imposed to reproduce the experimental testing conditions: the two external plates are fully restrained, and the slider is allowed to move only in the direction of its longitudinal axis (x-axis), even though it is acknowledged that the tolerances present in the physical prototype would allow small relative motion of the parts in the two transversal direction.

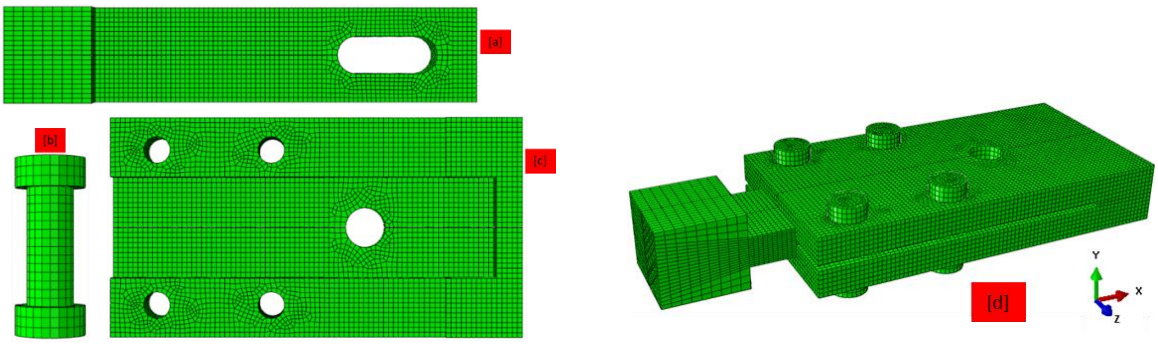

Figure 4-11. Parts of the numerical model, [a] slider, [b] bolt, [c] frictional/clamping plate, and [d] assembly.

The interaction properties between the surfaces in contact are defined by assigning a friction coefficient to all parts in contact. The same displacement time-histories defined during the testing campaigns 2 are used as input for the FE models, thus ensuring correspondence between experimental and computational tests.

To reflect the physical prototype's conditions, the $F_{perp\,(M)}$ is applied by modelling four bolts and applying a concentrated force to each bolt head, as per ABAQUS specific routine. The F_{pc} assigned to each bolt-like part is 5 KN, thus simulating the $F_{perp\,(M)}$ = 20 KN, measured for the test with 15 Nm of nominal bolt torque. This test was selected for the simulation because the device displayed less variability compared to the 10 Nm case, while providing almost 3 times

the energy dissipation capacity obtained by the test with 5 Nm torque. Moreover, for the 15Nm test, μ rapidly increases during the first 5 cycles, (from 0.32 to 0.36) and then remains quite stable throughout the rest of the test. Therefore, the value of friction coefficient is set to 0.36 to capture the "stable" phase and to 0.32 to reproduce the initial state of the device. In Abaqus the friction coefficient is defined specifying the value of the static friction coefficient only, as the design values obtained experimentally (μ_D)are an average over each cycle of load. These values are reported in Table 4-1 as μ_D and $\mu_{0\,(M)}$ for M = 15Nm.

The analysis involves two steps. First, a static analysis is performed to apply the bolt loads within the first time-step. In the second step, a sinusoidal displacement is imposed to the sliding part to reproduce the cyclic motion of the experimental activity (step two). In Figure 4-12a the device is presented as cut along section A-A and the slider is hidden to ease the visualization of the deformed shape of the sleeve plates at the end of Step 1: it is evident that the applied bolt's pressure produces a bending of the two external plates around the internal sliding element, confirming the output of the model proposed in Section 4.1. and Figure 4-4. As shown in Figure 4-12 the bending of the plates concentrates the contact area around the edges of the slider, producing a distribution of longitudinal shear stresses, computed in the second step, corresponding to the worn surfaces of the test shown in Figure 4-10.

a) Step 1 b) Step 2

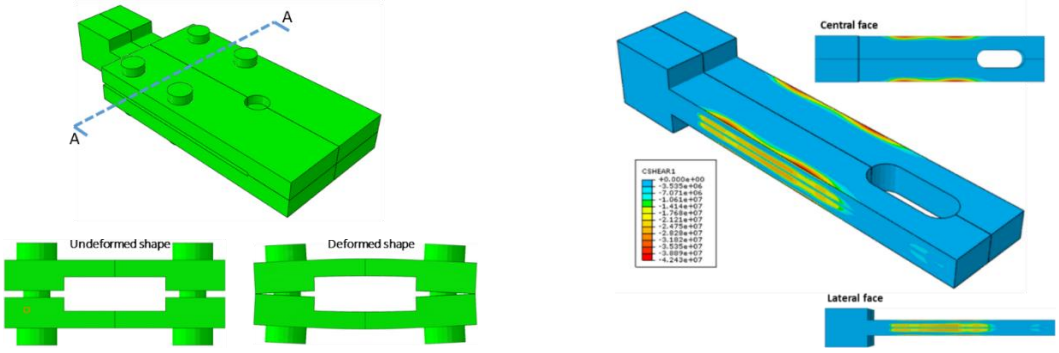

Figure 4-12. Results of numerical analysis: a) deformed shape following the tightening of the bolt for a value of 4.7 KN, b) distribution of shear stresses over the sliding element.

The sliding force required to exceed the friction resistance can be computed integrating the shear stress over the external surface of the slider. It was found that the friction force developed over the lateral faces (19.4 KN) is almost twice the one on the horizontal surfaces (10.1 KN). The large contribution of the lateral faces to $F_{sl\,num} = 29.8\ KN$, confirms that four pair of contact surfaces should be considered for the prototype ($n = 4$ in Eq. (4.12)). The value of F_{sl} is in good

agreement with the maximum value of slippage force $F_{sl\ (max)}$ = 31.1 kN measured experimentally for M = 15 Nm.

Figure 4-13 shows the numerical simulation's load-displacement loops for 20 cycles of imposed periodic displacement for $\mu = 0.36$. While the hardening behaviour and the slack at the inversion of load, are not reproduced, the values of slip force for 0.36 is within 6% of the experimental maximum value. Therefore, this limit value of $\mu = 0.36$ can be considered as the upper bound that identifies the device's operational range given a perpendicular pressure.

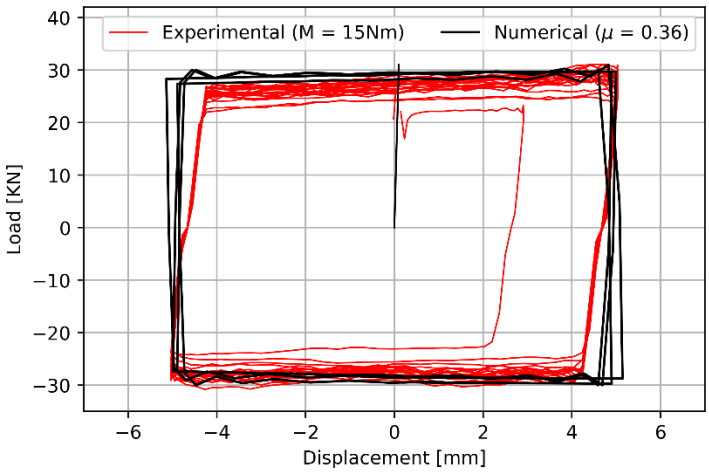

Figure 4-13. Comparison between computational a) and experimental results b)

4.4 Second generation prototypes

The results of the numerical analysis confirm the validity of the conceptual design of the device, but also the need for substantial refinements, to reduce wearing off of the surface and improve stability of the effective damping. Such observations have informed the design of a second prototype, whereby the basic concept is maintained, however the shape is altered to replace the internal flat slider and the sharp edges of the sleeves which caused the concentration of stresses.

The result of the new design is a cylindrical shape for the slider and its housing within the sleeve, as shown in cross section in Figure 4-14a. The shape is optimized reducing the distance, *e*, between the bolt's axial line and the extreme point of contact, namely point *O* in Figure 4-14a, and maximizing the variable moment of inertia of the plates, to reduce the bending effect.

Similarly to the procedure applied in Section 4.1, a simple analytical model (see Figure 4-14b) is developed to determine the deflection of the plate.

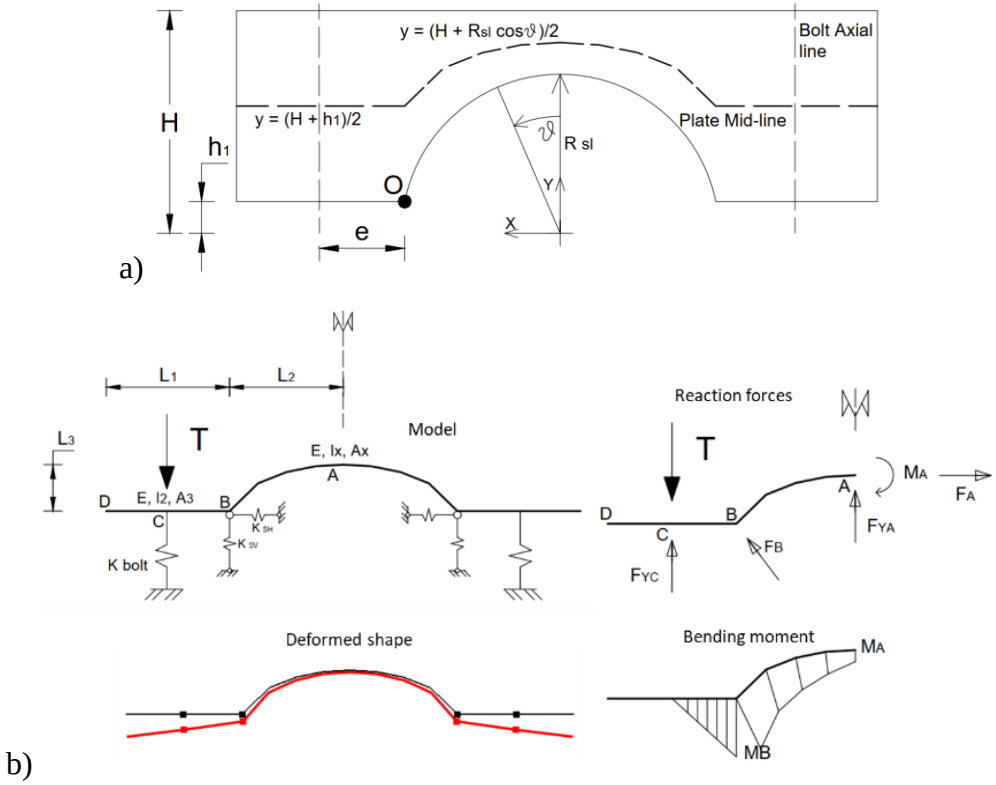

Figure 4-14. Refined prototype: a) Cross-section of clamping plate, b) analytical model

The results highlight that for the same values of vertical load, the deformation due to bending is reduced compared to the SteSq model, as the moment of inertia of the curved portion increases with the bending moment distribution. Moreover, the plate transmits no bending moment to the bolts, hence avoiding yielding of the bolts head.

This is confirmed by observing the resultant deformation across the cross section of a 3D numerical model of the new prototype produced in Abaqus, where transversal bending for the same level of applied bolt preload is negligible with respect to the results for the SteSq device presented in Figure 4-12. The model also proves that the new geometry results in larger overall contact area with smaller patches of localized stresses, an order of magnitude smaller than the ones computed for device SteSq, (see Figure 4-15b), implying that localized wear will be reduced.

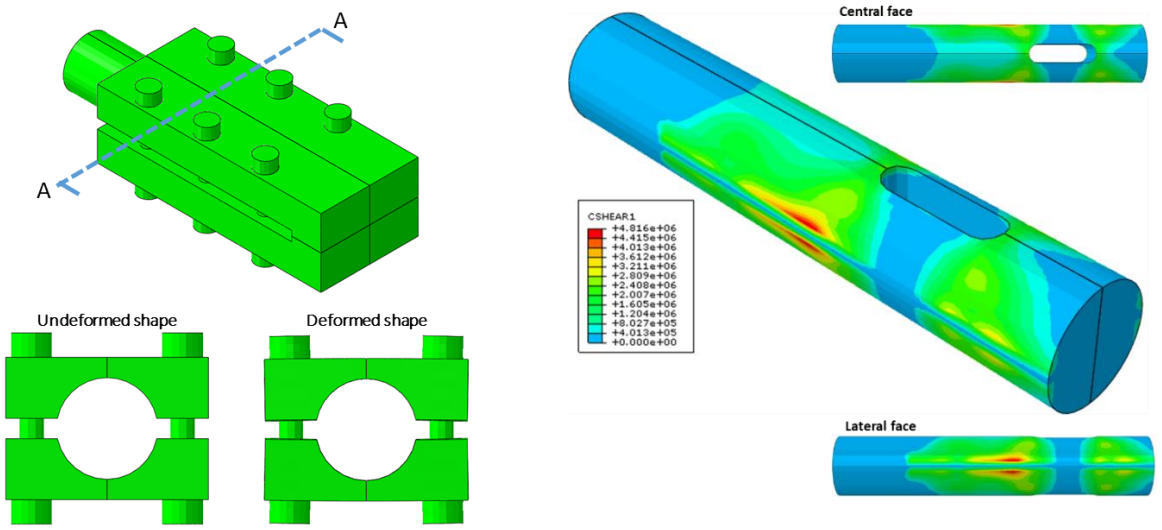

Figure 4-15. Results of numerical analysis: a) deformed shape following the tightening of the bolt for a value of 10.7 KN, b) distribution of shear stresses over the sliding element.

The change in shape also allows to address other concerns about the impact of the device in historic buildings: the overall width of the device is reduced so that it can be housed within the cored hole for the passive bonded anchor, without need for further removal of historic authentic material. The size of the bolts is reduced, and their number increased to deliver the same value of $F_{\text{perp (N)}}$.

However, the issue of abrasion and wear of the surfaces, is only partially resolved with the change in shape, as it also depends on the nature of the materials involved in the friction-controlled motion as already discussed in Section 4.1. Among the different materials that can be used for friction damping, in civil engineering application, the sliding of brass on steel exhibits a lower friction coefficient (μ =0.2), but also more stable force-displacement loops with lower material degradation than steel on steel. Alternatively, plastic-based materials, such as Teflon, are also commonly employed in wall-type dampers (Nabid, Hajirasouliha, and Petkovski 2017) and isolation systems (M. C. Constantinou, Reinhorn, and Watson 1988) in seismic retrofitting design. They produce stable force-displacement loops with low material degradation, but large values of applied perpendicular pressure can affect the friction force, as it reduces with increasing normal pressure. Aiming to achieve low cyclic degradation, stable friction coefficient and effective damping variation within the acceptable thresholds, the new prototypes with the geometry shown in Figure 4-16, are manufactured using three materials as frictional interfaces, namely steel, brass, and Fluorinated Ethylene Propylene (FEP), a plastic material known for its capacity to resist high temperatures and chemical agents.

a) b)

Figure 4-16. Refined prototype (BraCyl), b) device's components and functioning.

The prototype's name, types of material in contact, nominal friction coefficient of the materials in contact and modulus of elasticity of the weaker material as reported by manufactures, are shown in Table 4-2 for each prototype.

Table 4-2. Properties of revised prototypes

Prototype Name	Type of Contact	$\mu_{(N)}$	E [Gpa]
SteCyl	Steel on Steel	0.3	210
BraCyl	Brass on Steel	0.2	97
FEPCYl	FEP on Steel	0.15	0.7

4.5 Short-term assessment of revised prototypes

Following the methodology, the prototypes are tested for short-term stability. The value of k_m is expected to be affected by the shape of the bodies in contact and the bolts arrangement; hence the first test activity is repeated. Figure 4-17a shows the values corresponding to the new prototype's geometry which mounts class 12.9 steel bolts with 6 mm in diameter.

The linear regression provides a value of k_m= 0.37. While the increase in k_m with respect to the SteSq prototype is only 6%, the improved geometry shows two main advantages. Firstly, the relationship between torque and bolt preload remain linear for larger values of M, confirming that no loss in bolt preload occurs due to local plasticity. Secondly, for equal values of torque, the bolt preload is 25 % larger meaning that a larger perpendicular load can be achieved, as shown in Figure 4-17a. The ultimate torque is set to 36.5 Nm, as computed from Eq.(4.2), with $d = 6\ mm$, $k_m = 0.37$, $f_{ub} = 1200\ MPa$ and $As = 20.1\ mm^2$. However, for $M = 35\ Nm$ the bolts displayed brittle failure in most of the cases. This is due to the bending moment

produced during tightening, which becomes relevant as the bolt preload approaches the proof load (F_p = *16.8 KN*). The additional tensile stress associated to the bending deformation causes the yielding of the bolt along the bolt's shank, which then fails in a brittle manner, due to the lower ductility of 12.9 class bolts compared to 8.8 bolts. To avoid this effect, the ultimate value of reference torque is set to 30 Nm.

Following the updated design and calibration of the bolt torque, the three devices are subjected to cyclic loading to assess the reliability of the different friction interfaces. For this activity, a minimum of 3 prototypes are tested for each version of the cylindrical device. The SteCyl and BraCyl devices are tightened with 4 bolts at 15 Nm torque, while the FEPCyl is tightened with 6 bolts at 20 Nm torque, to compensate for its smaller nominal friction coefficient. Four pressure cells are installed below the head of four bolts to record the variation of the pretension transmitted throughout the testing activity. The testing apparatus also comprises an LVDT positioned on the slider to measure the relative motion of the slider with respect to the clamping plates as shown in Figure 4-17b. The tests are carried out imposing 20 sinusoidal displacement cycles with peak stroke *d= ±6 mm* and loading frequency *f = 0.1 Hz*.

a)

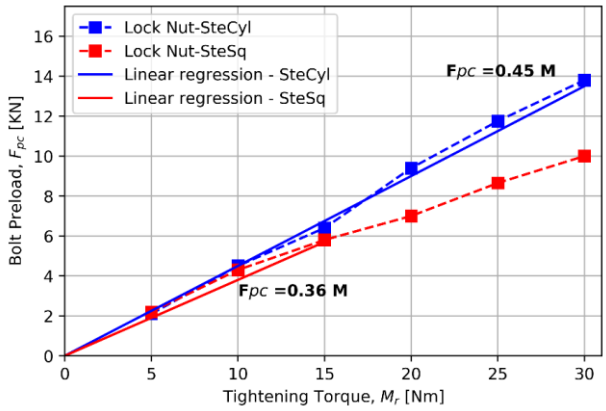

b)

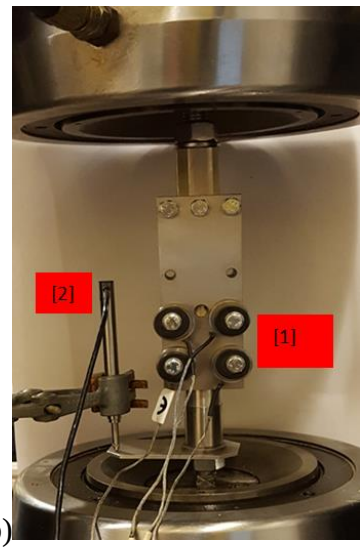

Figure 4-17: a) Correlation between bolt pretension (Fpc) and applied bolt torque (M), b) Testing apparatus [1] Load cells, [2] LVDT.

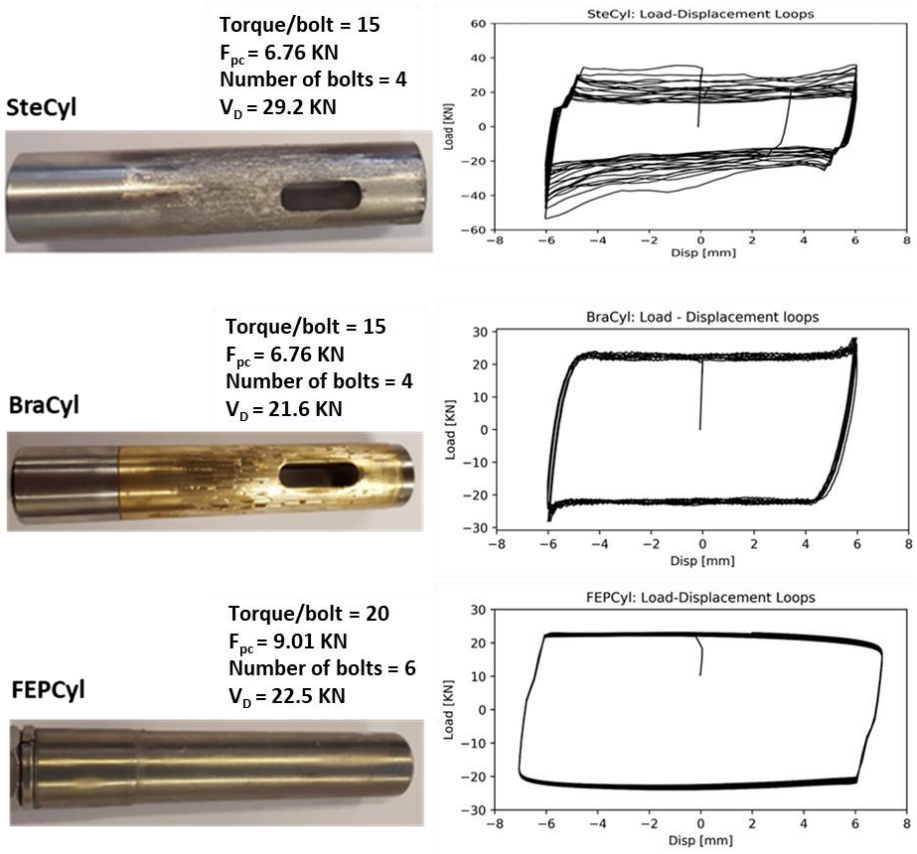

Figure 4-18. Comparison between the three model for revised prototype: wear conditions, load-displacement loops, and loading/geometry conditions.

Figure 4-18 shows the results for the three variants of the second prototype in terms of load-displacement loops. The figure reports also the number of tightened bolts, the nominal bolt preload, the design force and the wear condition of the sliders after 20 cycles of load. The results are summarised in Table 4-3, which also includes the values obtained for the SteSq at M = 15 Nm, for comparison. The three prototypes of BraCyl and FEPCyl behaved almost identically, with a sample-to-sample difference in maximum $\Delta\xi_{effb}$ of just 4% and 2% respectively, confirming that the contact interface plays the largest role in contributing to the stability of the devices. Conversely the SteCyl displayed a large variability (maximum $\Delta\xi_{effb}$ of 30%) and the most regular results are picked for display.

Table 4-3. Summary of the test's results

Variables		Prototype			
		SteSq	SteCyl	BraCyl	FEPCyl
M_r	[Nm]	15	15	15	20
F_{pc}	[KN]	5.36	6.76	6.76	9.01
$F_{perp\,(N)}$	[KN]	21.4	27.03	27.03	54.05
$F_{perp\,0\,(M)}$	[KN]	20	26.5	28	53
β	[%]	93%	98%	104%	98%
$\mu_{0\,(M)}$	[-]	0.32	0.16	0.19	0.103
$\mu_{max\,(M)}$	[-]	0.392	0.35	0.22	0.105
μ_D	[-]	0.36	0.27	0.21	0.104
$max(\Delta\mu_{(M)})$	[-]	11%	41%	10%	1%
V_D	[KN]	30.9	29.2	22.7	22.49
$F_{sl,3}$	[KN]	26.3	29.17	23.06	23.62
$F_{sl\,(mim)}$	[KN]	24.40	18	20.1	21
$F_{sl\,(max)}$	[KN]	31.1	51.5	24.4	23.62
$\xi_{effb,3}$	[-]	0.52	0.6	0.68	0.63
$max(\Delta\xi_{effb})$	[%]	18.3%	76%	10.4%	7.2%
S_w	[mm]	1.5	1.00	0.50	0.3

The SteCyl shows a dramatic increase in slip load between the first and the last cycles and severe signs of wear are noticeable both on the slider and the plates. The signs of abrasion are spread over all the surface of the cylindrical slider, rather than concentrated only on the edges, proving that the cylindrical shape determines a better use of the available contact area. On the other hand, the use of a larger contact area determines larger quantity of material dust and widely spread signs of degradation, which increase the occurrences of interlocking and adherence between the parts, thus increasing the resistance to sliding. As a result, for the SteCyl prototype $\Delta\xi_{effb}$ and $\Delta\mu_{(M)}$ reach a maximum of 76% and 40% respectively and a severe wear rate is registered. In the case of the BraCyl prototype, the application of the brass sleeve improves the stability of the load-displacement loops and the maximum $\Delta\xi_{effb}$is about 10%, thus within the threshold prescribed by EN 15129. Similarly, to the SteCyl and SteSq, the slippage force measured for the BraCyl increases with the number of cycles, but the hardening behaviour is less marked. For the FEPCyl prototype, the use of the FEP tube around the slider stabilizes even further the hysteresis loops and the $\Delta\xi_{effb}$ is no greater than 7.2%. The use of a propylene rather than a metallic material as friction interface has the additional effect of removing the load peaks noticeable when the slider inverts its motion, passing from a state of dynamic to a state of static friction.

For the loading conditions reported in Table 4-3, the variations of the $\mu_{(M)}$ ξ_{effb} during the test are summarized in Figure 4-19 for the three cylindrical prototypes and the SteSq at M = 15Nm. Both brass and FEP materials proved to be efficient friction interfaces as they present a stable friction coefficient throughout the test and a maximum damping variation below 10%. The FEPCyl prototype displays mild softening behaviour after the third cycle, registering a decrement of 1% in the friction coefficient with respect to the initial value, as expected for synthetic polymers subjected to cyclic sliding motion (M. Latour, Piluso, and Rizzano 2014).

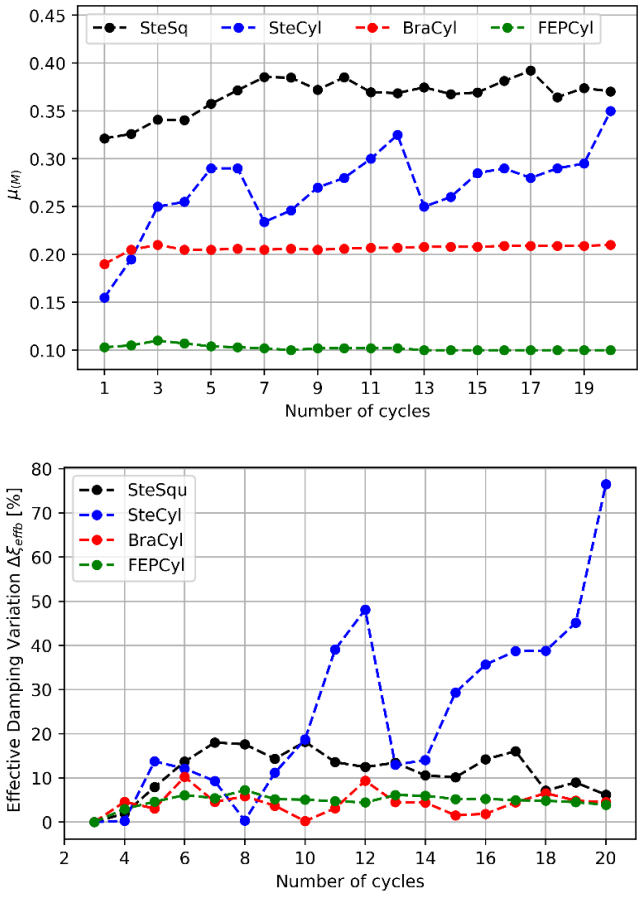

Figure 4-19. Variation of the friction coefficient $\mu_{(M)}$ and ξ_{effb} for 20 cycles of load. Comparison between the prototypes of the revised device and SteSq at M = 15Nm.

Given the abrasion depth and the computed max ($\Delta\mu_{(M)}$) (reported in Table 4-3), the S_w of BraCyl and FEPCyl is "mild with low wear rate". This result is expected as both the brass and FEP have lower elastic modulus *E* compared to stainless steel.

Eq. (4.11) provides reasonable results for metals, but in case of polymeric-based materials, such as FEP, other factors such as contact pressure (P), and the sliding speed (v) might affect the wear rate and the coefficient of friction (Cho and Kwon 2004). Therefore, to conclude the short-term assessment of the FEPCyl prototype, the maximum variations of μ_M and ξ_{effb} are

investigated for values of bearing pressure and sliding speed compatible with seismic engineering applications.

The displacement history of Eq. (4.10) is imposed at frequency values of 0.5 and 2Hz and exploiting the full sliding amplitude of the slider, d = ± 10 mm, as recommended by EN 15129. By varying the frequency of the displacement wave form while keeping the amplitude fix, the sliding velocities of 20 mm/s and 80 mm/s are obtained. The device is tested for two values of reference torque, 20 and 25 Nm, and the corresponding load-displacement loops are shown in Figure 4-20.

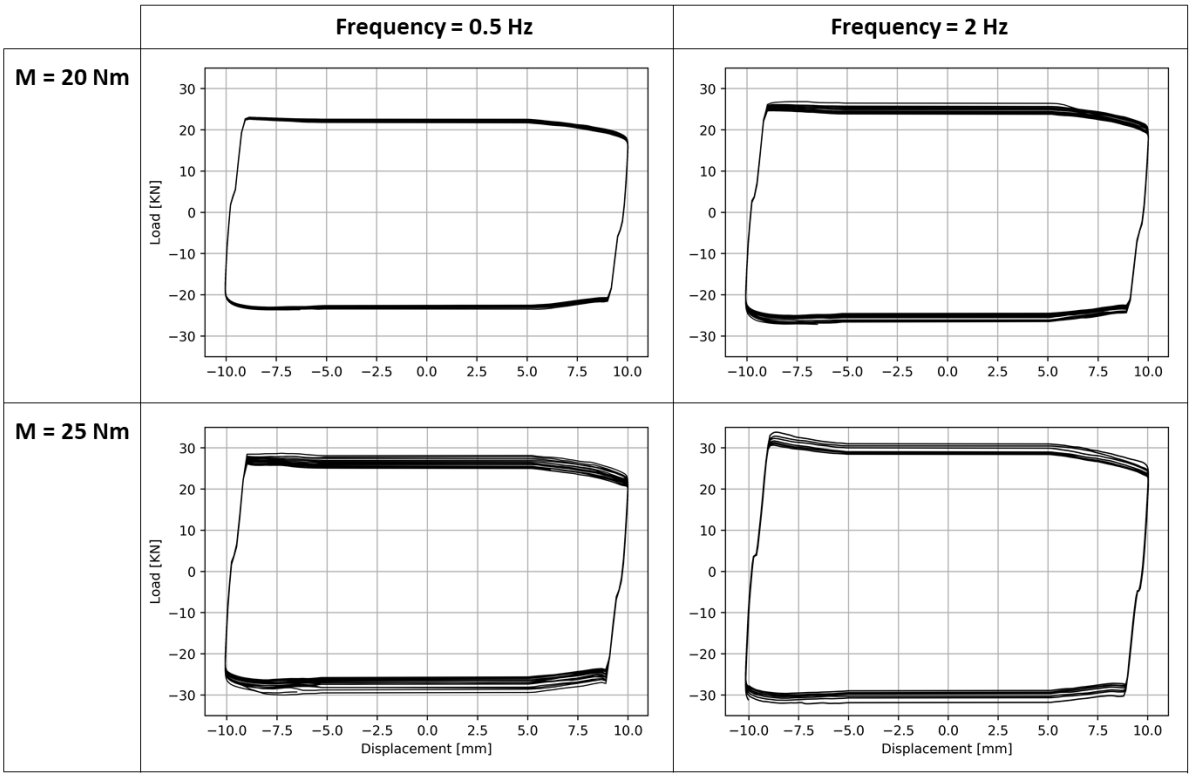

Figure 4-20. Load-displacement loops of FEPCyl at *f = 0.5 Hz* and *2Hz*, and *M = 20 Nm* and *25 Nm*

For the same value of torque to the bolts, larger values of slippage force are registered for the higher value of frequency. The friction coefficient was computed for each cycle according to Eq. (4.11), and the variation of μ_M is shown in Figure 4-21a. From the graph, it can be seen that μ_M increases with increasing velocities and that follows a softening behaviour during testing. Conversely, the friction is inversely proportional to the pressure acting on the slider. Figure 4-21b shows the evident effect of velocity and pressure on the sliding coefficient of friction for FEP. The mean values of friction coefficients over 20 cycles are reported, along with the value of μ_M at *f = 0.1 Hz* (sliding velocity = 4m/s), as obtained from previous tests. The value of the coefficient of friction increases with an increase in the sliding velocity up to a threshold beyond

which it remains constant. This value of velocity is between 100 and 200 mm/s. This experimental evidence is in agreement with the results found by other researchers which tested the correlation between values of friction coefficients, sliding velocity and applied pressure for plastic-based materials (B. A. Mokha et al. 1990; M. Constantinou, Mokha, and Reinhorn 1990).

a) b)

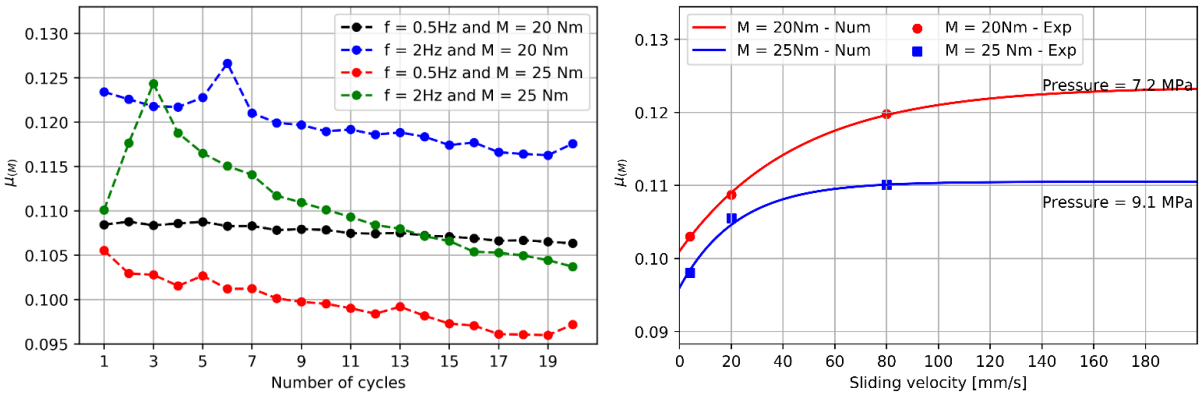

Figure 4-21. a) Variability of μ_M over 20 cycles of load for f = 0.5 and 2Hz, and M = 20 and 25 Nm. b) Variation of Sliding Coefficient of Friction with Velocity and Pressure

As proposed by Constantinou, et al. (1990), the coefficient of friction at sliding velocity V may be approximated by the following equation:

$$\mu_s = \mu_{max} - D_f \, exp(-aV) \tag{4.16}$$

in which μ_{max} is the coefficient of friction at large velocity of sliding (after leveling off), D_f is the difference between μ_{max} and the sliding value at very low velocity, a is a constant for given bearing pressure.

Table 4-4 presents values of μ_{max}, D_f, and a for various pressure conditions that resulted in the solid-line curves in Figure 4-21b. It is apparent that Eq. (4.16) reproduces the results of experiments with good accuracy and that it can be used for a more accurate description of the coefficient of friction for the FEP interface. The maximum variation of $\mu_{(M)}$ is within the limit of 15% and max ($\Delta\xi_{effb}$) is below 10% for all cases, meaning that the FEP interface is able to deliver a stable behaviour under different conditions of pressure and sliding velocity. For

practical uses, the value of $\mu_{(D)}$= 0.11 is recommended to compute the design force of the FEPCyl device.

Table 4-4. Values of μ recorded at different sliding velocities and numerical parameters to compute μ_s

Torque, M [Nm]	Pressure, P [MPa]	Frequency, f [Hz]	Sliding Velocity, v [mm/s]	$\mu_{(D)}$ [-]	max($\Delta\mu_{(M)}$) [-]	max($\Delta\xi_{effb}$)) [-]	μ_{max} [-]	D_f [-]	a [-]
20	7.3	0.1	4	0.103	1%	4.30%	0.123	0.026	0.022
		0.5	20	0.109	1.20%	1.90%			
		2	80	0.119	2%	5%			
25	9.1	0.1	4	0.094	2%	5%	0.11	0.014	0.045
		0.5	20	0.1	2.40%	6.60%			
		2	80	0.11	6%	9.0%			

4.6 Long-term stability - Laboratory tests on individual devices

Both BraCyl and FEPCyl present values of $\Delta\xi_{effb}$ within the maximum variation allowed by EN 15129 (EN 15129 2006), meaning that no further improvement of the design is required and that both device have a stable and reliable short-term behaviour. Therefore, in line with the testing methodology proposed, the long-term stability and reliability of the dissipative devices is experimentally investigated. Along with BraCyl and FEPCyl, the SteSq prototype is tested for the long-term behaviour. Even if it presents a maximum value of $\Delta\xi_{effb}$ above the limit of 10%, the variation is less pronounced than the SteCyl and hence considered in preference to the latter for the environmental aging.

According to EN 15129, the seismic device shall remain operational also for the range of environmental conditions expected during its projected service life. However, little guidance is given for what environmental conditions should be selected and how long should they be exposed to the aging process. Therefore, for the present testing activity, the expected environmental conditions are obtained by considering the average variation of the temperature and humidity in an earthquake-prone city over a period of 50 years, as discussed in section 4.1. L'Aquila, a city in the centre of Italy that suffered from a 6.3-magnitude earthquake in 2009 (Paganoni 2015) , is taken as reference for the temperature (T) and relative humidity (RH) ranges, which vary from -1° C to 27° C and from 50% to 80% respectively within a period of one year (Giuliani and Antenucci 2017). The first 5 cycles are shown in Figure 4-22b: each cycle is completed in one day and corresponds to the variation of temperature and humidity of one year. These values of T and RH represent the expected in-wall conditions of masonry walls,

as they are in good agreement with values recorded by long term field monitoring of historical buildings (D'Ayala and Aktas 2016; Aktas et al. 2017).

a)

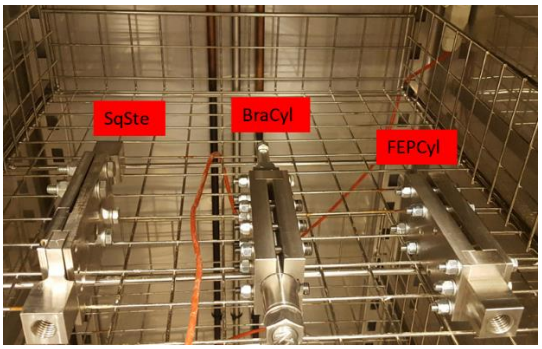

b)

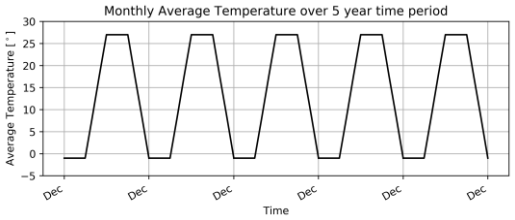

c)

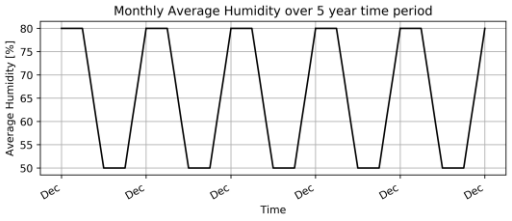

Figure 4-22: a) Devices positioned in the thermostatic cabinet, b) cycles of temperature and c) relative humidity

The devices are pre-tuned to the same values of reference torque imposed in the short-term analysis and then are placed in a thermostatic cabinet for 14 days, subjecting them to temperature and humidity cycles. Once the thermal and environmental conditioning is over, the "aged" devices are individually tested in displacement-control mode for 20 cycles of load (d_0 = ± 5mm, f_0 = 0.1 Hz) and the results compared with those conducted on the pristine devices (referred to as "unaged" devices). The devices are deemed to have a reliable and stable long-term behaviour if the variation in effective damping does not exceed a limit value of 15%. The initial preloading conditions and the values of the main variables are reported in Table 4-5.

Table 4-5. summary of results of loading test on aged devices

Prototype	M_r [Nm]	F_{pc} [KN]	$F_{perp\ (N)}$ [KN]	μ_D [-]	V_D [KN]	$F_{sl,3}$ [KN]	$F_{sl\ (min)}$ [KN]	$F_{sl\ (max)}$ [KN]	$\xi_{effb,3}$ [-]	$\max(\Delta\xi_{effb\_aged})$ [%]
SteSq	15	5.36	21.4	0.37	31.7	28.5	27.10	43	0.57	50.9%
BraCyl	15	7.14	28.57	0.20	22.9	22.8	21.5	25.2	0.64	10.5%
FEPCyl	20	9.52	57.14	0.110	25.14	25.1	23.5	25.6	0.64	6.4%

The weathering procedures proved useful into exploring the development of corrosion in the device's metal components. Looking at the results reported in Figure 4-23, the load displacement loops for the SteSq prototype show that the performances of this device are greatly

affected by the imposed aging conditions: the slip load is greater than the design force V_D and the device displays a hardening behaviour with the progressing of the test.

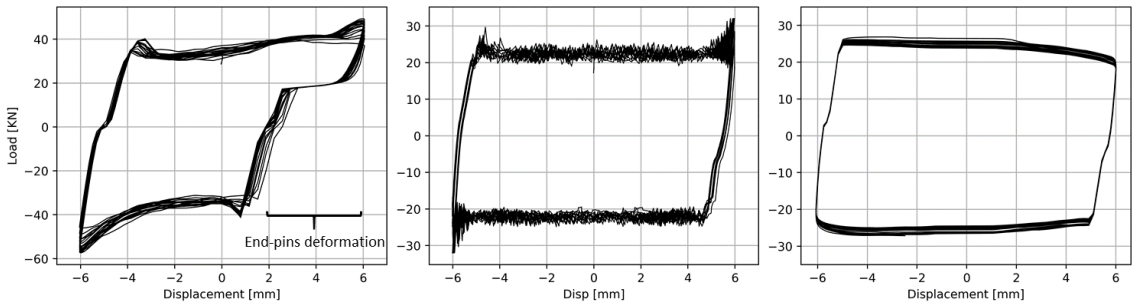

a) b) c)

Figure 4-23:. Results of load cycle test on aged devices: a) SteSq, b) BraCyl, c) FEPCyl

The central dowel pin used to control the slider's motion and the end-pins assembling the plates together showed severe signs of corrosion (Figure 4-24b). Dowel pins are used to keep device's components alignment purposes but had not been treated by the manufacturer to resist aggressive weathering conditions. This causes additional friction between the slider and the central dowel pin thus increasing the slippage load. In particular, the slippage force is almost twice the design slippage load in the stick-slip phase. Moreover, the corrosion weakened the mechanical strength of the end-pins which deform in shear when the motion reverses and the slider is pushed into the assembly. As a result, a relative motion of 2.4mm is recorded, as visible in Figure 4-23a. To avoid this negative effect in the second-generation prototypes and to increase the stiffness of the fix part of the device the pins were replaced with high strength bolts in the "design refinement" task.

Regarding the BraCyl prototype, the fastener that holds in place the brass tube of the BraCyl device failed during the first cycle of load and the test was suspended. A visual inspection of the device highlighted that the presence of two materials with different electrical potential in contact had caused the development of galvanic corrosion, as shown in Figure 4-24a. A class 12.9 zinc-coated fastener was adopted to replace the faulted one and the device was placed again in the thermostatic cabinet for 14 days before repeating the loading test. Because zinc is a lesser noble metal than iron steel, the zinc will corrode first, protecting the steel of the fastener against rusting until all zinc has dissolved (The European Stainless Steel Development Association 2009).

The load-displacement loops reported in Figure 4-23b highlight that the BraCyl prototype has a stable behaviour during sliding with a slip load comparable to the one obtained for a fresh

device. Nonetheless, the static load recorded when the slider inverts its motion is about 40% greater than the load recorded during motion, while the stick-slip phase was less evident (30% increase) for the unaged BraCyl prototype.

The FEPCyl device (Figure 4-23c) displays the most stable behaviour with a maximum variation of damping $\Delta\xi_{effb\,(aged)} = 6.4\%$ similar to the one computed for the unaged prototype ($\Delta\xi_{effb} = 7.2\%$). As for the unaged prototype, the FEP tube eliminates the end-run spikes, resulting in the most reliable behaviour among the three prototypes.

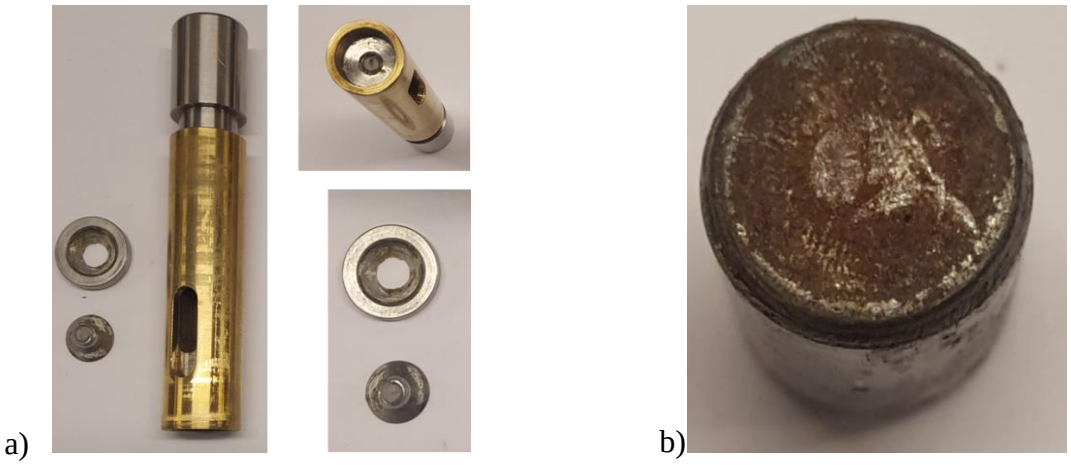

Figure 4-24:. a) Signs of galvanic corrosion of the BraCyl fastener b) corrosion of the central dowel pin for the SteSq prototype.

4.7 Summary of tests results and conclusions

This chapter presents and exemplifies the first task of the proposed validation methodology by assessment and refinement of friction-based dissipative devices. The methodology comprises three main activities: two experimental activities explore the short-term and long-term stability of the device under cyclic loading, comparing the test results with the performance requirements recommended by the appropriate standard. The third activity investigates, by advanced 3D numerical simulations, alternative design solutions able to reduce the maximum variation of the prototype's damping, max ($\Delta\xi_{effb}$), down to 10%, as recommended by the EN 15129 and to ensure long term stability by design. The max ($\Delta\xi_{effb}$) has proven to be effective in describing the device performance in terms of both the variation of the slippage load in respect to the nominal design force V_D for each cycle, and of the stability of the response within the 20 load cycles with respect to the reference third cycle.

The validity of the proposed methodology is first tested on the patented prototype of friction-based device, the SteSq, which is part of a dissipative anchoring system designed for the seismic strengthening of historical buildings. The results of the experimental activities highlighted that the performance of the SteSq device varies by 18% for the short-term test, beyond the limit set by EN 15129. This clearly outline a need for re-design.

The design by analysis leads to the implementation of a cylindrical slider, in place of the squared one, which proves to increase the contact area, and improve the clamping efficiency of the bolts. According to this result, three prototypes are produced and ad-hoc material, such as brass and FEP, are implemented as friction interfaces, to address the issue of high wear rates.

Compared to the SteSq, the second generation of prototypes reduces the deflection of the enclosing plate, thus achieving larger bolt preloading for equal values of torque. Under cyclic loading, the prototypes featuring the brass and FEP friction interfaces displayed 10% and 7% of variability in effective damping and less severe sign of wear, hence well within the EN 15129 performance requirement.

The procedure needed to compute the design force of the devices is obtained from the results of the experimental activities and draws on the basic formulas valid for bolted unions and dry friction. Nonetheless, the experimental results display that the formulation provided by EN 1090-2 for bolted connections overestimates the nominal perpendicular force, with an error of about 42% for the SteSq and of 28% for the cylindrical devices.

Therefore, two empirical values of k_m are computed specifically for the devices' geometry achieving an accuracy of above 95% between the nominal and recorded values of perpendicular force. Then, the design force V_D is computed in a straightforward way from Eq. (4.12) considering four friction surfaces ($n = 4$) and values of μ equal to 0.36, 0.21 and 0.11 for the SteSq, BraCyl and FEPCyl, respectively.

Additionally, the revised devices and the SteSq prototype are tested after being exposed to cycles of temperature and relative humidity for fourteen days in a thermostatic cabinet. This type of tests aims at evaluating the long-term stability of anti-seismic devices which is rarely investigated in literature, even though these devices often comprise different metals or high-tech materials that might be affected by aggressive environmental conditions. This lack of knowledge is partially due to the insufficient guidance of EN 15129: while stating that the effects of ageing should be evaluated by repeating the cyclic loading tests in different exposure conditions, it remains vague on the details, especially for displacement-dependant devices that

do not carry vertical loads. Given this lack of guidance, the ranges for the environmental variables were derived from expected in-wall conditions from masonry walls in an earthquake-prone region in relatively extreme climatic conditions (hot summers, cold winters, high level of moisture).

The test's results highlight the weakest parts of the devices, which in some case failed due to low corrosion resistance. Moreover, it is clear that the aging conditions can affect the performance of the devices: the SteSq displayed and increment in max ($\Delta\xi_{effb\_aged}$) up to 50% while the increment was less marked for the BraCyl and FEPCyl which remained within the limits of EN. The achieved stability of $\mu_{(M)}$ and ξ_{effb} will allow for a more accurate and simple design: the design force will better represent the actual slippage load, which must be smaller than the minimum capacity of the assembly to ensure the device's activation and the energy dissipation. Conversely, for the SteSq device V_D was defined as a range of values for each perpendicular load(D'Ayala and Paganoni 2014), due to the high wear rate of the friction surfaces and the resulting large variability of $\mu_{(M)}$, thus hindering the reliability of the design.

In conclusion, the methodology proved to be a valid tool for the complete assessment and validation of a friction-based dissipative device. Although the validity of the methodology was tested for a bolted slotted device, its use can be extended to other typologies of friction-based devices. For instance, devices consisting of an inner shaft shrink-fitted inside a second shaft would require a different test for the assessment of the imposed perpendicular load, but the performance parameters and procedural steps of the methodology remain valid.

In the next chapter, the refined dissipative devices are combined with the anchoring technology developed by Cintec International to complete the assembly of the dissipative grouted anchoring system (D-GAS). As previously outlined, this anchoring technology is widely applied for the strengthening of heritage buildings and provides a large load capacity well as corrosion resistance (Cintec International, Material safety data sheets, 2019).

5 Testing of Dissipative Grouted Anchoring System

5.1 Introduction

In the previous chapter, the friction-based dissipative device is investigated as an isolated element under several loading inputs and after being exposed to cycles of temperature and relative humidity. According to the experimental and numerical results, the initial prototype (SteSq) is partially redesigned and three prototypes (SteCyl, BraCyl, FEPCyl) are produced implementing alternative materials for the friction interfaces, i.e. brass and FEP, to address the issue of high wear rates.

This chapter presents two experimental campaigns carried out to evaluate the behavior of the Dissipative Grouted Anchoring System (D-GAS) featuring the new generation of devices. The D-GAS is connected to a set of masonry specimens and the system's performance is obtained for monotonic pull-out loading and cyclic loading.

Before introducing the experimental activity carried out by the author, a review of pull-out tests performed on grouted anchors is presented in Section 5.2 to discuss the state-of-the-art concerning this anchoring technology.

The first set of tests, reported in Sections 5.3 to 5.4, assesses the interaction between the masonry and the grouted anchorage. The performance of the D-GAS under monotonic pull-out loading is compared to that of a traditional Grouted Anchoring System (GAS) under the same loading regime to infer the influence of the device's activation on the capacity and failure modes of the anchoring system.

The second set of tests, presented in Section 5.5, aims at assessing the cyclic behaviour of a masonry connection strengthened by the dissipative anchoring system. To this purpose, a T-connection between orthogonal walls is cyclically loaded in the out-of-plane direction of the front wall to cause the relative detachment of the two panels and trigger the device's motion.

These two sets of tests are complementary and present an increasing level of complexity: for instance, the relative motion of the grouted sleeve is monitored in the first activity only, due to physical constrains of the second testing set-up. On the other hand, the test on the T-connection

is a superior representation of the problem at hand as it provides insight on the installation of the system in a real-case application and introduces a loading scenario which is more representative of a seismic-like action.

As discussed in the Chapter 3, the data collected during the experimental activity feeds into the development of a two Finite Element models, which are presented in section 5.4 and 5.5 for the first and second set of tests respectively.

5.2 Review of experimental pull-out tests of grouted anchors

When masonry corner locations – L or T-connection between walls – undergo seismic loading, the panel perpendicular to the direction of the main shock will tend to overturn as consequence of its comparatively lower flexural stiffness. The extent of the resulting relative detachment depends on the presence of former damages, on the quality of the materials and on the extent of overlapping of masonry units at the joint between the masonry panels. If grouted anchors are inserted to improve the connection between panels, the transmission of the seismic excitation to the metallic element relies on the bonding capacity developed at the steel-grout interface and at the grout-masonry interface. Because of the lower embedment length, the part of anchorage grouted in the wall perpendicular to the direction of seismic load is the most likely to fail, leaving the remaining part almost undisturbed, as observed in damage surveys following seismic events (Dizhur, Schultz, and Ingham 2016) and in experimental test on masonry connections (Paganoni and D'Ayala 2014).

Accordingly, the performance of grouted anchoring systems able to control the relative detachment of adjacent walls can be estimated by the test set-up commonly used to determine the pull-out capacity of grouted anchors. For reference, the set-up proposed by Silveri et al. (2016) is shown in Figure 5-1a: it reproduces the portion of stainless-steel anchor embedded in a masonry panel perpendicular to the main seismic action, while the pulling action of the testing apparatus simulates the reaction of the anchor lying within the wall parallel to the main shock direction. A similar testing set-up can be adopted to assess the performance of yielding and friction dissipative devices: these can be installed as add-on elements (marked in red in Figure 5-1b) in series between the anchor grouted in the wall and the pull-out jack, as previously done by D'Ayala and Paganoni (2014).

a) b)

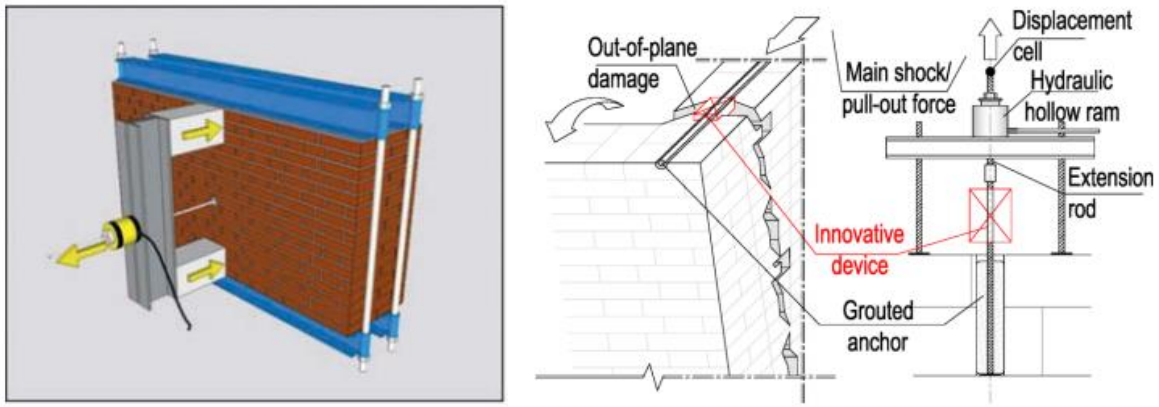

Figure 5-1 Experimental set-up of pull-out tests as performed by Silveri et al. (2016), and D'Ayala and Paganoni (2014)

Pull-out tests represent an effective way to reproduce – statically – the forces exerted on the grouted anchors and to determine a reliable estimate of pull-out force depending on the numerous parameters that can influence the behaviour of grouted anchors. Due to the uncertainty in the anchor's behaviour, pull-out tests are also carried out in-situ before installation under the same procedures of experimental tests to verify the load bearing capacity of the anchor and specific parent material they are embedded in. Given the lack of specific design clauses for anchors in masonry, the tests are performed according to the same protocols used for pull-out test of anchors in concrete substrata and of masonry bed-joint reinforcement, (EN 1881:2006 2006; EN 846-2:2000 2000), or according to accepted procedure in existing literature (Arifovic and Neilsen 2006; Algeri et al. 2010).

Seven experimental programs performed by different authors on different anchor types are reviewed in Section 5.2.1: Gigla and Wenzel 2000; Arifovic and Neilsen 2006; Paganoni and D'Ayala 2014; Moreira et al. 2014; Silveri et al. 2016; Ceroni et al. 2016; Ceroni and Di Ludovico 2020.

These tests investigate the influence of several parameters, such as type of masonry substrates, anchor's material, surface and length of embedment, grout thickness and strength, presence of stress transversal to the anchors, spacing between anchors, distance between anchors and wall's edge, etc., on the behaviour of grouted anchors. To the author judgment and knowledge, they represent the most comprehensive set of experimental programs performed on metallic grouted anchors to discuss the influence of the abovementioned parameters on the load and ductility capacity.

The focus of the review is on metallic anchors as they represent the strength-only element of the innovative anchoring system discussed in this thesis. Moreover, compared to other anchoring technologies, such as FRP anchors, metallic rods have been extensively explored and are already widely applied by professionals in conservation engineering, as they are cost effective and conforming to current conservation recommendations.

The empirical formulation commonly used to predict the load capacity of grouted anchors are reported in Section 5.2.2. The values reported by the authors for each experimental campaign are collected in a database, presented in Section 5.2.3, and used to propose an alternative set of empirical equations to derive the pull-out capacity. The relevant parameters are then normalised to obtain values of generic validity for design purposes.

5.2.1 Review of pull-out test on anchors embedded in masonry

For grouted anchors installed in masonry substrates, the observed experimental failure modes as classified by NIKER (2012) are:

- ***Cone Masonry Detachment failure*** (CMD), characterized by the detachment of a pseudo-conic portion of masonry around the anchor whose geometry is determined by the typology of masonry fabric, i.e. size of the units and thickness of the mortar joints.
- ***Slip failure at bar/grout interface*** (SBG), characterized by slip failure of the anchor from the surrounding grout due to loss of cohesion between the two elements
- ***Slip failure at grout/masonry interface*** (SGM), characterized by slip failure of the grout sleeve from the masonry due to loss of cohesion;
- '***Mixed' failure*** (MIX), characterized by the joint detachment of a masonry cone or slippage of bricks adjacent to the outer portion of the anchor and the slippage of the grout sleeve from the masonry.

The notation proposed by Paganoni and D'Ayala (2014) is used in this work to designate the anchor's capacity. The use of the term *slip* refers to the point at which the anchors reach their maximum load capacity. The relative motion between the anchor and the masonry, according to the failure mode displayed at the end of each test, is indicated as *elongation* and includes the elastic deformation of the rebar.

The first comprehensive experimental program aimed at filling the lack of code regulations on the load capacity provided by grouted anchors in masonry substrates were carried out by Gigla (Gigla and Wenzel 2000; Gigla 2004; 2012) . He performed more than 500 pull-out tests over several years on injected anchors embedded in clay bricks (Gigla and Wenzel 2000) and clay

brick panels (Gigla 2004). The author evidenced the positive effect of compressive stresses in the masonry around the anchor, with an increment of pull-out load by almost 40% when the compressive stress increased from 0 to 0.4MPa. Based on the experimental results, analytical formulations were proposed to correlate the bond strength of grouted anchors to the compressive strength of the injected grout. Additional tests were carried out on different types of steel bars (stainless and ordinary steel ribbed bars, threaded rods) with diameter 16 mm and embedded length of 200 mm in monolithic sandstones (Gigla 2012). Threaded rods provided a more effective bond behaviour with small displacements compared to the ribbed bars, which attained an ultimate load only 10% lower. Ribbed stainless steel bars attained the best performance in terms of both ultimate load and ductility.

Arifovic and Neilsen (2006) carried out an extensive experimental program on ribbed steel bars in clay bricks samples to observe the failure modes of grouted anchors and correlate it to their maximum loads capacity. Pull-out tests had highlighted that different failure modes may occur, due to the interaction of different materials (i.e. masonry, injection grout, anchor) and the presence of two interfaces (i.e. masonry-grout and grout-anchor). For each failure mode a set of analytical formulations were obtained by applying the theory of plasticity for anchors in masonry in analogy of the anchorage theory developed for anchors embedded in concrete (Eligehausen, Popov, and Bertero 1982; CEB 1994) .

In Paganoni and D'Ayala (2014) the performance of a grouted anchoring system patented by Cintec International was tested on walls made of Victorian clay bricks. These anchors have a fabric sleeve wrapped around the rebar that expands as grout is injected into it thus moulding into the shape and space within the wall. In this way, the grout flow is controlled, ensuring an even distribution along the embedment length and the expansion within the wall's voids provides additional mechanical bonding. The bars were embedded in two panels by means of cement-based grout and subjected to different average vertical compressive stresses (0.08–0.09 MPa and 0.7 MPa). When the higher compressive stresses were present, the ultimate load was in average 20% higher and a bond failure at grout-masonry interface occurred. Conversely, in case of lower compressive stresses, a mixed failure was observed. In addition, cyclic tests were performed on samples of T-shaped walls to investigate the seismic performance of grouted anchors and the influence of interaction between walls. A reduced maximum pull-out load was observed in cyclic tests results compared to monotonic pull-out load. This reduction was likely due to the lower compressive strength of the mortar used in the T-shaped wall.

The authors identify three main points on the capacity curve of the grouted anchor: point A corresponds to load and displacement obtained at first damage, point B corresponds to the maximum measured pull-out force $F_{\max(M)}$ and *slip elongation* d_s, while point C refers to ultimate force F_u and *elongation* d_u when a loss of 20% load carrying capacity occurs, i.e. $F_u = F_{MAX(M)} * 0.8$ (Park 1989). Beyond point C, the load capacity eventually drops, and the anchor reaches its ultimate capacity, unless further mechanical locking, arising while the anchor slides out of the cavity, allows for a further increase in stiffness and strength.

The authors propose a dimensioning procedure based on the strength capacity of the tested connection and on the assumption that the maximum load capacity of the anchor assembly should be larger than the seismic demand expected for the Ultimate Limit State (ULS), namely for the acceleration calculated for a seismic action with a probability of exceedance of 10% in 50 years (EN 1998-1:2004 2004). The ductility, computed as the ratio between the displacement at point C and point B, presents a narrow range of values and the average ductility is 1.9 (CoV = 56%) and 2.4 (CoV = 24%) for monotonic and cyclic loading, respectively. The displacements present a scattered distribution, the average yielding and ultimate displacement are 1.9 mm (CoV = 46%) and 3.7 mm (CoV = 60%) for the monotonic pull-out tests, and 5.3 (CoV = 136%) and 10.9 (CoV = 30%) for cyclic loading. Therefore, full exploitation of the anchors' potential also in terms of displacement capacity is not explored and displacement considerations are discussed only to ensure the compliance with the requirements on interstory drift (EN 1998-1:2004 2004; CMIT 2009).

A set of tests on the same anchor technology tested by Paganoni and D'Ayala (2014) were performed by Moreira et al. (2014) by means of pull-out tests on grouted anchors embedded in masonry limestone walls reproducing a typical masonry typology for a historic masonry building, to explore the influence on the anchor's performance of masonry substrates having weak mechanical properties (significantly smaller compressive strength of masonry compared to Paganoni and D'Ayala (2014) as shown in Table 5-1). The maximum loads of the bars placed at top of the walls showed a capacity approximately 30%, lower than the bars placed at the bottom, thus, confirming the positive effect of higher compressive stresses in the masonry around the bars. In this case, the cyclic behaviour also shows a degradation of strength capacity and stiffness with increasing cycles and an accumulation of residual displacements. A mixed failure characterized by cone masonry detachment and bond failure occurred in all tests. The anchors at the top displayed a larger ductility capacity compared to the ones at the bottom,

confirming that the anchors can provide a ductile connection, favourable for seismic performance.

A third extensive experimental program of pull-out tests was carried out by Silveri et al. (2016) using the same anchoring technology tested by Paganoni and D'Ayala (2014). The bonded length ($l_e = 400$ and 900 mm), the compressive vertical loading in the masonry walls (0.05, 0.1, 0.2MPa), the compressive strength of the grout (49 and 59 MPa for cement-based grouts, 9 MPa for lime-based grout), the strength and layout of mortar joints, and the loading history (monotonic or cyclic) are the parameters investigated.

The results provided by Silveri et al. (2016) showed little to no influence of the compressive stress on the anchor strength for low values of stress (0.05 or 0.1 MPa), while an increase of about 30% of the ultimate load occurred in case of stress equal to 0.2 MPa, in line with Gigla's results. The CMD failure never occurred confirming that the cone failure is unlikely to happen for "long" anchor, namely anchors with $l_e > 40\sqrt{d_h}$ where d_h is the diameter of the borehole. Conversely a SGM failure mode was frequently observed, in few cases jointly with the slippage of 2–3 adjacent bricks around the outer portion of the anchor (MIX mode). It was observed that the cyclic load history reduced the anchor strength of 20% in comparison with the same specimens tested under monotonic loads.

In Ceroni et al. (2016) the performance of injected anchors was studied, performing pull-out test on different types of masonry, changing the masonry units (clay bricks and vertically perforated units) and the type of mortar. Two series of in situ pull-out tests were carried out on injected anchors embedded in yellow tuff masonry walls. Anchors were embedded for 300 mm by means of cement-based and "pozzolana"-based grout, the latter having a significant lower compressive strength. The experimental results evidenced that a MIX failure was obtained for the cement-based grout, while the pozzolana grout led to lower pull-out loads and SBG failure.

Regarding the rebar materials, different solutions have been explored besides steel bars, such as, Glass Fibre Reinforced Plastic (GFRP) (Ceroni and Di Ludovico 2020), Carbon Fibre Reinforced Plastic bars (CFRP) (Ceroni and Di Ludovico 2020; G. Maddaloni et al. 2016).

In Ceroni and Di Ludovico (2020), the performance of innovative anchors made of GFRP and CFRP were compared to that of traditional steel ribbed bars. A special surface treatment was also made by wrapping the FRP bars with stainless steel fabrics (SRP) embedded in a putty to increase the bond performance along the injected grout/bar interface. The anchors were embedded in masonry prisms made of yellow tuff blocks. It was found that these anchors

display a similar or slightly better performance in terms of pull-out capacity compared to traditional steel anchors, when surface treatments are implemented. The ductility capacity is also similar, with the exception of the GFRP which display a long, stable ductile behaviour but a smaller strength capacity.

Following up on the work reported in Paganoni and D'Ayala (2014) in Maddaloni et al. (2016) a T-shaped masonry wall was tested to determine the improvement in the connection between orthogonal walls by means of a hollow pultruded carbon tubes (CFRP). The authors concluded that the system can significantly increase the horizontal force applied to the wall compared to an unrestrained wall, preventing the formation of cracks. Moreover, the tests highlight that effective strengthening solutions can increase the ultimate displacement and thus energy dissipation capacity of the wall.

The review of existing literature on injected anchors herein presented shows the influence of the embedment length on the performance of anchors, in terms of load capacity and type of failure mode. Long anchors mainly fail for a SGM mode and present larger maximum pull-out loads as the anchor grips on a larger portion of masonry. Accordingly, it is found that surface treatment of the anchors and the properties of injection grout positively influence the performance as they increase the mechanical bonding between the components of the anchor and the surrounding material. In particular, the comparison of the results obtained using Cintec's anchors (Paganoni and D'Ayala 2014; Moreira et al. 2014; Silveri et al. 2016) with the results reported by Gigla and Wenzel (2000) and Arifovic and Neilsen (2006) have highlighted that the fabric sleeve contributes to improving the displacement capacity of the grouted anchor. The mechanical locking between the bulges of the sleeve and the masonry cavity increases the range of displacement at sustained peak strength.

On the other hand a degradation in load capacity and a larger variability in elongation capacity under cyclic behaviour has been observed, suggesting that at present the extra strength obtained through the grouting cannot be fully exploited in a reliable way.

5.2.2 Formulae to predict pull-out load of grouted anchors in literature

Depending on the failure mode activated by the pull-out test, several formulations for predicting the maximum pull-out force of injected anchors in masonry elements are available in literature (Gigla and Wenzel 2000; Arifovic and Neilsen 2006; CEB 1994).

For the Cone Masonry Detachment (CMD), the analytical formulation inferred by Arifovic and Neilsen (2006) through experimentally based regression is:

$$F_{max} = 0.96\, h_{cone}^2 \sqrt{f_{c,m}} \tag{5-1}$$

where, $f_{c,m}$ is the compressive strength of the masonry and h_{cone} is the depth of the cone portion of masonry that is contributing to the pull-out force. The CMD is experimentally observed for "short" anchors ($l_e < 40\sqrt{d_h}$), for which the value of h_{cone} can be assumed equal to the embedment length l_e.

For the Bond Failure at Bar/Grout Interface (SBG), the empirical formulation provided by Gigla and Wenzel (2000) is :

$$F_{max} = \tau_g\, \pi\, d_b\, l_e \tag{5-2}$$

where:

$$\tau_g = \Phi_j \left(\frac{f_{c,g}^2}{500}\right) \tag{5-3}$$

The bond strength, τ_g, mainly depends on the compressive strength of the grout, $f_{c,g}$, and Φ_j is a reducing factor (set equal to 0.5 or 0.6 for bed or head joints) (Gigla and Wenzel 2000). There are two assumed distributions of shear stress for grouted anchors in concrete which are usually applied also to anchors embedded in masonry. One considers a constant distribution of stress along the embedment length, assumed for instance in Eq. (5-3) and valid for $l_e < 40\sqrt{d_h}$, and a second that assumes a decaying distribution of the shear stresses with the embedded length, which is recommended for $l_e > 40\sqrt{d_h}$ in (Doerr and Klingner 1989). According to the latter stress distribution, the maximum pull-out force is computed as:

$$F_{max} = \pi\, \tau_g d_b \left(\frac{\sqrt{d_b}}{\lambda'} \tanh\left(\frac{\lambda'\, l_e}{\sqrt{d_b}}\right)\right) \tag{5-4}$$

where d_b is the diameter of the bar and λ' is an elastic constant defined as:

$$\lambda' = \sqrt{\frac{4G_g}{tE_s}} \tag{5-5}$$

Where G_g is the shear modulus of the grout, t is the wall's thickness and E_s is the elastic modulus of the bar. For short anchors, Eq. (5-2) and (5-4) yield the same values of pull-out force. For long anchors, Eq. (5-4) should be considered because the linear correlation between embedment length and pull-out force is not supported by experimental evidence for $l_e > 40\sqrt{d_h}$.

For Bond Failure at Grout-Masonry Interface (SGM), Eq. (5-6) is proposed by Arifovic and Neilsen (2006):

$$F_{max} = C_1 \, d_b \, l_e \sqrt{f_{c,m}} \tag{5-6}$$

This formula can be interpreted as a variation of Eq.(5-2) where the bond strength at the grout-masonry interface is expressed as function of the square root of the masonry compressive strength, as frequently assumed for the bond strength of steel bar-concrete interface (Eligehausen, Popov, and Bertero 1982) and C_1 is empirically determined by numerical regression. It should be noted that Eq. (5-6) was derived by Arifovic and Neilsen (2006) for anchors with small embedment length $l_e < 40\sqrt{d_h}$ for which the hypothesis of uniform stress distribution is valid. Similar to the SBG failure, for anchors of length $l_e > 40\sqrt{d_h}$ the maximum pull-out force can be computed as:

$$F_{max} = C_2 \, \pi \sqrt{f_{c,m}} \, d_b \left(\frac{\sqrt{d_b}}{\lambda'} \tanh\left(\frac{\lambda' \, l_e}{\sqrt{d_b}} \right) \right) \tag{5-7}$$

In Eq.(5-7), proposed by Doerr and Klingner (1989), $C_2 = 1$ is obtained based on experimental pull-out tests performed on adhesive anchors embedded in concrete specimens. Both Eq.(5-6) and (5-7) are derived for anchors with borehole's diameter d_h almost identical to the diameter of the bar (see values in Table 5-1 for Arifovic and Neilsen (2006)), which explains why the d_b is considered despite the fact that the formula addresses the failure at the grout-masonry interface. Nonetheless, for anchor typologies with larger ratio between d_h and d_b such as the Cintec's anchorage, the borehole's diameter should be used to compute the maximum force and updated values of C_1 and C_2 needs defining (see section 5.2.3).

Finally, for the 'Mixed' failure mode (MIX), the following formulation is proposed (Cook 1993; CEB 1994):

$$F_{max} = C_3 \, \pi \sqrt{f_{c,m}} \, d_h \left(\frac{\sqrt{d_h}}{\lambda'} \tanh\left(\frac{\lambda' \, (l_e - h_{cone})}{C_3 \sqrt{d_h}} \right) \right) \tag{5-8}$$

This failure mode is frequently observed, and the pull-out force should be calculated as the sum of the two contributions previously introduced for cone and grout/masonry failure. Nonetheless as observed both for concrete (Doerr and Klingner 1989) and masonry (Ceroni and Di Ludovico 2020) substrates, the contribution offered by the cone portion is small compared to the interface bond contribution and therefore it is neglected in Eq.(5-8). Consequently, the embedment length is reduced by h_{cone}, which can be assumed as the minimum permissible effective embedment length, i.e. the greater between 51mm and 4 times the diameter of the anchor

according to Cook (1993) and the Building Code Requirements for Masonry Structures (MSJC 2013). The values of $C_3 = 34.7$ was obtained by numerical regression. Alternatively, Eq.(5-9) proposed by Arifovic and Neilsen (2006) can be adopted:

$$F_{max} = [C_4 \sqrt{f_{c,m}}\ (l_e - h_{cone})d_b + C_5 \sqrt{f_i}(l_u + d_b)d_b] \sqrt{\frac{d_b}{l_e}} \qquad (5\text{-}9)$$

Eq.(5-9) is made of two terms, where the first one is similar to the one proposed by the same authors for SGM failure (see Eq. (5-6)) with the embedment length reduced by h_{cone}, and, thus, is related to the bond stress contribution. The second term depends on the compressive strength of the mortar joint/ brick interface, f_i, and on the length of the masonry unit, l_u. Lacking specific indication, f_i can be assumed equal to the minimum value between the compressive strength of the mortar of the joints and of the masonry unit. In (Arifovic and Neilsen 2006) the values of $C_4$and C_5 are 3.93 and 37.44 respectively. As discussed for Eq.(5-6) and (5-7) the pull-out force provided by Eq. (5-9) should be computed considering the borehole's diameter if d_h is significantly larger than d_b.

The numerical factors in Eq. (5-6), (5-7), (5-8) and (5-9) are introduced to improve the agreement of the analytical formulae with the experimental values of pull-out force for each failure mode. Therefore, the validity of these empirical formulations is highly dependent on the experimental conditions of the performed tests. Many authors (Paganoni and D'Ayala 2014; Araújo, Oliveira, and Lourenço 2014; Moreira et al. 2014; Ceroni, Cuzzilla, and Pecce 2016) found that these formulations can lead to large overestimates or to too conservative predictions of maximum pull-out load, if the grouted anchors and the masonry wall present significantly different geometry and mechanical properties.

In light of these considerations and of the results of the experimental programmes discussed in section 5.2.1, alternative values for the numerical factors in Eq. (5-6), (5-7), (5-8), and (5-9) are proposed by the author to obtain a better correspondence between the experimental values and the analytical predictions.

5.2.3 Correlations of experimental and analytical formulations

A compendium of data obtained by experimental tests and a comparison of the strength capacity of different anchorage system is presented in Ceroni and Di Ludovico (2020). In the present study that database is extended by considering the displacement and ductility capacity of these tests. These are presented in Table 5-1. The slip elongation d_s, ultimate elongation d_u are

defined as in section 2.2. using the approach introduced by Paganoni and D'Ayala (2014). The ductility factor is computed as the ratio between d_u and d_y. Pull-out tests where the embedment length is shorter than $40\sqrt{d_h}$ are not included in this analysis, as short anchors are not a feasible option to connect orthogonal walls and are therefore outside the scope of this work.

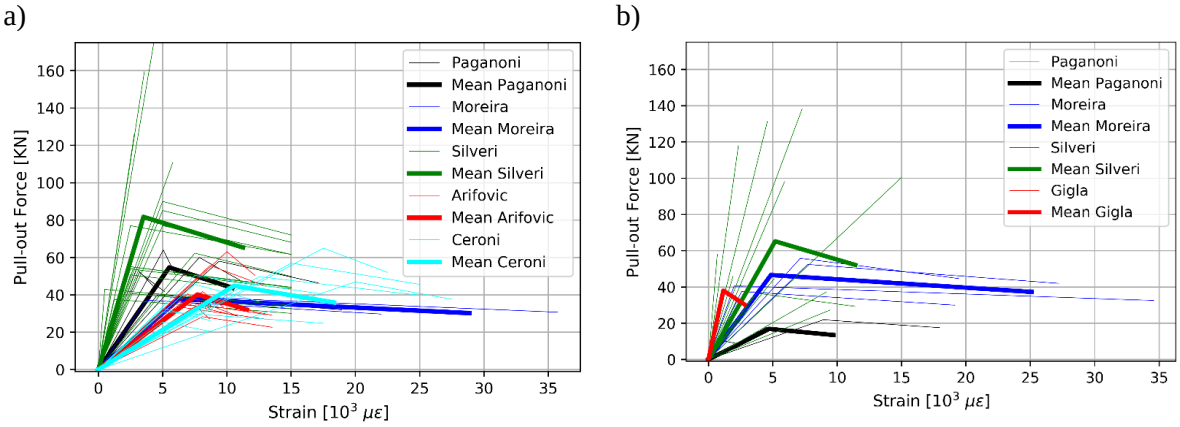

Figure 5-2 Capacity curves of grouted anchor under a) monotonic loading and b) cyclic loading

Figure 5-2 shows the results of the anchors tested in each experimental programme for monotonic and cyclic loading. The relative displacement of the anchor with respect to the wall is normalized to the value of embedment length l_e to obtain the longitudinal slip strain for the maximum and ultimate load. Even though only long anchors are reported, and the analysis is restricted to grouted anchors made of steel, the results' comparison between testing programmes is not straightforward because each test has been performed under different conditions. Nonetheless, a few observations are possible.

In terms of strain, for cyclic loading, a fairly good agreement is found between the data reported by Paganoni and D'Ayala (2014), Moreira et al. (2014) and Silveri et al. (2016). The average initial bond-slip strain and ultimate bond-slip strain are 0.005 (CoV = 15%) and 0.01 (CoV = 47%), which correspond to an average ductility factor of 2. In Moreira et al. (2014), larger values of ultimate longitudinal strain are obtained, possibly because two anchors, placed close to each other, were pulled simultaneously, causing a mixed failure mode that combines the sliding between the grout/masonry interface and the detachment of a masonry cone. The larger values of pull-out load obtained by Silveri et al. (2016) are expected due to longer embedment length l_e and large vertical load σ_c. Gigla and Wenzel (2000), Arifovic and Neilsen (2006)and Ceroni et al. (2016 and 2020) who investigated traditional injected anchors obtained a smaller value of average ductility factor, namely μ = 1.7 (CoV = 32%).

Table 5-1. Experimental database of grouted anchors embedded in masonry. [Part 1]

Authors	Test type	l_e [mm]	d_h [mm]	d_b [mm]	fc,g [MPa]	fc,m [MPa]	Anchor no.	σ_c [MPa]	$F_{max\ (M)}$ [KN]	d_y [mm]	d_u [mm]	μ [-]	Failure type
Paganoni & D'Ayala, 2014	MONOTONIC	350	80	16	50	6.7	a	0.7	60	2.8	3.8	1.4	SGM
							b		64	1.8	2.1	1.2	SGM
							c		54	1.0	1.6	1.5	SGM
							d	0.08	58	3.3	6.0	1.8	SGM
							e	0.09	40	1.6	6.6	4.1	SGM
							f		52	1.1	1.8	1.6	SGM
	CYCLIC	220				3.1	1T	0.08	10.9	0.8	2.5	3.2	MIX
							2T		17.8	5.1	10.0	2.0	MIX
							3T		21.9	10.0	20.1	2.0	MIX
Gigla,2004	CYCLIC	172	30	10	18.2	20	a	0.4	51	0.5	-	-	SBG
							b	0.3	42.5	0.5	-	-	SBG
							c	0	38	0.2	0.5	2.4	SBG
Moreira et al., 2014	CYCLIC	350	50	20	51.5	1.7	a_t	0.2	55.85	2.5	6.8	2.7	CMD
				16			b_t		53.6	-	-	-	CMD
				16			c_t		52.45	2.7	9.5	3.5	CMD
				20			a_b		40.6	0.7	12.1	17.3	MIX
				16			b_b		37.5	0.9	6.7	7.4	MIX
	MONOTONIC	350		20			a_b	0.2	38.4	3.1	16.8	5.4	MIX
				16			b_b		37.15	1.3	7.7	5.9	MIX
Arifovic &Nielsen, 2006	MONOTONIC	185	14	12	75	21.1	A.2.1	n.a.d	35.8	1.2	2.0	1.7	CMD
							A.2.2		41.7	1.5	1.8	1.2	CMD
							A.2.3		34	1.4	1.6	1.1	MIX
		230	18	16			A.2.4		63.1	2.3	2.8	1.2	SGM
							A.2.5		36.8	1.4	3.0	2.1	MIX
							A.2.6		33.7	1.4	3.0	2.1	MIX
		185	14	12			A.2.19		28.3	1.5	2.5	1.7	MIX
							A.2.20		36.3	1.6	2.5	1.6	SGM
							A.2.21		35.9	1.5	2.0	1.3	MIX
		230	18	16			A.2.22		40.5	1.6	2.0	1.3	MIX
							A.2.23		73.4	2.3	3.0	1.3	MIX
							A.2.24		55.7	2.0	3.0	1.5	MIX

Table 5-1 Experimental database of grouted anchors embedded in masonry. [Part 2]

Authors	Test type	l_e [mm]	d_h [mm]	d_b [mm]	fc,g [MPa]	fc,m [MPa]	Anchor no.	σ_c [MPa]	$F_{max\ (M)}$ [KN]	d_y [mm]	d_u [mm]	μ [-]	Failure type
Silveri et al., 2016	MONOTONIC	400	20	60	50	18	Wall 1	0.05	40.78	1.0	2.3	2.3	SGM
									77.04	2.0	3.6	1.8	SGM
									53.88	1.0	1.9	1.9	SGM
			60	20	50		Wall 2	0.1	37.58	0.5	2.9	5.9	SGM
									85.15	2.0	6.4	3.2	SGM
									42.93	0.2	3.0	15.0	SGM
							Wall 2	0.1	55.08	1.0	2.1	2.1	SGM
									62.3	3.0	5.9	2.0	SGM
									50.69	1.0	2.2	2.2	SGM
							Wall 3	0.2	54.8	1.1	2.4	2.1	SBG
									90.01	2.0	3.8	1.9	SBG
									77	1.0	2.1	2.1	SBG
	CYCLIC						Wall 6	0.06	35.01	1.4	-	-	SGM
									45.75	1.5	-	-	SGM
									37.27	3.7	-	-	SGM
							Wall 7	0.06	32.5	0.9	-	-	SGM
									44.55	2.0	-	-	SGM
									36.6	1.5	4.6	3.0	SGM
							Wall 8 (lime mortar)	0.06	27.22	3.8	-	-	MIX
									45.9	0.8	-	-	SGM
									29.3	1.3	-	-	SGM
	MONOTONIC	900					Wall 9	0.06	126.27	2.5	-	-	MIX
							Wall 10		159.39	3.2	-	-	MIX
							Wall 11		183.7	4.1	-	-	MIX
							Wall 12		110.82	5.2	-	-	MIX
	CYCLIC						Wall 13	0.06	118.2	2.1	-	-	MIX
							Wall 14		138.1	6.5	-	-	MIX
							Wall 15		98.13	5.3	-	-	MIX
							Wall 16		131.29	4.1	-	-	MIX
							Wall 17		57.96	0.6	-	-	MIX
							Wall 18		100.29	13.5	-	-	MIX
Ceroni et al. 2016	MONOTONIC	300	50	20	43.4	2	SC_1	n.a.d	57	6.0	10	1.7	MIX
							SC_2		65	7.0	9	1.3	MIX
							SC_3		49.7	5.0	10	2.0	MIX
					12.6		SP_1		50.4	3.0	7	2.3	SBG
							SP_2		47	8.0	11	1.4	SBG
							SP_3		45.6	3.0	5	1.7	SBG
Ceroni et al. 2020	MONOTONIC	250	25	10	7.65	6.05	MS10_1	0.4	32.7	2.0	3.5	1.8	MIX
							MS10_2	0.4	25.5	2.0	3.5	1.8	MIX
							MS10_3	0.4	31	2.0	7	3.5	MIX

In Figure 5-3a, the maximum pull-out loads found experimentally are compared to the analytical values predicted by Eq. 5.6 to 5.9 depending on the observed failure mode. The accuracy of the analytical formulas to predict the experimental results is measured considering the mean and coefficient of variation, CoV, for each failure mode. The mean value of each dataset is indicated by a larger marker to better visualize whether a formulation underestimates

(the mean value is above the horizontal dotted line) or overestimates the anchor's capacity (the mean value is below the horizontal dotted line).

Of 71 pull-out tests analysed, 33 anchors failed for bond slip of the grouted cylinder (SGM failure), 30 for the combined slip at the grout/masonry interface and cone detachment (MIX failure), 6 for bond-slip at the bar/grout failure (SBG failure), 5 for cone failure (CMD failure). For the SBG failure, both Eqs. (5.2) and (5.4) underestimate the anchor's capacity by one order of magnitude. Nonetheless, the number of pull-out tests that displayed this failure mode is considered too small to derive conclusions of statistical relevance and the SBG failure is not included in Figure 5-3.

For the SGM and MIX failure, alternative values of the numerical constants are presented in Table 5-2 to compensate for using the borehole's diameter in place of the bar diameter in Eq. (5-6), (5-7), and (5-9) and to obtain a better correlation between analytical and experimental results in Eq. (5-7) and (5-8), as they were obtained for concrete specimens. The alternative set of constants is obtained minimizing the difference between recorded values and predicted maximum capacity and reducing the coefficient of variation for each failure mode. The experimental-to-analytical ratios computed according to the alternative formulations are shown in Figure 5-3b, next to those obtained using the numerical constants defined by Arifovic and Neilsen (2006) and Cook (1993).

Table 5-2. Values of numerical constants for analytical formulation to predict the maximum pull-out force

	C_1	C_2	C_3	C_4	C_5
Arifovic [9]	3.79	-	-	3.93	37.44
Cook [39]	-	1	34.7	-	-
This study	0.5	0.28	3	2	30

For the SGM failure, the analytical formulations provide opposite results: Figure 5-3a shows that Eq. (5-7) overestimates the pull-out force, while Eq. (5-8) gives a conservative prediction and in both cases the variance is above 50%. On the other hand, Figure 5-3b shows better agreement between experimental and analytical values and values of variance below 50%, proving that d_h, and thus alternative constants, should be used in the formulations for SGM. Moreover, Figure 5-3b highlights what suggested by Giresini et al. (2020): a uniform model can be used to predict the anchor's pull-out load in case of weak substrates even for values of $l_e > 40\sqrt{d_h}$.

For the MIX failure, the elastic model expressed by Eq. (5-8) gives the best results both in terms of average ratio and scatter with a variance below 30%. Similar to the SGM, Eq. (5-9) benefits

from using d_h in place of d_b as better agreement is achieved between experimental and analytical results, even if the scatter remains largely above 50%.

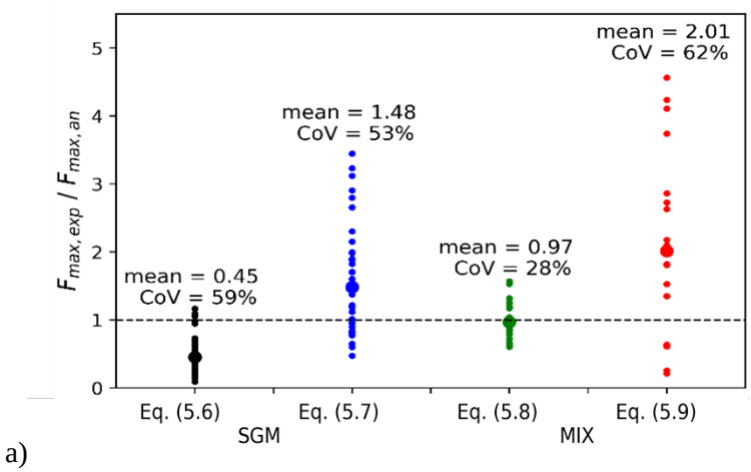

a)

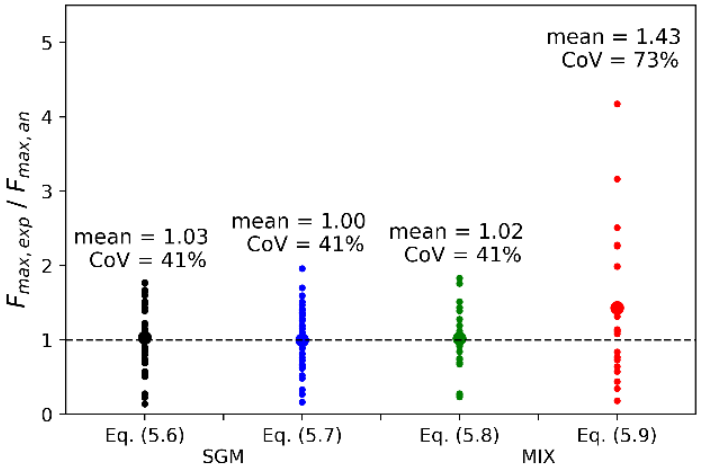

b)

Figure 5-3 Comparison between experimental and analytical values of pull-out force depending on the observed failure mode. The analytical values are computed according to the numerical constants defined a) by Arifovic and Neilsen (2006) and Cook (1993), b) by the authors of this thesis

In conclusion, the review of pull-out tests performed on grouted anchors with long embedment length highlights the expected failure modes to occur when the maximum pull-out force is attained. The experimental tests show that either the bond failure at the grout/masonry interface (SGM), or the mixed failure (MIX) with the detachment of a masonry cone and the bond slip of the grout sleeve, are the more common failure modes. The other two failure modes are rarely observed: the simple cone failure (CMD) is relevant to anchors with short embedment length, and thus not applicable to anchors connecting orthogonal walls. The failure at grout/bar interface (SGB) is observed in few cases as the bonding strength developed between the rebar and the grout is usually larger than the one developed between the grout and the masonry. Moreover, some anchoring technologies, such as the Cintec anchors have a locking system at

the end of the sleeve that prevent any relative slip between the grout and bar even once the bond strength between the two might be overcome.

Comparing the analytical formulations with the experimental values of pull-out force allows for a critical assessment of the models describing the stress distribution along the anchors. It is found that assuming a decaying distribution of shear stress gives the best results for the MIX mode, while both the uniform and the decaying stress distribution well describe the ultimate load for anchors failing according to the SGM mode. In the last analysis, the smaller value of force provided by Eq. (5-6) to (5-9), reduced by appropriate design safety factors, can be adopted as design load for the anchor. The definition of such design factors is outside the scope of this work and should reflect the level of knowledge the user can achieve, for instance, of the mechanical properties of the masonry substrate by means of destructive/non-destructive tests.

For design applications in real cases, the dimensioning of the strengthening system should be performed favouring the yielding of the rebar over the shear debonding of the anchor as the former is a ductile failure mode. Nonetheless, the yielding of the bar is rarely observed in experimental and in-situ pull-out tests, possibly because the composite action of high-strength grout and bar provides a larger tensile capacity compared to the bar on its own. Therefore, the design of "long" grouted anchors as anti-seismic system should be performed ensuring that the strength and elongation capacity attained either for the SGM or MIX failure mode are the governing parameter of the design. This consideration further highlights the need to introduce a dissipative component, such as the one proposed in this work, able to improve the behaviour of grouted anchors and avoid their brittle failure.

5.3 Pull-out tests on GAS and D-GAS

In the previous section the analysis of the pull-out tests available in literature allowed to collect a database of experimental results and propose alternative numerical constants to determine the expected load capacity of grouted metallic anchors.

In this section the results of pull-out tests performed on a grouted anchoring system with and without the friction-based device optimized in chapter 4 are presented. The results are commented with reference to the failure modes, the notation, and the analytical formulations provided in Sections 5.2.

This task comprises several activities and goals which are schematically illustrated in the flowchart of Figure 5-4 and will be commented in detail in the next paragraphs. The flowchart also includes the testing activity of the D-GAS fully grouted in a masonry connection presented in Section 5.5. This is done to avoid repetitions and because the outcome and controlling parameters identified in the pull-out tests directly feed into the second testing activity.

The first goal is to compare the performance of the dissipative grouted anchoring system (D-GAS) to its strength-only counterpart (GAS). As the tests are carried out on the same masonry panel under identical testing conditions, differences in performance between the two systems can be ascribed to the presence of the device only.

The tests on the D-GAS complement the results discussed in Chapter 4: the devices are tuned to provide the desired design slippage force according to Eq. 4.12 and the variation between design and measured values is checked against the tolerances provided by the EN 15129 (2006) which guided the refinement process commented in Chapter 4.

The results obtained for the GAS are used to enrich the database of Table 5-1 and validate the alternative analytical formulas, comparing the expected values to the ones predicted by the analytical formulas of section 5.2.2.

After each pull-out test, the damage level on the masonry panel is assessed by visual inspection. For the GAS, this activity allows for the identification of the failure modes that the anchor experienced when the maximum load was achieved. This is a crucial step, as the empirical formulations presented in Section 5.2.2 are grouped depending on the observed failure mode. For the D-GAS, the visual inspection would determine to what extent the activation of the device reduces the shear stress at the grout-masonry interface, thus prevent crack formation in the panel.

The experimental set-ups is reproduced in an Abaqus models to identify the modelling techniques that best simulate the experimental evidence. The main goal of this numerical activity is to obtain a detailed stress and strain fields of the modelled device and parent material and to investigate the areas where high stress concentrations are likely to occur. Moreover, this tool is used to predict the loading failure of the T-connection for the testing activity presented in section 5.5.

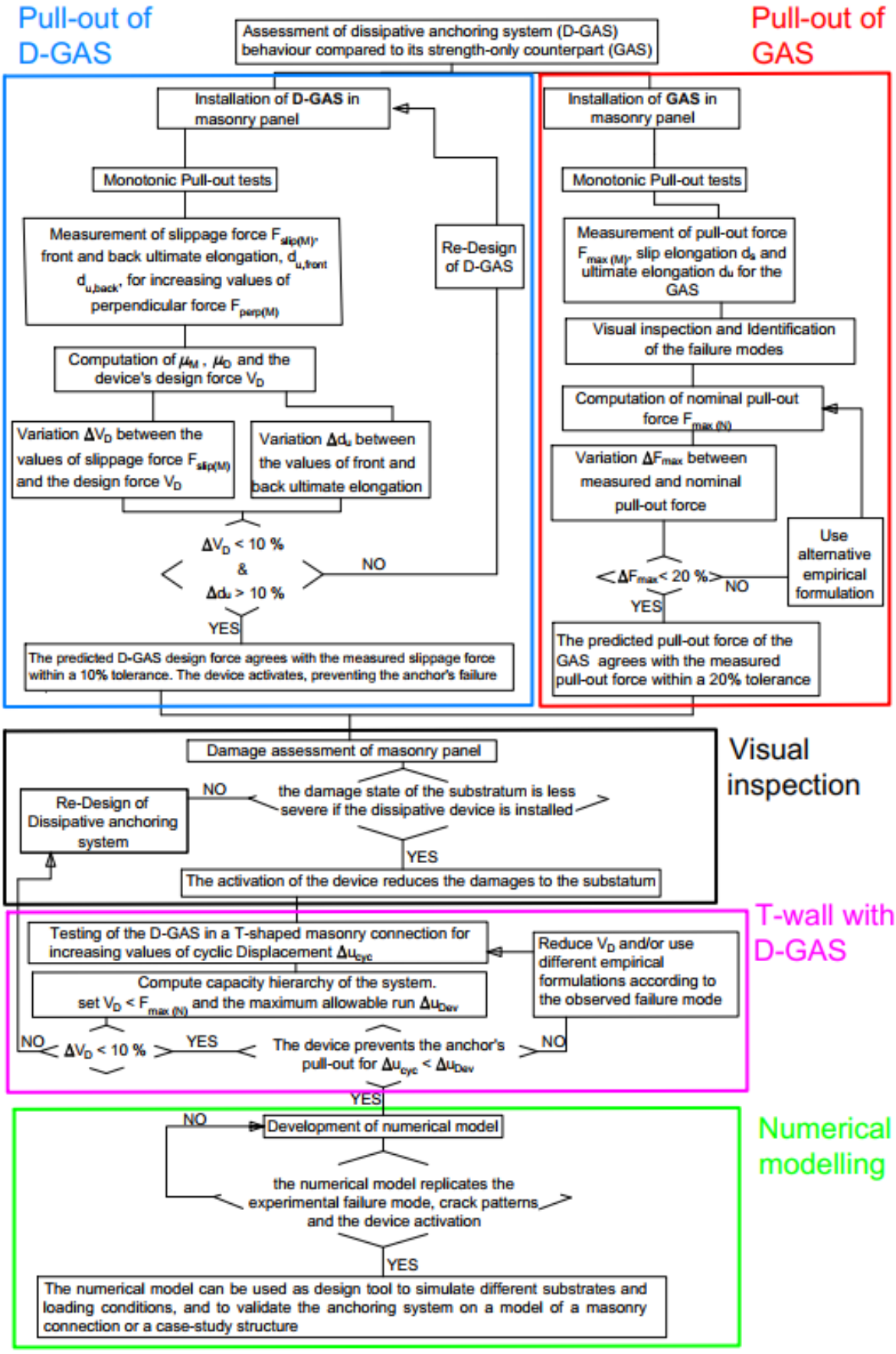

Figure 5-4 Methodology for performance comparison of D-GAS and GAS by pull-out test

5.3.1 Test set-up and instrumentation

The performance of the D-GAS connected to a steel bar grouted to a masonry panel is obtained by pull-out test, introducing the dissipative device between the free end of the anchor and the pulling apparatus. The obtained set-up, shown in Figure 5-5 simulates the D-GAS implementation in a real case masonry connection, where the device is installed at the interface between two orthogonal walls to control their relative motion under seismic loading.

Figure 5-5 Laboratory set up for pull-out test of D-GAS

The masonry panel used for the testing activity is built using clay bricks and natural hydraulic lime mortar, NHL 5, and its dimensions are shown in Figure 5-6a. Masonry units are fired bricks, sized 220 x 110 x 70 mm. The testing procedure is carried out according to the prescriptions of EN 846-2:2000 (2000) for testing of ancillary components of masonry. As stated before, given the lack of a technical literature specifically dealing with anchors in masonry the EN 846-2:2000 (2000) is taken as reference and integrated, when necessary, with the prescriptions on pull-out testing of anchors in concrete substrata (BS EN 1881:2006, 2006). The anchors are placed at a distance from each other sufficient to avoid interaction effects between adjacent anchors or between anchor and wall edges. The positioning of the anchors in respect to bed joints, head joints and masonry units is intentionally left random, so that results can be representative of the average behaviour of anchors in a mixed substratum. Nonetheless, the EN 846-2 (2000) specifies that at least one masonry joint be included in the area of coring, so as to avoid performing a pull-out from a single brick.

a) b)

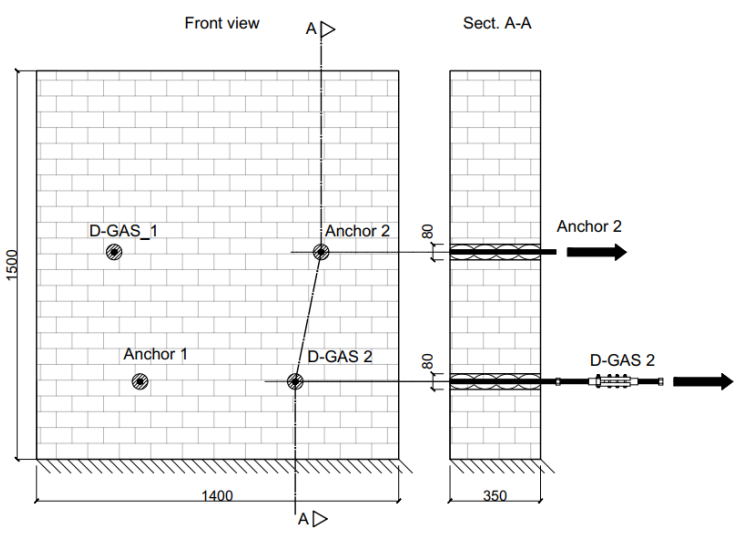

Figure 5-6 Test set up and dimensions of the wall panel.

With reference to the scheme shown in Figure 5-6 four holes are drilled throughout the thickness of the wall and four steel bars provided by Cintec International are installed. The characteristics of the tested anchors and of the cementitious grout are reported in Table 5-3.

Table 5-3 Summary of characteristics of grouted anchors

M16 bars, AISI 304 stainless steel (UNI 14301) class 70		
Nominal diameter	16 mm	
Cross sectional area	201 mm^2	
Yield stress	450 MPa	From producers
Ultimate tensile stress	700 MPa	
Anchor rod length	400 mm	
Embedded length	350 mm	equal to wall thickness
Drilling hole diamenter	80 mm	
Cementitious grout		
Grout compressive strength	50 MPa	

With reference to Figure 5-7a, one bar of each line is connected to the dissipative device, screwing the free end of the bar [1] in the fixed threaded connection of the friction-based dissipative device [2]. the cylindrical slider of the device [3] is then connected to the hydraulic pump [4]. The friction-based dissipating device featuring a stainless steel cylindrical internal slider (SteCyl prototype) is used in this testing activity. A detailed description of the device's geometry has been provided in Chapter 4.

Conversely, when the capacity of the two grouted anchors is assessed, the free end of the GAS is directly connected to the hydraulic pump, as shown in Figure 5-7b.

a)

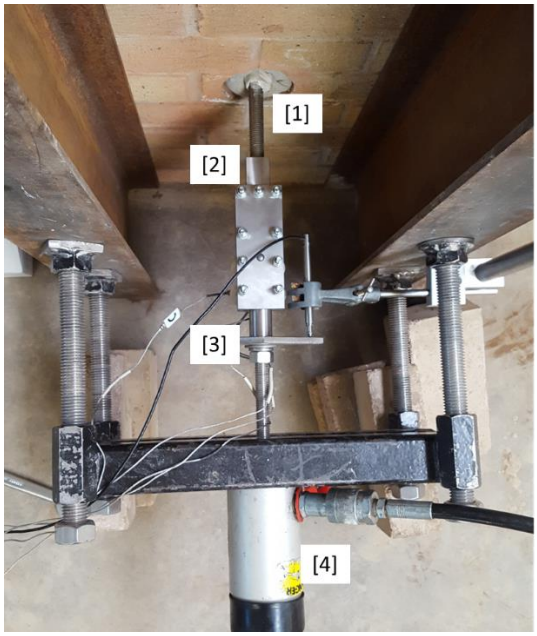

b)

Figure 5-7 Description of elements composing the testing set up for a) the D-GAS and b) the GAS.

The testing instrumentation comprises four donut load cells shown in Figure 5-8a, which are installed below the head of four bolts to record the pretension applied by a torque wrench and any loss in bolt pretension throughout the testing activity. In addition, two LVDTs were installed: one to measure the relative displacement of the slider with respect to the fixed part (front LVDT, shown in Figure 5-7a), the other on the back of the wall to detect the slip of the grouted sleeve (back LVDT, shown in Figure 5-8b)

Figure 5-8 Instrumentation: a) donut load cells, b) spring LVDT

Tests are performed in load control mode, with pull-out load being applied by a manual hydraulic pump whose load range is 0-140 KN in steps of 1 KN. The load is increased,

maintained constant for 15 seconds and then increased again. This pause between increments ensures that relaxation of the material at the interface and slip, if any, take place before the following load increment.

The test is considered complete when either the parent material or the anchors present damage, this being clearly detectable by visual inspection or by inability of further increasing the load, or when the target displacement of 10 mm is reached. Limitation of damage to finishes, and hence to the substratum in general, is indeed a main requirement of strengthening systems for heritage structures and should therefore be accounted for during tests. The limit displacement criterion is set considering that a 10 mm displacement is comparable with the maximum allowable drift for damage limitation, assuming d_r =0 .003, taken from DPCM (2011). This limit is also in line with the expected drift stated in FEMA 356 (2000) for unreinforced masonry buildings at the limit state of Immediate Occupancy.

The friction device is tested for different values of bolt preloading: if the device activates successfully and no damage is detected at the end of the test in the masonry, the whole procedure is repeated for a higher level of perpendicular force of the friction devices ($F_{\text{perp (M)}}$). The new value of $F_{\text{perp (M)}}$ determines a higher value of slip load of the friction plates ($F_{\text{slip(M)}}$) and hence different response of the anchor assembly.

The bond-slip capacity of the grouted assembly to the masonry depends on the strength of the masonry, which depends on the properties of the materials and on the vertical compression acting upon at the anchor location. The material characterization carried out before performing the tests is illustrated in the next section and the shear and compression strength of the masonry is determined.

The pull-out tests are performed under a low compressive strength coming from the self-weight of the courses of bricks lying on top of the anchor. This represents the most unfavourable scenario in terms of shear resistance of the masonry panel. Hence, it is taken as reference to validate the dissipative anchoring devices.

5.3.2 Material characterization

Upon commencing the pull-out tests, the mechanical characterization of the materials is carried out to determine the properties of the masonry units, the mortar and masonry according to relevant European standards, the EN 772 (2000) the EN 1015 (1999) and the 1052 (1999) respectively. Investigating the mechanical properties of the masonry allows a responsible use

of the analytical formulas to predict the maximum load capacity of the anchors, as the compressive strength of the masonry is required in the majority of the equations presented in section 5.2.2. Moreover, the material properties will be implemented in the numerical model to ensure correlation between the experimental and numerical results.

The mechanical properties of the lime mortar are obtained on 12 prismatic samples of dimensions 120X40X40 cast during the wall construction. The flexural strength of the mortar $f_{j,flex}$ is obtained averaging the values of flexural strength $f_{j,flex,i}$ obtained by three-point bending test: the prisms are placed with one longitudinal face in contact with the supporting rollers and a vertical load F is applied to the test specimens at a rate of 1.25mm/min. The flexural strength $f_{j,flex}$ is calculated from the following equation:

$$f_{j,flex,i} = \frac{1.5F_i l}{bd^2} \tag{5-10}$$

Where b and d are the internal dimensions of the prism mould, l is the distance between the supporting rollers and F_i is the maximum load applied during the ith test. The compressive strength of the mortar $f_{m,c}$ is determined on the broken halves of the prism by using a compression jig of the testing machine. The compressive strength of the brick units $f_{b,c}$ is determined by compression test on 6 bricks and it is found equal to 14.0 MPa (CoV 6%). The compressive strength of the masonry is obtained by Eq. (2.1) for K equal to 0.5 as prescribed by EN 6 1996-1-1 (2005) :

$$f_m = K f_b^{0.625} f_j^{0.25} = 3.3\ MPa \tag{5-11}$$

The shear strength of the masonry is obtained by triplet test, as defined by EN 1052-3 for 3 specimens with size 330x210x110 mm. The test, shown in Figure 5-9b, is performed with a lateral pre-compression σ_d of 0.1MPa and the average shear strength - obtained averaging the results on three masonry samples - is found equal to 0.5 MPa (CoV 12%).

The slip-shear stress curves obtained for three masonry specimens are plotted in Figure 5-10, which shows that the shear stress reaches a maximum for a shear strain between 0.005 and 0.01. It then reduces to 80% of the maximum shear without experiencing any further change in strength up to a strain of 0.06.

a)  b) 

Figure 5-9 Material characterization a) three-point flexural test, b) shear test

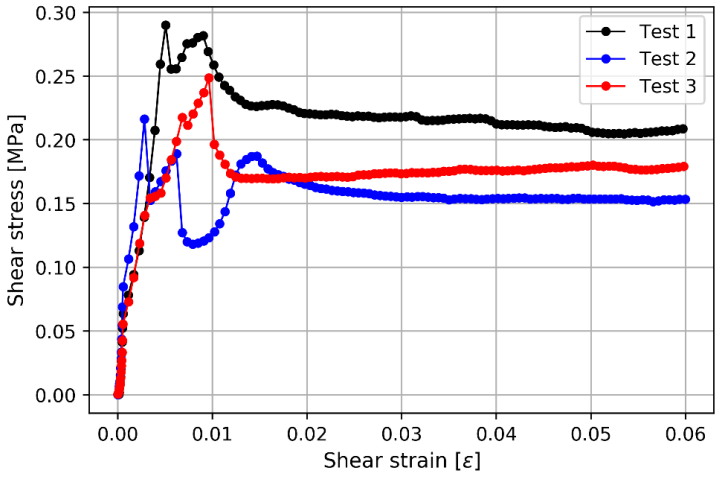

Figure 5-10 Results of shear test on three masonry specimens

From the average value of the maximum shear strength f_v, the initial shear strength, namely under zero compression, is determined inverting the equation of the shear strength provided by EN 6 1996-1-1 (2005):

$$f_{v0} = f_v - 0.4\sigma_d = 0.25 - 0.04 = 0.21\ MPa \tag{5-12}$$

The mechanical properties of materials at age of testing are summarized in Table 5-4.

Table 5-4 Results of material characterization

Material	Test type	Sample ID	Max Compression Force [KN]	Max Compression Strength [MPa]	Max Flexural Force [KN]	Max Flexural Strength [MPa]	Max Shear Force [KN]	Max Shear Strength [MPa]
Mortar	Compression	1-1	10.4	2.89	-	-	-	-
		1-2	10.55	2.93				
		1-3	10.58	2.94				
		1-4	11.22	3.12				
		1-5	10	2.78				
		1-6	9.04	2.51				
		2-3-1	8.7	2.72				
		2-3-2	8.01	2.50				
		2-5-1	7.04	2.20				
		2-5-2	7.87	2.46				
	avg (CoV %)		9.34 (14%)	2.70 (14%)	-	-	-	-
	3 point Flexural test	3PT 1-1	-	-	0.36	1.01	-	-
		3PT 1-2			0.44	1.24		
		3PT 1-3			0.41	1.15		
		3PT 1-4			0.39	1.10		
		3PT 1-5			0.43	1.21		
		3PT 1-6			0.37	1.04		
		3PT 2-1			0.26	0.73		
		3PT 2-2			0.16	0.45		
		3PT 2-3			0.35	0.98		
		3PT 2-4			0.09	0.25		
		3PT 2-5			0.26	0.73		
	avg (CoV %)		-	-	0.32 (34%)	0.90 (34%)	-	-
Brick	Compression	S1	335	14.97	-	-	-	-
		S2	326	14.58				
		S3	288	12.87				
		S4	289	12.92				
		S5	328	14.65				
		S6	311	13.89				
	avg (CoV %)		313 (6%)	13.98 (6%)	-	-	-	-
Masonry	Shear test-Triplet	M1	-	-	-	-	41.15	0.29
		M2					30.69	0.22
		M3					35.28	0.25
	avg (CoV %)		-	-	-	-	35.71 (12%)	0.25 (12%)

5.3.3 Results

For the set-up described above, two possible types of relative displacement are expected to occur: the first refers to the device's activation, the second to the failure of the grouted anchor embedded in the masonry panel. The relative slip occurring in the frictional device between the slider and the fixed elements is referred as Slippage mechanism, in accordance with the terminology defined in Chapter 4. The failure modes defined in section 5.2.1 are used to identify the failure of the strength-only part of the D-GAS. Other types of failure, such as the yielding of the steel profile, are not deemed likely to happen given the materials and the geometry of the assembly comprising the masonry wall, the anchor, and the frictional device. The dissipative anchoring system is schematically represented in Figure 5-11.

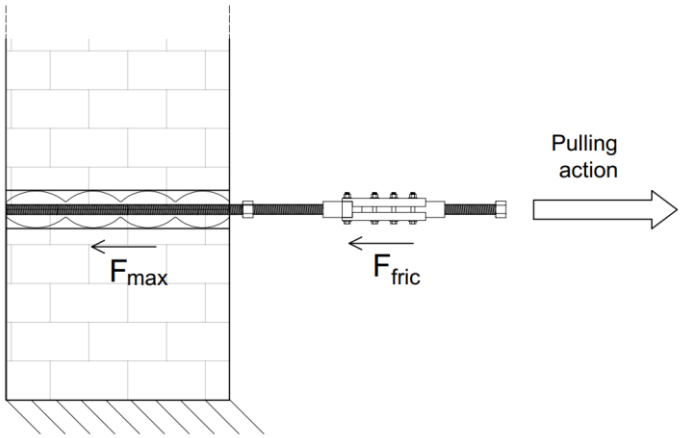

Figure 5-11 Representation of load scheme for the test set up.

The strength of the grouted portion is the maximum pull-out capacity of the anchor, F_{max}, while the device's strength F_{fric} is equal to the friction resistance the device provides as a function of the torque applied to the bolts. For incremental values of the pulling action, the relative slip of the slider with respect to the fixed part is designed to occur for a value of $F_{fric} < F_{max}$. Conversely, if the friction capacity applied to the device is larger than the load capacity of the embedded anchor, the grouted portion of the D-GAS will fail, and no slip of the slider will be recorded.

For the present testing activity, the friction force F_{fric} is the measured slip force $F_{\text{slip(M)}}$at which the device activates. This in turn depends on the perpendicular force $F_{\text{perp (M)}}$ recorded by the four load cells, the number of contact surfaces ($n = 4$) and to the friction coefficient μ_M, as already discussed in Chapter 4:

$$F_{\text{fric}} = F_{\text{slip(M)}} = n\,\mu_M\,F_{\text{perp (M)}} \tag{5-13}$$

Solving Eq. (5-13) for μ_M, returns the friction coefficient for each applied torque, and the design value μ_D is computed as the mean values of the obtained μ_M. For the five values of considered applied torque and the two devices, the obtained measured friction coefficient varies from 0.15 to 0.18, so that the mean value of 0.17 is assumed as μ_D. This result is in line with the values of friction coefficient discussed in Chapter 4 for the SteCyl: as the monotonic motion was not sufficient to cause any signs of abrasion on the components of the device, the obtained mean value reflects the friction coefficient of smooth steel surfaces in contact.

Then, the design force of the device V_D is determined using Eq.(5-14), and the variation between $F_{\text{slip(M)}}$ and V_D would determine the reliability of the dissipative system to perform to the desired level of slip force.

$$V_D = \mu_D \, n \, F_{\text{perp (N)}} \tag{5-14}$$

The instrumentation employed in the testing activity is able to record the instant at which failure occurs. Figure 5-12 shows the displacements measured by the two LVDTs on the first tested dissipative anchoring system, namely the D-GAS_1 at the bottom right corner of the wall (see Figure 5-6). The graphs refer to two load cases, namely Test ID:4 and Test ID:5 corresponding to 20 Nm and 25 Nm of torque couple per bolt. In the first load case, the design force was calculated equal to 24.4 KN from Eq. (5-14). The pull-out force applied by the hydraulic jack was equal to 24 KN when a relative motion between the slider and clamping plates of the device was recorded by the front LVDT (Figure 5-12a), showing a good agreement between the predicted and measured slip force.

For the load case corresponding to 25 Nm of torque couple per bolt, a value of V_D equal to 30.6 KN is estimated. A bonding failure between the grouted sleeve and the masonry wall (SGM failure) is observed for a pull-out force of 26 KN, highlighting that the load bearing capacity of the strength-only portion of the D-GAS, F_{max}, is smaller than the slip force $F_{\text{slip(M)}}$. The reading obtained from the two LVDT highlights that no relative slip between the front and the back end of the anchor was detected, as shown in Figure 5-12b. Instead, the slip of the grouted socket from the substrate occurs at about 300 seconds from the beginning of the test, namely when the applied load was equal to 26 KN.

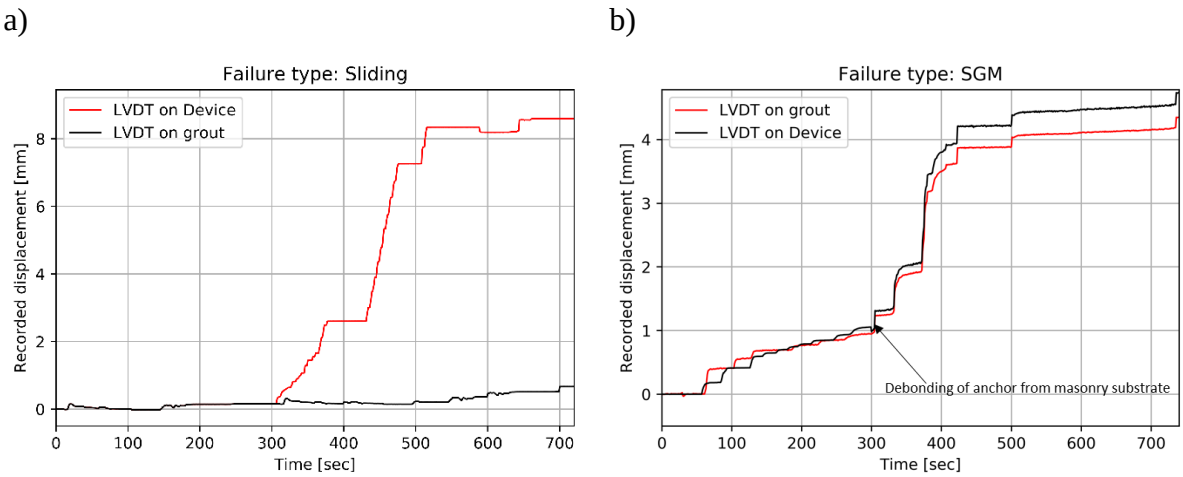

Figure 5-12 Recorded failure types: a) Test ID:2 and b) Test ID:5 corresponding to 10 Nm and 25 Nm of torquing couple per bolt respectively.

The recorded values of bolt loads are reported in Table 5-5 together with the measured perpendicular force $F_{\text{perp (M)}}$and the slip force $F_{\text{slip (M)}}$ for each Test ID. A good agreement is found between the measured and nominal perpendicular force, which proves that the empirical value of k_m = 0.37 and Eq. 4.3 provides an accurate prediction of the tightening action. The

variation ΔV_D between the recorded values $F_{\text{slip (M)}}$ and the design force of the device V_D is reported in the bottom line of Table 5-5.

Table 5-5 Summary of test results on D-GAS_1 for five cases of bolt tightening torque.

D-GAS 1								
TEST ID		1	2	3	4	5	μ_D	n
Applied torque [Nm]		5	10	15	20	25	0.17	4
Load Cell [KN]	1	2	3.8	5.5	7.6	7.6		
Load Cell [KN]	2	3.4	5.4	8.5	10.3	13.4		
Load Cell [KN]	3	3.8	4.3	5.3	8.3	16.8		
Load Cell [KN]	4	2.4	6.3	12.0	11.2	11.0		
$F_{PC(N)}$ [KN]		2.25	4.5	6.75	9	11.25		
Perpendicular Force $F_{perp(M)}$ [KN]		11.64	19.82	31.3	37.4	48.84		
Perpendicular Force $F_{perp(N)}$ [KN]		9	18	27	36	45		
Predicted F_{max} (Eq. 5.7) [KN]		25.5						
Measured F_{max} [KN]		26						
Slippage force $F_{slip(M)}$ [KN]		8	14	19	24	-		
Friction coefficient μ_M		0.17	0.18	0.15	0.16	-		
Device's design force V_D		6.1	12.2	18.4	24.5	30.6		
Variation ΔV_D[%]		31%	14%	3%	-2%	-		

Table 5-6 Summary of test results on D-GAS_2 for five cases of bolt tightening torque.

D-GAS 2								
TEST ID		6	7	8	9	10	μ_D	n
Applied torque [Nm]		5	10	15	20	25	0.17	4
Load Cell [KN]	1	3.3	5	7.5	10.8	14		
Load Cell [KN]	2	2.2	3.7	5	7	7		
Load Cell [KN]	3	2.6	6.5	10	12	15.5		
Load Cell [KN]	4	3.8	4.8	5.7	7.5	10.0		
$F_{PC(N)}$ [KN]		2.25	4.5	6.75	9	11.25		
Perpendicular Force $F_{perp(M)}$ [KN]		11.9	20	28.2	37.3	46.5		
Perpendicular Force $F_{perp(N)}$ [KN]		9	18	27	36	45		
Predicted F_{max} (Eq. 5.7) [KN]		25.5						
Measured F_{max} [KN]		28						
Slippage force $F_{slip(M)}$ [KN]		7	14	18	25	-		
Friction coefficient μ_M		0.15	0.18	0.16	0.17	-		
Device's design force V_D		6.1	12.2	18.4	24.5	30.6		
Variation ΔV_D[%]		14%	14%	-2%	2%	-		

The observed slippage force well agrees with V_D, with the larger variation computed for 5Nm of torque. As already observed, for the case of TEST ID:5, corresponding to an applied torque

of 25 Nm per bolt, the value of $F_{\text{slip (M)}}$ (26 KN) diverges from V_D (30.6 KN) due to the bond failure of the fabric sleeve. As the device was not active, the slippage force rather represents the maximum pull out force of the anchor F_{max}, and μ_M is not computed for this case.

Test ID 1 : 5 Nm

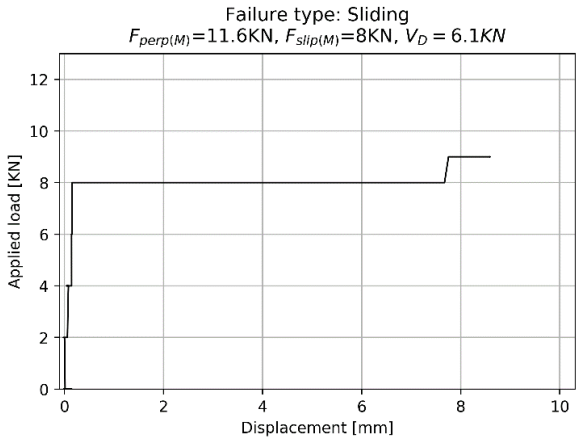

Test ID 2 : 10 Nm

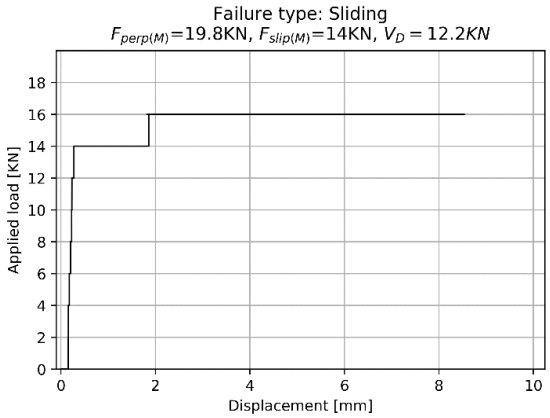

Test ID 3;15 Nm

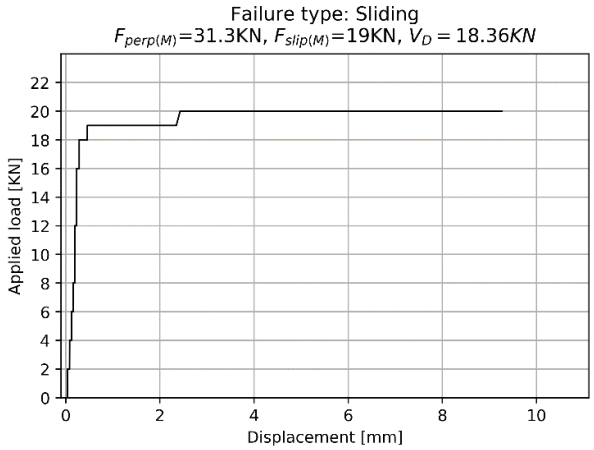

Test ID 4 : 20 Nm

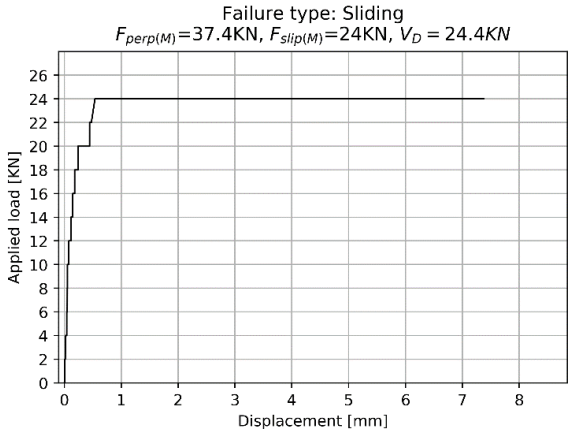

Test ID 5: 25 Nm

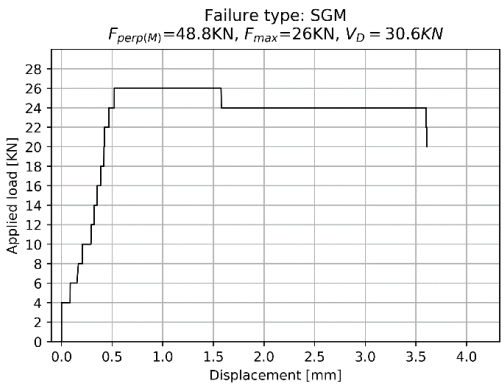

Figure 5-13 Force-displacement curves of the dissipative anchoring system for increasing values of bolt pretension.

Similar results are obtained for the D-GAS_2, which displays similar values of slip force, and which also failed at the grout-masonry interface for an applied torque of 25Nm, as reported in Table 5-6.

Figure 5-13 presents the relative displacement recorded by the LVDTs against the load applied during the test, for the D-GAS_1. The curves clearly indicate when the device is activated, initiating the relative sliding between the frictional plates.

Initially, the system behaves as a standard anchor and a relative displacement of about 0.5 mm is recorded due to relative sliding between the grouted sleeve and the masonry. When the pulling force equals the device friction force F_{fric} , the relative motion of the frictional plates is triggered: the internal slider moves outwards under steady load and small to no displacement is recorded by the LVDT monitoring the sleeve motion. For the wall connected to the dissipative anchoring system, minimal damages were detected in the bed joint due to sliding and mechanical locking of grouted sleeve, causing the small changes in stiffness visible in the load-displacement curves. After the transition from "standard-anchor" behaviour to fully frictional behaviour no incremental damages are recorded in the substratum.

In Figure 5-14 the force-displacement curves are grouped together to show the overall behaviour of the two D-GAS for all pre-loading conditions except for the case of 25Nm of tightening torque. It should be noted that the initial stiffness of the systems is almost constant, an average value of 48.6 KN/mm (CoV = 6%) was computed, highlighting that no slip occurred at the grout-masonry level before the device activation.

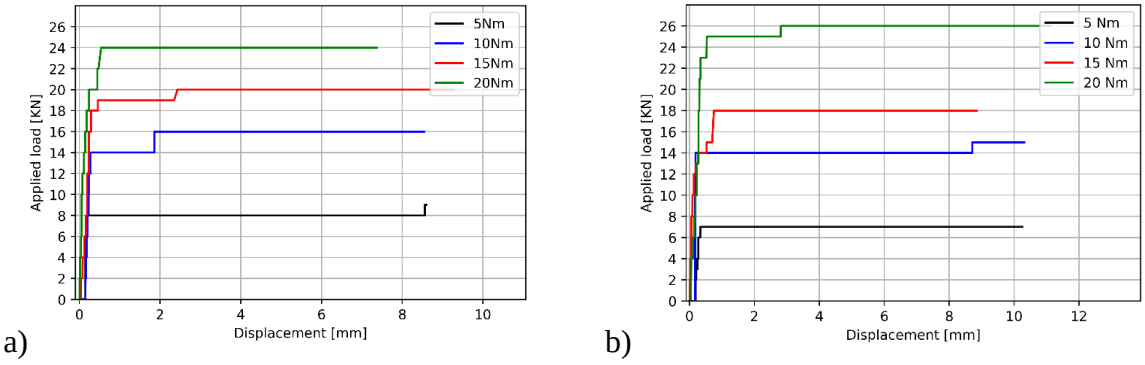

Figure 5-14 Pull-out curves of dissipative anchoring systems: a) D-GAS_1, b) D-GAS_2

Finally, one set of pull-outs was carried out connecting the hydraulic jack directly to the two steel bars grouted in the masonry. Considering that the D-GAS 1 and D-GAS 2 are also representative of a grouted anchoring system for an applied torque of 25 Nm, as the anchorage

failure preceded the device's activation, four load-displacement curves are obtained for the GAS, as shown in Figure 5-15.

a) b)

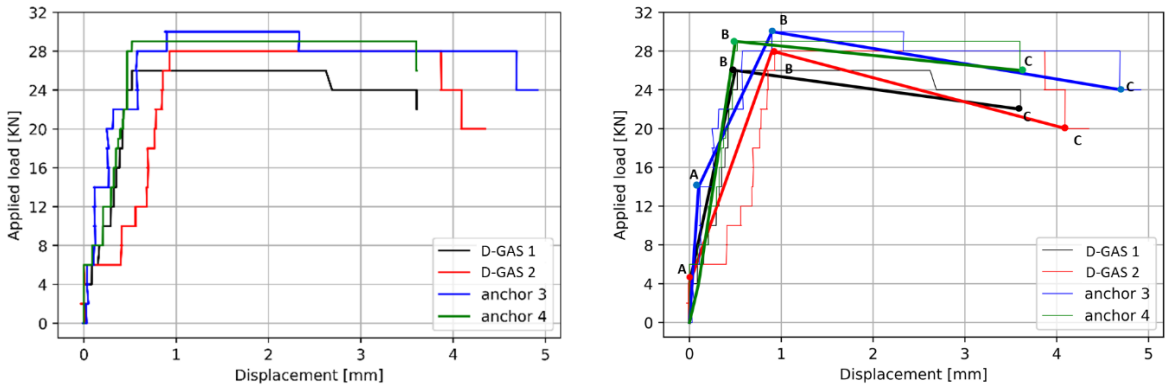

Figure 5-15 Results of Pull-out test on grouted anchors

The saw-like appearance of the load-displacement curves is due to the fact that the load was increased by a 1-KN ramp step causing an immediate relative displacement, if any, followed by a drop in the pressure of the hydraulic pump. Therefore, a linear interpolation is provided to investigate the behaviour of the systems. Looking in details at load-displacement curves in Figure 5-15b, it emerges that each curve presents indeed more than one change in stiffness, thus identifying:

- The first appearance of relative movement (point A);
- The achievement of maximum load (point B);
- The achievement of maximum displacement under sustained load (point C);

These threshold points identify idealised curves for the behaviour of the standard grouted anchor. It is observed that, for the standard anchors tested in this campaign, failure at the interface between the grouted sleeve (SGM failure mode) and the parent material is the main mode and the first to occur, then followed by a progressive decrement of the load capacity and cracking of other elements of the assembly according to other failure modes.

Accordingly, the comparison between the measured pull-out load and the predicted maximum capacity of the anchor is carried out considering both Eq. (5-6) and (5-7) and the numerical constants available in literature and obtained by numerical regression in this study. The results are reported in Table 5-8: the measured values significantly diverge from the formulation for the uniform and decaying distribution of shear stresses, when using the numerical constants provided by Arifovic and Cook. In accordance with the reviewed pull-out tests, Eq. (5-6)

overestimates the load capacity of the anchors, while Eq. (5-7) appears to be highly conservative. Conversely, the numerical constants proposed in this work in Table 5-2 provide a better agreement between numerical and experimental values, slightly conservative in both cases, with a difference never greater than 20%. These results confirm that current formulations reported in literature, used to predict the pull-out load of grouted anchors are not suitable when the borehole's diameter is significantly larger than the bar's diameter.

Table 5-7: Summary of pull-out test on GAS: load-slip capacity at Point B and observed failure types

l_e [mm]	d_h [mm]	d_b [mm]	fc,g [MPa]	fc,m [MPa]	Anchor no.	F_{max} [KN]	d_s [mm]	d_u [mm]	μ [-]	Failure type
340	80	16	50	3.3	D-GAS 1	26	0.6	3.6	6.0	SGM
					D-GAS 2	28	0.9	4.1	4.6	SGM
					Anchor 1	30	0.9	4.7	5.2	SGM
					Anchor 2	29	0.6	3.7	6.2	SGM
					Mean (CoV%)	28 (5%)	0.8 (12%)	4.0 (11%)	5.5 (5%)	SGM

Table 5-8 Summary of pull-out test on GAS: comparison with the empirical formulation

Anchor no.	F at point B F_{max} [KN]	Eq. (5.6)				Eq. (5.7)			
		Arifovic	ΔFmax	Melatti	ΔFmax	Cook	ΔFmax	Melatti	ΔFmax
D-GAS 1	26	37.5	-44%	24.7	5%	8.1	69%	25.5	2%
D-GAS 2	28		-34%		12%		71%		9%
Anchor 1	30		-25%		18%		73%		15%
Anchor 2	29		-29%		15%		72%		12%

The loads at point A for anchors 2 and 4 are below the pull-out capacity calculated on the basis of the square root of the compression strength of the masonry. A better correlation is achieved if the pull-out capacity is calculated using the shear strength obtained from Eq. (5-12), as reported in Table 5-9. Therefore, it is likely that point A represents a first micro-cracking at the interface between grout and parent material at the outer portion of the anchor, possibly a shear failure of the mortar joints near the anchor. For the D-GAS 1 and Anchor 2, the influence of the confinement of the surrounding material is lower as they are installed in the upper portion of the wall. This would explain why Point A is not clearly visible on these load-displacement plots.

Table 5-9 Comparison between empirical formulation and experimental results for the GAS

Anchor no.	F at point A	Eq. (5.7)		F at point C [KN]	Eq. (5.8)	
		Melatti	ΔF_A		Melatti	ΔF_C
D-GAS 1	-	6.8	-	22	13.2	40%
D-GAS 2	6		-13%	20		34%
Anchor 1	14		51%	24		45%
Anchor 2	-		-	26		49%

The peak capacity of the four anchors is quite consistent and it is related to the chemical bonding and friction between grout and masonry. Because the mechanical properties that the grout displays are considerably greater than the masonry strength, it is reasonable to assume that the square root of the masonry's compressive strength should be the governing parameter to determine the ultimate capacity. Similarly, as the SGM failure is observed in all four cases, the borehole diameter should be rightfully used in place of the bar's diameter.

The cause of the recorded motion identified by point C is a mixed mode of tensile failure of masonry mortar joints and bond failure between the grouted sleeve and the parent material. The failure identification is based on the LVDT displacement recordings and on visual inspection of the portion of wall around the bar. The crack shown in Figure 5-16 opened just above and below the drilled hole along the mortar-brick joints. As a result, the whole system comprising the threaded bar and the grouted sleeve was pulled out by about 4 mm, being unable to resist the applied load.

Accordingly, the recorded ultimate load is compared to the load capacity predicted by the empirical formulations for the MIX failure mode. It is found that Eq. (5-8) gives the best approximation (see Table 5-9), even if the prediction is considerably smaller than the measured values. This is explained considering that the numerical constants of the equations of the MIX mode presented in in Section 5.2 are obtained with reference to the maximum load capacity, rather than from the ultimate recorded load. In general, the latter presents a large scatter as two resisting mechanisms are acting simultaneously, and it is hard to quantify whether the compression strength of the masonry or the tensile strength of the mortar is the dominant parameter.

a) b)

Figure 5-16 Modes of failure observed during tests: a) bond failure and tensile failure of upper mortar joint, b) bond failure and tensile failure of upper and lower mortar joints.

By comparing the performance of a strength-only anchor and a frictional anchor, it is possible to conclude that whilst standard anchors are very stiff and fail for small displacements, which are due to failure of the bond between the substratum and anchor assembly and/or failure of the mortar-brick bond around the borehole, the frictional anchor provide large displacement with relatively small, if any, damage to the masonry. The larger part of the total displacement is due to the sliding motion of the internal plate, which provides ductility to the whole assembly. The formation of large cracks and the failure of the bonding action between the anchor and the masonry are prevented once the device is tuned to activate for a pulling action smaller than the computed capacity of the grouted anchors.

The tested grouted anchors and the two D-GAS at 25Nm of torque present a consistent peak load capacity, which the adopted empirical models seem to be able to predict, even if in a conservative manner. Being able to estimate the maximum pull-out capacity of the anchor F_{max} is a crucial step to determine the design slippage load and ensure that the device activates before the causing the bonding failure of the grouted anchor.

In the next section, a numerical model calibrated on the results of the pull-out test is presented. Building a reliable model able to predict the behaviour of anchors grouted in a masonry substrate will prove to be an important step towards the validation of the dissipative anchoring system and the development of a design tool.

5.4 Computational analysis

The pull-out tests highlight that the behaviour of the dissipative anchoring system is stable and reliable: the device shows minimal variation between the design slip load and the recorded one (below 15 % in 88% of cases) and the stiffness of the system remain constant before the device's activation, meaning that severe cracks to the parent material are prevented.

The final validation of the D-GAS, namely its implementation in a case-study structure subjected to dynamic loading, is pursued through numerical analysis in Chapter 6.

To this purpose it is crucial that the numerical model can accurately simulate the response of a set of dissipative anchors embedded in a building. Therefore, in this section a numerical model reproducing the experimental set-up of the pull-out tests is developed to calibrate the response of the model on the experimental results.

As already observed during the experimental campaigns, the most critical element of the anchor assembly is the interface between the grouted socket and the surrounding masonry. It is the capacity of this element, especially in comparison with the capacity of the dissipative device that is installed in series with the anchor rod, that determines the performance of the whole assembly, and hence of the strengthened connection. Therefore, the focus of the numerical activity will be the optimisation of the material and element properties apt to reproduce the real-life behaviour of the tested typology of anchors.

5.4.1 Model and material

A numerical model of the dissipative device connected to a steel bar embedded in a masonry wall was produced, as shown in Figure 5-17, aiming at an accurate simulation of the structural behaviour of the injected anchors. The numerical model is a detailed 3D finite element model, developed in Abaqus CAE 6.14 and validated against the available experimental results.

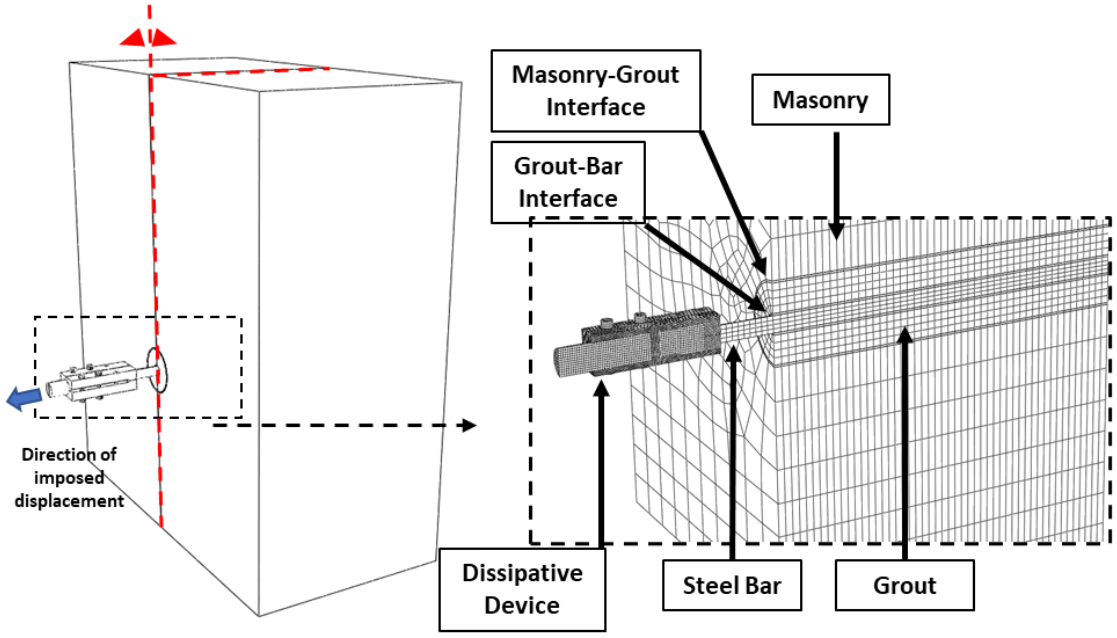

Figure 5-17 Numerical model – Undeformed shape and components of the model.

Three-dimensional volume elements were used for the mesh since an accurate stress distribution is relevant for a clear understanding of the stress field and of the structural behaviour. Figure 5-17 shows the elements comprising the final assembly: the dissipative device, as already described in Chapter 4, the steel bar, the masonry, the grout-bar interface, and the masonry-grout interface.

The model simulates only half of the test set-up, as it presents a vertical axis of symmetry (marked as a red dotted line in Figure 5-17) and focuses on the prismatic portion of the masonry

wall enclosed in the reaction frame. The vertical edge representing the part of wall in contact with the reaction frame is restrained for horizontal out-of-plane displacements, while the base is fully restrained as it did not display any movement during the test. The full depth of the masonry wall is reproduced as the determination of the shear stress distribution along the length of the bar and grouted core is one of the objectives of the numerical analysis. The motion of the steel bar is rigidly coupled to the device's end plate, by defining appropriate tie constrains between the two surfaces in contact. The stress field attained in various parts of the model can be visualised running a displacement-controlled static analysis and computing the resisting forces exerted by each element comprising the assembly. Even if the experimental activity was performed as load-driven due to the available testing apparatus, it is decided to run a displacement-controlled analysis for the numerical activity as it provides higher efficiency and better numerical stability (Zheng et al. 2005). A monotonic displacement is applied to the internal slider of the device with a maximum magnitude of 30 mm to exploit the full run of the device ($\Delta u_{dev} = 20mm$) and induce pull-out failure of the bonded portion of anchor. The direction of the applied displacement is shown in Figure 5-17.

As previously done in Chapter 4 for the numerical activity, the built-in routine of Abaqus is used to simulate the concentrated force acting on each bolt head. It is decided to validate the model's performance on the test ID 4 corresponding to 20 Nm of bolt torque. For this test case, the device displayed the largest slippage load, and thus largest dissipative capacity, while preventing the pull-out of the anchor. According to Table 5-5, the bolt load was set at 9 KN per bolt element, the friction coefficient to 0.16, which results in a design slippage load of 24.5 KN according to Eq. (5-14). Cohesive elements are generally used to bond two bodies and they degrade after applying load due to the tensile or shear deformation. Therefore, a set of cohesive elements were introduced at the masonry-grout interface ("Outer interface") and at the grout-bar interface ("Inner interface"), as shown in Figure 5-18 to simulate the bonding properties among the single components, i.e. the steel bar, the grout and the masonry.

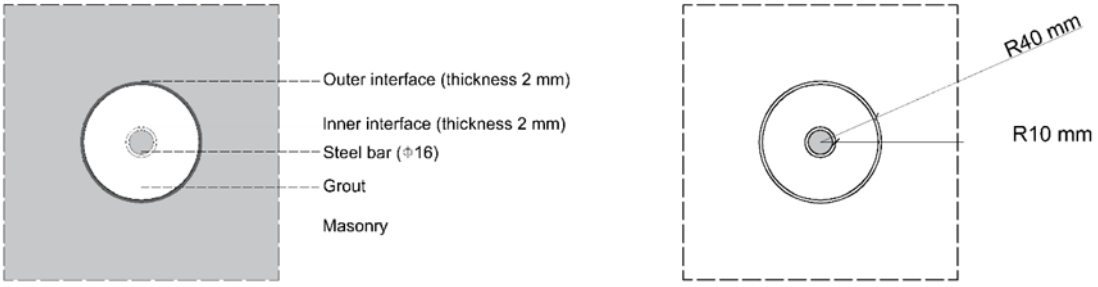

Figure 5-18 Numerical model – components and geometrical features

Abaqus CAE allows the selection of cohesive elements to which a bilinear elastic traction-separation law is assigned. A typical traction-separation response is presented in Figure 5-19: it consists of one traction component (Mode I) and two shear components (Mode II, in plane shear and Mode II, out-of-plane shear).

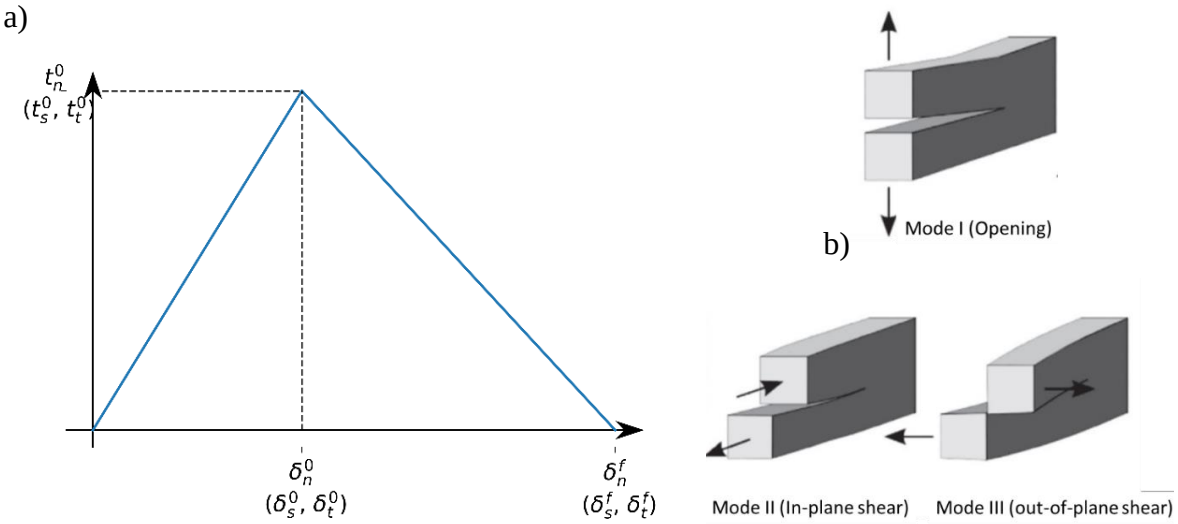

Figure 5-19 Traction/shear-separation response and fracture modes

In the first linear part, the traction vector consists of a normal traction component t_n and two shear components t_s and t_t. These components represent mode I, II and III of the fracture modes shown in Figure 5-19. Also, in this model δ_n^0, $\delta_s^0, and\ \delta_t^0$ represent the corresponding initial separation caused by pure normal, in-plane and out-of-plane shear stresses, respectively. Note that Figure 5-19 is a symbolic representation of the traction $\boldsymbol{t}$ and the separation vector $\boldsymbol{\delta}$, whose components can be assigned independently from each other.

When the maximum resistance is reached, the interface elements display a progressive degradation, represented by the second part of the traction-separation law, which is driven by a damage process. The numerical parameters defining the mechanical properties of these cohesive elements are calibrated to replicate the experimental results obtained from the pull-out tests performed on the anchor embedded in the masonry wall. These highlighted that the most likely failure was the slip of the bar-socket assembly, caused by the loss of mechanical bonding between the grouted socket and the surrounding material. To simulate this mechanical bonding in the numerical model, the following procedure is adopted.

Firstly, a bilinear idealized curve is computed to represent the average behaviour of the tested anchors. The analytical curve is obtained averaging the load values of the significant points B and C, reported in Table 5-8 and Table 5-9, and the values of slip and ultimate elongation

reported in Table 5-7. Point A was not included because the analysis software does not allow for the implementation of a trilinear curve and because point A was not clearly identified on all curves.

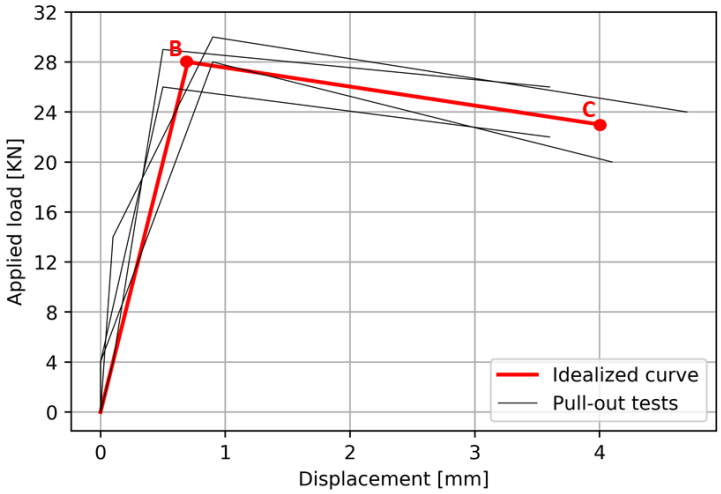

Figure 5-20 Bilinear idealized curve and summary of pull-out tests on GAS

Then, the maximum shear stress τ_{max} (corresponding to t_s in Figure 5-19a) of the interface is computed considering the shear strength at zero pre-compression and the vertical pre-compression acting perpendicularly to the shear action:

$$\tau_{max} = \tau_{max,0} + 0.4\sigma_d \tag{5-15}$$

The pull-out tests were performed without applying a vertical precompression and the only contribution in terms of perpendicular force is coming from the self-weight of the portion of wall above the anchors. However, this contribution is rather small ($\sigma_d = 0.01\ MPa$ for the anchors at the bottom) and the second term of Eq. (5-15) is assumed equal to zero. Hence, τ_{max} is computed from the maximum load capacity of the idealized curve $F_{\text{max,I}}$ (Point B):

$$\tau_{max} = \tau_{max,0} = \frac{F_{\text{max,I}}}{A_{ext\ int}} = 0.33\ MPa \tag{5-16}$$

Where a uniform distribution of the shear stress in the longitudinal direction of the grout-masonry interface is assumed and $A_{ext\ int}$ is the external lateral surface of the cohesive interface equal to:

$$A_{ext\ int} = \pi dL = \pi\ 0.08\ 0.35 = 0.088\ m^2 \tag{5-17}$$

The shear stiffness G_1 of the external interface is computed as:

$$G_1 = \frac{\tau_{max}}{\gamma} = \frac{F_{\max,I}}{A_{ext\ int}\,\gamma} \tag{5-18}$$

Where γ is the shear angular deformation computed considering the thickness of the cohesive interface *T* and the mean slip elongation d_y reported in Table 5-7:

$$\gamma = \frac{d_y}{T} \tag{5-19}$$

Failure of the interfaces in the direction normal and transversal to their longitudinal axis (Mode I and Mode III in Figure 5-19) is not expected as the pulling action exerts a shear deformation in the longitudinal direction only. Therefore, the traction behaviour of the interfaces in Mode I and Mode III are assumed as perfectly elastic.

For the internal interface, the shear strength is obtained by Eq.(5-3), as estimated by Gigla from experimental pull-out of anchor that displayed failure at the bar-gout interface. The properties adopted to define the elastic behaviour of the materials, as well as the parameters needed to define the traction-separation law for the interfaces are provided in Table 5-10.

Table 5-10 Materials Properties

Material name	E [MPa]	G1 [MPa]	Density Kg/m^3	Max stress (Point B)		Displacement at ultimate Load (Point C) [mm]
				Normal direction [MPa]	Longitudinal direction τ_{max} [MPa]	
Masonry	1500	-	2141	CDP	CDP	CDP
Grout	2000	-	2000	ELASTIC	ELASTIC	ELASTIC
Steel	200000	-	8000	ELASTIC	ELASTIC	ELASTIC
External interface	1500	328	2141	ELASTIC	0.33	4.0
Internal interface	50000	2500	2000	ELASTIC	2.50	4.0

The damage evolution, after the maximum stress is attained, is defined according to a displacement-based criterion, setting the ultimate displacement that the interface can display and the slope of the descending branch of the idealized curve. According to the obtained experimental values, the displacement threshold is set equal to the mean ultimate elongation d_u reported in Table 5-7.

The mesh is finer around the anchors where higher stress variations occur and coarser in the regions where the stress distribution is more uniform, which is a typical approach when dealing with masonry structures with considerable dimensions. Brick elements (C3D8R, eight-node linear brick with hourglass control) are used for the mesh of all the parts, except for the

simulation of the bond between different materials, where tri-dimensional interface elements (COH3D8, eight nodes on each surface) were applied.

Masonry is heterogeneous and anisotropic material due to different materials of its components, namely the units and the mortar joints in the two directions. Considering the masonry as a homogeneous (macro-modelling) or heterogeneous (micro-modelling) material is a key decision when modelling masonry walls. In general, micro-modelling approaches lead to more accurate results, as different constituents of the masonry are considered. Different properties of both units and mortar, such as Poisson's ratio, Young modulus and inelastic characteristics are considered for a more realistic prediction of the local behaviour of masonry. Nevertheless, this method may be inefficient in terms of computational cost is applied to large scale models (Bolhassani et al. 2015)

As the aim of the computational activity is to simulate the dynamic response of a case-study structure strengthened by the D-GAS system, it is decided to adopt another modelling approach that considers the masonry as a homogeneous material where the mortar and units are defined with average mechanical properties. This method is used for large-scale models in such a way that mortar joints and units are smeared into one isotropic or anisotropic material. For the present study, masonry was assumed as an isotropic material using the Concrete Damage Plasticity (CDP) model available in Abaqus to simulate the nonlinear response of the masonry components. The CDP model has been developed to predict the behaviour of concrete and other quasi-brittle materials such as rock and mortar under cyclic loading (Bolhassani et al. 2015). Cracks in tension or crushing in compression are the main failure modes of this model. The tension and compression damage can be tracked separately, as shown in Figure 5-21.

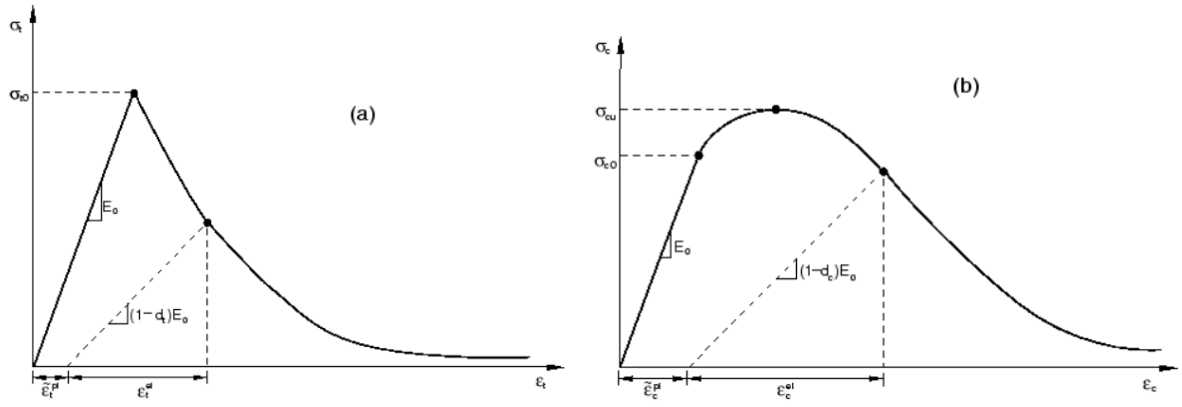

Figure 5-21 Response of concrete to uniaxial loading – a) compression damage evolution, b) tension damage evolution (Abaqus theory manual)

Although a CDP approach is conceived for isotropic fragile materials like concrete, it has been widely shown that its basic constitutive law can be also adapted to masonry (Valente and Milani 2016; Bayraktar et al. 2018).

The material properties of the masonry obtained by testing are adapted to the CDP model according to the study carried out by (Kaushik, Rai, and Jain 2007). In this study, the stress-strain curves for masonry can be computed using an analytical model that requires only the compressive strength of bricks and mortar as input data. The ascending part of the stress-strain curve serving as the compressive strength evolution is represented by a parabolic curve, which is a good fit with several experimental investigations. The parabolic variation is expressed in nondimensional form in terms of stress and strain ratios as:

$$\frac{f_m}{f'_m} = 2\frac{\epsilon_m}{\varepsilon'_m} - \left(\frac{\epsilon_m}{\varepsilon'_m}\right)^2 \tag{5-20}$$

where f_m and ϵ_m are the compressive stress and strain in masonry, respectively and ε'_m is the peak strain corresponding to f'_m. Further, the parabolic curve can be extended in the descending part of the stress-strain curve until f_m drops to 90%; the corresponding strain can be calculated using Eq. (5-20). After the stress level of 0.9 f_m is reached on the descending part, the curve can be simplified as a straight line up to the residual stress in masonry, i.e. 20% of f_m. The resulting curve for the monotonic evolution of the compressive stress is shown in Figure 5-22a. The equation used to estimate ε'_m can be found in the referenced paper.

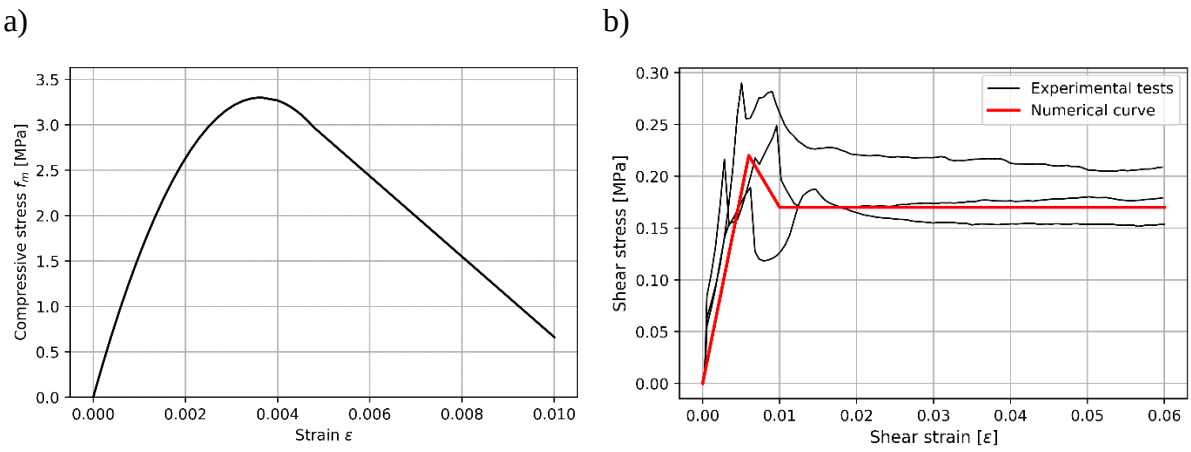

Figure 5-22 Stress strain relationship assigned to the CDP model for the compressive (a) and tensile behaviour (b) of the masonry material

As shown in Figure 5-21 when the specimen is unloaded from any point on the strain softening branch of the stress-strain curves, the unloading response is weakened, and the elastic stiffness of the material appears to be damaged (or degraded). The degradation of the elastic stiffness is

characterized by the tensions and compression damage variables, d_t and d_c which can take values from zero, representing the undamaged material, to one, which represents total loss of strength. The equations to determine these variables and the evolution of the stress-strain curves during loading and unloading cycles are defined in the Abaqus manual (Abaqus, Dassault Systems 2019).

The experimental results showed that cracks are expected in proximity of the anchors, when the shear stresses exceed the bonding strength of the mortar-brick interface. Therefore, the maximum tensile strength of the masonry is modelled according to the maximum shear strength $f_{v0} = 0.21\ MPa$ obtained in Eq. (5-12) for the triplet test of the masonry samples. Finally, the values of the inelastic parameters needed to complete the definition of the CDP model are defined in Table 5-11. These are adopted by several authors (Bolhassani et al. 2015; Valente and Milani 2016; Bayraktar et al. 2018) who adapted the CDP model to the analysis of masonry structures.

Table 5-11 Parameters of the CDP to model masonry material

Dilatation angle	Eccentricity	σ_{b0}/σ_{c0}	K	Viscosity parameter
10^o	0.1	1.16	0.666	0.002

5.4.2 Results

A numerical analysis is performed applying a 30 mm displacement to the slider's free end. The imposed monotonic displacement results in a sliding force that is numerically equilibrated by the system, proportionally to the properties of the materials assigned to the single parts. Figure 5-23 plots the displacement of a reference point located on the free end of the sliding part against the resulting force that equilibrates the applied displacement.

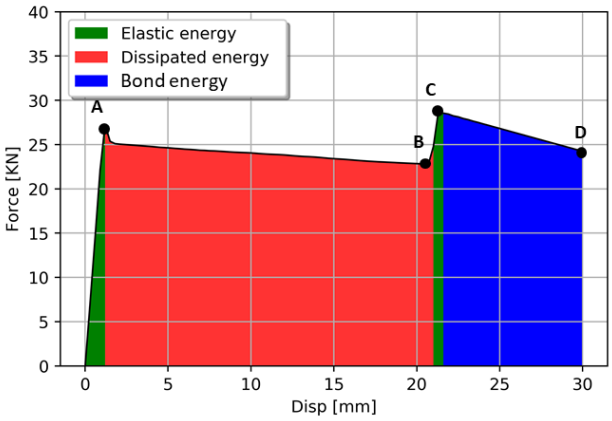

Figure 5-23 Energy dissipated by the system under monotonic load

The results' analysis focuses on four critical points along the force-displacement output curve, illustrated as Points A to D in Figure 5-23, which represent the changes in behaviour of the anchoring system for increasing displacements. The first point, Point A, represents the increment at which the applied force exceeds the friction resistance, and the sliding central part starts moving. The device activates for a slippage force equal to 25 KN, close to the design value ($V_D = 24.5$ KN). At Point B, the slider part comes in contact with the central pin which restricts the permitted run to 20 mm. Between point A and B the slippage force decreases by 8%, due to an equivalent decreasing pressure generated by the clamping plates as the slider moves outward. For increasing displacements, the dissipative device and the steel bar behave as a strength-only anchoring system applying a shear force to the masonry wall through the outer interface. Point C represents the maximum shear resistance the interface can provide, after which the interface displays a gradual degradation, representing – in the physical model – the progressive loss of bonding between the grout and parent material, and microcracking in the masonry. Finally, at Point D the outer interface deforms to the set value of the ultimate elongation (given in Table 5-10) and the pull-out resistance drops to zero.

Figure 5-24 illustrates the stress distribution of the device, the bar, and the wall, for incremental values of displacement. The focus is on the displacement increments at which the dissipative system activates (point A), reaches its maximum run (Point B), behaves as a strength-only grouted anchor (Point C), and fails (point D).

For the wall, the distribution of the shear stress (S13) is displayed to visualize the shear stress induced on the wall as it opposes the pulling action. On the bar and the device, the Von Mises stresses are displayed, as both parts feature isotropic and homogeneous materials.

From Figure 5-24, it is clear that the device activation determines a reduction of the shear stress on the wall. During the slippage motion, the shear stresses display a homogeneous distribution along the drilled hole, and the maximum value of the shear stress is smaller than τ_{max}. The design slippage force is smaller than the maximum pull-out force that the outer interface can reach, and the wall display a linear behaviour. Moreover, the energy imparted to the system is mainly dissipated by the device while a smaller amount is stored as elastic energy in the bar and in the outer interface. Integrating the area below the load-displacement curve between the origin and point A and between point A and B returns the elastic and dissipated energies respectively (green and red areas in Figure 5-23), which are reported in Table 5-12 as a percentage of the total input energy.

Conversely, the shear stress rapidly increases after the device has reached its final position, because the system behaves a strength-only assembly with limited displacement capacity and high stiffness. At Point C, the shear stress on the outer interface equals τ_{max} , inducing a shear stress distribution in the masonry that exceeds the maximum bonding strength (0.21MPa). This finds correspondence with the crack pattern identified on the portion of wall near the anchor when the maximum pull-out force is attained. In fact, the numerical model highlights that cracks due to bond failure at the mortar joints should be expected along the length of the anchor, where the shear stress are higher (see the blue area for point C in Figure 5-24)

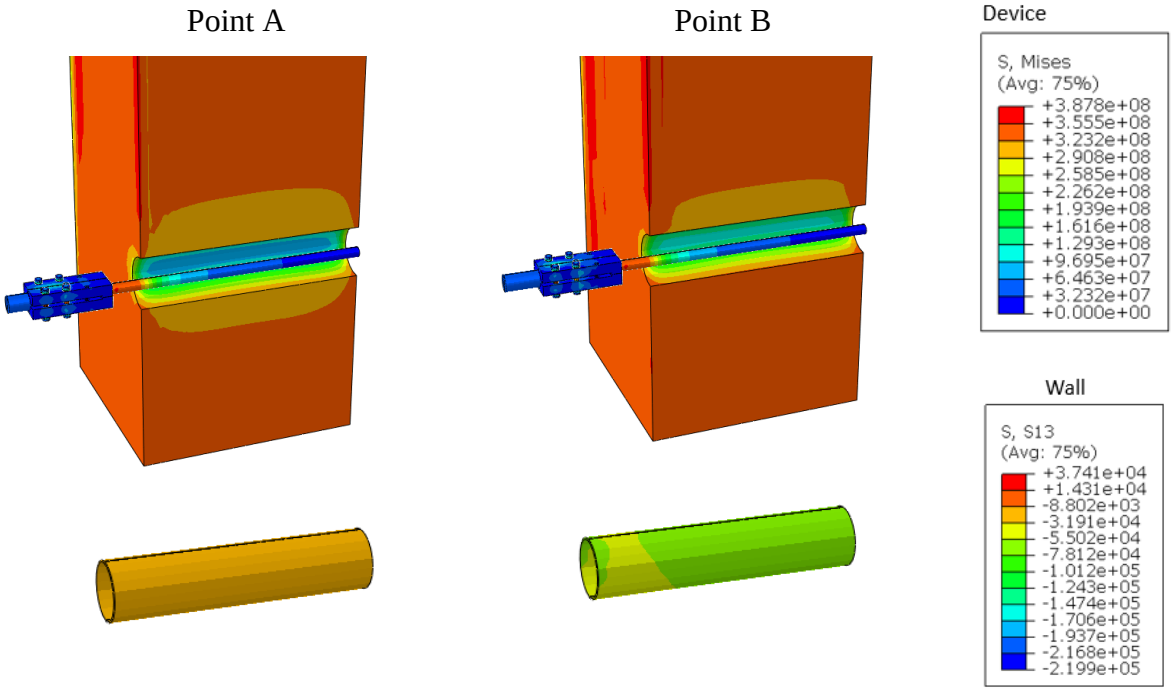

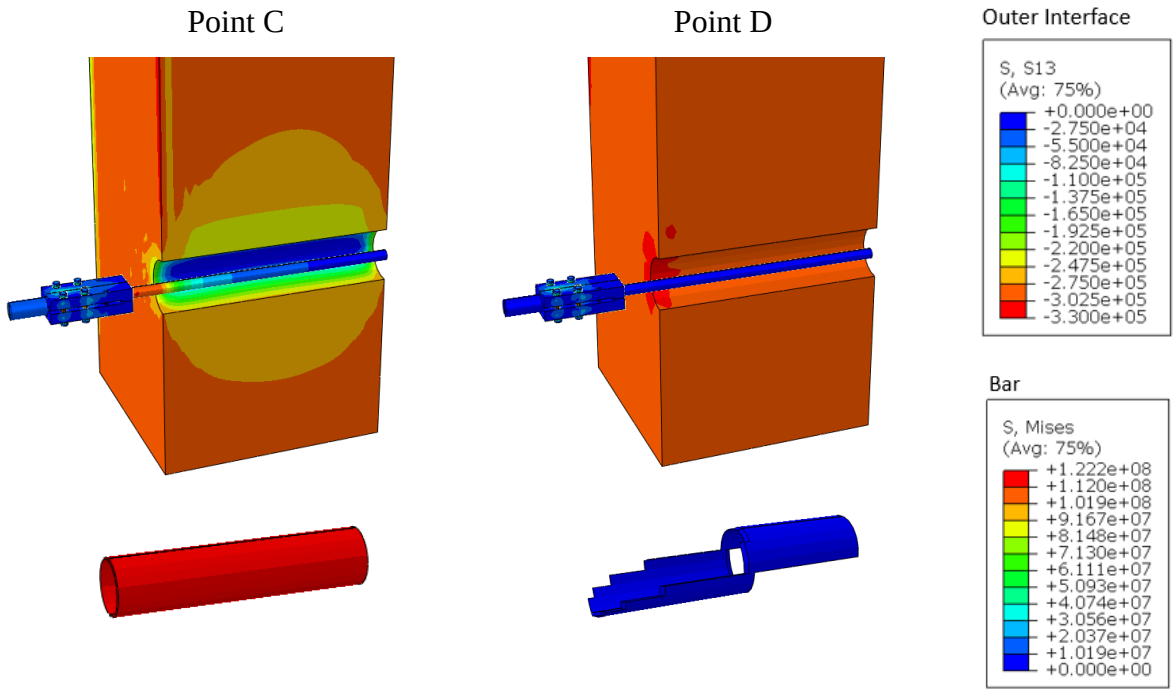

Figure 5-24 Stress distribution on the wall, bar, and device parts for incremental values of displacements (all stresses in Pa)

When the shear stress on the outer interface equals τ_{max}, the shear displays a progressive degradation, which ultimately results in the failure of the interface and the complete debonding of the anchoring system. From point C to point D, the blue area between the force-displacement curve and the x-axis represents the energy dissipated in the post bond failure deformation. Although this energy adds up to almost a third of the imparted energy, it is important to notice that this energy dissipation is linked to the damage evolution of the cohesive interface which represents the microcracking propagation in the physical wall. Conversely, the device dissipates without inducing permanent damages to the assembly.

Table 5-12 Results of numerical analysis: peak stress in the parts of the assembly and energy balance.

	Pull - out Load [KN]	Pull - out Disp [mm]	Parts				
			Device Mises [MPa]	Bar Mises [MPa]	Wall S13 [MPa]	Outer Interface S13 [MPa]	Energy [%]
Point A	25	1	377	122	0.19	0.27	1%
Point B	23	21	392	138	0.17	0.22	69%
Point C	29	22	377	156	0.22	0.33	2%
Point D	0	30	387	11	0.01	0	28%

It can be concluded that the numerical model is able to reproduce the GSM failure mode observed in the pull-out tests, and the pick loads corresponding to the device's activation and

ultimate capacity of the grouted element are also in agreement with the experimental values and with the expected design values.

The shear stress distribution is constant along the interface length, in line with what found by Giresini et al. (2020) who considers a uniform distribution of the shear stress for "short" embedment length (see Section 5.2.3). The constitutive law assigned to the external cohesive interface well represents the average maximum shear stress obtained from the pull-out test, as shown in Figure 5-25.

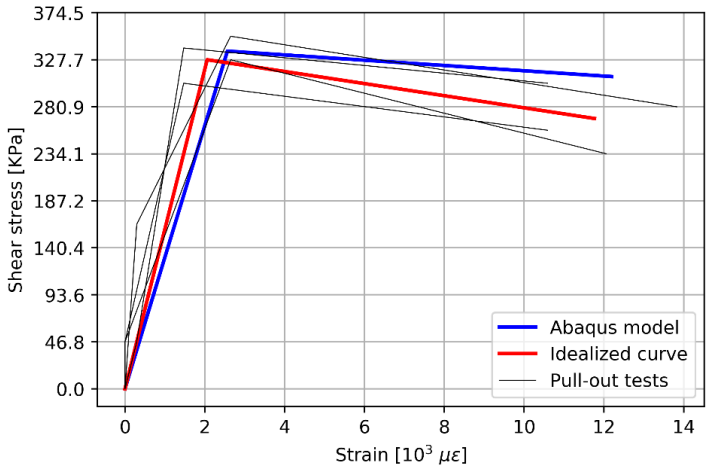

Figure 5-25 Experimental idealized stress displacement curve and damage evolution as implemented in Abaqus model

The results presented in this section show that the implementation of the dissipative device improves the performance of metallic grouted anchors under monotonic pull-out loading. The test set-up allows determining the capacity of the GAS and D-GAS and their failure modes for a masonry substrate. However, the focus is on the head portion of a wall's connection undergoing horizontal loading as the set-up neglects the phenomena occurring in the other masonry panel of the connection and on the portion of anchor grouted into it. Therefore, the experimental procedure is not exhaustive as it does not include the effects that the anchoring system produces on the connection's behaviour.

To investigate these effects, the experimental tests performed on a connection of two masonry walls strengthened by the D-GAS are presented in the next section.

5.5 Tests of dissipative anchoring system embedded in a T-shaped masonry connection

The Dissipative grouted anchoring system is designed to be installed in connections of two orthogonal masonry walls, such as the front (often referred to as façade) and a side walls of a monumental building. As already outlined in Chapter 3, the device activates when an external action exceeds the connection's load capacity, and the two walls start moving relative to one another. The internal slider of the device controls the amplitude of this motion, which is often called rocking motion, and dissipates energy through friction. Therefore, the system's performance depends on four main assumptions:

- The walls separate for an external load smaller than the pull-out capacity of the anchors.
- The crack at the walls' interface propagates on the side wall along a pseudo-vertical line, passing through the location of the device.
- For an external action directed orthogonally to the façade, the rocking is limited to the front wall, while the side wall is assumed motionless.
- The mechanism of motion does not change throughout the duration of the event, as a result for instance of an inversion in the action's direction.

To investigate these assumptions an experimental activity was carried out at the School of Engineering of Cardiff to test the D-GAS on T-shaped specimens of a connection between two walls. The spine wall reproduces the wall parallel to the seismic action and the "head" of the T represents a section of a panel undergoing out-of-plane damage. Such type of damage is recurring in historic buildings due to the lack of a good-quality connection between adjacent walls, which is recreated in the specimens by ensuring a modest overlapping of bricks at the joint.

This set-up includes the longer part of the anchor and the second wall and allows investigating the mutual interaction between the connection and the anchoring system. The specimens were built in December 2019 and the tests were scheduled for spring 2020 before the outbreak of coronavirus disease (COVID-19) forced the experimental activity to stop. The tests were resumed in May 2021 when restrictions in the UK were lifted, and the laboratory could be accessed. Thus, the first sample of the strengthened T-shaped wall was tested, and the preliminary results are included in this chapter as they represent an important step towards the validation of the D-GAS. In the next two subsections, the test set-up, the deployed instrumentation, and the testing methodology are detailed. The numerical model of the

connection implemented in Abaqus to predict the load capacity of the connection is introduced in section 5.6.3: drawing on the results of the previous testing activities, the use of cohesive interfaces is proposed to simulate the evolution of the traction capacity of the connection under out-of-plane action. These predictions are validated against the obtained experimental results to determine the feasibility of this modelling technique to model masonry connections. The preliminary analysis of the results is discussed in section 5.6.4 and it will inform the testing methodology for the second sample of T-connection. The complete results will be available in a future journal publication.

5.5.1 Test set-up and instrumentation

The brick courses are purposely designed to create a weak connection between the orthogonal walls to ease their separation during loading. The weak connection is simulated by the repetition (six times) of three courses as illustrated in Figure 5-26. Thus, the resulting connection between front and spine wall consists in a course overlap of 110 mm. To further reduce the connection's capacity, the joint overlapping varies along the wall height: within each repetition, one course is lacking the connection.

The specimen's height is 1600 mm, the width of the head and spine wall are 1520 mm and 1000 mm, respectively, the thickness of both panels is 340 mm. The T-shaped masonry specimens are built using the same typology of bricks and lime mortar adopted to build the panel for the pull-out tests. A vertical load is applied to the front wall to generate uniform pre-compression of 0.1 MPa by means of two threaded bars connected to semi-spherical hinges at the base and to an I-beam at the top of the block. Strain gauges are glued on the steel bars after removing the threads on a portion of the uprights long 50mm, as shown in Figure 5-27, to monitor the variation of vertical load during the test.

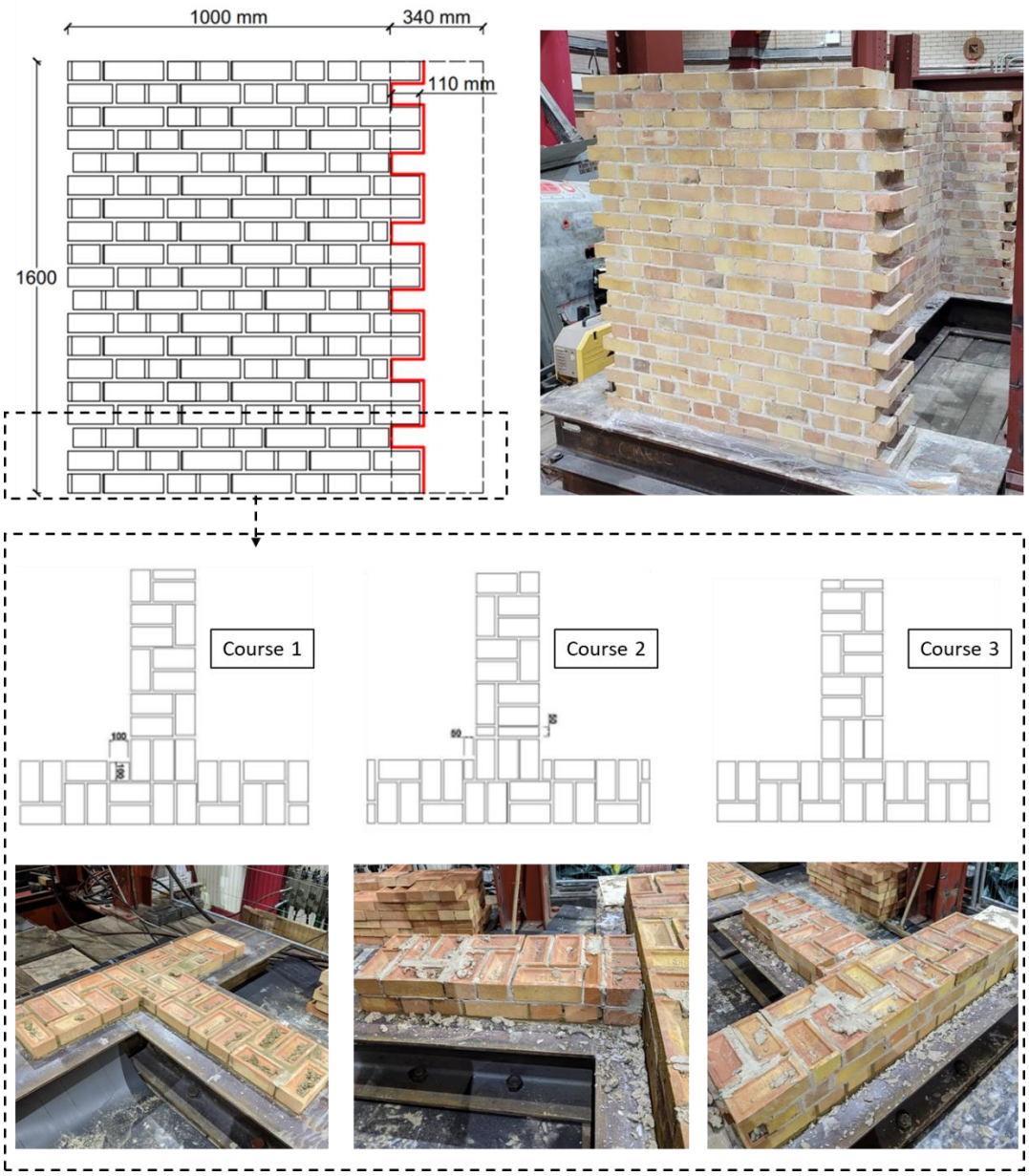

Figure 5-26 Construction phases of T-shaped masonry walls

A vertical load of 80 KN is applied directly to the spine wall by a hydraulic jack to simulate the reaction that the rest of the building would provide to prevent horizontal sliding and rotation of the T-shaped specimen as a rigid body during loading.

The test is performed in displacement-control mode: the horizontal displacements are applied by means of a hydraulic actuator (maximum load ± 300 kN, stroke ± 300 mm), located at a distance of 1300 mm height from the specimen foundation. The actuator is connected to a hinge mechanism comprising a spherical heavy-duty rod end and steel brackets able to accommodate up to 5 mm of vertical displacement. In turn, this mechanism is welded to a channel, which is connected to the surface of the front wall by eight bolts passing through the wall and tightened against steel end plates at the back of the wall, as shown in Figure 5-28.

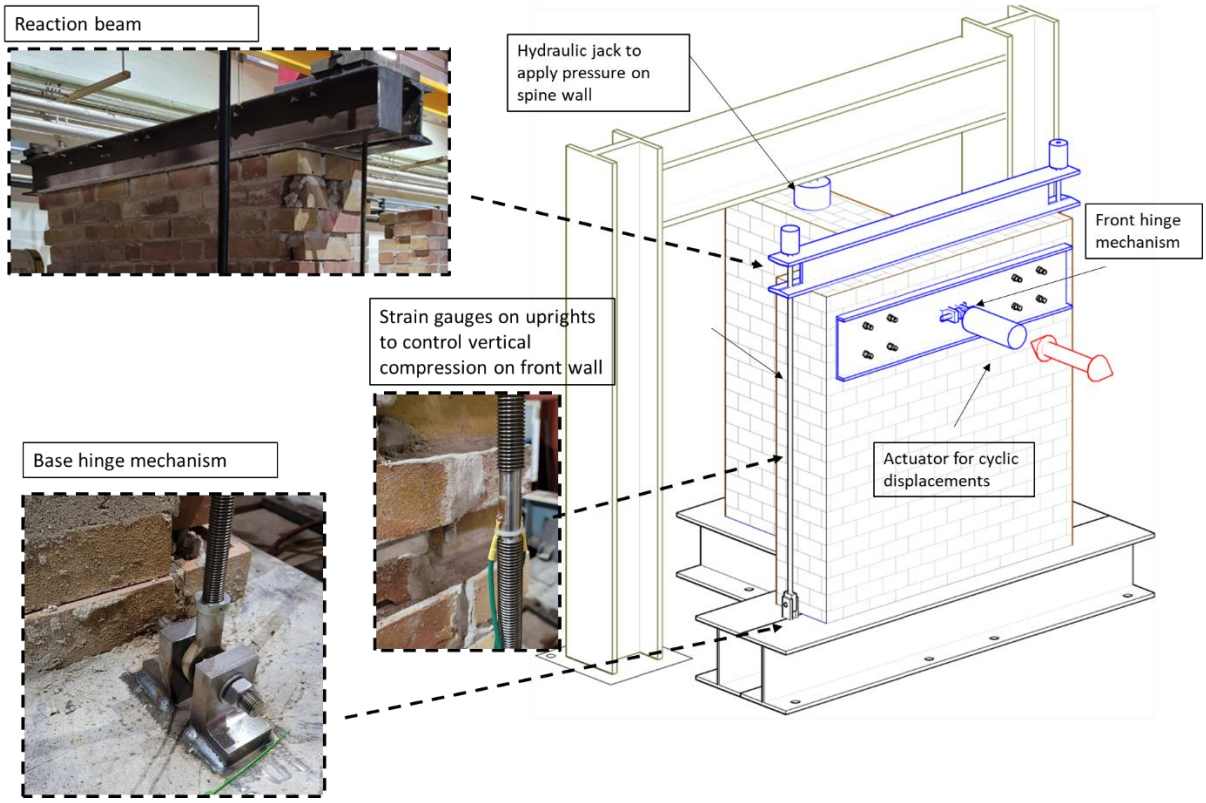

Figure 5-27 Testing set-up for cyclic loading of T-shaped wall

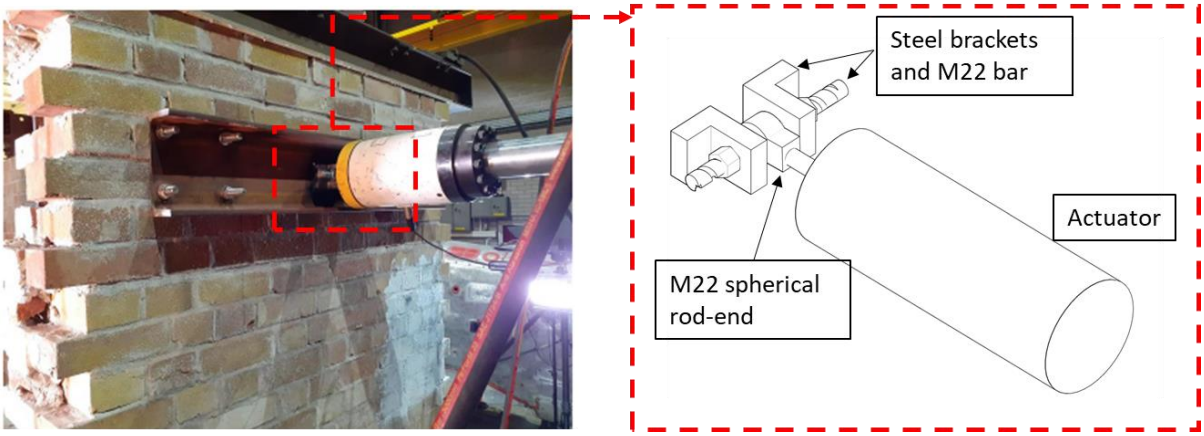

Figure 5-28 Detail of connection between actuator and front wall

The specimens are fitted with a dissipative anchoring system, comprising two anchor rods, wrapped into two expanding fabric sockets and screwed in the threaded connections of a BRACyl device. The complete assembly is shown in Figure 5-29.

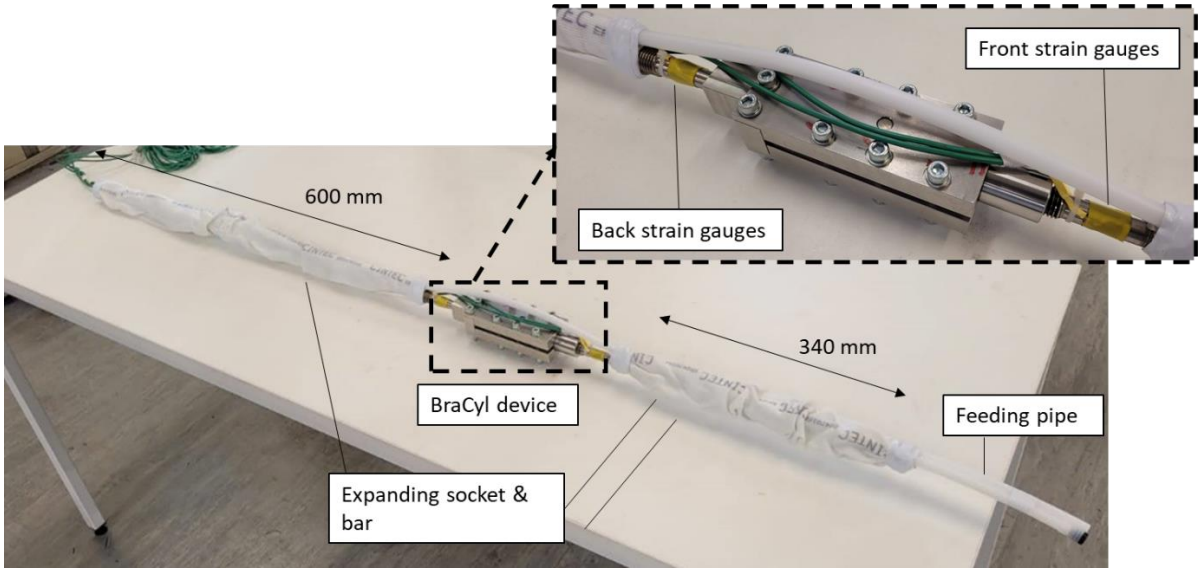

Figure 5-29 Dissipative anchoring system implemented on T-shaped wall

Having assembled the D-GAS, the device is tuned for the desired slip load and displacement capacity. The latter is achieved by setting the BraCyl to its fully retracted position, namely ensuring that the internal slider is fully inserted into the clamping plates: as shown in Figure 5-29, the brass sleeve is not visible, and the device provides 20mm of controlled displacement. For sake of comparison, the fully extended configuration of the BraCyl, namely when the slider motion is limited by the central pin, is illustrated in Figure 4.16.

The slip load is set according to the load hierarchy introduced in section 5.4. The maximum bond capacity of the front portion of the anchor $F_{max,front}$ determines the upper limit for the design slip load V_D of the device. $F_{max,front}$ is computed considering the maximum shear strength that the anchor can develop at the grout-masonry interface τ_{max} and the surface of embedment A_{emb}:

$$F_{max,front} = \tau_{max}\, A_{emb} \tag{5-21}$$

where the shear is assumed uniformly distributed along the interface, and it is computed from Eq. (5-15) to include the additional contribution of the vertical precompression:

$$\tau_{max} = \tau_{max,0} + 0.4\sigma_d = 0.37\ MPa \tag{5-22}$$

where $\tau_{max,0}$ was obtained experimentally from the pull-out tests. The resulting maximum load capacity of the front anchor is:

$$F_{max,front} = \tau_{max}\, A_{emb} = 0.37\ 0.9 = 33.5\ KN \tag{5-23}$$

Accordingly, it is decided to set the BraCyl to a design slip load equal to 90% of the anchor's capacity. This is achieved tightening the six bolts of the device to a torque of 15Nm, which results in a bolt load of 6.76 KN (see table 3 of Chapter 4) and in a design slip load of:

$$V_D = 4 * 0.2 * 6 * 6.76 = 32\ KN \quad (5\text{-}24)$$

Then, the D-GAS is inserted at 1300 mm from the base of the wall, as shown in Figure 5-30, into an 80mm core-drilled hole. To visualize the final position of the system, Figure 5-30 shows the exploded view of the strengthened connection.

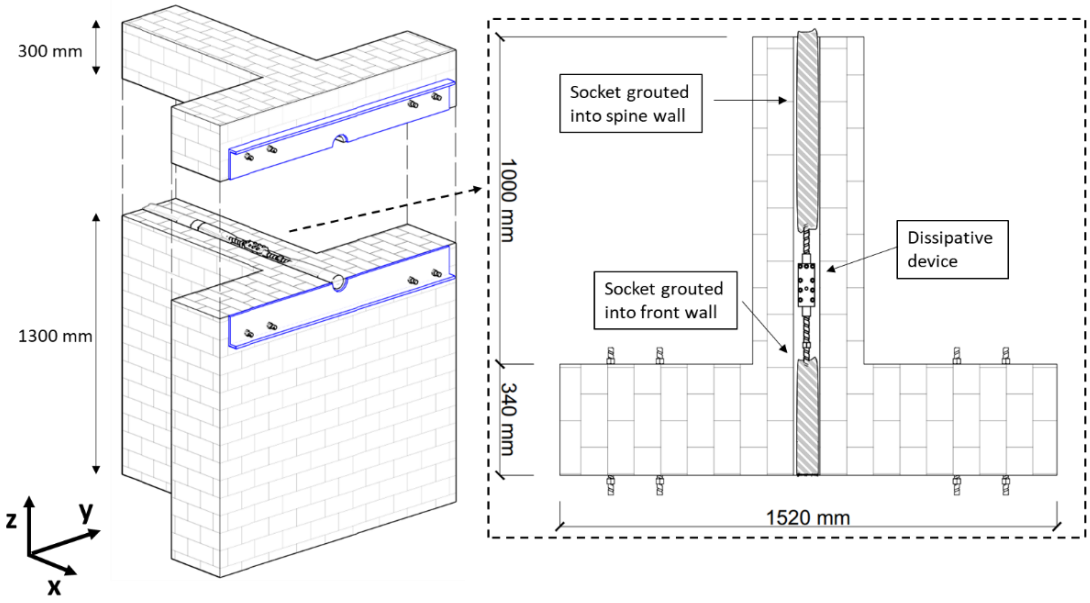

Figure 5-30 Exploded view of the T-connection at the location of dissipative anchoring system

The final step of the D-GAS installation is the injection of the grout into the sockets by means of two 10 mm tubes: the grout penetrates through the textile sleeve for fixation of the injected body in the hole. In Figure 5-31, the flexible sockets are shown before and after completion of the injection process, note that the feeding pipe is extracted as grouting progresses.

The same masonry typology and anchor technology used for the pull-out tests is selected for this testing activity. Therefore, the mechanical and geometrical properties of the single components can be obtained from Table 5-3 and Table 5-4. The rear part of the anchoring system has an embedment length of 600 mm, a grout-free recess of 50mm is left on both bars to machine the space to glue four strain gauges on each side of the device (see Figure 5-29). These gauges will record the changes in strain during the test, identifying the device slip load.

a) Front anchor b) Back anchor

Figure 5-31 Installation of D-GAS and grout injection a) front anchor b) back anchor

A video gauge system is set on one side of the wall to measure the relative motion of the front wall with respect to the spine wall. The focus of the system is on the upper portion of the wall where the crack is expected to form and propagate during the test. The position of the tracking points on the surface of the wall is shown in Figure 5-32: as the test progresses the video gauge system records the components of the displacement in the X-Z plane of these points. The position of the tracking points (TP_i) is strategic to identify the typology of out-of-plane failure mechanism that the wall will develop. For instance, larger horizontal displacements u_x recorded at point 1 compared to point 4 and almost zero u_x at point 6 would imply the separation of the two panels and a rigid rotation of the front wall around a horizontal hinge line.

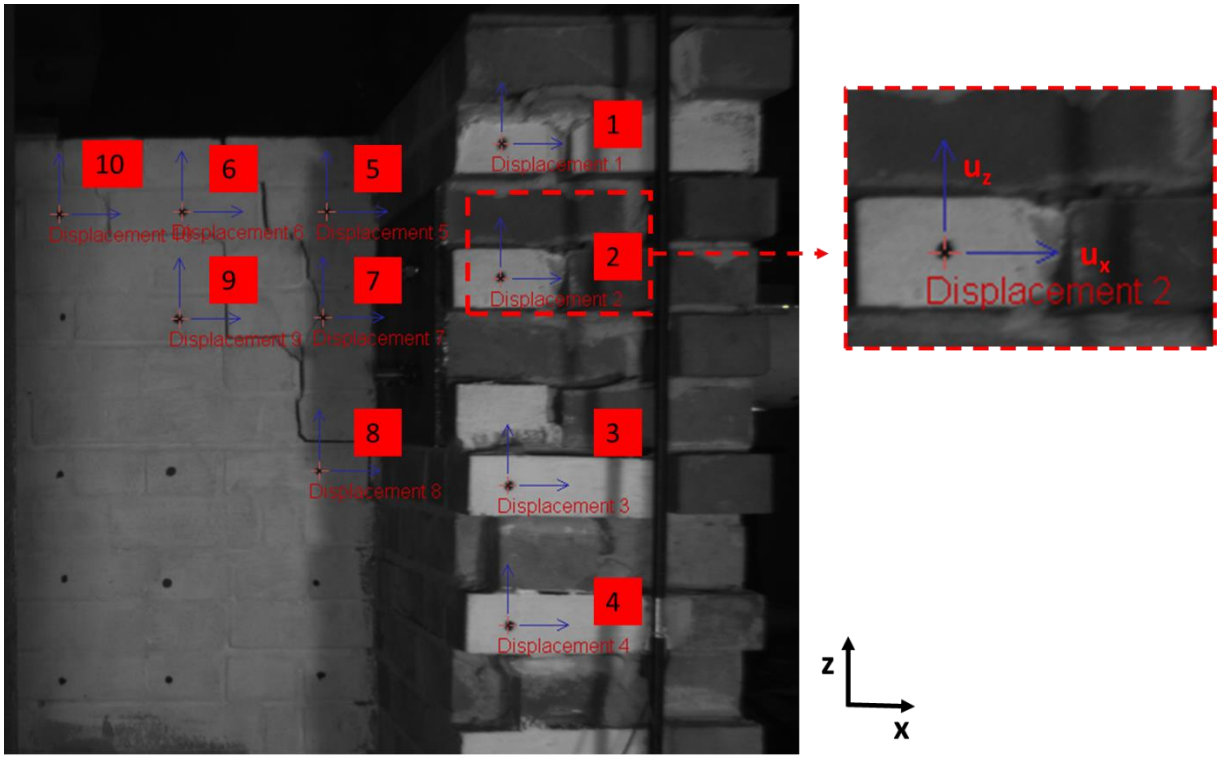

Figure 5-32 Location of tracking points (TP) on the cracked surface of the specimen

On the other side of the wall, a Digital Image Correlation (DIC) system in stereo configuration is used to achieve the superficial strain map and displacements, including out-of-plane thanks to two 8MP cameras. The walls are prepared with a stochastic black and white speckle pattern as shown in Figure 5-33. To post-process the images, a MATLAB code is used (MATLAB R2019b 2018). While the load is applied, images of the wall's side are recorded at the sampling frequency of 12 frame/minute for applied displacement smaller than or equal to 18mm and 6 frame/minute for applied displacement greater than 18mm. The images are then processed subdividing them into matrices of data (subset) and comparing the speckle pattern in each subset with the one of the reference images (first frame). A correlation function is generated for each subset, for instance using the Cross Correlation or the Sum of Squared Difference criteria, and the deformation (and strain) vector field is obtained. An extensive review of the DIC methodology and principles can be found in Longana (2014).

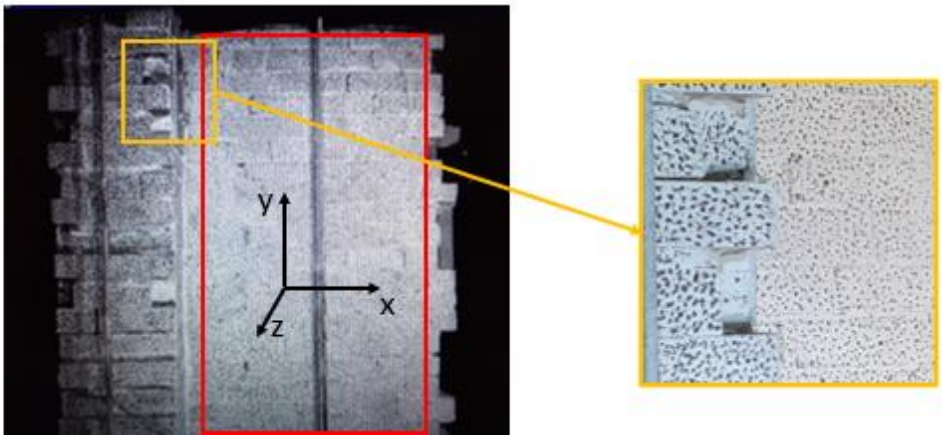

Figure 5-33 Stochastic speckle pattern on side surface of the T-shaped specimen

The parameters of the DIC system are reported in Table 5-13.

Table 5-13 Parameters of the DIC system

Characteristic	Set-Up
Technique used	Stereo DIC
Software	DaVis 8.0
Subset size (pixels)	51 x 51
Step size (pixels)	24
Camera	Imager X-light 8MP
Lens	Hama 24mm f/1-2.8D
Exposure (µs)	28000
Image Resolution (pixels)	3539 (w) x 2659 (h)
Frame rate (Hz)	0.2, 0.1
Focal length (mm)	25.3835
Spatial resolution (mm)	14.226
Displacement resolution (pixels)	0.0302
Strain resolution (ε)	4.9838e-04

5.5.2 Testing methodology

Cyclic load is applied by the hydraulic actuator on the front wall under displacement control, while applying constant vertical pressure (0.1 MPa) on the front and spine walls. Initially, successive cycles are progressively increase by 3 mm of displacement amplitude until the walls' separation is induced or visible damages occur, as shown in Figure 5-34.

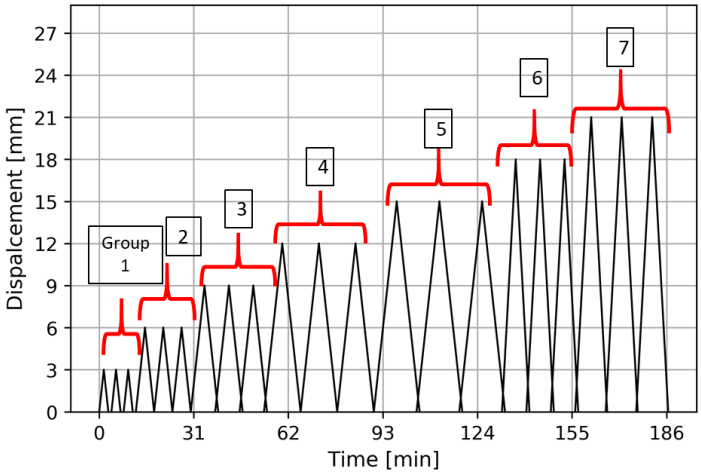

TEST PLAN				
Group	Max disp [mm]	Disp rate [mm/min]	Max drift [%]	DIC frame rate [frames/min]
1 (3 cycles)	3	2	0.23%	12
2 (3 cycles)	6	2	0.46%	12
3 (3 cycles)	9	2	0.69%	12
4 (3 cycles)	12	4	0.92%	12
5 (3 cycles)	15	4	1.15%	12
6 (3 cycles)	18	6	1.38%	12
7 (3 cycles)	21	8	1.62%	6

Figure 5-34 Groups of displacement cycles for the test up to the walls' separation

Then 10 cycles of load are imposed to assess the cyclic behaviour of the device. The displacement rate ranges between 2 and 4 mm/min: the lower rate is used for the initial 4 groups of cycles, the highest for the remaining cycles (groups 5, 6, and 7 in Figure 5-34 where the drift is calculated as the ratio between the horizonal imposed displacement and the distance between the specimen's foundation and the actuator location, 1300 mm).

Finally, the actuator is set to exceed the maximum displacement that the device can provide (20mm) to cause the bonding failure of the anchor. Then, three load cycles are imposed to determine the performance of the strength-only portion of the anchoring system.

5.5.3 Computational analysis

To assess the complexity of mechanisms that determines the horizontal force required to activate the out-of-plane local failure of the front wall, a numerical model of the test set-up is implemented in Abaqus. The model draws on the results obtained from the numerical analysis of the pull-out test, given that both wall specimens present the same typology of masonry and constituent materials, and the same anchoring technology. As previously discussed, a good correspondence was achieved between the numerical and experimental activity; thus, some key

features of the pull-out model are implemented for the T-shaped model, such as the parameters of the CDP and the use of cylindrical cohesive interfaces to model the bonding capacity between grout and masonry. Conversely, the interface modelling the interaction between the bar and the grout was not included, as the failure between the grout-bar interface is not activated for the level of forces considered.

The novelty of this model consists in two additional cohesive elements implemented at the interface between front and side walls to reproduce the connection between adjacent walls. These can be assigned with an "equivalent traction capacity" which corresponds to the capacity of the connection to resist the imposed out-of-plane motion. This modelling approach developed by the author (Melatti, D'Ayala, and Modolo 2019) draws on the approach firstly proposed by D'Ayala and Speranza (2003) and has some conceptual similarity with the rigid macro-block modelling approach recently proposed by Casapulla et al. (2019) which can be used to assess the response of masonry structures and experimental masonry specimens (Maione et al. 2021) to out-of-plane action. The latter computes the lateral capacity of the connection considering the frictional resistance developed by the specimen at the bed joint and the contribution of anchoring systems if included. Minimizing the lateral capacity for a set of failure mechanisms that the specimen/structure can develop returns the expected failure mode. However, this method is not able to simulate the stresses transferred by the anchors as the bonding strength at the anchor/masonry interface is not modelled. Thus, the crack pattern with a strengthening layout is not exactly predicted (Maione et al. 2021). Conversely, the finite element model presented in this work uses cohesive interfaces running along the full height of the wall, as well as at the anchor/masonry interface to simulate both an "opening" fracture mode (Mode I in Figure 5-19b) between the two connected walls and the pull-out failure of the anchor.

The parts composing the model and the main dimensions are illustrated in Figure 5-35 in exploded view.

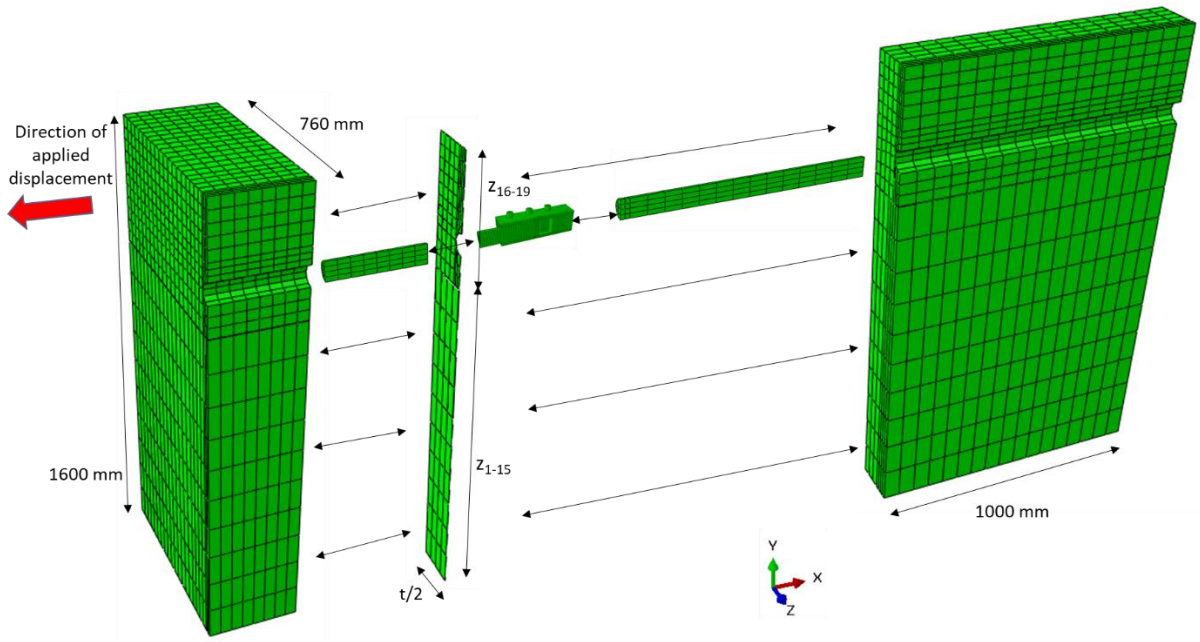

Figure 5-35 Numerical model of half T-shaped wall

According to their geometry, a slip strength is assigned in the direction of the thickness of the cohesive elements at the wall's connection, namely the normal component t_n of the traction vector, and it is computed considering the contribution of the bond strength of the mortar vertical joints and of the shear strength developed at the contact surfaces between masonry courses of the T connection. According to literature studies linking the bond strength of masonry to the mechanical properties of its constituents (Sarangapani, Venkatarama Reddy, and Jagadish 2005; Costigan and Pavía 2013), the bond strength f_{bond} is estimated equal to 0.2 MPa considering the compressive strength and type of lime mortar and the compressive strength of the masonry.

The shear strength can be computed considering the shear strength at zero precompression $f_{v0} = 0.21\ MPa$ found experimentally by triplet test (see Section 5.3.2) and considering the additional contribution of the normal compressive stress σ, as expressed by Eq. (5-12). Following the approach proposed by D'Ayala and Speranza (2003), the slip capacity that opposes the out-of-plane loading can be computed as a stepwise function of the height h_i of the wall above the position of the unit at level *i* and the weight of the wall above the course considered (including the applied pressure p = 0.1 MPa). With reference to Figure 5-36, the given formula is obtained for the slip capacity of each course *i*:

$$C_i = f_{bond} h_b t \ + \ s\ t\ \tau_i = f_{bond} h_b t \ + \ s\ t\ [c_0 + (h_i\ (\gamma g) + P) \tan(\varphi)] \qquad (5\text{-}25)$$

Where s is the overlapping length, t is the thickness of the wall, h_b is the brick height, and γg is the wall's weight per unit of volume.

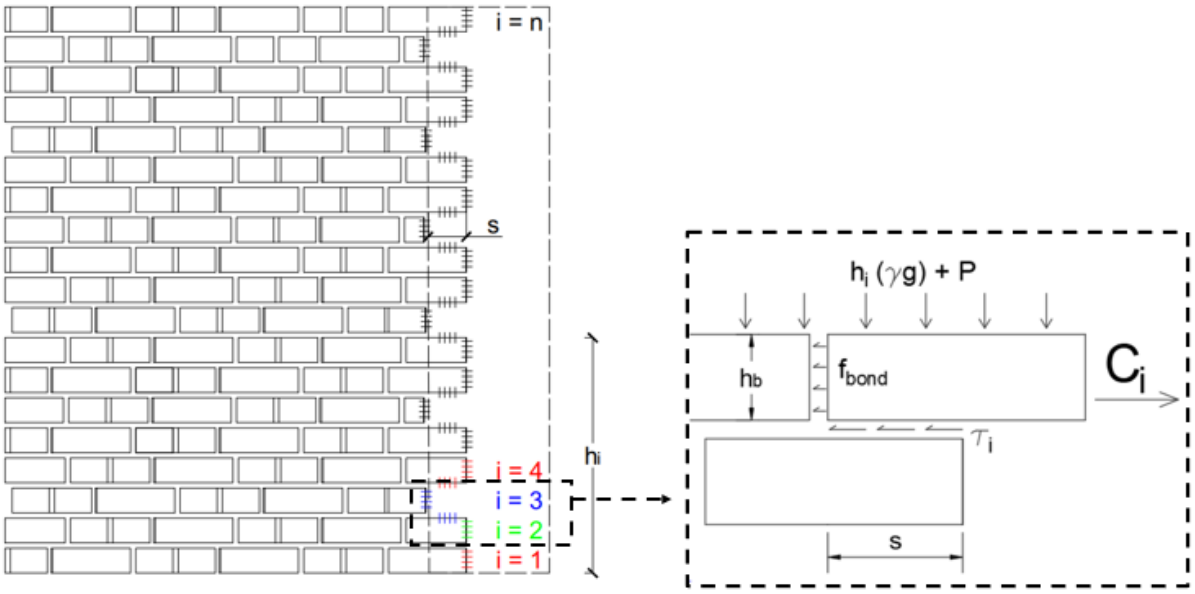

Figure 5-36 Connection line of wall specimen: location of shear and traction surfaces along weak line

The slip capacity C_j of a portion of connection composed by m courses is therefore computed adding up the traction capacity of the m head joints composing the wall's portion and considering the number of courses that develops a shear surface. These are identified by a factor S_i equal to one if the shear surface is present and zero if it is lacking for each i-th course. For the tested wall, S_i is:

$$S_i = \begin{cases} 0 & for\ i = 1, 2, 5, 8, 11, 14, 17 \\ 1 & elsewhere \end{cases} \tag{5-26}$$

The slip capacity C_j of a portion of wall comprised between courses i and m, can be computed as:

$$C_j = \sum_i^m C_i = \sum_i^m f_{bond}(h_b\ t) + s\ t \sum_i^m [c_0 + (h_i\ (\gamma g) + P)\tan(\varphi)]\ S_i \tag{5-27}$$

Where h_b is the height of the brick. In the Abaqus model, the slip resistance is modelled assigning a traction-separation law to the cohesive interfaces. As shown in Figure 5-35, two interfaces and are modelled, representing the slip resistance of the connection above (C_2) and below (C_1) the location at which the anchor is installed. Therefore, the lower interface

represents the first 15 courses, and has a height equal to the distance of the anchor from the base z_{D-GAS}. Its traction strength t_1 is computed as:

$$t_1 = \frac{C_1}{A_{interf}} = \frac{C_1}{z_{1-15}\, t}$$
$$= \frac{1}{z_{1-15}\, t}\left(\sum_{1}^{15} f_{bond}(h_b\, t) + s\, t \sum_{1}^{15}[c_0 + (h_i\, (\gamma g) + P)\tan(\varphi)]\, S_i\right) = \quad (5\text{-}28)$$
$$= \left(f_{bond} + \frac{s}{z_{1-15}} \sum_{1}^{15}[c_0 + (h_i\, (\gamma g) + P)\tan(\varphi)]\, S_i\right) = 0.5\ MPa$$

Similarly, the traction strength of the upper interface, which represents the top 4 courses, is:

$$t_2 = \frac{C_2}{A_{interf}} = \frac{C_2}{z_{16-19}\, t} = 0.4\ MPa \quad (5\text{-}29)$$

When the traction strength is reached, a displacement-based criterion is selected to determine the damage evolution. As the failure involves the slip of a set of courses over the interlocking length of the connection *s*, the ultimate displacement is obtained according to the results of the shear test. The strain at which the stress decreases by 80% is used to determine the ultimate slip displacement

$$\mathrm{d_u} = \varepsilon\, s = (0.01)\ (110) = 1.1\ mm \quad (5\text{-}30)$$

The results of the shear test highlight that the friction components is present even for values of strain greater than 0.01. However, the portion of wall involved in the rocking mechanism would display a vertical displacement as well as a horizontal one, which would result in the complete separation of the courses initially in contact. Therefore, the constitutive law for the shear behaviour shown in Figure 5-22b is "cut" to the value of displacement corresponding to $\mathrm{d_u}$.

The shear strength of the cohesive interface representing the bonding capacity of the anchor is computed from Eq. (5-15) considering the results of the pull-out test and the additional contribution of the vertical precompression:

$$\tau_{max} = 0.33 + 0.4\sigma_d = 0.37\ MPa \quad (5\text{-}31)$$

The material properties adopted in the model are summarized in Table 5-14.

Table 5-14 Material properties of numerical model

Material name	E [MPa]	G1 [MPa]	Density Kg/m^3	Normal direction [MPa]	Longitudinal direction [MPa]	Ultimate Displacement d_u [mm]
Masonry	1500	-	2141	CDP	CDP	CDP
Grout	2000	-	2000	ELASTIC	ELASTIC	ELASTIC
Steel	200000	-	8000	ELASTIC	ELASTIC	ELASTIC
External interface	1500	328	2141	ELASTIC	0.37	4.0
Connection interface 1-15	1500	1500	2141	0.4	ELASTIC	1.1
Connection interface 16-19	1500	1500	2141	0.5	ELASTIC	1.1

When a monotonic displacement of 40 mm is applied to the upper region of the front wall the wall starts tilting forward around a base hinge line and the displacement is numerically equilibrated by the combined contributions of the vertical interfaces in traction and of the anchor. For increasing displacements, the upper interface is the first to reach its maximum traction capacity and ultimate displacements, determining a gradual reduction of the traction force opposing the slip action. The drop in load capacity is illustrated in Figure 5-37, which plots the displacement of a node of the front wall located at $z = z_{1-15}$ against the resulting force that equilibrates the applied displacement. At 0.7 mm of horizontal displacement, the connection's strength reaches the maximum equivalent traction capacity and then progressively reduces as the vertical cohesive interfaces progressively reach their ultimate displacement capacity. For a horizontal displacement of $d_u = 1.1\ mm$ the required pulling action decreases by 18% and it is balanced by the friction force provided by the device and by the stabilizing action of the self-weight and vertical precompression of the front wall.

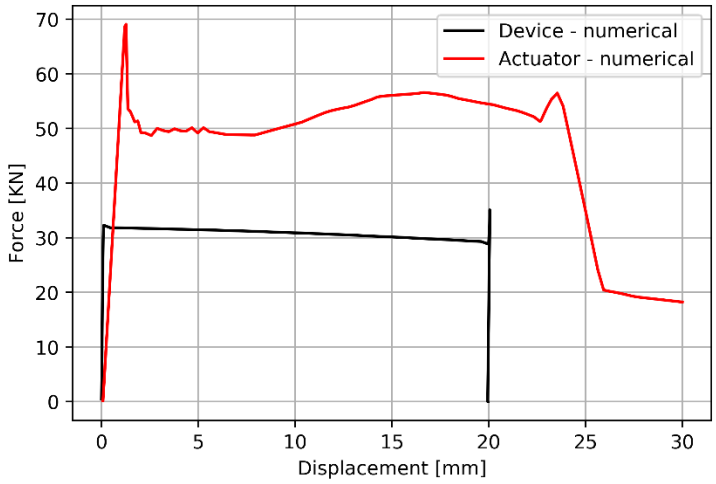

Figure 5-37 Numerical prediction of the maximum traction capacity of the T-shaped wall and of the device's load during test

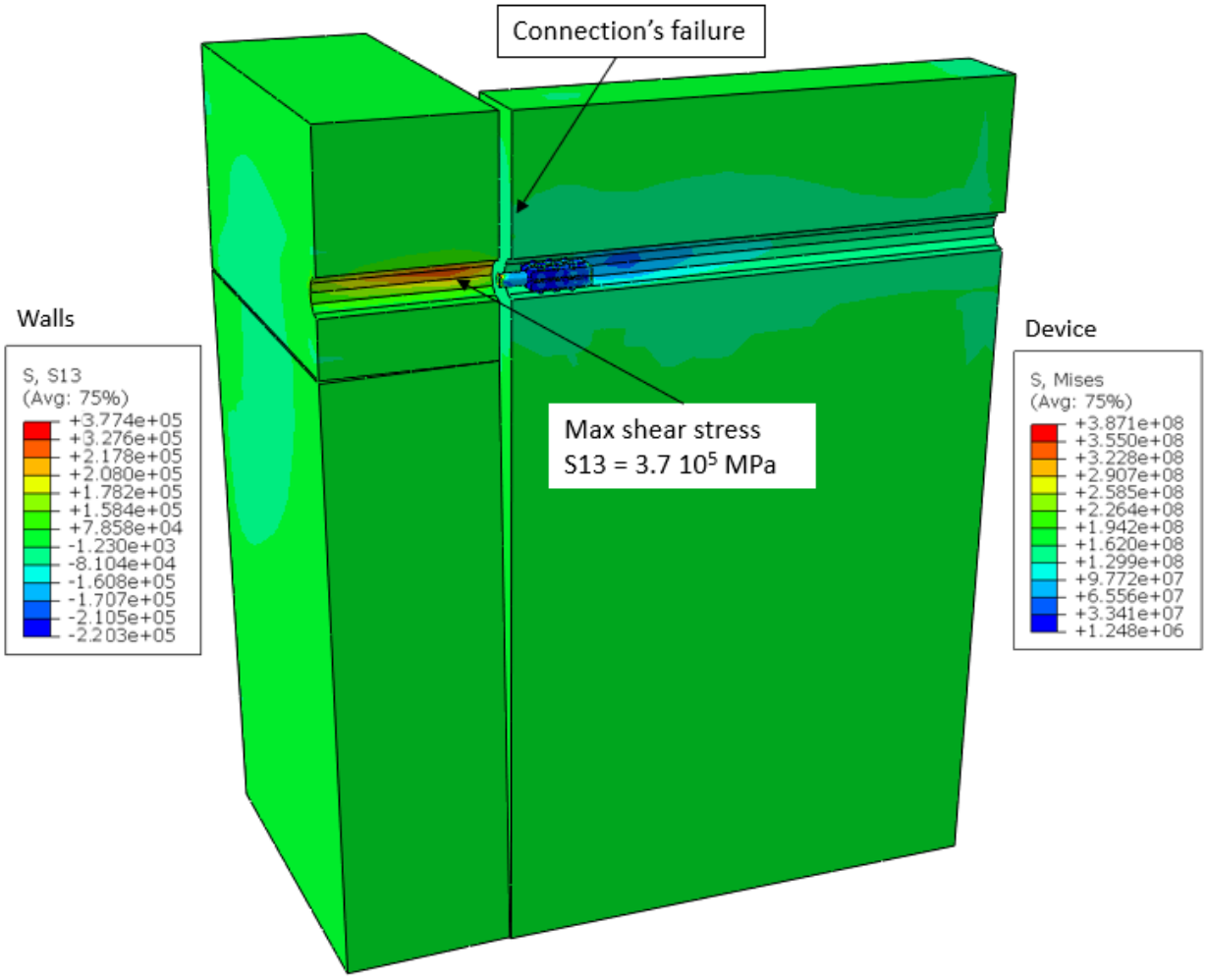

Figure 5-38 Stress distribution on the front and spine walls and on the device after traction failure of the connection

The walls' separation triggers the motion of the device, which slides under a constant slip load of 32 KN as shown in Figure 5-37. In turn, the load of the anchor induces an average shear stress of 0.37 MPa on the front interface, meaning that the front interface is at its maximum load capacity, as illustrated in Figure 5-38.

5.6 Test results

For the described test set-up, failure is expected to occur initially by vertical and sub diagonal in-plane cracking of the spine wall, and eventually by failure of the head of the anchorage according to one of the failure modes described in the previous sections.

For the first 6 groups of cycles, the assembly displayed a linear behaviour: as illustrated in Figure 5-39a, the load increases linearly with the imposed displacement showing no significant stiffness reduction between groups of cycles.

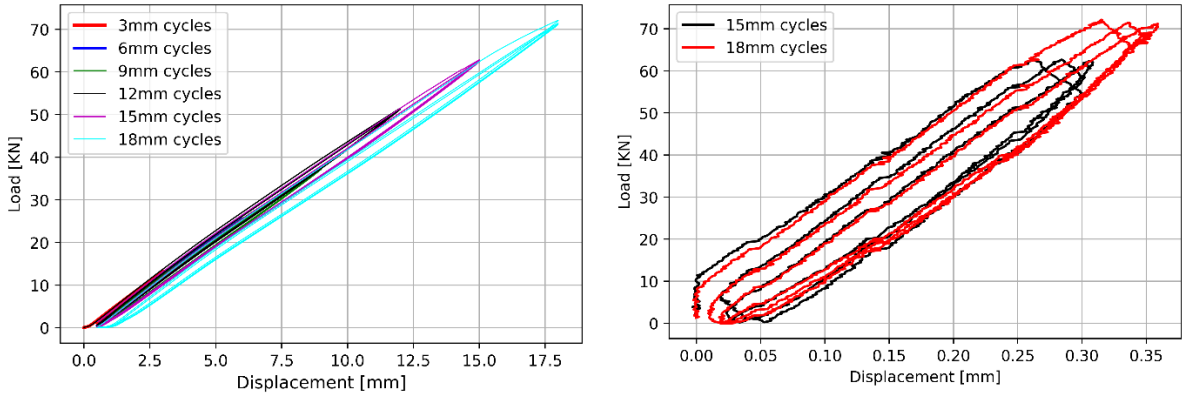

Figure 5-39 Load-drift curve for first 6 groups of cycles

However, the relative displacement captured by the video gauge system between the front and spine wall is substantially smaller with a maximum amplitude of 0.35 mm between the tracking points 1-6, as shown in Figure 5-39b. This highlights that most of the displacement occurs as elastic deformation of the front hinge assembly connecting the wall to the actuator (see Figure 5-28). At the 7th group of cycles, a vertical crack opened at the joint between the two walls following the weak pattern provided during the preparation of specimens by leaving the bricks at the joint with a smaller overlapping. The sudden failure is identified by the drop in load capacity, which reduces from 72 KN to 46 KN and the separation of the two panels equal to 9.6 mm, as shown in Figure 5-40. The activation of the device can be inferred by the presence of the horizontal load plateau and by the constant value of maximum load reached in each subsequent cycle. As the device is active, 10 cycles are imposed at a displacement amplitude of 21 mm to determine if the cyclic behaviour is detrimental to the masonry substrate, causing for instance the bond failure of the grouted portion of the anchor. The hysteresis cycles shown in Figure 5-40 reveal a stable behaviour with an average value of maximum slippage load of 42 KN.

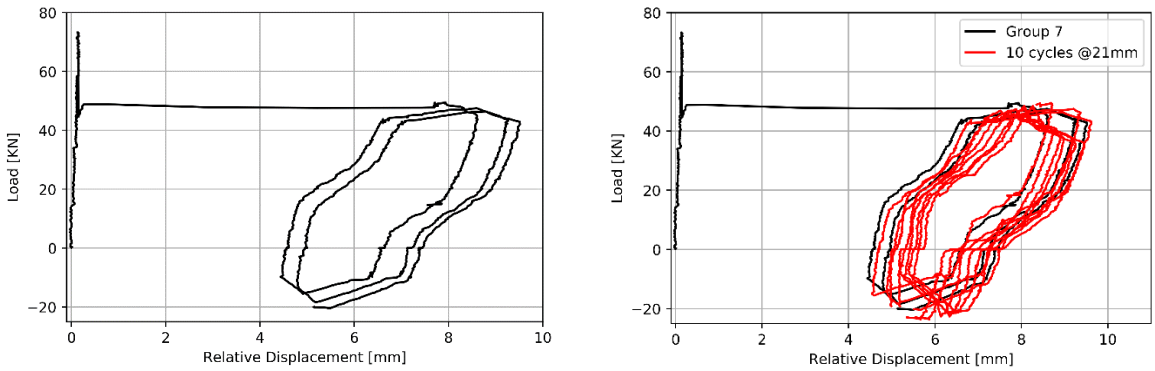

Figure 5-40 Hysteresis cycles of device after walls' separation a) 3 cycles at 21 mm of amplitude, b) 10 further cycles at 21mm of amplitude

Figure 5-41 Horizontal hinge line and crack propagation on front and spine panels.

The T-shaped wall displays rigid rotation of the front wall around a horizontal hinge line at a height of 1m from the base of the wall and a progressive development of diagonal cracks in the spine wall, as shown in Figure 5-41. Comparing the images recorded by the DIC system before and after cracking, it is possible to identify the extent and magnitude of the rocking motion. As shown in Figure 5-42, the upper portion of the specimen displays a 5mm of vertical displacement (Y-direction) and 6 mm of horizontal displacement (X-direction), and the

cracking line on the side surface of the specimen is well captured by the x and y displacements.

a) Before cracking

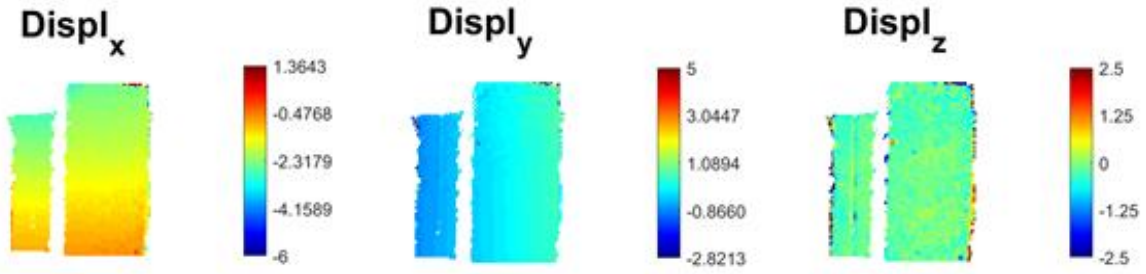

b) After cracking

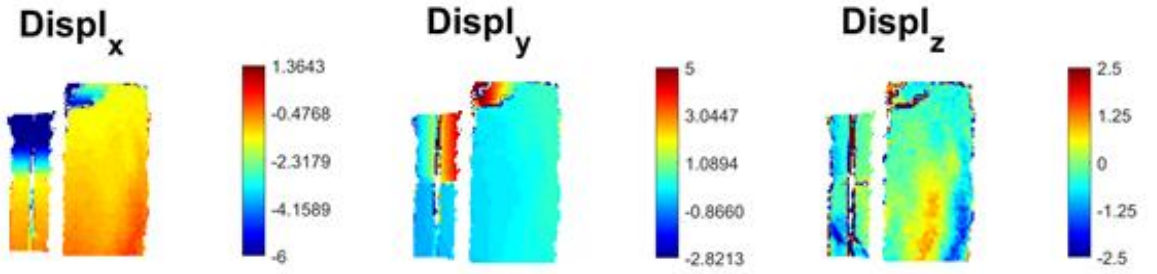

Figure 5-42 DIC test results for Group 7 (21 mm of imposed displacement)

A monotonic displacement is then applied to induce the bonding failure of the Dissipative anchoring system. To this purpose the load is increased at 8mm/min to achieve a walls' separation equal to the maximum displacement capacity of the device (20mm). As shown in Figure 5-43a, the load reaches a plateau for a load of 41 KN and then drops to 10KN at 22 mm due to debonding of the front portion of the anchor. Figure 5-43b shows the load evolution over time: in the dotted box, the drop in load for a relative displacement of 22mm is illustrated.

The anchor is still able to produce a restraining force after failure possibly due to friction between the grout and the masonry substrate, but the load and displacement capacity become less regular and stable. This is clearly shown by the three load cycles imposed at 55mm which cause a progressive separation of 30, 33 and 41 mm for a peak load per cycle of 44, 43 and 38 KN, and for which significant changes in stiffness are detected.

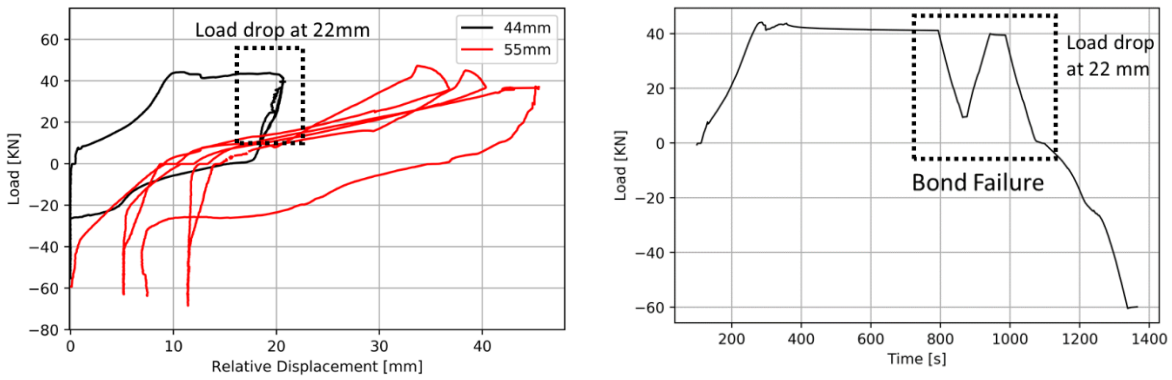

Figure 5-43 a) Load-displacement cycles of D-GAS for imposed displacement of 44 and 55 mm b) Load-time plot of cycle at 22 mm of relative displacement

It can be concluded that the dissipative system succeeds in providing a controlled displacement capacity that improves the response under cyclic loading. The activation of the friction device allows preventing the failure mode observed in the pull-out tests of the GAS, namely the shear debonding of the front anchor, until later stages of tests when the device reaches its maximum slippage capacity.

The crack width of the specimen greatly intensifies for larger imposed displacements (see Figure 5-39), allowing a visual inspection of the device. This confirms that the location of the device along the anchor's longitudinal axis is well designed as the vertical crack develops in correspondence of the slider position. With reference to Figure 5-44, a visual proof of the device's activation is the displaced position of the BraCyl's brass sleeve which was fully inserted (see Figure 5-29) into the device before installing the D-GAS in the wall specimen.

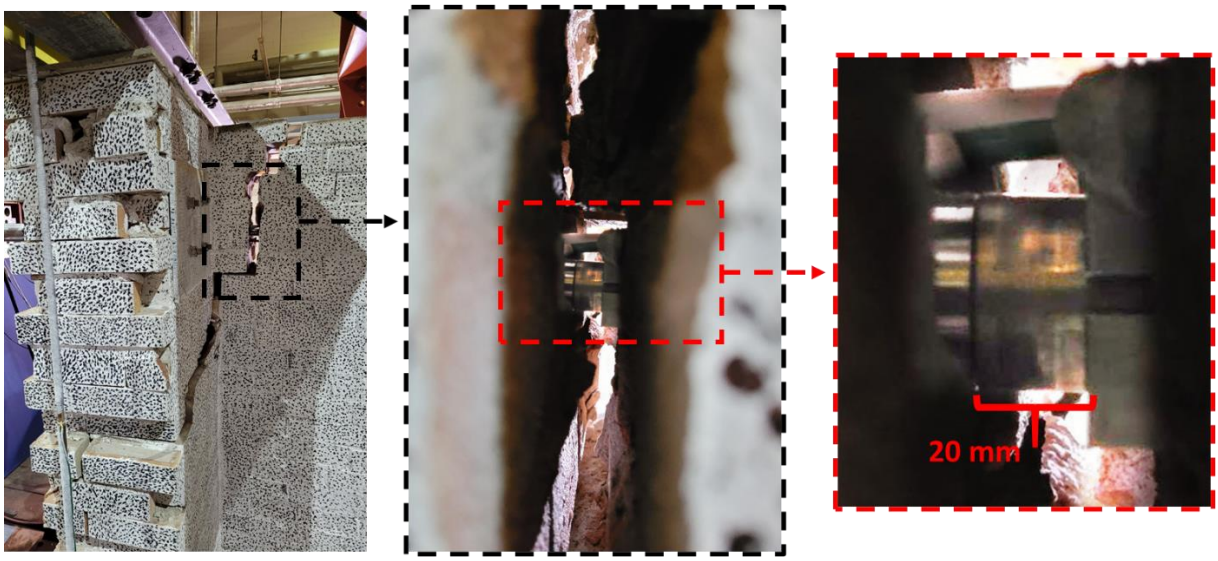

Figure 5-44 Visual inspection of device through the separation crack.

The strain recorded on the bars connected to the device are shown in Figure 5-45 (load groups 1-6) and Figure 5-46 (load group 7). From the comparison, it is clear that the contribution of the anchoring system becomes relevant when the specimen cracks, with strain increasing from 60 to 2500 $\mu\varepsilon$ when the traction capacity of the connection is compromised.

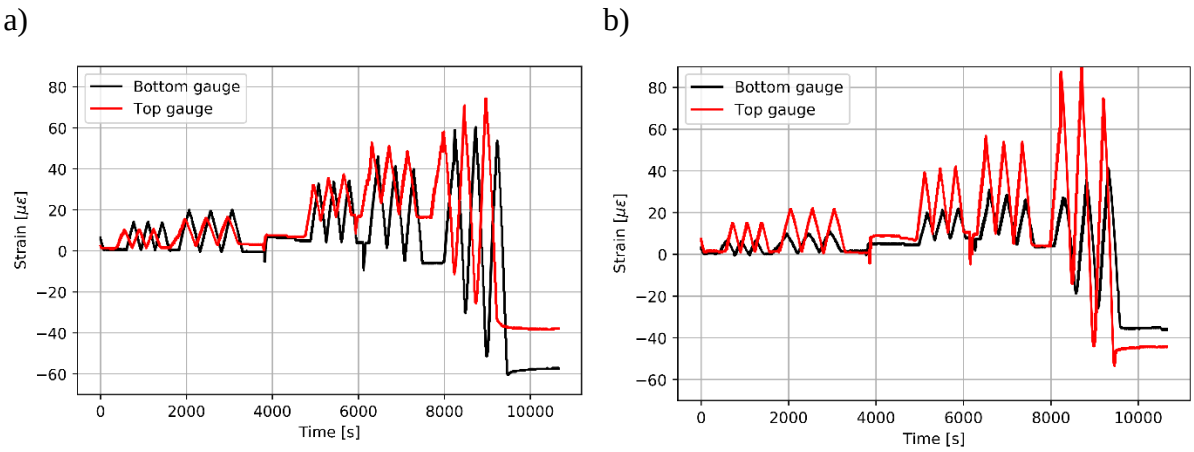

Figure 5-45 Strain recorded for the group cycles 1-6 on the a) front grouted bar, b) back grouted bar

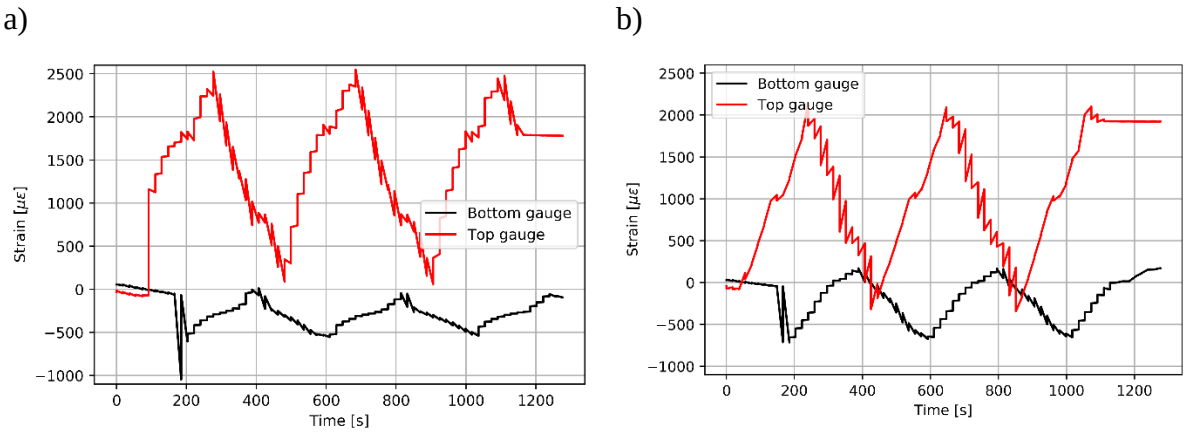

Figure 5-46 Strain recorded for the group cycle 7 on the a) front grouted bar, b) back grouted bar,

The couple of gauges are installed on the upper and lower part of the bar as shown in Figure 5-47 recording strain readings which differ in magnitude and sign. Thus, it can be deduced that the rocking motion induces a bending moment in the anchor.

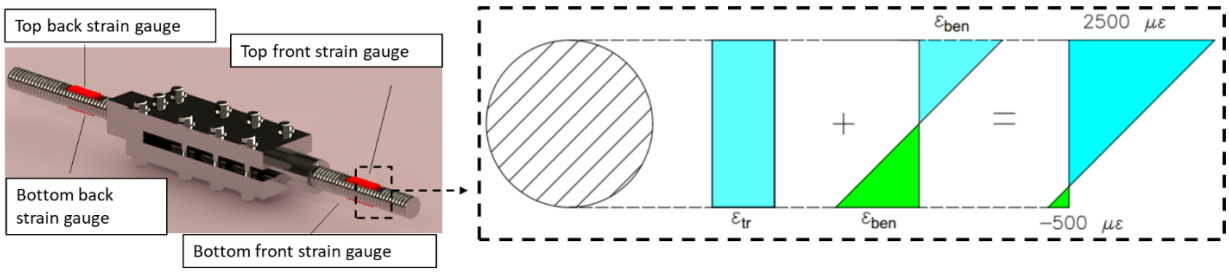

Figure 5-47 Location of strain gauges and strain distribution on instrumented section

Assuming the anchor's section under the combining effect of axial traction and bending stress, the resulting strain acting on the instrumented section is:

$$\begin{aligned} \varepsilon_{tr} - \varepsilon_{ben} &= -500\ \mu\varepsilon \\ \varepsilon_{tr} + \varepsilon_{ben} &= 2500\ \mu\varepsilon \end{aligned} \tag{5-32}$$

Which means that the traction strain ε_{tr} is:

$$\varepsilon_{tr} = 1000\ \mu\varepsilon \tag{5-33}$$

Which correspond to a traction force of:

$$F = \varepsilon_{tr} EA = 0.001\ 220000\ 154 = 33.8\ KN \tag{5-34}$$

This value of traction force is the maximum traction force experienced by the anchor during the experimental activity. As it well agrees with the design slip load of the device ($V_D = 32.4\ KN$), it can be concluded that the variation between the measured activation load of the device and the design one is equal to 4%.

The fact that the maximum load applied by the actuator during the rocking motion is larger than the restraining action provided by the anchoring system is explained considering the additional load required to overcome the stabilizing action provided by the uprights F_V and the self-weight W of the wall. Considering the position of the hinge line, the equilibrium equation for the rigid-body rotation of the detached front wall is:

$$V_D h + (F_V + W)\frac{t}{2} - F_a h = 0 \tag{5-35}$$

where F_a is the actuator force and h is the vertical distance between the actuator and the hinge line passing through *O*, as shown in Figure 5-48a. Solving Eq. (5-35), the force F_a required to initiate the rocking motion is 45.3 KN, which correspond well to the load applied by the actuator.

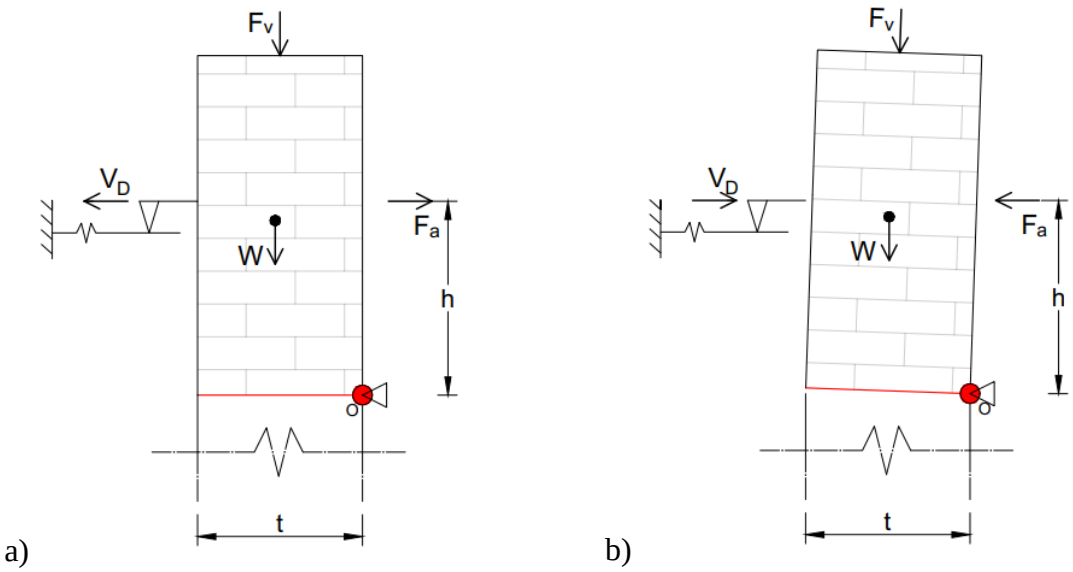

Figure 5-48 Rotation of upper block around hinge line a) outward direction, b) inward direction

Conversely, when F_a reverses to push the wall back to its vertical position, while the vertical applied forces work in favour of the actuator, the device produces an overturning moment, as the friction force is always opposed to the direction of motion. With reference to Figure 5-48, the force required by the actuator is:

$$F_a = \frac{\left(V_D h - (F_V + W)\frac{t}{2}\right)}{h} = 22.2\ KN \tag{5-36}$$

which is in good agreement with the maximum compression force applied by the actuator in the cycles in figure 5-40. The tests results are summarised in Table 5-15 and Table 5-16

Table 5-15 Summary of test results: device values

Device	Applied torque [Nm]	$F_{PC(N)}$ [KN]	Number of bolts	Perpendicular Force $F_{perp(N)}$ [KN]	Slippage force $F_{slip(M)}$ [KN]	Friction coefficient μ_D	Device's design force V_D	Variation ΔV_D[%]
BraCyl	15	6.76	6	40.56	33.8	0.20	32.448	4%

Table 5-16 Summary of test results: design values

Max elastic force [KN]	Max elastic relative disp [mm]	Max rocking load [KN]	Min rocking load [KN]	Height of hinge line *h* [mm]	Prediction of load to rock after crack [KN]	Prediction of load to restore vertical position [KN]
72	0.35	45	-20	800	45.3	22.2

A good comparison between the numerical prediction and the experimental values is achieved, especially for the load causing the wall's separation and the load during the relative motion of the walls. This proves that the numerical model presented in this chapter is able to capture the

overall performance of the strengthened connection and that the cohesive interfaces are a suitable to reproduce the load hierarchy of the strengthened connection.

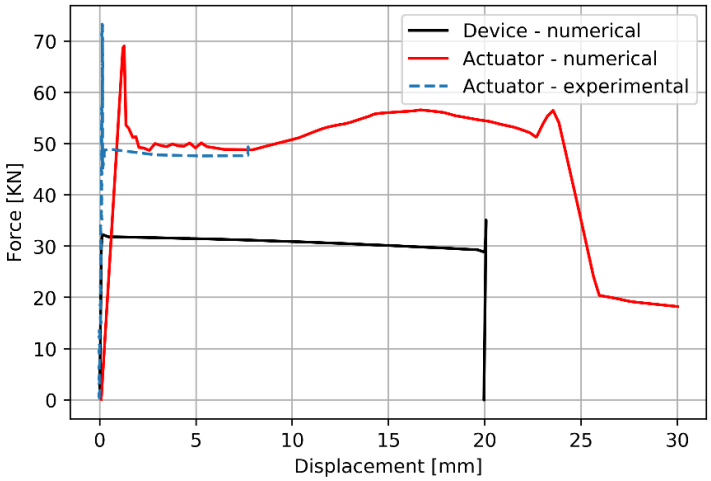

Figure 5-49 Load-displacement capacity of strengthened connection: comparison between experimental results and numerical prediction

For larger displacements, Figure 5-49 shows that the numerical model overestimates the pulling action because the observed portion of wall participating to the mechanism is smaller compared to the one assumed in the model, hence a smaller pulling force is required.

This difference is illustrated in Figure 5-50 which compares the experimental crack propagation with the walls' separation obtained by the numerical model.

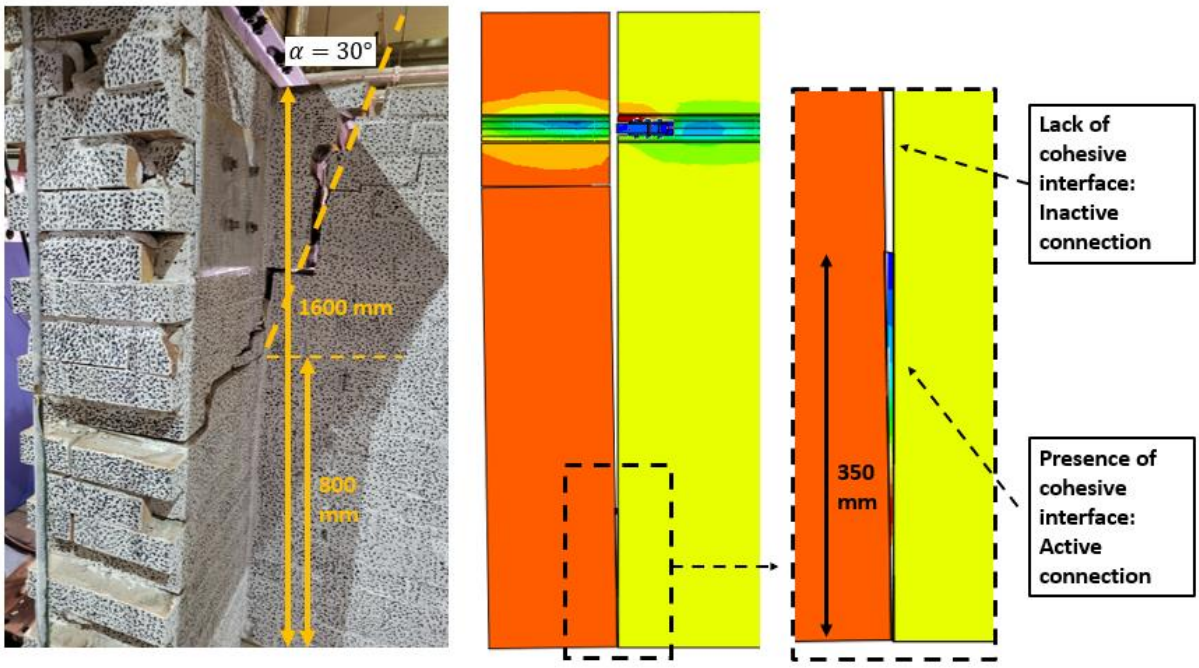

Figure 5-50 Wall's separation: comparison between experimental and numerical

For the laboratory specimen, the vertical crack starts at a height of 800 mm from the base and propagates horizontally through the front wall and at a 30° angle through the spine wall. Accordingly, a future Abaqus model could feature a new set of horizontal and diagonal interfaces to better approximate the experimental crack pattern.

5.7 Conclusions

Chapter 5 deals with the experimental assessment of the Dissipative Grouted Anchoring System (D-GAS) which combines the new generation of friction-based dissipative devices presented in Chapter 4 and the grouted anchors developed by Cintec International.

The aim of the reported experimental work is twofold: to assess the performance of the D-GAS as connected to a masonry substrate and to outline an experimental procedure that can be used as guidance for the assessment and design of connection strengthening system. As previously commented, current prescription regarding the experimental procedures for the assessment of structural connection, do not cover in detail the issues typical of heritage buildings.

The performance of the strengthened connection is a combination of the performance of the dissipative device, of its interaction with the substrate and of the response of the structural elements to which they are applied. Therefore, the experimental procedure is split into two phases, following a procedure which is the logical reflection of an increasing level of complexity: the anchoring system is first coupled to a single masonry panel to investigate the effect of the device on the substrate, then it is installed in a masonry connection to verify its activation and performance under cyclic loading.

The devices employed for the testing are the SteCyl and the BraCyl prototypes described in Chapter 4, which features a cylindrical steel-on-steel and brass-on-steel contact interface respectively. For the first testing activity, Cintec International provided the installation of four steel bar grouted within the thickness of the masonry panel by means of a special fabric socket able to expand within the cavities of the wall when the grouted in injected. The required borehole diameters are about 76mm and the embedment length is 340 mm enough to realise a sufficient bond between elements in contact. The free end of the anchor is connected to the SteCyl device which is monotonically loaded by means of a hydraulic jack to induce a pulling action. The pull-out tests aim to identify a set of parameters that, together with those already identified in respect to the isolated devices, can define the performance of the system device-

anchor-substratum. Furthermore, pull-out tests allow a first comparison between standard and dissipative anchors, thus justifying the use of the devices in light of the benefits they have in respect to their strength-only counterpart. The tests successfully prove that the devices can address some of the drawbacks that are identified for standard anchors, such as the identification of damage in the substratum, even for small relative displacement between the grouted anchor and the masonry. Compared to the results obtained testing the pull-out capacity and failure modes of GAS, the frictional device homogenises the response of anchors, considerably reducing, or eliminating damage to the parent material. It allows for controlling the activation load that initiates its sliding motion to the point that almost no relative displacement is detected in the other elements of the anchor assembly.

The test results are also used to enrich a database that collects the main parameters describing the performance of grouted anchors and verify a set of empirical formulations proposed in this work to predict the maximum pull-out load and ductility capacity for this anchor typology.

The set-up of the second testing activity reproduces a corner connection between two masonry walls, strengthened with a dissipative anchoring system. This testing activity allowed supplementing the information obtained by pull-outs through the simulation of a more complex scenario - full structural connection rather than only one wall panel - and a different loading input - cyclic action instead of monotonic pull. The results highlight that the D-GAS can provide stable load-displacement loops which are representative of a reliable energy dissipation capacity. This test represent a crucial step towards the validation of the D-GAS, as it allows validating a set of assumptions at the base of the dissipative system's performance. Under cyclic loading, the connection displayed a pseudo-vertical connection which triggered the device's activation without causing the debonding of the anchor. This proves that the hierarchy of capacity designed according to the empirical formulations proposed in this work allows the front wall of a connection fitted with a D-GAS to develop a controlled rocking motion.

The experimental results feed in the calibration of a computational model, which reproduces the experimental set up in order to understand better the rules that governs the behaviour of the dissipative anchoring system. Drawing on the model developed for the isolated device presented in the previous chapter, a model of the single panel and of the T-shaped connection is developed. The Finite Element model described in the paragraphs above succeeds in replicating the observed failures by means of a set of cohesive elements calibrated on the experimental evidence. A sound correspondence between experimental and numerical results builds confidence in using a numerical software to predict the behaviour of D-GAS for

circumstances which are difficult to reproduce in a testing environment, such as extreme loading conditions or applications of the system to large-scale structures. In fact, the results of the experimental and numerical analysis presented in this section will be extended in the next chapter to model the implementation of the D-GAS to a historical masonry building. This activity will demonstrate the effectiveness of the D-GAS as installed in real case structures subjected several loading conditions, such as seismic-like base accelerations.

6 Design procedure for the implementation of grouted anchoring systems.

6.1 Introduction

As discussed in Chapters 1 and 2, current codes give very little guidance in terms of design procedures for strengthening systems of historic structures in earthquake prone areas. To keep to the European example, both EC8 (EN 1998-3:2005) and the Italian guidelines (DPCM, 2011) recommend techniques suitable for heritage structures, and describe the steps needed to assess the initial conditions of the structures, such as the on-site mechanical characterisation of the construction materials. The Italian code (DPCM; 2011) also gives instructions as far as computational modelling goes. On-site investigations and numerical simulations enable the comparison between the current behaviour of the structure and the enhanced response achievable by strengthening. Thus, the need for a structural upgrade is determined and its extent minimised, still ensuring a sufficient level of safety. Nonetheless, the codes remain vague when it comes to the design of the strengthening elements to the purpose of optimising the intervention.

For traditional, strength-based systems, the practicing engineer should possess sufficient knowledge to carry out a preliminary design according to a Force-Based (FB) approach and then assess the improvement of the overall structural response according to the code instructions. For instance, if traditional anchor ties are implemented, these can be designed simply considering the ultimate overturning equilibrium of the macro element modelled as rigid blocks, given the peak ground acceleration, corresponding to a specific site and return period for the life safety performance level. In the equilibrium equation, the contribution of the anchoring system to the stability of the wall under lateral load is proportional to the maximum load capacity obtained from pull-out tests, via safety factors. Using this simple method, the number, and dimensions of anchors per metre height of the wall, needed to prevent the wall from overturning due to the seismic action, can be determined.

Nonetheless, this approach presents several shortcomings. The use of the peak ground acceleration to derive the seismic demand comes from the assumption that unreinforced

masonry (URM) possesses very limited ductility, so that the strengthened system is designed to maintain the structure in its elastic range, assuming that any lateral deformation is transient, considering this the only safe configuration (Sorrentino et al. 2017). Therefore, the peak ground acceleration, namely the acceleration corresponding to infinitely stiff foundation solidly connected to a perfectly rigid upper structure, is considered the governing parameter to compute the seismic demand and the anchors are dimensioned to remain in their elastic phase for the expected seismic acceleration. For acceleration demands corresponding to high magnitude earthquakes, this may lead to over-dimensioned ties and anchoring plates, and unfeasible designs, especially for historic buildings where minimum intervention criteria may limit the number and sizing of the intervention (Paganoni and D'Ayala 2014).

As introduced in the literature review (Chapter 2), seismically excited unreinforced masonry walls can display Out-Of-Plane (OOP) rocking motion without overturning, and the seismic vulnerability of the macroelements can be evaluated also according to Displacement-Based (DB) design methods. These methods allow to adequately reduce the seismic demand according to the ductility capacity that the whole structural system can provide. Therefore, strengthening interventions that increase the ductility capacity of the structure present a reduced levels of intrusiveness if designed according to a DB method compared to a FB approach, as they further reduce the seismic demand.

For the case of Grouted Anchoring Systems (GAS), their design as an aseismic strengthening system based on a performance-based approach is hampered by the evidence from pull-out tests showing that ductility provided by grouted anchors is frequently limited and highly unpredictable (Paganoni and D'Ayala 2014; Silveri et al. 2016; Ceroni and Di Ludovico 2020). Although experimental pull-out tests do not fully represent the performance of anchors installed in a building, grouted anchors are currently designed to work in the elastic range and their ductility is considered as an additional capacity that the wall can potentially develop during the seismic event (Moreira et al. 2014).

The use of the friction-based dissipative device presented in this thesis can improve the performance of grouted anchors. As experimental, and computational results discussed in the previous chapters have shown, the dissipative devices successfully improve the behaviour of standard grouted metallic anchors by providing a source of quantifiable and stable ductility to the strengthening system, thus limiting, or even fully preventing, damage in the substratum.

This stable behaviour under cyclic loading, the displacement capacity and rocking behaviour that monumental structures often exhibit during earthquakes (Giuriani and Marini 2008) can be combined to propose a DB methods to design the seismic strengthening of a historic structure by means of grouted anchoring systems.

In this chapter a DB capacity approach (Melatti and D'Ayala 2021) is proposed, applying the N2 method proposed in the Eurocode 8 (EN 1998-1:2004 2004) to derive the seismic vulnerability of walls to OOP failure. The design approach is presented in Section 6.2 for walls in three configurations, namely unstrengthened, strengthened by GAS and strengthened by D-GAS. In section 6.3 such design procedure is validated by non-linear time-history analysis (NLTHA), whereby the response is obtained through numerical integration, using code-defined accelerograms to represent the ground motions (EN 1998-1:2004 2004).

For this task two approaches are proposed: the first assumes the wall as a rigid body and solves its equation of motion by direct numerical integration. To this purpose a program is coded by the author using the Python programming language (Python Software Foundation). The second consists in a NLTHA performed in Abaqus, using the modelling techniques presented in the previous chapters. This method presents a higher level of model detailing compared to the first approach but a greater computational cost.

In Section 6.4, the design method is applied to a case-study structure, namely the Oratory of San Giuseppe dei Minimi, a church that suffered severe, but repairable out-of-plane triggered damage, during the 2009 seismic events in L'Aquila (Italy). The strengthening solutions adopted to improve the seismic performance of the building are validated by NLTHA in section 6.5 to obtain the optimal design solution.

6.2 Displacement-based structural assessment of walls vulnerable to out-of-plane failure

The design procedure presented in this Chapter allows identifying the vulnerability of a masonry building to OOP failure and designing the best anchoring solution to improve the seismic performance of the structure. The design procedure is explained with reference to grouted anchoring systems, which are widely used to strengthened historic structures, minimize the aesthetic impact on the structure, and facilitate the intervention on façade walls requiring

access from only one side of the wall. Nonetheless the design procedure has the potential to be easily expanded to other anchoring systems as it will be discussed in the Chapter 7.

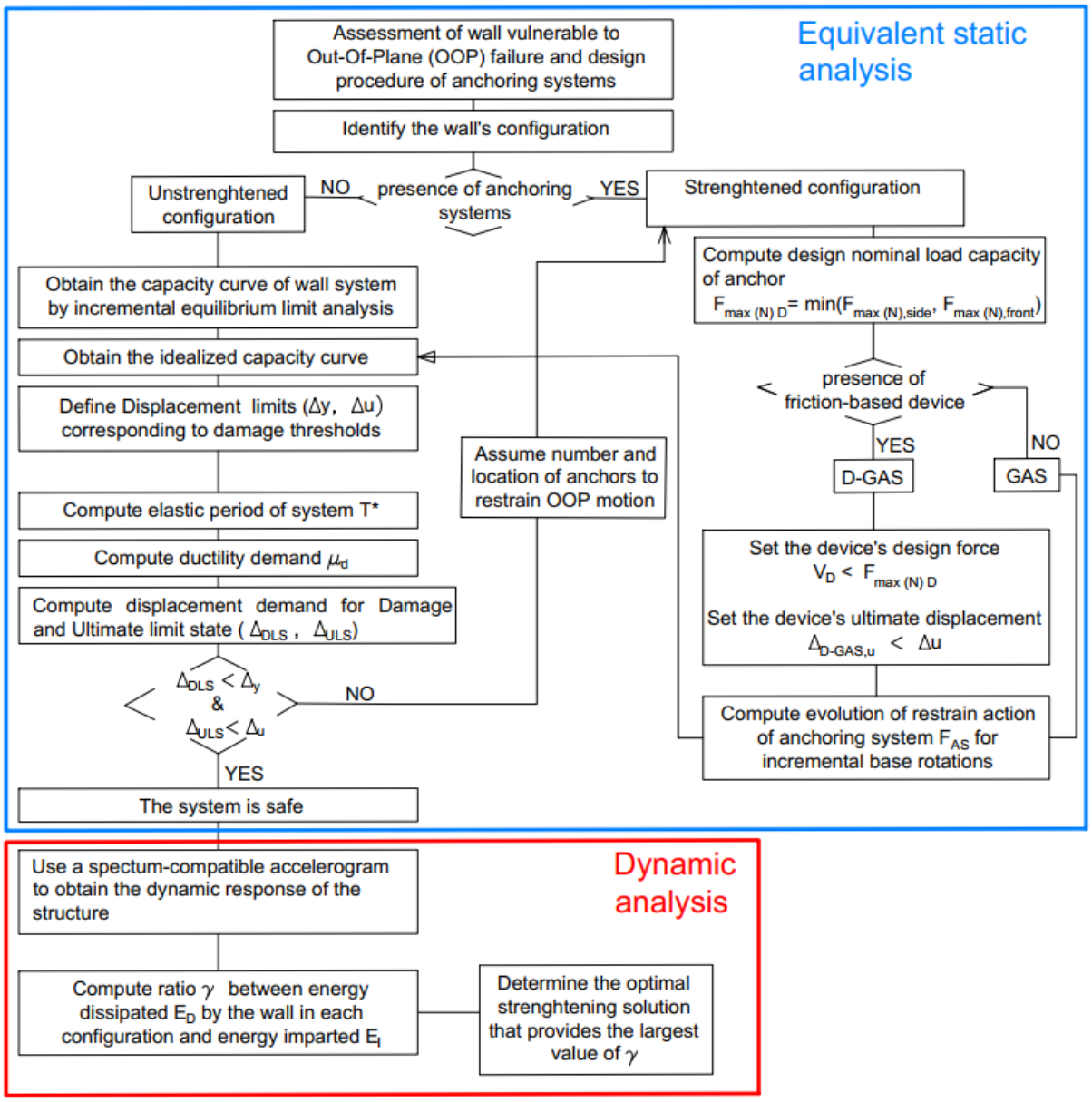

Figure 6-1 Horizontal Flowchart of the assessment and design procedure of seismic strengthening by anchoring systems

The flowchart presented in Figure 6-1 represents schematically the assessment and design procedure adopted, which consists of two steps: in the first one, the performance associated to the out-of-plane (OOP) failure mode is assessed for the wall in its original (unstrengthened) configuration. To achieve this, in section 6.2.1 an equivalent static assessment of the wall's capacity is performed comparing the displacement demands obtained through inelastic spectra to a set of threshold displacements corresponding to the progression from linear to nonlinear behaviour of the system. If the demand exceeds the system's capacity, the GAS and D-GAS are

proposed as strengthening system to prevent the OOP failure in section 6.2.2 and 6.2.3. The contribution of the anchors is included in the model by an idealised non-linear constitutive law obtained from the load-strain curves presented Section 5.2.3 of Chapter 5. The presence of the dissipative device is included by limiting the tensile capacity of the anchor to the sliding threshold of the device and by increasing the ultimate displacement capacity to account for the full capacity of the slider.

6.2.1 Static out-of-plane assessment of unstrengthened wall

Several procedures are available in literature to derive capacity curves for masonry structures. In the macro-element approach, the entire building is subdivided in a number of blocks which are identified by assuming a predefined crack pattern. D'Ayala (2005) identified a set of 12 possible modes of failure and used a kinematic approach to identify the collapse load multiplier (λ) that determines each collapse. The values λ are computed considering the geometry and materials of the selected building as obtained from site inspections and laboratory tests. The lowest value of λ identifies the mechanism that is more likely to happen for the selected building. Having converted the parameters of the selected mechanisms to those corresponding to an equivalent nonlinear SDOF system, the capacity curve of the idealized system can be obtained (D'Ayala 2013) (D'Ayala 2013).

In this work the load-displacement capacity of walls prone to one-sided rocking motion is computed considering an equilibrium limit analysis, following the procedure initially proposed by (Lagomarsino 2015). This approach allows to compute the ductility capacity of the system, and thereby to obtain a capacity curve which is then used to determine the performance points by intersection with inelastic demand spectra following the N2 approach (Fajfar 2000) as recommended by the Eurocode 8 (EN 1998-1:2004 2004).

The non-linear model shown in Figure 6-2 can be developed to determine the capacity of the system: the front wall (façade) is modelled as a single-degree-of-freedom (SDOF) block which can rotate on one side only and is subjected to dead loads and to horizontal seismic action.

It is assumed that the wall can only rotate around a base hinge line, excluding intermediate locations of the hinge line. This assumption is identified as the most penalizing one in terms of wall's stability as, for equal rotations, the case of base hinge line leads to larger top displacements and maximum mass participating to the rocking mechanism. As the D-GAS can provide a limited controlled displacement, it is crucial to verify that the displacement demand is within the device's capacity for the case that leads to the largest top displacement for equal

base rotations. However, intermediate location of the hinge line can be verified in case the geometry, the opening layout or the presence of additional constrains suggests that another hinge line might develop. In these cases, the position of the hinge line can be predicted by using the equations provided by Sorrentino et al. (2008). The equilibrium equation can be written as:

$$mg\,\mathrm{R_G}\sin(\beta_G - \theta) - mg\,u_\theta(\theta) = \lambda_\theta\, mgR_G\cos(\beta_G - \theta) \qquad (6\text{-}2)$$

where R_G is the distance between the centroid *G* and the geometrical corner *O*, g is the gravity acceleration, m is the mass of the wall per unit of length, θ is the wall angular displacement, and β is the *arctan (B/H)*.

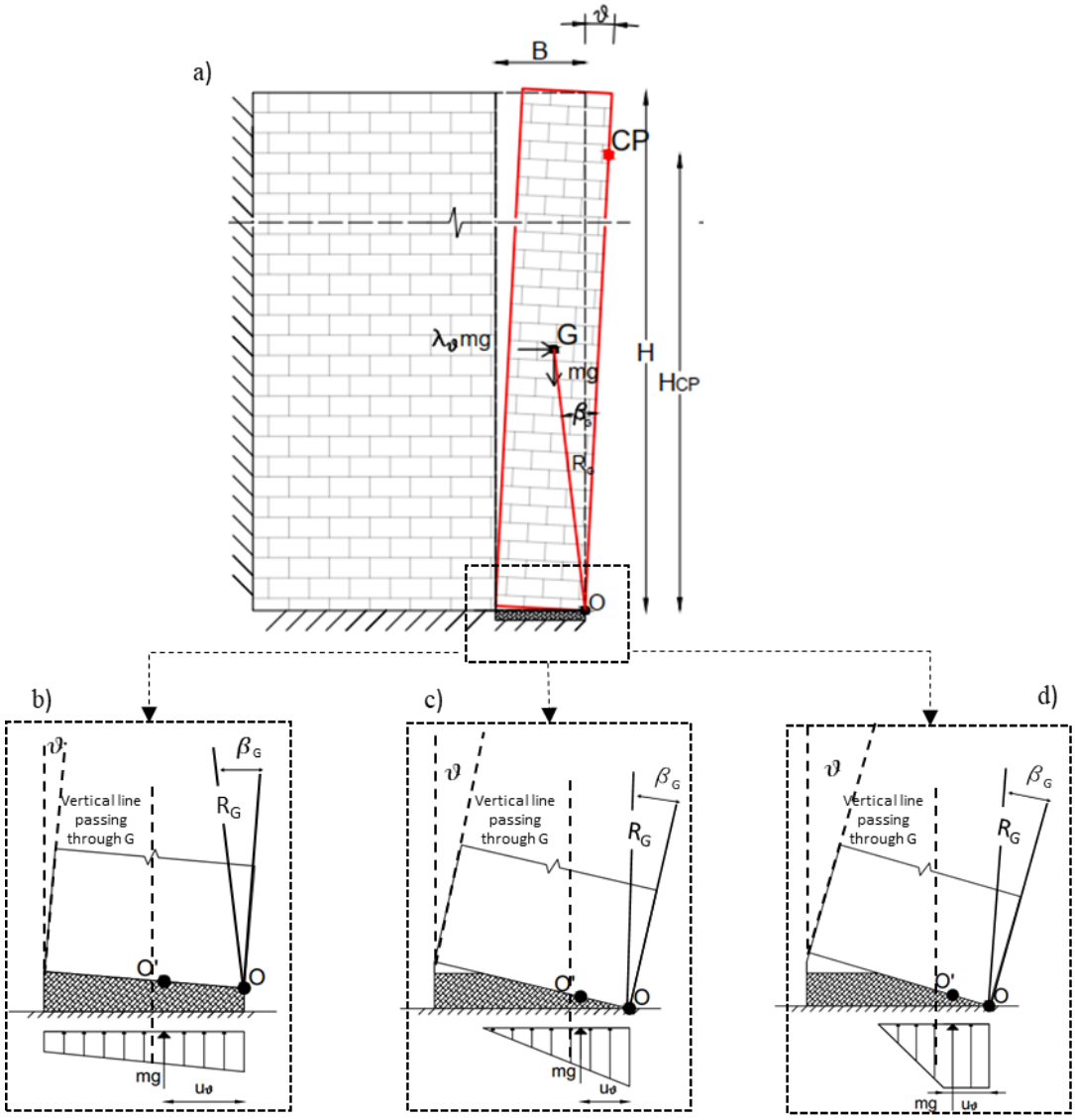

Figure 6-2 One-sided displaced configuration of unstrengthened wall a) resting on a deformable interface of finite strength: evolution over rotation θ of interface stress distributions for (b) full contact, (c) partial contact and (d) toe-crushing (Figure adapted from (Costa et al. 2013))

To account for the finite stiffness of the foundation and of the block simulating the masonry wall, a flexible interface can be modelled at the base of the block, as proposed by (Costa et al. 2013; Mehrotra and DeJong 2018; AlShawa et al. 2019). Such interface has normal stiffness $k_n = E/e$ (E = Young's modulus, e = thickness of the interface), width B equal to the thickness of the wall. The finite compressive strength f'_m of the materials in contact is accounted for by considering the stress block of Figure 6-2d.

The Eq. (6-2) considers equilibrium of moments around the instantaneous centre of rotation of the body O', which corresponds to the intersection of the base line of the block with the line of action of the stress block resultant at the base. As shown in Figure 6-2, Point O' migrates from perfect alignment with the vertical line passing through the centroid G for $\theta = 0$, towards the geometrical edge O as θ increases and the portion of the section in contact decreases. The inward shift of the rotation point determines a reduction of the stabilizing moment provided by the self-weight, as the lever arm reduces to the horizontal distance between the vertical lines passing through G and O', respectively. In Eq. (6-2) this reduction is accounted by the term $mg\, u_\theta(\theta)$, where $u_\theta(\theta)$ represents the distance between O' and O. Following Costa's approach (Costa et al. 2013) and with reference to Figure 6-2 the position of the reaction force assumes different expressions as a function of the increasing value of the rotation θ:

$$u_\theta(\theta) = \begin{cases} \dfrac{B}{2} - \dfrac{B^3 k_n \theta}{12\, mg} & 0 < \theta \le \theta_{PC} \\ \dfrac{1}{3}\sqrt{\dfrac{2mg}{B^3 k_n \theta}} & \theta_{PC} < \theta \le \theta_{TC} \\ \dfrac{1}{2}\left(\dfrac{mg}{f_m} + \dfrac{f_m^3}{12\, mg k_n^2 \theta^2}\right) & \theta \ge \theta_{TC} \end{cases} \tag{6-3}$$

Full contact is assumed for cases in which the rotation is less than the rotation θ_{PC} corresponding to partial contact of the base and given by Eq. (6-4):

$$\theta_{PC} = \frac{2mg}{B^2 k_n} \tag{6-4}$$

Beyond this point, horizontal cracks form on the left-hand side and only part of the cross section is in compression. Eq. (6-5) provides the rotation at which the toe-crushing failure occurs, namely the compressive stress is equal to the compressive strength of the masonry f_m and vertical cracking occurs at the base on the right-hand side:

$$\theta_{TC} = \frac{f_m^2}{2k_n mg} \tag{6-5}$$

Solving Eq. (6-2) for incremental values of θ returns the capacity curve of the unstrengthened system shown in Figure 6-3 a, where the values of acceleration multiplier and horizontal displacement are normalized with respect to those of a wall resting on a rigid interface. The horizontal displacement refers to a Control Point (CP) arbitrarily identified at height H_{CP} and are computed as:

$$\Delta = H_{CP} \tan\theta \tag{6-6}$$

The initial part of the curve is shown in detail in Figure 6-3 b to illustrate the stiffness reduction of the wall for relative displacements of CP greater than the one causing partial contact of the base Δ_{PC}, and the decrement in capacity for Δ greater than the displacement at the toe-crushing failure at the wall's base Δ_{TC}.

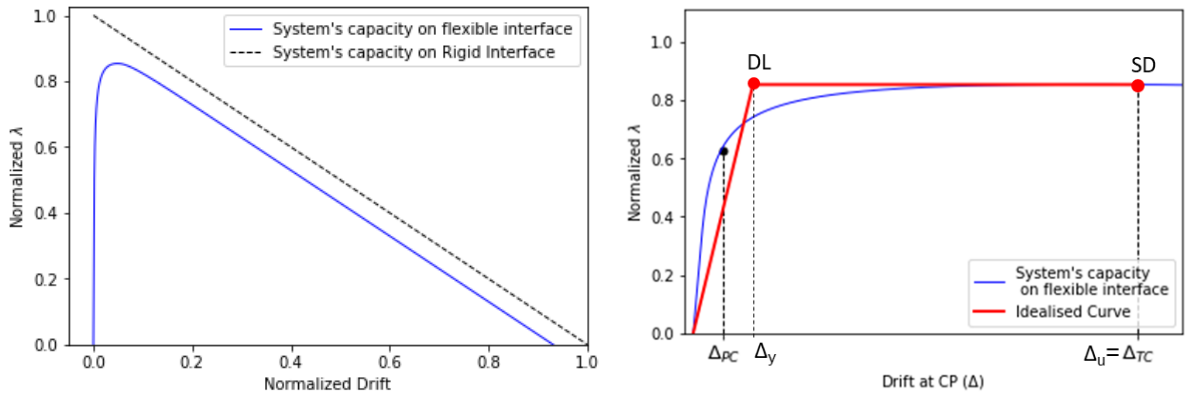

Figure 6-3 a) Capacity curve of the unstrengthened wall resting on flexible interface, b) enlargement of the initial portion of system's capacity and idealized capacity curve

The initial part of the curve is shown in detail in Figure 6-3 b to illustrate the reduction of the wall's stiffness for displacements greater than the one causing partial contact of the base Δ_{PC}, and the decrement in capacity after the toe-crushing failure of the wall's base Δ_{TC}.

For the obtained capacity curve, it is possible to identify a set of damage thresholds which refer to increasing level of damage in the structure. According to the assessment procedure proposed by Dolšek and Fajfar (2008) and the N2 method (EN 1998-1:2004 2004), these are defined as the states of Damage Limitation (DL) and of Significant Damage (SD), corresponding to the displacement when the system starts to degrade and reaches its ultimate deformation Δu. The damage thresholds are typically identified on a linearized elastic-perfectly plastic relationship which simplifies the behaviour of the real system up to its ultimate displacement Δ_u, set equal to Δ_{TC} for the unstrengthened wall. The idealized curve shown in Figure 6-3 b is obtained

assuming that the linearized system will reach the same ultimate displacement Δ_u and acceleration a_u of the real one and imposing equal energy deformation for both systems. From the linearized system, the yielding point of coordinates (Δ_y, λ_y) is used to identify the limit state of DL and the elastic period T_{el} of the system can be deduced as:

$$T_{el} = 2\pi \sqrt{\frac{\Delta_y}{\lambda_y g}} \tag{6-7}$$

The term *yielding* is used with respect to the idealized curve to identify the beginning of the ductile phase of the linearised system.

This method provides a simple procedure to compute the capacity of an unstrengthened wall and defines the displacement thresholds corresponding to two damage levels for the system.

The seismic assessment of the system is then performed according to the N2 method, described in detail in the EC8 (EN 1998-1:2004 2004). Here, it suffices to recall that the displacement demand for a predetermined Limit State (LS) depends on the displacement of the system at yielding Δ_y and on ductility demand μ_d:

$$\Delta_{LS} = \mu_d \, \Delta_y \tag{6-8}$$

Where μ_d is function of the ratio between the spectral accelerations corresponding to the elastic and inelastic system, and of the value of elastic period T_{el} with respect to T_C:

$$\mu_d = \begin{cases} \left(\frac{S_{ae}(T_{el})}{S_{ay}} - 1\right)\frac{T_C}{T_{el}} + 1 & if\ T_{el} < T_c \\ \frac{S_{ae}(T_{el})}{S_{ay}} & if\ T_{el} < T_c \end{cases} \tag{6-9}$$

The system is deemed safe if the seismic displacement demand Δ_{LS} is smaller than the displacement capacity associated to the selected limit state (LS). Hazard levels are associated with predefined probabilities of exceedance in a reference interval (e.g. 10% in 50 years) or, equivalently, predefined return periods (e.g. 475 years). Moreover, the seismic hazard is associated with the reliability of existing buildings. Hazard levels thus defined are then further modified through a coefficient depending on the importance of the building considered. Importance is mainly related to the requirement that the structure remains operational after an earthquake. By relating required performance targets and hazard levels, four considered return periods (TR) are proposed for each type of asset (Figure 6-4 Lagomarsino and Cattari 2015) . To take into account the varying importance and significance of each asset, the use of the following three values, to modify the return periods, is proposed: Use coefficient (γ_U), Building

coefficient (γ_B) and Artistic coefficient (γ_A). These factors are defined as a function of the building use, its cultural and historical value and the presence of relevant artistic assets in the building (Lagomarsino and Cattari 2015). Three independent coefficients are required because of the great variety of cultural heritage assets. Some highly important structures, from the historical and architectural point of view, are rarely used. In this case, it is necessary to prevent collapse, while life safety and immediate occupancy are not priorities. On the contrary, less important architectonic structures may be strategic or public buildings, for which use and safety performance are fundamental. Moreover, sometimes artistic assets are located in buildings that present no particular relevance from the architectural point of view; in these cases, the artistic coefficient can increase the seismic hazard for the verification of the artistic assets' performance.

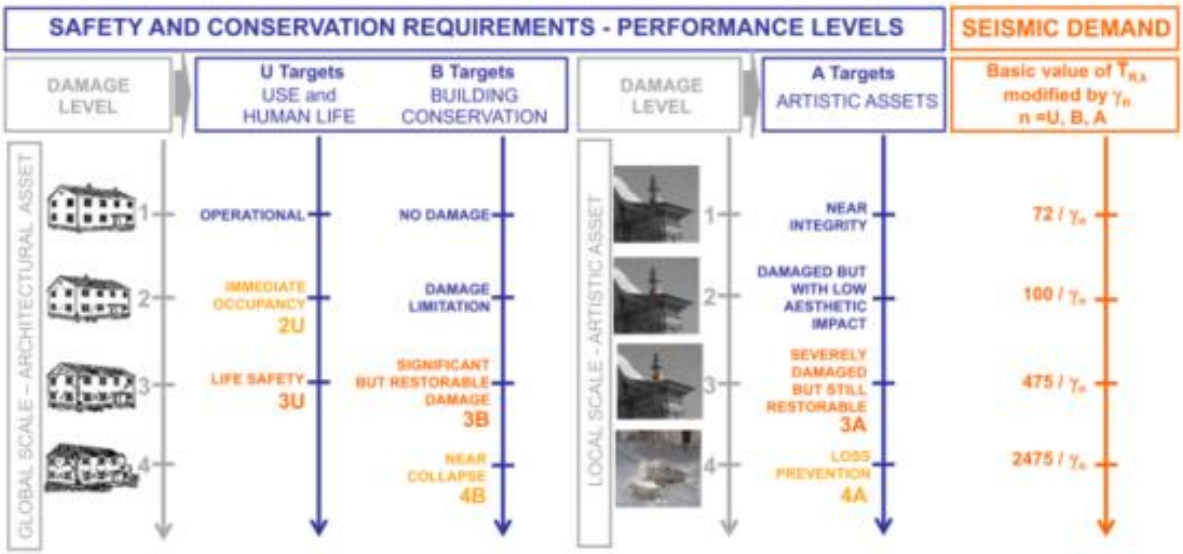

Figure 6-4 a) Damage levels, performances and related return periods in years (Lagomarsino and Cattari 2015)

The same values adopted in the international standards are proposed (EN 1998–1 2004), except for the Damage Level 2, for which a return period of 100 years is assumed, instead of 225 years; this corresponds to accepting a probability of occurrence of 40% in 50 years instead of 20%. This value is similar to the reference value for the design of new building according to Eurocode 8 (EN 1998–1 2004), which for Damage Limitation requirement considers TR = 95 years (probability of 10% in 10 years). The motivation of this departure from international standards on existing buildings is that ancient masonry buildings suffer moderate damage even for low intensity earthquakes (due to the negligible tensile strength of masonry), but the occurrence of some cracking is not detrimental for the preservation of the cultural heritage asset. Thus, the

adoption for DL2 of a too demanding hazard level would require in most of the cases relevant retrofitting, which conflict with the principle of "minimum intervention".

If the performance of the system does not comply with the code requirements, the implementation of strengthening systems must be considered. In the next section, a grouted anchoring system (GAS) and an innovative dissipative anchoring system (D-GAS) are presented, and the contribution offered by these systems to the capacity of the wall is computed.

6.2.2 Static out-of-plane assessment of wall strengthened by GAS

Grouted anchors are typically installed to improve the connections of orthogonal wall in HMB, preventing the OOP separation of the masonry panels during a seismic event. Under the hypothesis that the wall remains in its perfectly vertical position for the PGA corresponding to an expected seismic action (CMIT 2009), the GAS and the wall are assumed to remain in their elastic/linear range. The force that the anchor must resist can be computed following a force-based approach and must be checked against the maximum pull-out force F_t that the anchor can sustain, according to the failure mode of the anchor.

A second design approach is to assume that the seismic force exceeds the anchor capacity and that an OOP mechanism develops.

In this case, the non-linear model presented for the unstrengthened wall is modified to consider the restraining action $F_{AS,i}$ provided by each anchor placed at height $H_{t,i}$ from the base of the wall. With reference to Figure 6-5 the equilibrium equation of the wall strengthened by GAS is presented in Eq. (6-10):

$$mg\,\mathrm{R_G}\sin(\beta_G - \theta) - mg\,u_\theta(\theta) + \sum_1^n F_{AS,i}\,R_{AS,i}\cos\left(\beta_{AS,i}\right) = \lambda_\theta\, mgR_G\cos(\beta_G - \theta) \tag{6-10}$$

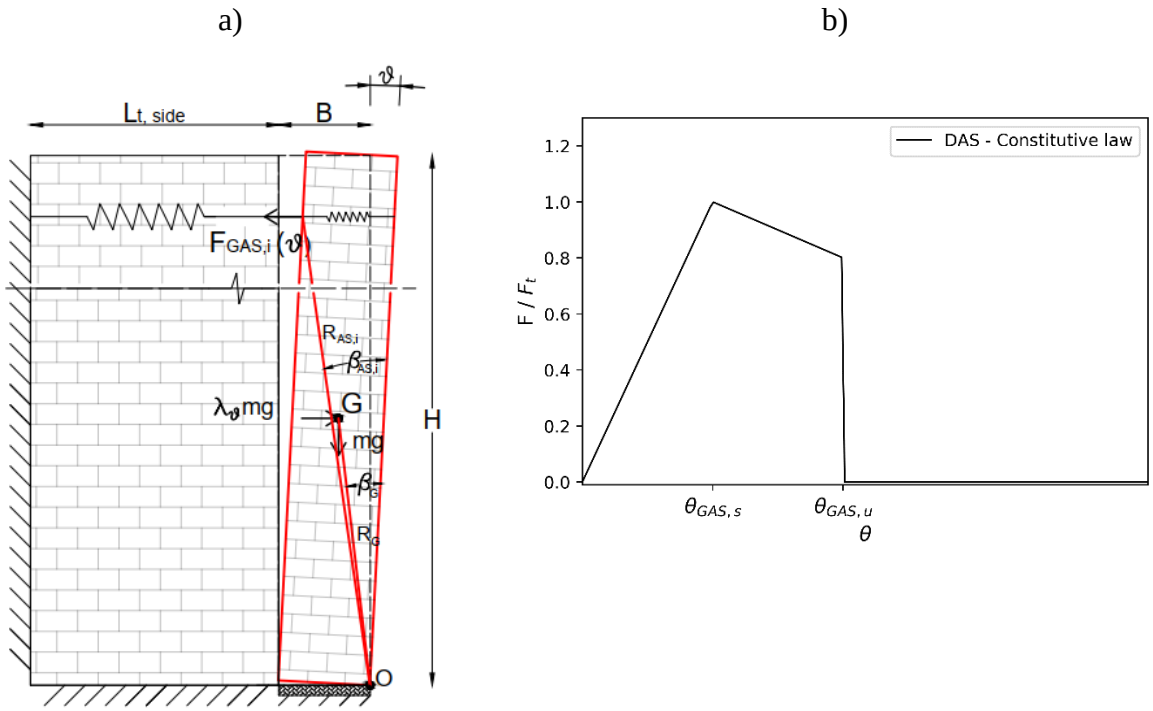

Figure 6-5 a) One-sided displaced configuration of a wall restrained by a GAS, b) Idealized monotonic behaviour of grouted anchors for increasing rotations

This model assumes that, as a result of a capacity design process, no failure in the adjacent masonry occurs and that no change of mechanism takes place, from single body to multi-bodies (D'Ayala and Shi 2011; Abrams et al. 2017). The restoring action provided by the GAS is characterized by its slip strain ($\varepsilon_s = 0.005$) and ultimate strain ($\varepsilon_u = 0.01$) obtained in the previous chapter on the basis of the displacement capacity of grouted anchors in pull-out tests, assuming also for the tie a bilinear behaviour. The rotations thresholds corresponding to the maximum and ultimate load capacity are computed respectively as:

$$\theta_{GAS,s} = \tan^{-1}\frac{\mathrm{d_s}}{H_t} = \tan^{-1}\frac{\varepsilon_s \; l_e}{H_t} \tag{6-11}$$

$$\theta_{GAS,u} = \tan^{-1}\frac{\mathrm{d}_u}{H_t} = \tan^{-1}\frac{\varepsilon_u \; l_e}{H_t} \tag{6-12}$$

where l_e is the effective embedment length, namely the thickness of the front wall. The ultimate load is computed as the 80% of $F_{\max(N)}$in accordance with the convention adopted for the experimental database in Chapter 5. An idealized relationship between F_{AS} and θ is obtained considering that the force increases linearly up to the slip rotation θ_s, experiences a linear degradation up to θ_u and then then drops to 0, as shown in Figure 6-5b, and formalized by the set of Eq.(6-13):

$$F_{AS}(\theta) = F_{GAS}(\theta) = \begin{cases} \dfrac{F_{\max(N)}}{\theta_{GAS,s}}\theta & 0 < \theta \leq \theta_{GAS,s} \\ F_{\max(N)}\left(1 - 0.2\dfrac{\theta - \theta_{GAS,s}}{(\theta_{GAS,u} - \theta_{GAS,s})}\right) & \theta_{GAS,s} \leq \theta \leq \theta_{GAS,u} \\ 0 & \theta \geq \theta_{GAS,u} \end{cases} \quad (6\text{-}13)$$

The anchoring system is designed as the first component to fail, meaning that it will reach the ultimate rotation $\theta_{GAS,u}$ before the toe-crushing failure occurs at θ_{TC}. This condition is shown in Figure 6-6 where the capacity curve of a wall strengthened by two GAS is presented in terms of horizontal displacement of the control point and normalized acceleration multiplier: the anchors largely increase the load capacity of the system up to the displacement $\Delta_{GAS,u}$ after which the overturning moment is balanced by the self-weight of the wall only, as it was for the case of unstrengthened walls. Because of this sudden loss in capacity, it can be considered that the ultimate deformation Δ u for the "wall-with-GAS" system corresponds to the failure of the topmost anchor. On this assumption, the idealized curve and the damage states are obtained, as shown in Figure 6-6 and the ductility capacity of the strengthened system is computed as:

$$\mu_c = \frac{\Delta_u}{\Delta_y} \quad (6\text{-}14)$$

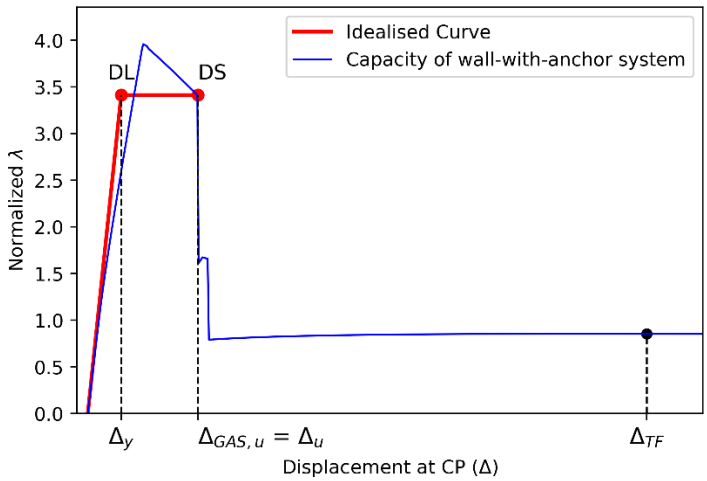

Figure 6-6 Capacity curve of the "wall-with-GAS" system, including idealized capacity curve and damage limit states

Despite the large load capacity offered by the GAS, the anchoring system displays a reduced ductile behaviour between yielding and failure. Moreover, the horizontal path does not refer to the yielding of the steel rebar, which would offer a longer ductile behaviour, but of the brittle debonding of the grout from the surrounding masonry according to the most recurring failure

modes highlighted in Section 5.2.1. In fact, the contribution of the steel bars to the ductility capacity can be neglected if the longitudinal stiffness of the front portion of the steel bar K_{tie} is significantly larger than the bond stiffness of the grouted front portion K_{bond}. For instance, the anchors tested in the pull-out had a $K_{tie} = \frac{EA}{L} = 1.21 * 10^8\ N/m$, namely five times larger than the bond stiffness ($K_{bond} = F/d_s = 2.3 * 10^7\ N/m$), which would result in a negligible elongation of the steel bar compared to the bond slip.

Therefore, the use of the dissipative device, able to provide a larger ductile behaviour becomes imperative to improve the seismic performance of such systems.

6.2.3 Static analysis of wall strengthened by D-GAS

The insertion of a Dissipative Grouted Anchoring System (D-GAS) at the connection between perpendicular walls (Figure 6-7 a) determines that the friction-based device (Figure 6-7 b) allows for a controlled displacement of the out-of-plane wall.

a) b)

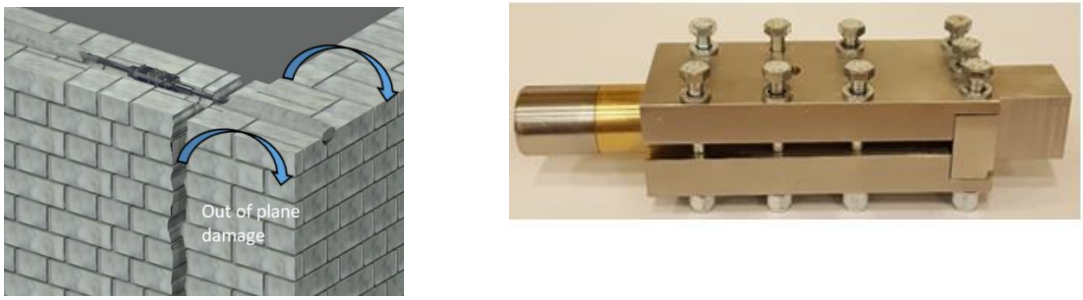

Figure 6-7 a) insertion of dissipative anchoring system at the connection between orthogonal walls, b) friction-based device

The system is schematically represented in Figure 6-8 a by a system of springs and a slider representing the grouted anchors and the device, respectively. The strength of the grouted ties, $F_{bond,side}$ and $F_{bond,front}$, is determined considering the capacity of the bond strength developed between the ties and the parent material. According to the failure modes observed for grouted anchors, a load bearing capacity of each anchor's portion is assumed according to the set of equations proposed in Chapter 5.

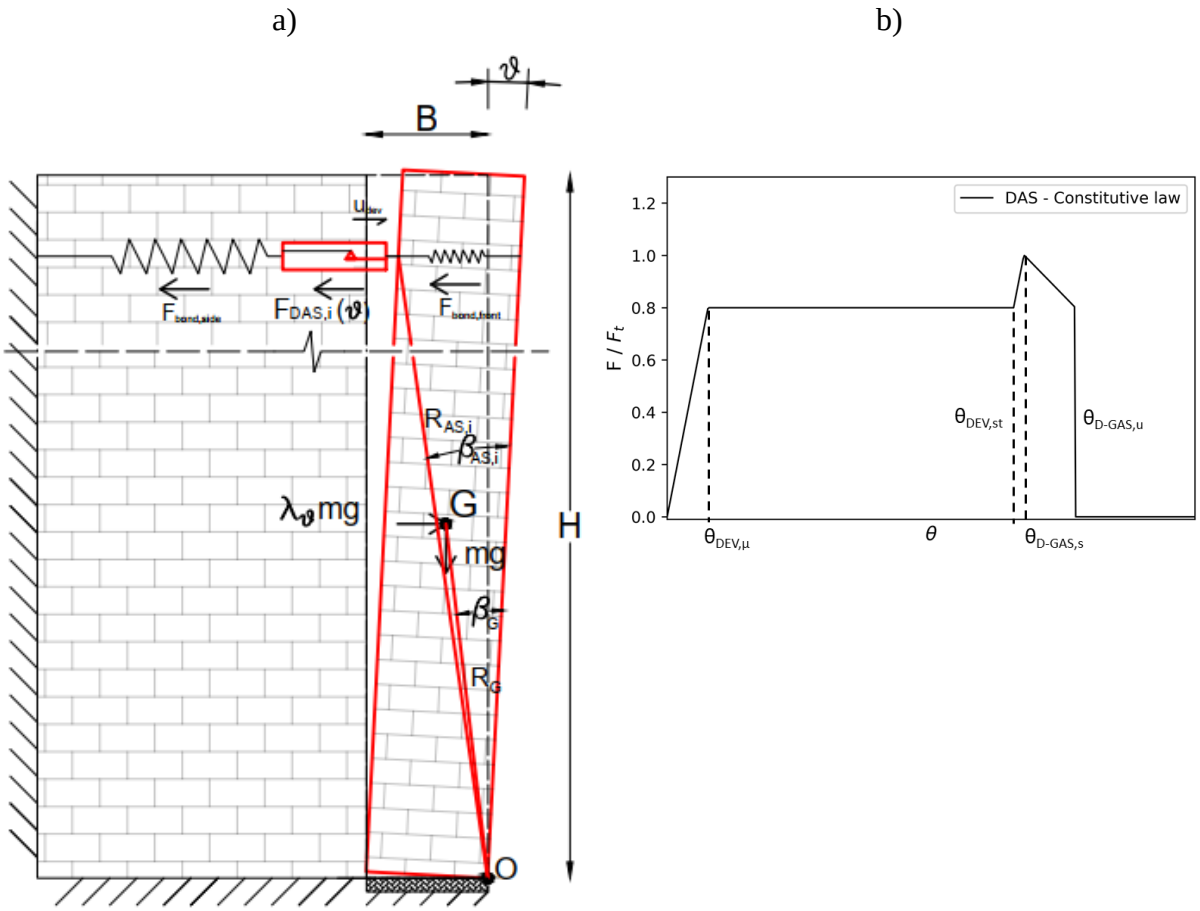

Figure 6-8 a) One-sided displaced configuration of a wall restrained by a D-GAS, b) Idealized monotonic behaviour of D-GAS for increasing rotations

Conversely, the slippage load at which the device activates is equal to the friction resistance F_{fric} the device is designed to provide. The system is adjusted to have F_{fric} at the bottom of the anchor strength hierarchy, so that, during an earthquake, the detachment of the façade from the side walls triggers the activation of the device and prevents the pull-out failure of the anchors. Therefore, the device is tuned to activate for a design slippage load V_D smaller than the load capacity that the two grouted steel elements can provide. The strength design check is expressed by Eq. (6-15) :

$$V_D < F_{\max(N)D} = \min\left(F_{\max(N),side}, F_{\max(N),front}\right) \tag{6-15}$$

The sliding motion is bounded to a maximum displacement by a steel solid pin, with strength capacity greater than the anchor bond strength, and results in the dissipation of the input seismic energy. Once the maximum allowable run Δu_{DEV} is achieved, the system behaves like a grouted anchor up to ultimate failure, as shown in Figure 6-8 b. Considering the combined ductility of anchor and device, the capacity of a wall restrained by D-GAS is assessed on a Displacement-based approach, computing the force provided by the D-GAS for increasing rotations:

$$F_{AS}(\theta) = F_{D-GAS}(\theta) = \begin{cases} \dfrac{F_{\max(N)}}{\theta_{GAS,s}}\theta & if\ 0 < \theta \le \theta_{\mathrm{DEV},\mu} \\ F_{\max(N)}\, C_{D-GAS} & if\ \theta_{\mathrm{DEV},\mu} \le \theta < \theta_{\mathrm{DEV,st}} \\ F_{\max(N)}\, C_{D-GAS} + \dfrac{F_{\max(N)}}{\theta_{GAS,s}}\left(\theta - \theta_{\mathrm{DEV,u}}\right) & if\ \theta_{\mathrm{DEV,st}} \le \theta < \theta_{D-GAS,s} \\ F_{\max(N)}\left(1 - 0.2\dfrac{\theta - \theta_{D-GAS,s}}{(\theta_{D-GAS,u} - \theta_{D-GAS,s})}\right) & if\ \theta_{D-GAS,s} \le \theta \le \theta_{D-GAS,u} \end{cases} \quad (6\text{-}16)$$

C_{D-GAS} is the activation coefficient of the D-GAS. It varies between 0 and 1 (excluding the extreme points) and determines the device's slippage force V_D as a fraction of the anchor's capacity $F_{\max(N)}$. The rotation at which the device activates, $\theta_{\mathrm{DEV},\mu}$ and stops, $\theta_{\mathrm{DEV,st}}$, and the rotations at which the D-GAS reaches its maximum and ultimate capacity ($\theta_{D-GAS,s}$ and $\theta_{D-GAS,u}$) are obtained as:

$$\begin{aligned} \theta_{\mathrm{DEV},\mu} &= \theta_s C_{D-GAS} \\ \theta_{\mathrm{DEV,st}} &= \theta_{\mathrm{DEV},\mu} + \arctan\left(\frac{\Delta u_{DEV}}{H_t}\right) \\ \theta_{D-GAS,s} &= \theta_{GAS,s} + \arctan\left(\frac{\Delta u_{DEV}}{H_t}\right) \\ \theta_{D-GAS,u} &= \theta_{GAS,u} + \arctan\left(\frac{\Delta u_{DEV}}{H_t}\right) \end{aligned} \quad (6\text{-}17)$$

For this model the longitudinal stiffness of the steel bars is neglected

For incremental rotation of the wall's base, the ultimate rotation of the D-GAS $\theta_{D-GAS,u}$ must precede the toe-crushing failure of the wall's base, to preserve the integrity of the wall. This condition is formally expressed as:

$$\theta_{GAS,u} + \arctan\left(\frac{\Delta u_{DEV}}{H_t}\right) < \theta_{TC} \quad (6\text{-}18)$$

Which allows computing the allowable sliding capacity of the dissipative device once θ_{TC} is determined. The improvement in displacement between the two systems is quantified by the ratio, η, between the respective ultimate rotations:

$$\eta = \theta_{D-GAS,u}/\theta_{GAS,u} \quad (6\text{-}19)$$

The capacity curve for the "wall-with-D-GAS" system is shown in Figure 6-9 a for the case of two D-GAS with C_{D-GAS} set at 0.7. The idealized curve obtained applying the equal energy principle and assuming that the system has the same ultimate displacement and acceleration capacity of the real one, may not provide a good approximation of the anchor's capacity, as it may result in a significant reduction of the elastic stiffness and overestimation of the load capacity as shown in Figure 6-9 a. Instead, the optimized bilinear curve in Figure 6-9 a can be obtained by minimizing the difference in elastic stiffness *K* and ultimate acceleration multiplier λ between the optimized (index "O"), the real (index "R"), and the ideal system (index "I"):

$$\min(\Delta K_{o-R} - \Delta\lambda_{O-I}) = \min\left(abs\left(\frac{K_O - K_R}{K_R}\right) - abs\left(\frac{\lambda_{u,O} - \lambda_{u,I}}{\lambda_{u,I}}\right)\right) \quad (6\text{-}20)$$

By plotting the difference in stiffness and acceleration multiplier (ΔK_{o-R} and $\Delta\lambda_{O-I}$) it is possible to identify the optimal stiffness and ultimate acceleration multiplier (K_O , $\lambda_{u,O}$) as the intersecting point of the two curves, as shown in Figure 6-9 b. From this, the yielding displacement Δ_y is easily computed as:

$$\Delta_y = \frac{\lambda_y}{K_O} = \frac{\lambda_{u,O}}{K_O} \quad (6\text{-}21)$$

On the graph shown in Figure 6-9 b, the optimal point is close to the parameters corresponding to the "real behaviour" of the system, meaning that the optimized curve provides a better approximation of the actual system's capacity, than the initially assumed idealised curve. Therefore, the yielding and ultimate damage limit states are identified on the optimized curve as shown in shown in Figure 6-9 a.

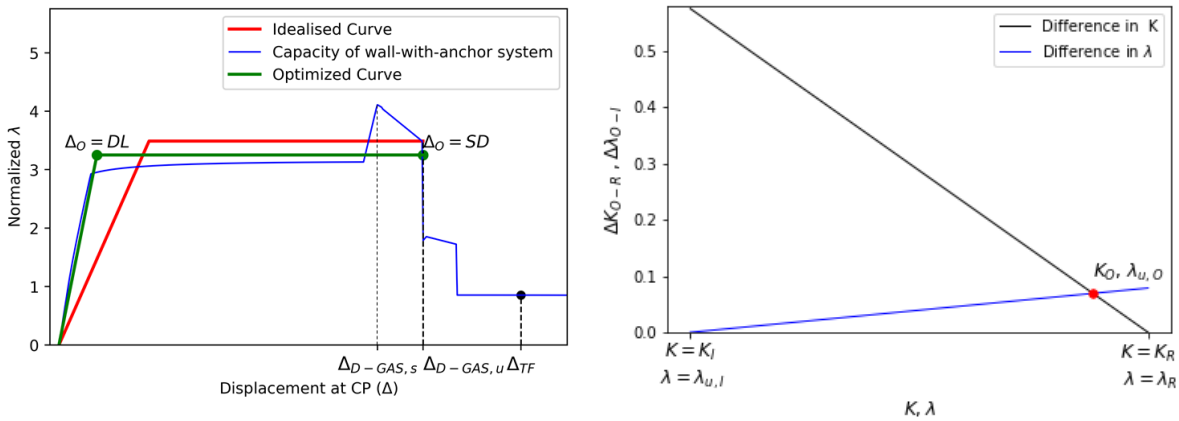

Figure 6-9 a) Graphical representation of optimal stiffness K_O, b) Capacity curve of the "wall-with-D-GAS" system, including damage limit states

Comparing the capacity curves obtained for the unstrengthened and strengthened walls, it can be concluded that the implementation of the D-GAS improves both the strength and ductility capacity of the system. The design of the GAS and D-GAS according to the N2 method would require dimensioning the number and sizing of the system ensuring that the expected seismic performance does not exceed the capacity. Nonetheless, this static procedure might overlook some critical aspects of the behaviour of walls during seismic events. A critical aspect concerns the computation of the inelastic displacement demand, obtained by Eq. (6-8) according to the value of expected ductility (Eq.(6-9)). This relation is appropriate for several typologies of structures, such as reinforced concrete frames with masonry infills (Dolšek and Fajfar 2008), and needs to be verified for the model of wall restrained by anchorages proposed in this study. This can be achieved by verifying that the displacement demand predicted by the static analysis is close to the horizontal displacement experienced by the system for a corresponding ground motion. Therefore, in the next paragraph a dynamic analysis of the wall in different configurations is proposed to validate the results of the assessment and design procedure proposed in this work.

6.3 Validation of DB method by Non-linear Time-history Analysis

The Displacement-based procedure proposed allows assessing the vulnerability of historical masonry walls to out-of-plane failure, verifying the safety of the macro-element to an expected seismic action. In order to determine the reduction in vulnerability of systems retrofitted with anchors, the N2 method (Fajfar 2000) has been extended to accommodate the particular capacity curves representative of walls strengthened by traditional and dissipative anchoring systems as outlined in the previous section.

Depending on the type and sizing of the strengthened configuration assumed, the displacement capacity of the wall and the inelastic seismic demand vary, therefore the design solution is not unique. Moreover, this equivalent static procedure neglects relevant aspects of the motion, such as the evolution of the system over time and the dissipated energy. By contrast, a nonlinear dynamic analysis fully considers the evolution of motion and the effect of inertial forces during reversal loads such as seismic actions. Hence, to determine a more accurate response of the system in the original and strengthened configurations, verify the assumptions made in the static equivalent analysis, and determine the optimal design solution, the structural behaviour is investigated by means of nonlinear time-history analyses.

In Paragraph 6.3.1, the front wall is modelled as a rigid block with one degree of freedom, namely its base rotation around the hinge line. The rocking motion of the block undergoing a seismic base acceleration cannot be derived in its close-form solution (Housner 1963), but it can be numerically computed via a state-space formulation that can accommodate the non-linear nature of the problem (Makris and Zhang 1999). Following this approach, several authors solved the motion equations for different rocking scenarios, calibrating the results with experimental data on masonry sub-assemblages (Al Shawa et al. 2012; Giresini, Sassu, and Sorrentino 2018). Recently, the one-sided rocking equation of rigid blocks was derived by AlShawa, et al. (2019) for the case of a wall strengthened by ties and by Giresini et al. (2021) for the case of a wall strengthened by a viscous damping system. In this thesis, the one-sided rocking equation of a rigid block undergoing seismic acceleration is solved numerically for the case of an unstrengthen wall and a wall with GAS/D-GAS. To this purpose, a Python code is developed to obtain the rocking motion by Direct numerical Integration (DI). This tool allows to obtain the maximum rocking amplitude experienced by the system and compare it with the expected performance points obtained by the DB method to validate the static method.

Paragraph 6.3.2 presents the assumptions made to develop a 3D model in Abaqus subjected to dynamic analysis to study the same overturning phenomenon of masonry walls connected orthogonally by dissipative anchor. Drawing on the results of the computational activities presented in Chapters 4 and 5, this model includes the detailed geometry and mechanical properties of the analysed structure, as well as the equivalent traction capacity of the masonry connection and the mutual interaction between grouted anchors and parent material. Due to the model's complexity, this analysis presents a high computational cost, especially for the case of the structure strengthened by D-GAS. However, the results are useful to validate the ones obtained by the DI method, which presents a reduced computational cost.

6.3.1 Non-linear time history analysis – Rigid body - Direct Integration (DI) method

A numerical approach can be set out by extending the assumptions and constraint used to derive the limit static behaviour, represented by Eq. (6-2), to the dynamics motion resulting by subjecting the walls to a seismic input. Adapting the classical equation of rigid body rocking (Housner 1963) to the present case of one-side rocking, the equation reads as follows:

$$\ddot{\theta}(t) + p_\theta^2 \left[\sin\left(\alpha - \theta(t)\right) - \frac{u_\theta}{R_G} + \sum_1^n F_{AS}(\theta)\, H_{t,i} \frac{cos\theta(t)}{mgR_G} + \frac{\ddot{u}_g}{g} \cos[\,\alpha - \theta(t)] \right] = 0 \qquad (6\text{-}22)$$

where $p_\theta = \sqrt{mgR_G/I_\theta}$ is the frequency parameter, I_θ is the polar moment of inertia of the wall with respect to the instantaneous centre of rotation O', and R_G is the distance between the body centroid and O'. Similar to the kinematic approach, the presence of *n* anchors at heights $H_{t,i}$ is taken into consideration by adding their contributions as a stabilizing moment opposing the overturning moment produced by the base acceleration.

When the block is in motion it will dissipate energy at every impact with the side wall and the foundation. Al Shawa et al. (2012)proposed a coefficient of restitution for the case of a façade laterally restrained on one side by transverse walls to account for the energy dissipated at impact. The value of *e* is obtained considering that within one rebound the front wall impacts twice with the base and once with the side wall in different - but close in time – instants. Imposing the conservation of momentum, the coefficient of restitution is obtained as the combination of the three impacts:

$$e = -1.05\, e_f e_{tr} e_f = 1.05\left(1-\frac{3}{2}\sin^2\vartheta_c\right)^2\left(1-\frac{3}{2}\cos^2\vartheta_c\right) \tag{6-23}$$

where the coefficient 1.05 was determined experimentally and the negative sign implies a rebound after the impact. With the obtained value of *e* it is possible to numerically solve Eq. (6-22) to perform a nonlinear time history analysis alternative to equivalent static procedures for the assessment of HMB (Alshawa et al. 2012).

In this thesis, an open-source program (available on GitHub at the following link: https://github.com/victormelatti/Nonlinear-rocking-of-walls) is presented to perform the analysis. To solve the second-order Ordinary Differential Equations (ODE), Eq. (6-22) is turned into two first-order equations by defining a new dependant variable $\omega = \dot{\theta}$. The state vector of the system becomes:

$$y(t) = \begin{pmatrix}\theta(t)\\ \omega\end{pmatrix} \tag{6-24}$$

And the time-derivative vector $f(t)$ is:

$$f(t) = \dot{y}(t) = \begin{pmatrix}\omega\\ -p_\theta^2\left[\sin(\alpha-\theta(t)) - \frac{u_\theta}{R_G} + \sum_1^n F_{AS}(\theta)\, H_{t,i}\frac{cos\theta(t)}{mgR_G} + \frac{\ddot{u}_g(t)}{g}\cos[\alpha-\theta(t)]\right]\end{pmatrix} \tag{6-25}$$

The numerical integration of Eq. (6.25) is performed with the ODE solver available in Python, namely the *integrate.odeint()* function available in the *SciPy* package. This function takes as inputs the time-derivative vector $f(t)$, the initial conditions of rotation and angular velocity, and the seismic acceleration to return an array of the rotations $\theta(\hat{t})$ caused by the acceleration $\ddot{u}_g(\hat{t})$ and by the inertial forces at each time step $\hat{t}$.

To compare the static and dynamic results, a spectrum-compatible accelerogram is used as ground motion acceleration in Eq. (6-22). Because real accelerograms have specific frequency and amplification content and are not directly related to the code-defined design spectrum, spectrum-compatible accelerograms can be obtained, based on the modification of actual ground motions. Several methods have been proposed in literature to generate spectrum-compatible accelerograms. In this work, the code developed by Ferreira et al. (2020) is used: it determines the response spectrum of the accelerogram and returns its best fit to the design spectrum locally relevant. This procedure allows the use of a single accelerogram to induce an inelastic response consistent with the design scenario defined by the appropriate code, rather than running several analyses to account for the inherent hazard uncertainty and limitation associated with considering an individual accelerogram. However, future work could include the validation of the numerical model using a suite recorded accelerograms, scaled to the desired intensity.

From Eq. (6-22) it is clear that solving the equation of motion for $n = 0$ returns the dynamic response of the unstrengthen structure. The presence of the GAS and D-GAS is included by selecting the appropriate constitutive law between Eq.(6-13) and Eq. (6-16) to be used in place of F_{AS}. For both strengthening systems, the proposed DB design takes into consideration their ductility, i.e. the hysteretic energy dissipation of ductile structures, to reduce the seismic demand and compute the performance of the system. Solving the equation of motion of the strengthened systems allows the direct comparison between maximum horizontal displacement experienced by the rocking wall $\Delta_{max,rk}$ and the deformation that the system is expected to display according to the static procedure for a selected limit state, Δ_{LS}. The variation between static and dynamic maximum displacement is expressed by the following ratio:

$$\beta = \frac{\Delta_{LS}}{\Delta_{max,rk}} \tag{6-26}$$

For values of β close to unit it can be assumed that the $\mu - T$ relation provided by the code (EN 1998-1:2004 2004) gives a good approximation of the dissipative energy of the system and that the use of Eq. (6-8) and (6-8) can be extended to the case of walls strengthened by anchors.

Moreover, the dynamic analysis can be used as a supplementary tool for the design method to determine the optimal design solution, comparing the energy dissipated by each strengthen configuration, E_D, with respect to the seismic energy E_I imparted to the structure during the seismic action. The ration γ is therefore computed as:

$$\gamma = \frac{E_D}{E_I} = \frac{\int_0^{S_T} F_t \, ds_T}{\int_0^{S_G} m\ddot{u}_g(t) \, ds_G} = \frac{\int_0^{T} F_t \, \dot{s}_T(t) \, dt}{\int_0^{T} m\ddot{u}_g(t) \, \dot{\theta}(t) \, R \, dt} \tag{6-27}$$

where T is the duration of motion, $\dot{\theta}(t)$ is the angular velocity and s_G and s_T are the displacement experienced by the center of mass and the anchor, respectively.

6.3.2 Non-linear time history analysis – 3D model - Abaqus

A finite element model can be implemented in Abaqus to investigate the behaviour of a structure under seismic input and determine in detail the rocking motion of the front wall for different strengthening solution. The model should be functional to the representation of the failure mode expected for the analysed structure, namely the separation and outward tilting of the façade from the side walls and should present an acceptable level of computational cost. Accordingly, only a portion of the building involved in the OOP failure can be modelled if it is reasonable to assume that the remaining of the structure and the presence of the surrounding buildings do not significantly affect the rocking response of the structure.

The modelling strategies, already calibrated on the experimental results in previous chapters, are combined in this model. The cohesive elements introduced in Chapter 5 to model the connection of the T-shaped specimen can be used to reproduce the poor-quality connection between the façade and the side walls. Implementing a set of interfaces along the full height of the connected wall allows simulating the equivalent traction capacity of the connection as a function of the building's height. Assuming *n* interfaces, each j-*th* interface has a traction strength t_j equal to the slip resistance C_j offered by that portion of wall divided by the interface area:

$$t_{n,j} = \frac{C_j}{A_{interf}} \quad for\ j = 1,2,..n \tag{6-28}$$

Where C_j can be computed according to Eq. (5.28) of Chapter 5. A second set of cohesive interfaces can be used to model the bonding strength of the anchors, as previously shown in Chapter 5, once the maximum shear strength capacity obtained using Eq. (5.17) and the ultimate elongation are computed. The Concrete Damage Plasticity can be adopted to simulate the

nonlinear response of the masonry components, having determined the mechanical properties of the masonry's constituent elements, as explained in section 5.4.1. Finally, the model of the friction-based device presented in Chapter 4 can be implemented in the analysis of the system strengthen by means of D-GAS. The external surface of the slider can be assigned with a specific value of friction coefficient according to the type of material used as friction interface and a bolt load can be assigned to apply the bolt precompression.

The model is subjected to the same base acceleration of the rigid body to provide a comparison between the rocking motion obtained by direct integration (DI) of the equation of motion and the one obtained by the FEM model. The comparison is in terms of the maximum rocking amplitude $\Delta_{max,rk}$ and the maximum rocking accelerations $a_{max,rk}$ computed for a control point on the model to determines the influence that the detailed geometry and the connection strength have on the real performance of the building.

In the next section, the assessment and design method is applied to a case study structure in need of seismic upgrade. Having determined its vulnerability to out-of-plane failure, a design scheme for the implementation of traditional and innovative anchoring solutions is proposed and the optimal design solution is justified by dynamic analysis.

6.4 Application of the design procedure to a case study

The previous section presented a SDOF model to assess the detachment and eventually the OOP failure of a façade within a building subjected to seismic action. The model can include the presence of grouted anchoring systems able to increase the load-bearing capacity of the wall, and of dissipative anchoring system, which additionally increase the displacement and energy dissipation capacity of the strengthen system. Either static or dynamic analyses can be performed to determine whether the wall will experience OOP rocking for a selected seismic acceleration and the best strengthening strategy to balance the overturning motion and prevent extensive damages to the structure.

The oratory of San Giuseppe dei Minimi, a church that suffered severe damage during the 6.3-magnitude earthquake occurred in L'Aquila (IT) in 2009, is selected as case-study to discuss the validity of the presented model and the benefit of introducing a dissipative system into a wall prone to overturning. The structure displayed a clear pseudo-vertical crack opening at the interface between the façade's quoins and the rubble masonry of the side walls, with the upper

portion of façade tilting forward as a whole, as visible from Figure 6-10 a. This failure mechanism, commonly observed in many historical buildings after the 2009 earthquake (D'Ayala and Paganoni 2011), is typical of façade walls with poor connection with the orthogonal walls and causes them to behave independently from the rest of the building (Sorrentino et al. 2017). Therefore, the selected case study is an ideal candidate for the implementation of grouted anchoring system, which restores the interaction between orthogonal walls.

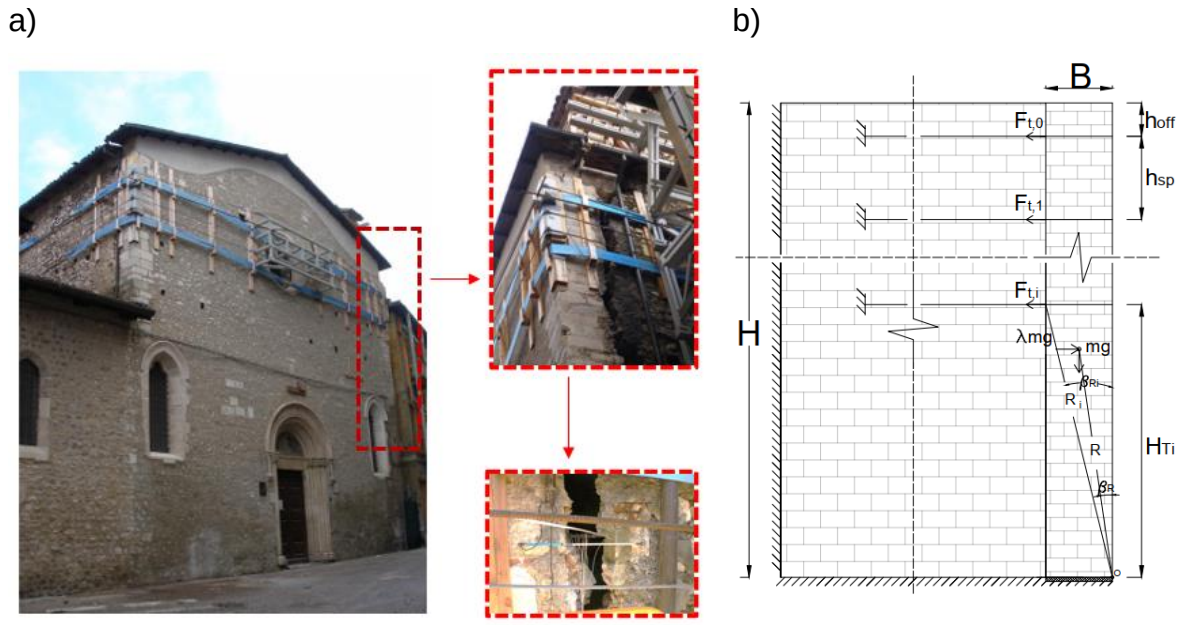

Figure 6-10 The oratory of S. Giuseppe dei Minimi in L'Aquila, Italy. a) The crack between the front wall and side walls as seen from the outside, (b) representation of the façade as restrained by three anchors

According to the assessment and design procedure of section 6.2, the façade is modelled as a single rigid body able to rotate around a base hinge, according to the geometrical dimensions of the church reported by (Paganoni 2015; Al Shawa 2011). The presence of openings cannot be included in the model as the block geometry is 2-dimensional and the length of the wall is considered only to compute the mass participating to the motion. The mechanical properties of the masonry, shown in Table 6-1, are used to model the elastic interface that determines the initial stiffness of the wall and the rotation corresponding to the toe-crushing due to the compression limit strength. The results of the static and dynamic analysis in terms of OOP displacement are compared to the damage observed for the structure in the aftermath of the seismic event to determine the ability of the model to capture the typology and extent of the damage.

Table 6-1. Dimensions and mechanical properties of materials of the façade

Façade Geometry				Mechanical properties		
Base	Height	Length	Mass Density	Compressive Strength	Shear Strength	Tensile Strength
B	**H**	**D**	**ρ**	**f_m**	**τ**	**t**
[m]	[m]	[m]	[KN/m^3]	[MPa]	[MPa]	[MPa]
1	12.5	13.7	20.3	3.2	0.24	0.24

The two strengthening options, GAS and D-GAS are designed and tested to determine the optimal strengthening solution. Regarding the anchoring typology, the technology developed by Cintec's is considered both for the GAS and D-GAS as it is widely used to restore heritage buildings and has large load capacity. The anchors are installed at the corner connection between the façade and the orthogonal walls, the borehole and the total embedment length dimensioned according to the masonry characteristics in Table 6-1 and the manufacturer technical recommendations, as indicated in Table 6-2. The force-based design is firstly considered to determine the number of anchors to be used and their location along the height of the wall. A symmetrical distribution of the anchors on the two sides of the façade and a constant vertical spacing between anchors is assumed. The location of the top-most anchor is selected as control point (CP) as it will experience the largest displacements. For sake of comparison between original and strengthened configuration, all displacements are computed with respect to the same CP in the three configurations. It should be noted that prior to implementing grouted anchors to restore the global integrity of the structure, localized intervention aimed at improving the mechanical characteristics of the masonry should be implemented, if necessary. Mortar injections, deep repointing or the insertion of transversal connectors can improve the shear strength and the in-plane stiffness of the walls, allowing the anchors to develop sufficient mechanical bonding with the substrate and thus the expected load capacity.

The parameters defining the seismicity of the L'Aquila region according to the Eurocode 8 (EN 1998-1:2004 2004) are reported in Table 6-3. These are used to build the design spectra for the Damage and Ultimate limit states, DLS and ULS. As commented in section 6.2.1, a return period of 100 years is considered for the Damage Limit state. The compliance of the structural response with the inelastic seismic demand corresponding to the two limit states is verified in the static analysis.

Table 6-2. Dimensions and mechanical properties of grouted anchors

Anchor diameter	d_b [mm]	16
Hole diameter	d_h [mm]	50
Embedment length (front wall)	$l_{e,f}$ [mm]	4000
Embedment length (side wall)	$l_{e,s}$ [mm]	4000
Distance from top	h_{off} [mm]	800
Anchor spacing	h_{sp} [mm]	1000
Reduction factor	ϕ_j [-]	0.5
Grout compressive strength	$f_{c,g}$ [MPa]	50
Grout/masonry Bond	τ_g [MPa]	2.5
Elastic constant	λ' [-]	0.51
Mass participation factor	e* [-]	1
Behaviour factor	q [-]	2

Table 6-3. Parameters defining the seismicity of the considered zone.

PARAMETERS	Earthquake return period	Peak ground acceleration	Site response coefficient	Confidence Factor	Corner Period
	T_R [years]	a_g [g]	S [-]	C_f [-]	Tc [s]
DAMAGE LIMIT STATE (DLS)	100	0.104	1.57	1	0.51
ULTIMATE LIMIT STATE (ULS)	475	0.26	1.57	1	0.51

The accelerogram of the main shock of the 2009 earthquake (as recorded at the station of L'Aquila, Valle Aterno, Centro Valle, station code AQV) is adapted to fit the design spectrum for each limit state and used as input for the time-history analysis. The obtained accelerograms and spectra are reported in Figure 6-11 .

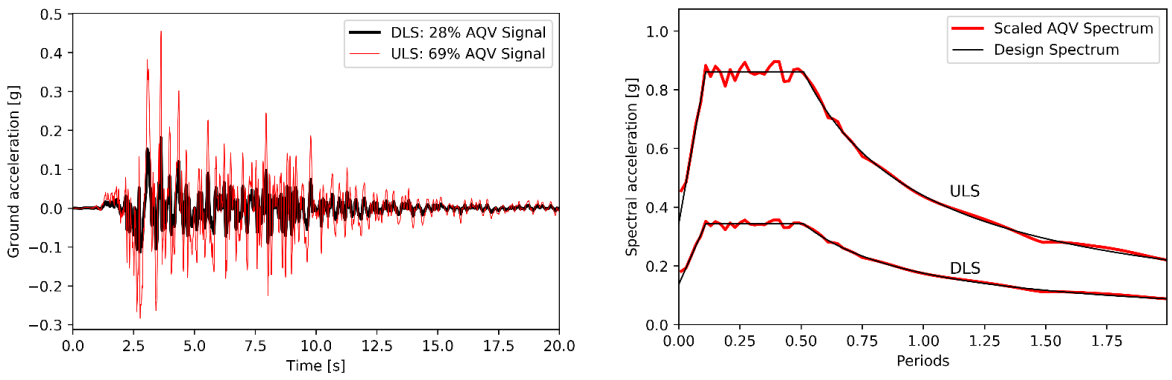

Figure 6-11 Adaptation of the AQV earthquake signal according to the design spectra for (a) Damage Limitation and (b) Severe Damage limit states

6.4.1 Seismic performance of the original structure

The static assessment procedure introduced in Section 6.2 is adopted to evaluate the capacity of the wall in the original configuration and its safety for a selected seismic action. The elastic and inelastic demand spectra are computed for the values reported in Table 6-3 corresponding to the Damage and Ultimate limit states (DLS and ULS) and the performance points are obtained by their intersection with the capacity curve, as illustrated in Figure 6-12 for the ULS. These demand thresholds represent the displacement demand that the system needs to verify for the selected seismic action.

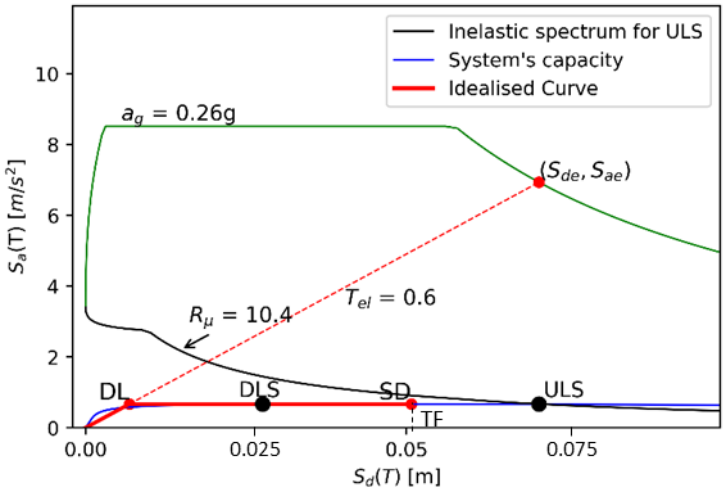

Figure 6-12 Performance points corresponding to the DL and SD limit state for the wall in the unstrengthened configuration.

With reference to Figure 6-12 , the following results are obtained. From the idealized capacity curve, the elastic period $T_{el} = 0.6s$ is obtained. As it is larger than $T_C = 0.51\ s$, the "equal displacement rule" applies, namely the displacement of the inelastic system is equal to the displacement of the corresponding elastic one with the same period (Fajfar 2000).

Thus, the displacement demand is $S_d = 0.027m$ and $S_d = S_{de}(T_{el}) = 0.07\ m$ for the DLS and ULS respectively. At the ULS, the displacement demand is larger than the displacement that causes the toe-crushing failure of the wall's base, meaning that the structure will suffer severe damage in case of a seismic event with magnitude similar to the one considered for the ULS limit state. The wall will suffer damages even for earthquakes of smaller magnitude, as the performance point corresponding to the DLS falls beyond the elastic capacity of the wall.

From the analysis's results, it can be concluded that the façade of the church will experience the detachment from the side walls and toe-crushing failure will occur at the wall's base for the considered seismic event at ULS. Nonetheless, the wall is not expected to overturn as the vertical line passing through the centre of mass falls within the wall's base for the maximum

estimated value of displacement. This finds correspondence with the damages observed during site inspections, as already discussed with reference to Figure 6-10 a. After the detachment, the wall is likely to undergo rocking motion, changing direction of rotation depending on the direction of the seismic acceleration and of the inertial forces. The dynamic evolution of the damage can be predicted performing a time-history analysis, which is presented in Section 6.5.

To reduce the vulnerability of the wall to OOP failure and protect its integrity, the implementation of traditional and innovative anchoring system is proposed in the next section and the improvement in seismic performance is determined.

6.4.2 Seismic performance of the structure strengthened by GAS

As shown in the previous section, the structure's seismic performance is inadequate, and therefore the implementation of seismic strengthening is necessary. As previously discussed, it is decided to use a set of grouted anchors to control the OOP mechanism. Initially, the GAS is dimensioned according to the Force-Based procedure presented in Section 6.2.2. From the parameters defined Table 6-2 and Table 6-3, the load multiplier that determines the collapse mechanism is computed as:

$$\lambda_0 = \frac{a_{g(ULS)} S\, e^*}{q} = 0.27 \qquad (6\text{-}29)$$

Where q is the behaviour factor, $e^*$is the mass participation factor and S is the site response coefficient, as defined in Table 6-2 and Table 6-3. The maximum load that the GAS can provide is bounded by the bonding resistance of the front portion of the anchor. This can be computed using the set of equations provided in 5.2.2 and the set of constants presented in 5.2.3:

$$F_t = min(90\,KN, 86KN, 140\,KN) = 86\,KN \qquad (6\text{-}30)$$

For the considered mechanical properties of the masonry and the geometrical dimensions of the anchor, it is found that the design load is governed by bond failure at the grout/masonry interface (GSM). The number of anchors n is found solving the equilibrium equation given in Eq. (6-2) for $\theta = 0$ and $\lambda_\theta = \lambda_0$. It is found that 3 anchors are needed to ensure that the anchoring system does not fail for the design seismic action.

The design of the anchoring system is obtained following the FB method, namely three anchors are considered on each side to restrain the out-of-plane motion. This is then verified by

computing the capacity of the strengthened system for incremental base rotations and comparing it with the seismic demand expected for the site.

a) Number of anchors = 3

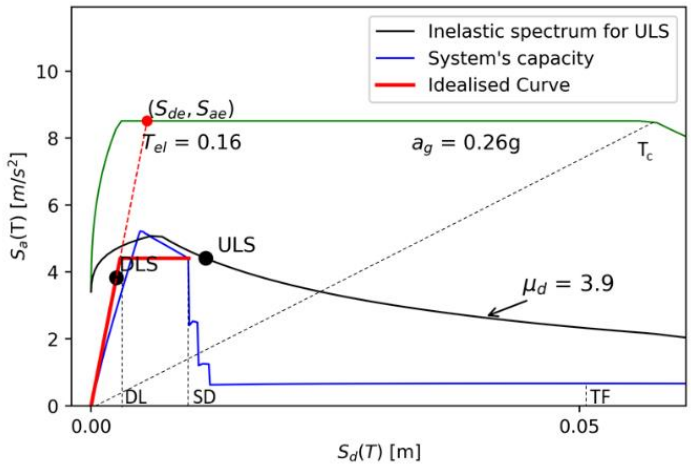

b) Number of anchors = 4

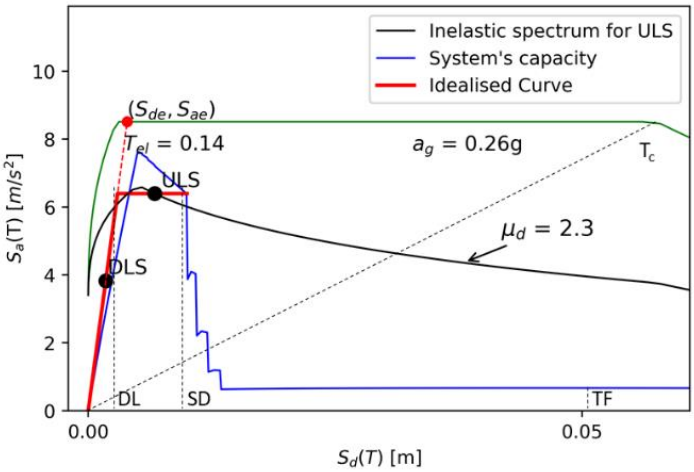

Figure 6-13 Performance point determination for wall strengthened by a) three anchors and b), four anchorson each side of the façade.

As plotted in Figure 6-13a, the strengthening system is effective for the seismic action associated to the DLS, as the performance point falls within the elastic capacity of the anchor. On the other hand, the ductility demand $\mu_d = 3.9$ corresponding to the ULS is larger than the ductility capacity of the grouted anchor ($\mu_c = 3.1$), and the displacement demand would cause the failure of the anchors. With the failure of the topmost anchor, the capacity of the system significantly reduces as the anchors at the highest location provide the larger contribution to the stabilizing moment. The evolution of the system can be investigated by dynamic analysis to determine if the wall would exceed the limit displacement corresponding to the toe-crushing failure, marked as “TF” in Figure 6-13, after the anchor’s failure.

To improve the seismic behaviour, the number of anchors is increased to 4 on each side. As illustrated in Figure 6-13b, the design is now adequate to provide enough strength to reduce the ductility demand. Nonetheless the feasibility of the intervention is ultimately regulated by the principles of minimum intervention and non-intrusiveness enshrined in the ICOMOS/ISCARSAH chart (ICOMOS 2003).

6.4.3 Seismic performance of the structure strengthened by D-GAS

To further improve the response of the strengthened wall, the analysis is performed considering the D-GAS in place of traditional grouted anchors, meaning that Eq. (6-16) and Eq. (6-17) will determine the capacity curve and performance. According to Eq. (6-17), the allowable sliding capacity of the dissipative device Δu_{DEV} is set equal to 30mm.

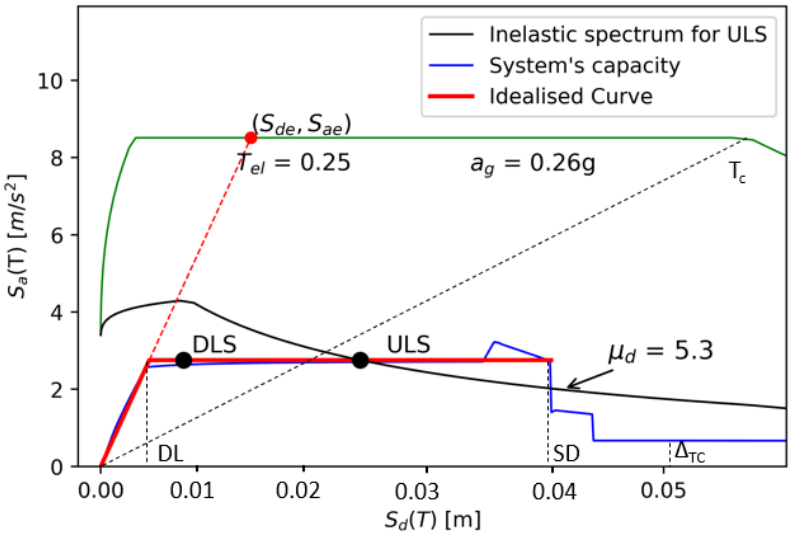

Figure 6-14 Capacity curve and design check for wall strengthened by a dissipative device connected to grouted anchors (D-GAS).

The performance points corresponding to the Damage and Ultimate limit states, shown in Figure 6-14, are both on the horizontal branch of the idealized system's capacity curve, meaning that the seismic demands will activate the device. The device determines an increment in the displacement capacity, with a "rigid shifting" of the critical points corresponding to "yielding" and "ultimate" displacement by a quantity equal to the device's displacement capacity. As a result, at the ULS limit state the device exploits half of its full sliding capacity. Moreover, the increased ductility determines a smaller acceleration demand which can be controlled by two

anchors rather than four, thus reducing the impact on the aesthetic of the building, the installation costs, and the loss of original material.

In conclusion, the use of the D-GAS has the main advantage of reducing the number of anchors required. This is simply explained considering that a smaller number of anchors determines a smaller value of yielding acceleration S_{ay} and reduces the initial stiffness of the system resulting into a larger elastic period and ductility demand μ_d. Therefore, it is obtained that the inelastic demand is smaller in terms of accelerations and, from Eq. (6-8), larger in terms of displacement. A summary of the analyses' results performed for the different configurations is given in Table 6-4. The performance points for the DLS and ULS are compared to the DL and SD thresholds for each system, highlighting that the D-GAS provides the best design solution, as the implementation of the dissipative devices reduces the number of required anchors by 50%. For sake of comparison, the values of stiffness of each system normalized to the stiffness of the wall in the unstrengthen configuration are reported in Table 6-4, as well as the ductility capacities.

Table 6-4 Summary of displacement demands and capacities for the wall in different configurations

Configuration	Disp capacity at DL Δy [m]	Disp capacity at SD Δu [m]	Disp demand DLS Δ_{DLS} [m]	Disp demand ULS Δ_{ULS} [m]	Normalized Elastic stiffness [-]	Ductility capacity μ_c [-]	$\Delta_y > \Delta_{DLS}$	$\Delta_u > \Delta_{ULS}$
Original	0.007	0.05	0.03	0.07	1	7.4	NO	NO
3 GAS	0.003	0.01	0.002	0.013	15.1	3.3	YES	NO
4 GAS	0.003	0.01	0.002	0.008	21.95	3.3	YES	YES
2 D-GAS	0.004	0.04	0.008	0.026	6.5	9.3	Yes-Sliding	Yes-Sliding

6.5 Dynamic analysis of case study structure

The performance of the case-study structure is investigated by non-linear time history analysis to validate the results of the design procedure based on a static approach. Two model are presented: the first assumes that the OOP mechanism can be modelled as a rigid block rocking on a flexible foundation and neglects the connection between the front and the side walls. The second is a FEM model that simulates the detailed geometry of the structure and the connection between walls. Due to the high level of detail and complexity, the second model has a higher computation cost.

6.5.1 Rigid body model – the original configuration

The resulting rocking motions of the unstrengthen wall for the DLS and ULS scaled accelerogram are reported in Figure 6-15 , along with the accelerations at the Control Point (CP) and the damage thresholds. For the seismic acceleration scaled to the DLS the maximum displacement of the control point exceeds the DL limit Δ_y, namely the displacement corresponding to the beginning of the plastic phase on the idealized curve. Similarly, for the ULS, a maximum displacement of 0.12 m is reached at about 2 seconds, well above the displacement of the SD threshold Δ_{TC}, reported in Figure 6-15 b as a red dotted line. Nonetheless, the wall survives the ground motion and the OOP failure: the rotations are about 12% the ultimate rotation α that the wall can withstand.

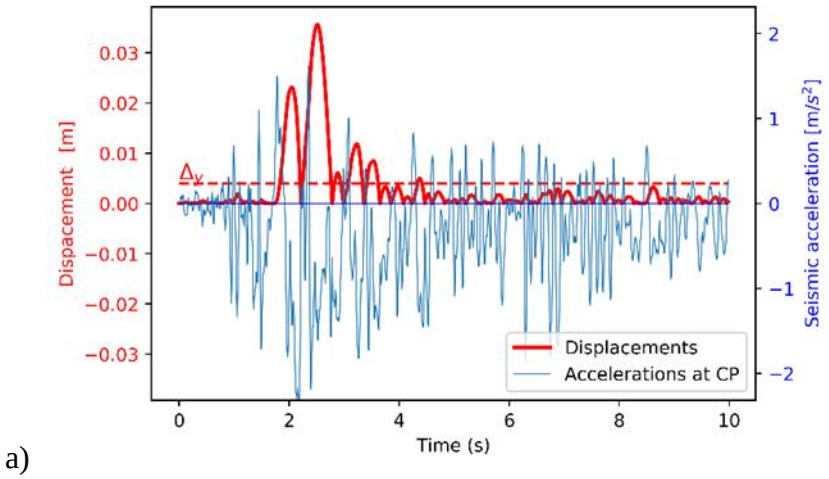

a)

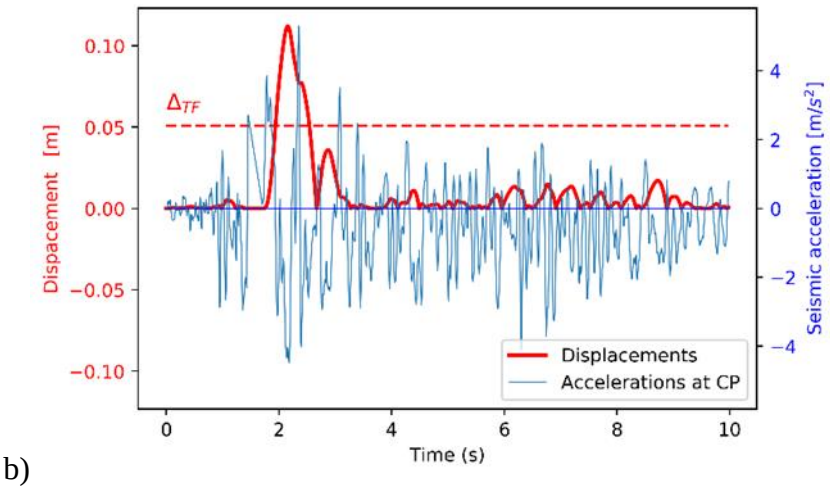

b)

Figure 6-15 Rocking motion of unstrengthened wall: displacements of control point and seismic input a) for the Damage control state design accelerogram b) for the Ultimate limit state design accelerogram

These results are in line with what obtained by the DB approach, which predicted that the displacement demands would exceed the damage thresholds for both limit states. Nonetheless,

the maximum displacement at ULS ($\Delta_{max,rk}= 0.12m$) is 70% larger than the corresponding displacement predicted by static analysis ($\Delta_{ULS}= 0.07m$) as it is recognised that the period of vibration of rocking walls depends on the oscillation's amplitude (Housner 1963; Sorrentino et al. 2017). Therefore, for large magnitude of OOP displacement computed using conventional elastic-based capacity curve, the oscillation's amplitude could be highly underestimated and the most accurate way to assess the wall displacements is to compute the wall response by integrating the equations of motion. In fact, the displacement $\Delta_{max,rk}$ well represents the damage extent observed onsite for the considered building.

Conversely, good agreement between static and dynamic demand is obtained for the DL limit state where the vibrations have smaller amplitudes: the dynamic response confirms that the maximum base rotation is below the rotation limit for the toe-crushing failure and the maximum displacement of the control point is only 16% larger than the one predicted by the DB approach.

A second dynamic analysis is performed for the wall strengthened by traditional grouted anchors and the dissipative anchoring system to check the design solutions proposed in the previous sections. Moreover, the analysis aims at evaluating the dissipative capacity of the D-GAS compared to a traditional anchoring system.

6.5.2 Rigid body model – The strengthened configuration

The direct integration of the equation of motion is performed for a model of rocking wall including the strengthening systems. For the GAS, Eq. (6-22) is solved considering the design obtained following the FB and DB approaches to check if the number of anchors is sufficient to prevent the wall from experiencing large rocking oscillations. The rocking motion displayed in Figure 6-16 a shows that the anchoring system fails if 3 anchors are placed on each side of the façade: the anchors reach their full load and displacement capacity at about 2 seconds when the horizontal displacement of the CP is equal to 1 cm. It is assumed that the wall behaves as if unstrengthened after the anchor's failure (point "AF" in Figure 6-16 a) even if they would keep providing a restraining action on the façade in a real scenario. Nonetheless this action would be limited as highlighted by pull-out tests where the anchor's force reduces up to 70% for large slippage (Moreira et al. 2014; Paganoni and D'Ayala 2014) and it is safely assumed equal to zero.

With reference to the case of an unstrengthen wall, it is evident that the GAS determines a change in the wall's response, delaying the peak oscillation's amplitude. Nonetheless, after the

anchors have failed, large horizontal displacements that would cause severe damages and cracks to the structure are computed.

The analysis confirms that the dimensioning of the GAS provided by the force-based design is not adequate. As the system has limited ductility, the value of behaviour factor q =2.0 assumed in Eq. 6-28 in accordance to the code's (EN 1998-1:2004 2004) suggestion to compute the horizontal acceleration multiplier should be reduced, as there is no guaranty that once the motion is activated the ultimate displacement is not exceeded. The value of q = 1.0 suggested by (Sorrentino et al. 2017) for rocking systems with limited displacement capacity should be used in Eq. (6-29) instead to determine the correct number of anchors.

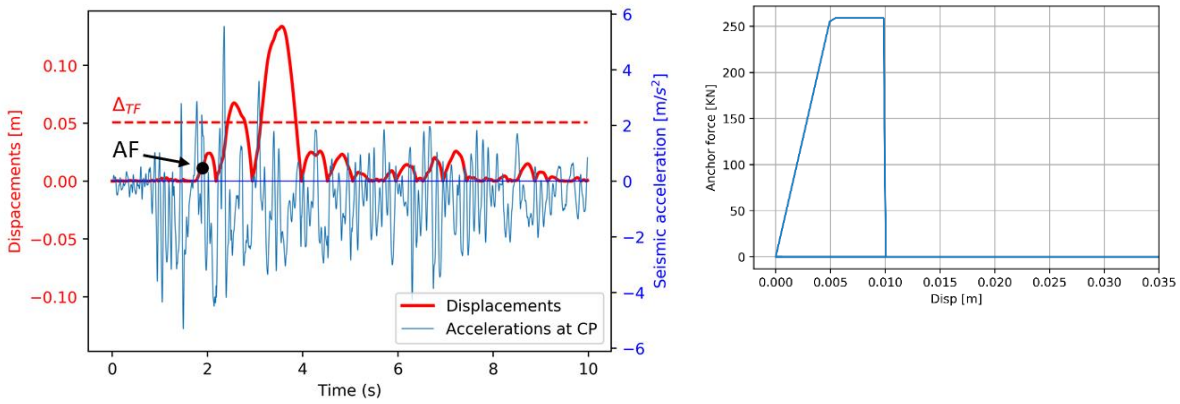

Figure 6-16 Rocking motion of wall strengthened by GAS: a) displacements of control point and seismic input, b) load-displacement loops of anchoring system if three anchors are provided.

A third dynamic analysis is conducted considering the number of anchors (n = 4) suggested by the DB approach with the resulting displacement history shown in Figure 6-17 a. As shown in Figure 6-17 b, the GAS yields, but it does not fail for the whole duration of the seismic action, as predicted by the static method.

The anchors undergo a large number of oscillations with small amplitude due to the high stiffness of the system. Despite the large number of oscillations, the amplitude of the rotations is below the anchor's yielding threshold (Δ_y in Figure 6-17 a) in more than 50% of the cases, resulting in a small value of dissipated energy, as reported in Table 6-5.

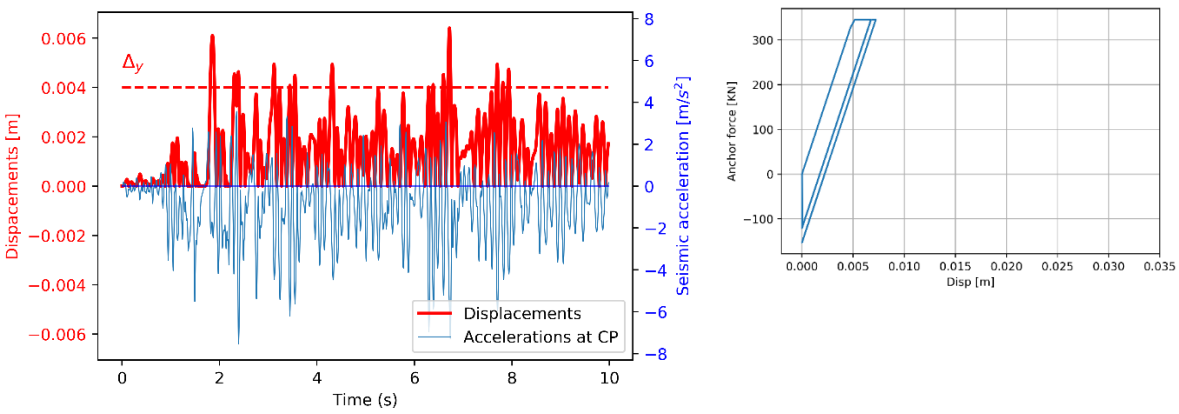

Figure 6-17 Rocking motion of wall strengthened by GAS: a) displacements of control point and seismic input, b) load-displacement loops of anchoring system if four anchors are provided.

Finally, the analysis is performed for the case of wall strengthened by the D-GAS. According to the DB design, two anchors equipped with the dissipative device are considered on each side to connect the façade to the side walls. The device is set to start sliding at 80% of the maximum capacity of the single anchor ($C_{DAS} = 0.8$). According to the displacement limit indicated by Eq. (6-18) the allowable run of the device is set at 30 mm, which corresponds to an improvement in displacement capacity with respect to the GAS of $\eta = 4$. The rocking motion and dissipative loops are reported in Figure 6-18. The maximum amplitude of the rocking motion is about 29mm (Figure 6-18a), which well agrees with the displacement capacity identified by the performance point for the ULS. The device provides additional displacement capacity to the anchoring system, which slides without failing for the whole duration of the seismic event.

This results in a large dissipation capacity: the area enclosed within the hysteresis curve shown in Figure 6-18b represents the energy dissipated by the anchor for the duration of the seismic input and corresponds to 50% of the energy imparted to the system by the seismic input. Figure 6-17 b and Figure 6-18b show that the force-displacement relationships derived in section 6.2.2 and 6.2.3 are displacement dependent, as the obtained hysteretic curves are typical of displacement dependant devices, such as friction devices (see Figure 2.8 for a comparison with the idealized force-displacement loops of hysteretic friction devices).

Also, the friction device of the D-GAS works as a “braking system” providing an acceleration which is always opposite in direction to the seismic one, thus reducing by 36% the maximum acceleration that the system experiences compared to the unstrengthen wall. As a result, the maximum displacement occurs at the beginning of the considered seismic action, while smaller oscillations are recorded after the device starts dissipating.

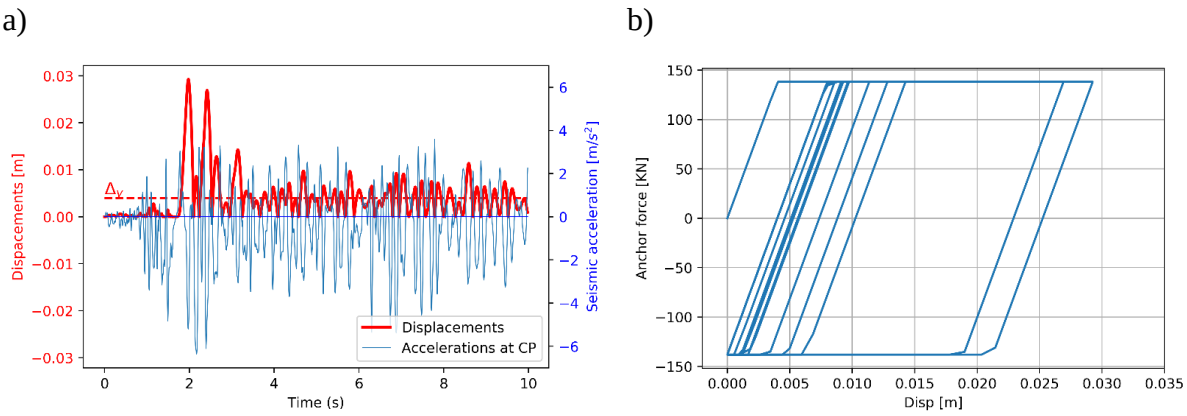

Figure 6-18 Rocking motion of wall strengthened by D-GAS: a) displacements of control point and seismic input, b) Dissipative loops of two D-GAS per side.

Table 6-5 summarise the results of the dynamic analysis for the four configurations and the two limit states. The overall performance of each configuration is expressed through the ratios γ and β: the first defined by Eq. (6-27) account for the percentage of energy dissipated during the motion with respect to the input seismic energy. The second (Eq. 6-27) represents the agreement between the displacement demand computed by static approach and the dynamic maximum displacement

Table 6-5 Summary of time-history analysis performed for the wall in different configurations

Configuration	η [-]	Seismic Energy E_I [Kg m²/s²]		Dissipated Energy $E_{D\ (GAS/DAS)}$ [Kg m²/s²]		γ [-]		Max acceleration a_{max} [m²/s²]		Max displacement $\Delta_{max,rk}$ [m]		β [-]	
		DLS	ULS	DLS	ULS	DLS	ULS	DLS	ULS	DLS	ULS	DLS	ULS
Original	-	1207	3582	0	0	0%	0%	1.61	5.57	0.035	0.12	0.86	0.6
3 GAS	1	538	5576	0	194	0%	3%	1.41	5.55	0.002	0.13	1.00	0.10
4 GAS	1	524	3291	0	48	0%	1%	1.68	3.56	0.002	0.007	1.00	1.14
2 DAS (C_{DAS} = 0.8)	4	611	3533	7.6	1776	1%	50%	1.41	3.54	0.005	0.029	1.60	0.90

At DLS the amount of energy dissipated by the anchorage with and without the device is negligible, between 0 and 1% of the input energy. This is simply explained considering that the anchor remains in its elastic phase and that the seismic load is sufficient to induces just few millimetres of slippage in the devices. Good agreement is found between the seismic displacement demand and the maximum displacement obtained by rocking analysis, with values of β close to 1 in most of the cases. This means that the $\mu - T$ relation presented in Eq. (6-9) provides a good approximation of the ductility and energy dissipation of the system and therefore can be adopted also for the case of rocking walls strengthened by traditional and innovative anchors. Only for the 3 anchors-system, the displacement demand for the ULS is 10 times smaller than the one obtained by NLTHA: as pointed out before, this anchoring design is

not sufficient to resist the displacement demand and would lead to the failure of the system after which large displacement are obtained.

In conclusion, both the GAS with four anchors and the D-GAS with two anchors provide effective strengthening solutions, but it is clear that the D-GAS represents the best design in term of reduced accelerations, energy dissipated, and minimal disruption to the system's integrity. The comparison with the results of the dynamic analysis, shows that the design procedure is able to provide a reliable method for determining the vulnerability of walls to OOP failure and the optimal strengthening solution to control such motion and prevent severe damages to the structure.

As already discussed, both methods of analysis present several simplifications and assumptions, such as the lack of traction and friction capacity of the connection to resist the seismic action and presence of openings on the façade. To investigate the influence of these factors on the dynamic response of the front wall and to validate the design tool, a detailed model of the front and side wall of the building is implemented in Abaqus. In the next Section the rocking motion of the church façade is investigated and compared to the one obtained with the 2-dimensional model.

6.5.3 FEM model – Geometry and model validation

A portion of the church selected as case study is reproduced in a FEM model to investigate the behaviour of the structure under seismic input and determine in detail the rocking motion of the front wall for different strengthening solution. As previously discussed, the model combines several modelling techniques, such as the use of cohesive interfaces to model the interaction between adjacent walls and the bonding strength of the anchors.

To reproduce failure mode displayed by the structure after the L'Aquila earthquake of 2009 and reduce the computational cost of the analysis, it is decided to model only a portion of the building, the façade and the sidewalls, as it is assumed that the remaining of the structure and the presence of the surrounding buildings did not significantly affect the rocking response of the structure. The roof and the belfry are considered only in terms of stiffness, mass, and constraints. The complete numerical model is shown in Figure 6-19.

a) b)

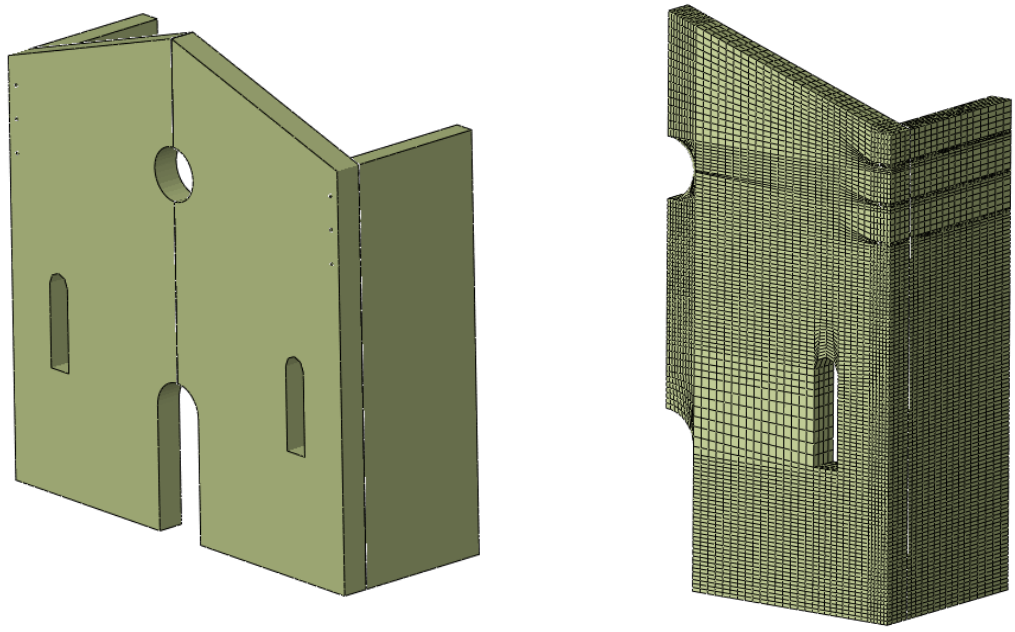

Figure 6-19 a) Complete numerical model of san Giuseppe dei Minimi (IT) b) meshed model cut along symmetry plane

The results obtained from the previous numerical activity showed that the cohesive elements can effectively be used to model the equivalent traction capacity of masonry connections. Therefore, the cohesive interfaces introduced in Section 5.5.3 to model the connection of the T-shaped specimen are here used to reproduce the poor-quality connection between the façade and the side walls.

A set of 13 cohesive interfaces (*n=13*) are implemented along the height of the wall's interface to reproduce the poor-quality connection between the façade and the side walls. They are assigned with an equivalent traction capacity in the direction of their thickness *T*. As shown in Figure 6-20 a, each j-*th* interface represents 10 courses, equivalent to a strip of wall 1m high, and has a traction resistance $t_{n,j}$ equal to the slip resistance offered by that portion of wall C_j divided by the interface area:

$$t_j = \frac{C_j}{A_{interf}} = \frac{C_j}{1\ t} \quad for\ j = 1,2,..,13 \tag{6-31}$$

Where t is the thickness of the side wall. C_j can be computed according to Eq. (5.28) of Chapter 5 assuming zero pressure p, a bond strength f_{bond} equal to 0.2 MPa estimated from the compressive strength of the masonry reported in Table 6-1 and for a type of lime mortar comparable to the one characterized In Section 5.3.2.

As the shear stress linearly increases with the compressive stress, the interfaces have higher equivalent traction resistance moving from the top to the bottom of the wall. The graph Figure 6-20 b shows the values of equivalent traction resistance according to the location of the interfaces as measured from a control point (CP), referenced in Figure 6-20 a. CP is a node of the facade at 0.8m from top of the side walls, which is a possible level for the insertion of the top anchor if a strengthening scheme is designed. This choice will ease the results comparison between the results obtained from model for the original and strengthened configuration.

a) b)

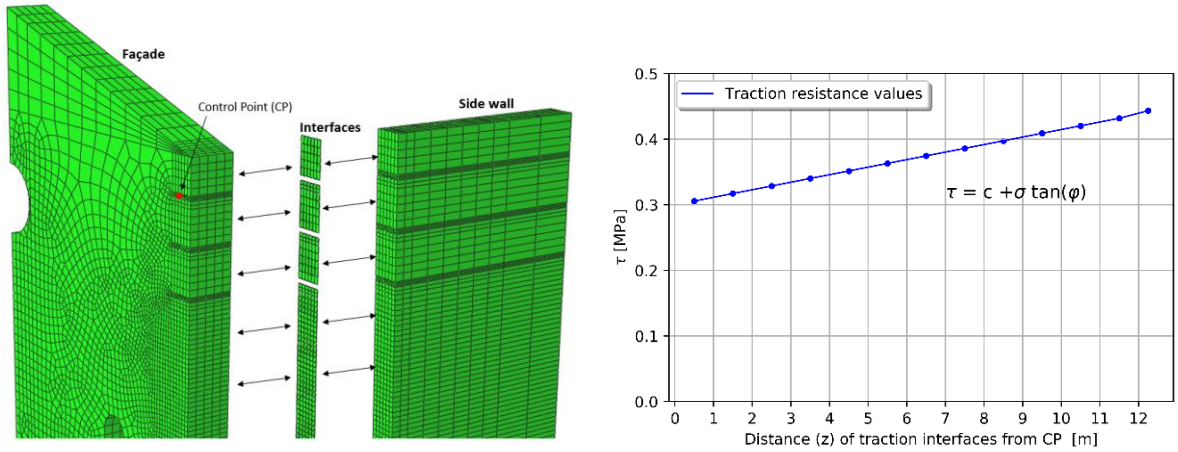

Figure 6-20 Model of unstrengthened walls: a) location of interface part with respect to walls b) Traction resistance of the cohesive interfaces along with the height of the wall

The resulting constitutive laws assigned to the cohesive interface at z = 0 m (upper interface) and the cohesive interface at z = 12.5 m (lower interface) are shown in Figure 6-21 . The strains are expressed as a percentage of the initial thickness of the interface (T=2 mm).

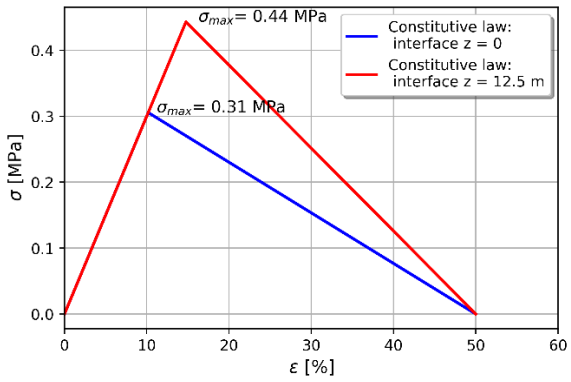

Figure 6-21 Constitutive laws of cohesive interface at z = 0 m (upper interface) and z = 12.5 m (lower interface)

The shear strength of the cohesive interfaces representing the bonding capacity of the anchor is computed from Eq. (5-15) considering the results of the pull-out test and the additional contribution of the self-weight of the wall. The parameters defining the material's properties of each part are shown in Table 6-6.

Table 6-6. Material parameters for numerical model

	Material Parameters						
Part	E [MPa]	G1 [Pa]	G2 [Pa]	Mass Density [ρ] [N/m^3]	Maxs Traction [σ_t] [MPa]	Damage Initiation [γ_0] [-]	Ultimate damage [γ_u] [-]
Façade	1500			2141			
Side walls	1500			2141			
Interface (i)	1500	1500	1500	2141	$s[nc_0 + \sum h_i(\gamma g) \tan(\phi]$	σ_t / E	$\Delta u / T$

Initially the model is analysed in its original, unstrengthen configuration to verify the initial set of assumptions and calibrate the model. A modal linear analysis is performed to compare the modal shapes and natural frequencies with those experimentally obtained by other authors for the selected building (Paganoni 2015). The results represent a good agreement with small differences that can be ascribed to the fact that the model represent the building in its undamaged configuration, while the dynamic characterization was carried out on the damaged structure. The model is able to capture the fact that the out-of-plane bending of the façade is the main mode. The result reported in Figure 6-22a is compared to the frequency value obtained by Paganoni (2015) who modelled the structure in Algor Simulator also using 3D elements (Figure 6-22b), and with the results measured by the University of Padua, UPD, through dynamic characterization of the damaged structure (Figure 6-22c).

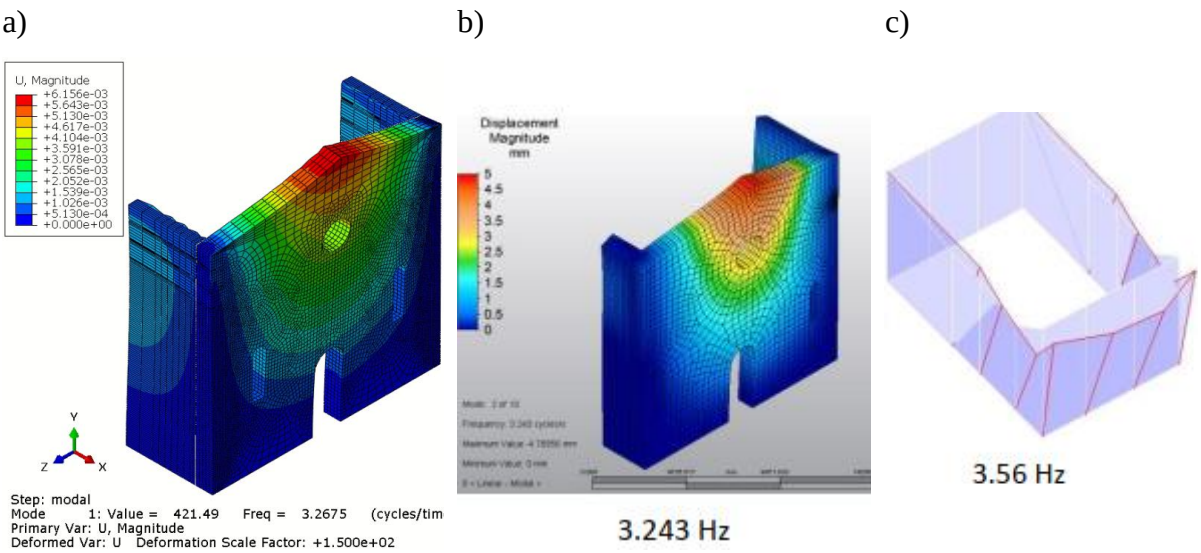

Figure 6-22 Natural frequency and shape of the main vibrational mode as obtained by a) Abaqus, b) Algor, c) UPD monitoring system

The numerical analysis carried out on Abaqus aims at providing a realistic model able to capture the one-sided rocking motion of a masonry wall under seismic acceleration. It is of primary importance to determine if the Abaqus Implicit solver is accurate at the instant at which impact occurs to avoid unrealistic attenuation or amplification of the rocking response. Therefore, a free-rocking analysis is performed to compare the numerical coefficient of restitution e_{abaq} to the analytical values e_{ana} available in the literature. Compared to two-sided rocking, few experimental tests have been performed to explore the coefficient of restitution for one-sided motion. From the experimental results reported by Sorrentino and Al Shawa (Sorrentino, AlShawa, and Decanini 2011; Alshawa et al. 2012), it emerges that energy dissipation is not constant at every impact but amplitude-dependent: larger dissipation is associated to larger impact velocities. The value of *e* suggested by the authors and reported in Eq. (6-23) is used as reference to validate the coefficient of restitution obtained by the Abaqus analysis. The former is calculated by Eq. (6-23), while the latter by the definition of coefficient of restitution, e.g. by dividing the velocity just after impact with the one just before it.

To study the one-sided-rocking motion, an initial rotated configuration was imposed to the façade. The façade is disconnected from the side walls by suppressing the vertical cohesive interfaces and it is rotated by $\theta_0 = 0.65\alpha$, which corresponds to a horizontal initial displacement of the control point of 0.6m. Figure 6-23 a) reports the results of the free-rocking analysis in terms of displacements and velocities over time of the control point CP. Figure 6-23 a) also reports the results of the rocking analysis performed by direct integration of the Eq. (6-22) for the free-vibration case ($\ddot{u}_g = 0$). The equation is solved considering a rectangular rigid block resting on a flexible interface, whose mechanical behaviour is defined by Eq. (6-3).

For both models, the rocking motion of the façade ceases after 4 impacts with the side constrain, where the first impact occurs at about 1.75s. Some difference between the evolution of the rocking motion after the first impact can be noted. At every impact, similar velocities are recorded at the instant when the façade hits the foundation (red dots in Figure 6-23b), but larger rebound velocities (blue dots) are computed for the Abaqus model, leading to larger oscillations' amplitude.

Moreover, the impacts do not result in an immediate rebound of the façade that bends inwards, as the thickness of the side wall is only 1/8 of the façade depth and therefore the lateral constrain is limited to the corner portion of the structure. Conversely the rigid block displays a perfect rebound at each impact, as it is assumed that the lateral constrain acts on the full depth of the block.

a) b)

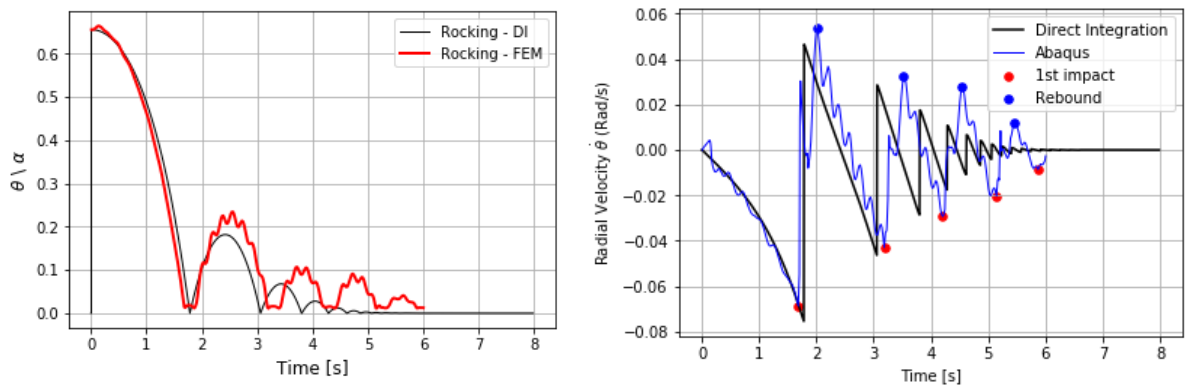

Figure 6-23 a) Normalized base rotations and b)velocities over time of the control point CP for free-rocking analysis. Comparison between Abaqus output and direct integration of the Eq. (6-22)

For the Abaqus model, the impact with the side walls reveals the existence of high-order vibration components, as a secondary oscillation occurs in the longitudinal direction of the wall. The second-order oscillation are obtained by the model as the façade is modelled as a deformable 3D part while they are not detected if the wall is modelled as a rigid block. The coefficients of restitution are reported in Table 6-7 along with the analytical one, which by definition does not change during the analysis.

Table 6-7. Coefficients of restitution obtained from Abaqus model and direct integration

Impact number	Time instant [s]	Velocity [m/s]		Coefficient of restitution [-]		
		1st impact	rebound	e_{Abq}	e_{Ana}	Δ [%]
1st	1.68	0.8	-0.62	-0.78	-0.62	26%
2nd	3.18	0.5	-0.377	-0.75	-0.62	21%
3rd	4.2	0.34	-0.32	-0.96	-0.62	54%
4th	5.14	0.23	-0.13	-0.58	-0.62	-7%

Comparing the numerical and analytical values of the coefficients of restitution, it is found that e_{abq} is larger than the analytical value for the first 3 impacts and smaller by 7% for the last impact. Thomaidis (Thomaidis, Camara, and Kappos 2017) compared the rocking response of a 2D Abaqus model to that of a 2D rigid block and reports a difference between numerical and analytical values that ranges between -13% and +7%. The larger difference found in this work can be ascribed to the tridimensionality of the Abaqus model, to the different shape of the façade with respect to the rigid block, to the presence of openings and the different lateral constrains.

6.5.4 Ground motion sequences

The modal analysis showed a good agreement with the natural frequency obtained by other authors and captured the fact that the out-of-plane bending of the façade is the main mode. The

free vibrational analysis presents analytical values of coefficient of restitution similar to the ones computed according to Eq. (6-23). Although they are computed with different approaches (Internal solver for Abaqus, conservation of the angular moment and calibration with experimental data for Eq. (6-23)), the energy dissipated at each impact of the façade with the side walls is comparable.

For the next analysis, the recording of the ground motion acceleration obtained during the 2009 earthquake in L'Aquila is applied to the Abaqus numerical models to determine the response of the structure to seismic input. For sake of comparison with the DI numerical approach, the L'Aquila ground motion is scaled to the Damage Limitation (DL) and the Significant Damage (SD) limit states presented in the displacement-based design.

For these analyses, the façade and the rigid block start from a vertical resting position and the interfaces presented in the paragraph 6.5.3 - modelling the weak connection between adjacent walls - are implemented. To reduce the computational time the analysis is restricted to the first 8 seconds of the recorded ground acceleration which contains the largest accelerations.

The resulting rocking motions for the two limit states are reported in Figure 6-24 and show a good agreement in terms of oscillations' amplitudes with the DI method. This result highlights that the latter can be used as a simple assessment tool to determine the vulnerability of heritage buildings to OOP failure. At about 1 second, the seismic accelerations induce the maximum value of traction stress in the upper interface elements, causing their failure. Once the damage is initiated, it propagates down the height of the wall and the orthogonal walls start oscillating independently. The CP experiences a maximum relative displacement from the sidewall of 0.11 m at time step 2.450 s and the height of the separation at the end of the analysis is about 6.8 meters.

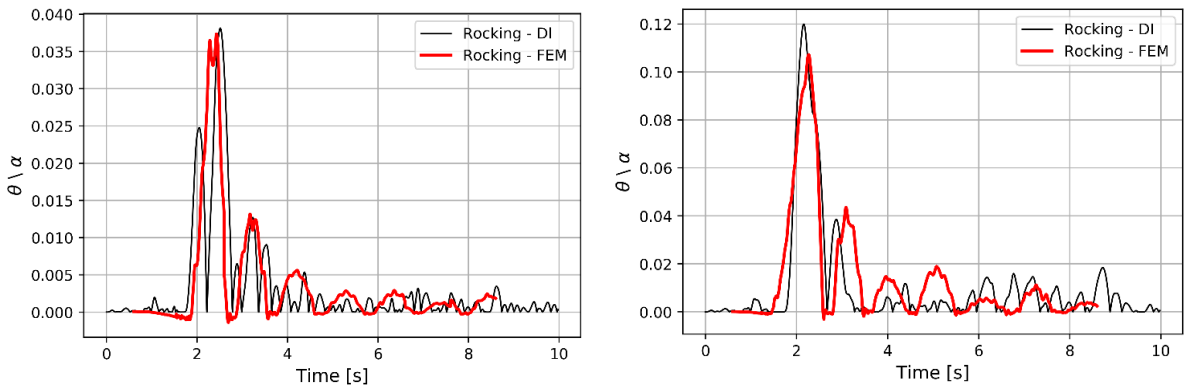

Figure 6-24 Rocking motion of front wall for a) Damage and b) Ultimate Limit state

These results show that the FE model is able to reproduce the typical failure mechanism detected on site in the aftermath of a seismic event, when major cracks at the interface between cross walls are often observed. The analysis shows that the connection capacity simulated by the interfaces is not sufficient to restrain the walls. The lack of effective lateral constrains determines the façade detachment from the side walls and it deforms similarly to a cantilever beam undergoing bending. The model is deemed suitable for predicting the response of the structure in other case scenarios, for instance the structure strengthened by grouted anchoring systems.

6.5.5 The strengthened structure

A second model is implemented to investigate the benefit of introducing a strengthening system able to improve the connection between the cross walls that experienced mutual separation.

As previously done, two strengthening systems are compared: first the GAS is implemented modelling a set of metallic anchors which reconnect the sets of perpendicular walls. The anchors are embedded within the thickness of the walls mimicking a real installation: a cylindrical shaped hole is cut into the front and side wall to fit the anchors which are modelled by means of three-dimensional elements. A set of cohesive interfaces are defined to govern the mutual interaction between the anchor and the surrounding part. As discussed in Chapter 5, the cohesive interfaces are able to reproduce the bonding action between the anchor's grout and the masonry as well as the damage evolution once the maximum shear capacity is reached. The anchors are placed along the height of the façade according to the layout determined by the design procedure, as shown in Figure 6-25a.

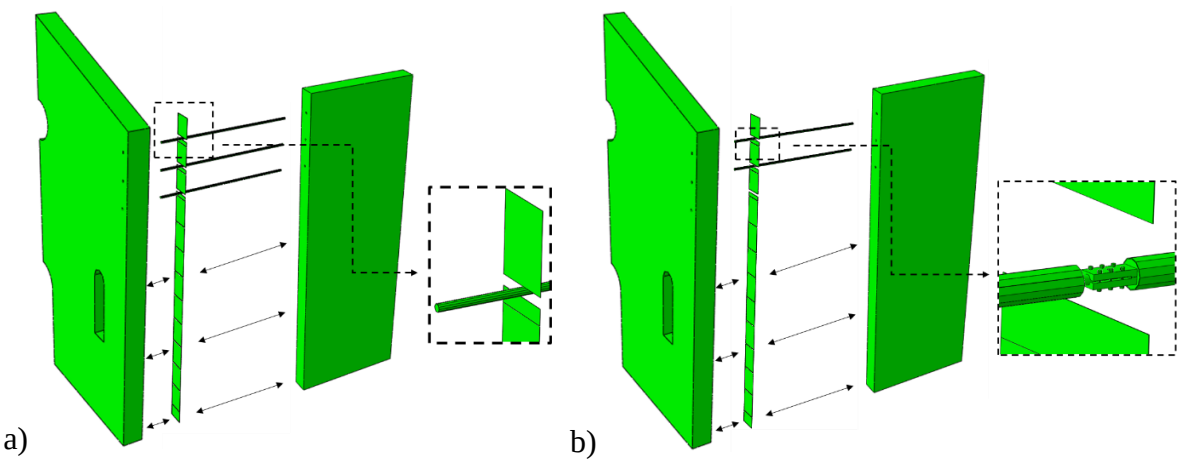

Figure 6-25 Numerical model of the structure in the strengthened configuration: implementation of a) three GAS and b) two D-GAS

Three anchors are modelled to validate the results of the static and dynamic analyses presented in Section 6.4, which showed that the anchors would fail for a seismic acceleration corresponding to the ULS. The obtained rocking motion is plotted in Figure 6-26 , where the rotations are normalized to the value of the ultimate rotation α that the wall can withstand. For sake of comparison between the two dynamic analyses, the rocking obtained by direct integration (DI) of the equation of motion is also shown. The Abaqus analysis stopped at about 2 seconds after the anchors have all experienced debonding from the surrounding part, which happened for a normalized rotation of about 0.01. For this base rotation, the cohesive interfaces modelling the bond capacity of the anchors fail due to large shear deformations and the dynamic impacts between the anchor and the walls determine convergency problems to the Abaqus solver, as their mutual interaction is no longer defined.

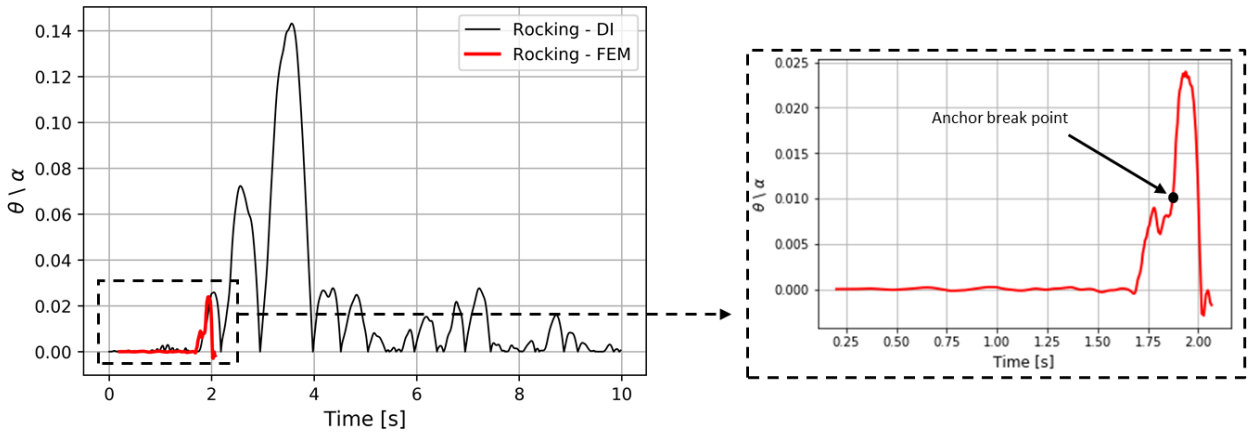

Figure 6-26 Rocking motion for wall strengthened by 3 grouted anchors

As already commented for the dynamic analysis by direct integration, the GAS determines a change in the wall's response compared to the unstrengthened configuration, delaying the peak oscillation's amplitude, but large oscillations can be expected as the structure would behave as unstrengthened after the anchor's failure.

A second dynamic analysis is performed modelling the dissipative device and connecting it by tie constraint to two portions of the steel ties, as shown in Figure 6-25b. The position of the device at the interface between the two walls is strategic to exploit the rocking motion that the structure displays for large base accelerations. Two D-GASs are implemented on each side of the structure to reproduce the strengthening layout proposed in Section 6.3.3. Figure 6-27a shows the normalized rocking motion: the walls separate, and the rocking amplitude remains within the maximum run of the device, thus avoiding the anchor's pull-out. The energy dissipated by the device during the time step of the simulation is represented by the area within

the load-displacement-loops, which are shown for the topmost anchor in Figure 6-27b. Considering the contribution of the four D-GAS (two on each façade-sidewall connection) it is computed that 45% of the input energy was dissipated by the devices. This results in a reduction of maximum acceleration experienced by the façade. Comparing the model with two D-GAS per side with the unstrengthen model, 50 % reductions in maximum accelerations is obtained, as shown in Figure 6-28. The reduced accelerations and the smaller oscillation's amplitude would result in an improved control of the pounding effect, preventing side damages on the walls at the moment of the impact between walls.

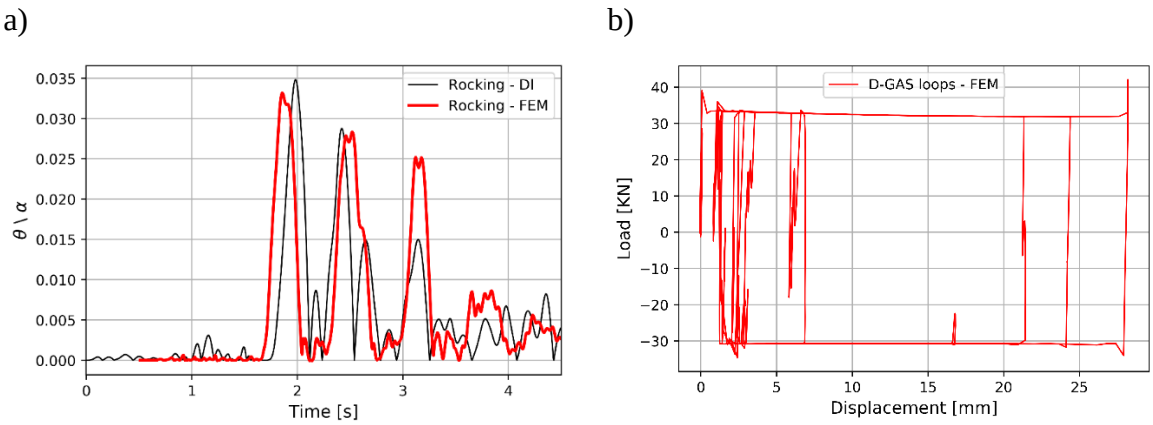

Figure 6-27 Normalized rocking motion of façade strengthened by D-GAS, b) Load-displacement loops obtained from the FEM analysis for the device connected to the topmost anchor.

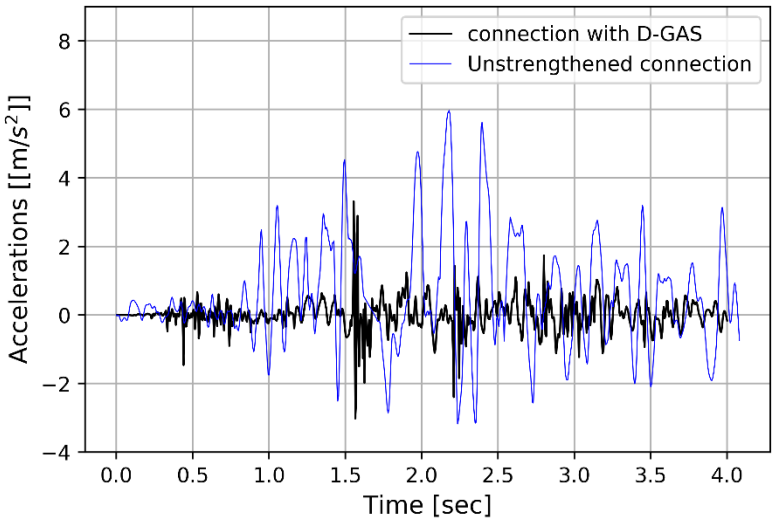

Figure 6-28 Accelerations at CP for the structure in the unstrengthened configuration and strengthened by 2 D-GAS

These results are in good agreement with the ones obtained by direct integration of the motion equations. However, the two methods of analysis are quite different.

The Abaqus model presents a higher level of detail. This results in a more accurate analysis of the building performance: for instance, the presence of cohesive elements at the wall's interface allows simulating the connection's strength that opposes the external loading, which is neglected in the DI model, and in turn determines the crack's height. This difference has little influence on the response of the case-study structure because poor-quality connections were assumed (thus the need for the anchoring system), so that the interfaces reached their maximum strength/slip capacity for small accelerations. Conversely, this modelling technique can significantly change the structural response if good-quality connections are assessed as a result of a site inspection, as they could delay or avoid the wall's separation.

The Abaqus analysis presents a considerably higher computational cost compared to the DI method. Its use should be preferred to perform the structural analysis of a single masonry building in need of seismic upgrade against OOP failure, but it becomes unfeasible to assess the seismic vulnerability of the historical building portfolio of a region. For this type of analysis, the model developed in Python would represent a better tool as it only requires the knowledge of the front wall's geometry and its mechanical properties. Having assessed the vulnerability to OOP failure, the combination of the DI method with the static design procedure can be used to perform the preliminary design of an anchoring system.

6.6 Conclusions

To conclude the validation process followed in this dissertation, Chapter 6 presents the development of a design procedure for the dissipative anchoring system and discusses it with reference to an example of its implementation to a case-study structure.

The development of a design procedure is deemed crucial for the application of the D-GAS concept to real case studies. In fact, the paucity of innovative, ductility-based strengthening techniques applied to heritage structures might indeed be ascribed, among the others, to the lack of detailed prescriptions: although design codes stress the importance of providing effective connections, prescriptions on how to effectively achieve that remain mainly qualitative.

Strengthening techniques based on damping systems and ductile elements would bring considerable advantages to the seismic protection of historic buildings. The reduction in load demand and the possibility of controlling the structural response for different performance levels are two among the considerable benefits one could resort. The fact that strength-based

techniques are still widely applied in practice points out to the difficulties of end users in sourcing reliable methodologies for the design of strengthening solutions based on ductility and energy dissipation concepts.

In the previous chapters, the focus has been purposely on data collection and result's interpretation to investigate the parameters meaningful to the performance of the grouted anchoring systems (GAS) and its innovative counterpart (D-GAS). In this Chapter, this experimental and computational data is implemented in an analytical model that can be used to assess the vulnerability of walls to out-of-plane failure and design a strengthening solution based on these anchoring systems. The method is based on a set of threshold displacement values that the wall in each configuration (unstrengthened wall, wall with GAS, wall with D-GAS) should not exceed to preserve its integrity during rocking motion. These represent the system's capacity. Then the performance points for the system with respect to the design seismic actions are computed, thus obtaining the displacement seismic demand. The assessment of the walls vulnerability in the original state and the feasibility of using either the GAS or the D-GAS system to control the tilting mechanism is carried out verifying that the displacement demands are smaller than the threshold values.

Finally, to verify the design procedure and quantify the benefit of adding the dissipative device to grouted anchors, the design solutions proposed for the GAS and D-GAS are compared looking at the dynamic evolution of the wall in each configuration obtained performing a non-linear time-history analysis. For this analysis two models are proposed: the first, developed in Python, has a reduced computational cost and provides an immediate estimation of the dissipated energy during the rocking motion. The second, developed in Abaqus and based on the modelling techniques developed in the previous chapters, has a higher computational cost as it accounts for a detailed description of the structure's geometry and capacity, for instance by including the equivalent traction capacity of the wall's connections.

Some key assumptions are made in developing the model, such as a vertical crack at the wall's intersection and considering the portion of anchor grouted in the side wall as fixed. This assumptions are based on the evidence of past experimental tests' results (Paganoni 2015; G. Maddaloni et al. 2016)) and on an experimental activity carried out by the author on the T-shaped connection. Throughout this work, it is assumed that the rigid rocking motion of the front wall is the occurring failure mode because D-GAS is specifically designed to tackle this failure mode and other mechanisms are not considered. This focus is supported by field investigations carried out in the aftermath of seismic events in several regions Speranza

(referenced in Chapter 2) and predictive models such as the FAMiVE model developed my D'Ayala and Speranza which highlighted that such mechanism leads to the highest level of structural damage and danger for people. The D-GAS is designed to improve the pitfalls of anchors such as the bonding failure of the grouted portion and the experimental tests have highlighted that a strengthened masonry connection developed a single body rocking motion preventing the development of a two-body rocking system, which presents a higher level of complexity and unpredictability. However additional large-scale testing should be performed to investigate the behaviour of the D-GAS on other failure mechanisms that might develop and ensure that the D-GAS does not have a penalizing influence them. For instance, once the vertical overturning is prevented, then two mechanisms can occur: a vertical arch with maximum displacement between the hinge and the position of the anchor and if the anchors are positioned too far horizontally between them a horizontal arch failure can develop. Both require higher collapse load factor than the overturning. Therefore, they will need to be computed with the new constraint conditions determined by the presence of the D-GAS.

The method is applied to the façade of the oratory of San Giuseppe dei Minimi, which rocked without collapsing during the L'Aquila (IT) 2009 earthquake to compare the performance of the historic building in its original configuration, and as restrained by grouted anchoring system with and without the device inclusion.

The results show that the unstrengthened façade would display large displacements under the considered seismic action causing large crack openings at the corner connection. In fact, this conclusion is in line with the crack pattern and damage extent observed on site. The implementation of the GAS significantly increases the connection's stiffness and prevents the crack opening. Given the limited displacement capacity that the anchor display, the design of the GAS should be performed according to a DB design, which verifies that the displacement demand is smaller than the anchor's capacity. Conversely, a design procedure based on a strength-only dimensioning criterion led to an inadequate design for the presented case-study as the number of anchors was insufficient to resist the displacement demand. This is explained considering that typical strength-based design procedures refer to dry anchors which are designed to plastically yield and display a larger displacement capacity compared to their grouted counterpart. Therefore, the value of behaviour factor, $q = 2$, assumed for the FB design of dry anchors should be reduced to $q = 1$ for the case of grouted anchors.

The building performance increases if the D-GAS is considered as larger ductility capacity allows for a reduction in the seismic demand and thus a smaller number of anchors is required

to resist the horizontal loading. The wall displays a controlled rocking motion, with the oscillation's amplitude below the threshold value identifying the toe-crush failure. The D-GAS activates without causing the anchor's debonding both for the Ultimate Limit State and the Damage Limit State, proving that the system is beneficial also for less intense earthquakes as it is able to damp the seismic accelerations that could cause damages to the artistic assets of the building. At ULS the D-GAS dissipates 50% of the seismic energy, compared to just 1% of traditional grouted anchors, and reduces the linear accelerations at the control point by 37% with respect to the wall in its original configuration.

These results highlight that the dissipative device is fit for the seismic strengthening of masonry structures. In particular, historic buildings would benefit of the implementation of the innovative system connected to grouted anchors because it would reduce the number of the required anchors, resulting in less invasive installation procedures.

The comparison with the results of the dynamic analysis, shows that the design procedure is able to provide a reliable method for determining the vulnerability of walls to OOP failure and the optimal strengthening solution to control such motion and prevent severe damages to the structure. The proposed design procedure has a general value, as it could be extended to other anchoring system able to restrain the OOP motion. For instance, the procedure can be easily adapted to steel ties connecting opposite walls, by defining the constitutive law correlating the yielding elongation of the ties to the base rotation of the wall.

7 Conclusions and future work

7.1 Background and research goals

In the past decades, considerable results have been achieved into understanding the phenomena that control the dynamics of historic buildings with masonry loadbearing structures, during seismic events. Experimental tests and site investigations have concluded that structural connections between the structural walls play a crucial role to transmit the seismic forces among them and prevent the out-of-plane mechanism.

However, the development of tailored techniques for improving the behaviour of structural connections and the application of concepts at the forefront of seismic engineering hardly follow when designing strengthening interventions.

Such technical gap stems from several issues. Firstly, the challenge of reaching a compromise between strengthening solutions based on innovative techniques and the requirements typical of the conservation of heritage assets. Secondly, few recommendations and case studies are available to guide the development, testing and implementation of energy-based systems for historic structures.

This research project proposes a strengthening system for anchoring walls of historic buildings able to meet the requirements of both modern seismic engineering (EN 1998:2005 2011; DPCM 2011; FEMA 547 2006; EN 15129 2006) and conservation best practice (ICOMOS-ISCARSAH 2021). At the same time, this dissertation provides a methodology can be adopted to guide the design and optimization of strengthening systems similar to the one proposed in this work. The results achieved in developing the dissipative anchoring system and the design procedure developed for its implementation are discussed in the following, including the limits of the present work. A section outlining the impact of the present work and the future research needs in this context, completes the Chapter.

7.2 The Dissipative Grouted Anchoring System (D-GAS)

The conceptual design of the proposed Dissipative Grouted Anchoring System (D-GAS) draws on an existing and well-established strengthening technique, namely metallic grouted anchors.

Metallic grouted anchors are used to improve the connection between orthogonal set of walls. They ensure that the structure can exploit the in-plane capacity of the walls parallel to the main seismic action, while preventing the overturning failure of the walls perpendicular to it. Furthermore, this anchoring typology is economically viable, familiar to the professionals working in the construction industry and conservation field as it offers several advantages from the point of view of conservation practice, such as little obtrusiveness ad compatibility with the masonry substrate. The type of anchoring system chosen for this project, namely the grouted anchoring system developed by Cintec International, is particularly feasible for the implementation in heritage building. It can be concealed from the original element and material of the structure, being fully grouted within the thickness of the wall, and provides a fabric sleeve that avoids overflowing of the grout from the drilled cavity.

However, anchors locally increase the stiffness of the connection and for high levels of seismic intensity considerable damages in the form of diagonal in-plane cracking of wall panels and pull-out/punching of the anchors are likely.

The D-GAS exploits the advantages that the grouted anchoring technology presents while tackling its pitfalls. A friction-based dissipative device is designed as an add-on to provide a controlled displacement capacity. This entails that, during a seismic event, the connection will experience a controlled out-of-plane damage, rather than just relying on the in-plane strength of the side wall, but this controlled failure is decided for a level of seismic intensity by setting the devices to perform accordingly. Although the presence of the dissipative devices modifies the dynamic response of a structure, the outward tilting of walls remains the dominant failure mode. However, in this case the opening of cracks is controlled and taken advantage of, as the D-GAS reduces the accelerations that the wall experiences, thus reducing the level of damage to the surrounding material.

The dissipative anchoring system allows for a shift in design philosophy, from load to displacement capacity in line with the modern principles of seismic engineering, which fosters the exploitation of ductility and hysteretic damping. The D-GAS can be designed according to a performance-based design procedure to meet set performance targets, depending on the expected earthquake intensity. Such design methodology is at the core of the design concept of

the devices and allows their optimisation in term of number, size and characteristics, according to both the principles of minimal intervention and structural reliability, also recommended by the ICOMOS/ISCARSAH (2021).

7.3 The validation process

A validation methodology is set out to assess the performance of the dissipative anchoring system and at the same time provide an example of how to proceed to the development of a strengthening system for masonry connections. The validation process is broken down into substages proceeding to testing from the lowest to the highest level of complexity: each component of the D-GAS is characterized to ensure that each element fulfils a specific function. Accordingly, the friction-based device is tested in its isolated configuration to determine its dissipative and ductility capacity, the anchors rods are tested (with and without the device) as connected to masonry specimens to characterise the grout to masonry bond through the whole range of loading up to failure. The experimental characterization is functional to build a hierarchy of capacity, so that the system is able to respond selectively to the seismic input.

Alongside every experimental activity, numerical models are implemented in Abaqus with the purpose of identifying suitable modelling techniques that can reproduce the experimental results. Indeed, computational models calibrated on experimental results are the necessary means whereby the calculations and checks required by design codes for seismic strengthening are carried out.

The results and novelty of the numerical and experimental activities are summarised in the next subsections for each validation step.

7.3.1 Refinement of the devices

The methodology developed in this validation step and detailed in Chapter 4, presents several aspects of novelty. First, it provides a set of parameters ($\xi_{effb}, \mu,\ S_w$) that determine whether the performance of friction-based dissipative devices is within the current code's limitations. Accordingly, it was possible to refine the existing prototype of friction-based device, namely the SteSq device, and manufacture two new prototypes, the BraCyl and FEPCyl, that present lower material degradation and a more stable force-displacement loops during cyclic loading. Secondly, the methodology addresses the issue of long-term durability of the devices, which is

marginally tackled by the EN 15129 (2006) and rarely performed by researchers assessing the behaviour of anti-seismic dampers for heritage buildings, despite the fact that long terms effects of corrosion and bolt relaxation can significantly change the behaviour of the devices. This activity allowed further refinement of the prototypes replacing the parts that displayed signs of corrosion after being exposed to an aging process.

Finally, the methodology proposes the use of a numerical model calibrated on the experimental evidence to identify the whole range of possible load-displacement curves beyond the ones recorded experimentally. Such approach falls in line with the indications of EN 15129:2009, which prescribes to identify the boundary values that define the performance of dissipative devices.

7.3.2 Performance of D-GAS

The methodology developed in this validation step and detailed in Chapter 5, is purposedly a combination of novel and consolidated activities to assess the performance of anchoring systems. The experimental validation entails a series of monotonic pull-outs and cyclic tests which focus on the behaviour of grouted anchors and the D-GAS when embedded in masonry specimens.

Due to lack of code provisions on the experimental assessment of strengthened masonry connections, the testing set-ups are developed adapting those proposed by other authors in previous testing campaigns. From the pull-out tests, it emerged that the knowledge on the performance of grouted anchors embedded in masonry substrata is still limited. For instance, the formulations available to predict the maximum pull-out capacity of anchors are quite inconsistent with the experimental evidence, especially for grouted anchors with large bore-hole diameter. Therefore, new formulations are proposed in this work for this anchoring technology to fit the data available in the literature and the obtained test results.

Connecting a dissipative device to a grouted anchor successfully prove that the devices can homogenise the response of anchors, and considerably reducing damage to the parent material. Setting the activation load to be smaller than the maximum pull-out load of the anchor, the anchor remains within it elastic phase and almost no relative displacement is detected in the other elements of the anchor assembly.

Testing of sub-assemblages of masonry connections strengthened by anchoring systems are seldom performed, the two most recent testing activities have been performed by Paganoni and

D'Ayala in 2014 and by Maddaloni et al. in 2016. The results of this testing activity validates the load hierarchy which assumes that the grouted anchors have the highest capacity, followed by device load and ultimately by the traction capacity of the connection. Accordingly, a vertical crack is identified at the walls' interface and the front wall displays a controlled rocking motion. While the rocking amplitude is within the displacement capacity of the device, the pull-out failure of the grouted anchors is prevented. Conversely, exceeding the displacement capacity determines the shear failure of the front anchor.

Besides the results obtained on the D-GAS performance, the T-connection tests present novel aspects in the terms of the technology used to capture the relative displacement of the walls during loading. The video gauge and the Digital Image Correlation (DIC) systems are used to monitor the two sides of the specimen, capturing the crack pattern, and quantifying the damage extent. The use of this systems allows replacing the extensive LVDT network used in previous research, which counted up to 19 sensors.

Numerical models are implemented in parallel to the testing activity to identify the most suitable modelling technique that best fit the response of the anchoring systems. To this purpose a Concrete Damage Plasticity (CDP) material is calibrated on the results of the mechanical characterization tests and the use of cohesive interfaces with traction-separation response is proposed to model the bonding action between the grouted anchor and the masonry and the equivalent traction capacity of the T-connection.

Differently from other macro-modelling approaches based on rigid-block elements (Maione et al. 2021), or non-linear links between walls (Pantò et al. 2017) and from discrete modelling techniques (Mercuri et al. 2020), the developed numerical model uses 3D block elements that allow simulating the initial capacity of a masonry connection, the detailed geometry of the device and the bonding strength of the anchor. This tool will be used to validate the design procedure detailed in Chapter 6 and discussed in the next Section.

7.3.3 Implementation of a Design Procedure

The results of the experimental and numerical validation are collated and feed into the development of a multi-level performance-based design procedure for the application of innovative strengthening systems to heritage structures.

The procedure is illustrated in Chapter 6 and exemplified designing a hypothetical strengthening intervention for the façade of a historical church in Italy that displayed a clear damage pattern due to an overturning mechanism after the L'Aquila earthquake of 2009.

The design procedure contains both elements of capacity and performance design and it is structured in cycles that are iterated as long as the layout, dimensions and properties of the anchors and of the devices determines a structural response that comply with the prescribed requirements, both in terms of load and drift.

The procedure provides guidelines that address the issue of the technical gap affecting the seismic strengthening of historic structures, for instance providing a set of threshold displacements (Δy and Δu) which refer to increasing level of damage in the structure, both in the original and strengthened configuration.

The design procedure is validated by dynamic analysis either solving numerically the rocking equation of motion of a rigid body (named DI method) or implementing an Abaqus model using the modelling techniques developed in the previous steps of the validation process. These two analysis options present different levels of complexity and model's detailing which determine a different computational cost of the analysis. Accordingly, they can be used to provide a preliminary or a detailed assessment of the building vulnerability, respectively, depending on the needs of the end-user.

The procedure is applied to the case-study structure, assessing its initial vulnerability to ground motion accelerations and proves that D-GAS is the best design solution to control the out-of-plane damage. Thanks to their ductility, energy dissipation capacity, and flexibility in terms of settings, the devices allow achieving the desired performance in terms of drift, reducing the experienced accelerations and limiting the number of anchors needed for the intervention. Standard anchors are still an option, but their performance is not as efficient: a higher number of anchors must be implemented, so that the strengthening intervention results more disrupting, and yet localised damage is likely.

7.4 Impact

The results obtain in the present study provide a strong argument in favour of the use of dissipative systems to address the lack of suitable modern techniques for the seismic protection of heritage structures. The validation methodology proposed in this work is meant to provide a guidance for the development of such systems: a set of activities and procedural step are proposed to ensure that the code's requirements are met. The methodology was applied to a prototype of dissipative device leading to the development of a new generation of dissipative grouted anchoring system (D-GAS). This is line with the code recommendations, in terms of stability of the hysteresis loops, design flexibility and durability, and respect the requirements of compatibility and reduced obtrusiveness of intervention of conservation engineering.

Based on this evidence, it is believed that the D-GAS and the proposed method have potential to become of particular interest not only for research purposes, but also at a commercial level, as the current market offer limited solutions for the strengthening of historical building compared to newly built structures. Besides its use on undamaged heritage structures that present high vulnerability to OOP failure, the D-GAS has the potential to be used on buildings that have already experienced damages from seismic events. Rather than relying on shoring systems to temporarily support the portion of damaged building, dissipative anchors can be implemented to restore the connection between walls and provide energy dissipation capacity to prevent that the progression of damage increases through swarms of seismic events. During the six-months event seismic swarm that hit Italy between August 2016 and January 2017, for instance, the number of unusable buildings increased from 9% to 40%, as the shoring system were not sufficient to prevent further damages to the structures (Putrino and D'Ayala 2019). Conversely, the D-GAS can be used as preventative measure: its installation can be completed within few days (depending on the required number of anchors) to exploit and control the damage that the building already displays. Once the seismic swarm has decreased its intensity and occurrence, the front wall can be pushed to its vertical position to recentre the dissipative devices and other interventions, such as injections can be used in parallel in presence of weak or highly damaged substrates.

Additionally, the D-GAS can be applied to other construction typologies that are likely to develop an out-of-plane mechanism during earthquakes. For instance, retaining walls and bridge abutments are prone to overturning during seismic events as the horizonal thrust of the ground is magnified by the seismic acceleration. Steel ties are typically used to anchor the wall

and prevent their failure and therefore they could benefit from the implementation of a dissipative device able to reduce the horizonal accelerations that the wall experiences and allow a controlled motion.

7.5 Limitations and future work

The presented experimental tests proved the design concept, validating the assumed load hierarchy and the development of a rocking mechanism after the wall's separation. However, several additional test can be proposed to further validate its performance: firstly, cyclic tests on the second T-shaped masonry specimen are currently undergoing with the FEPCyl prototype installed. This prototype displays a smaller value of slippage load, which will allow a clear-cut difference between the slippage motion of the device and the maximum pull-out force that the anchor can provide. Additionally, C or L connections instead of a T connection, or floor/wall connections rather than wall/wall connections can be tested, as well as other loading programmes and set-up can be recreated in the laboratory to widen the range of testing scenarios. Moreover, large-scale testing could be proposed to determine the dynamic impact of the D-GAS on the system. Results of shaking table tests could be compared with those achieved by other strengthening techniques available in the technical literature. During the present research project, it was not feasible to explore all the possible testing and design scenarios with the available financial resources and within the set timeframe.

Another challenge regards extending the obtained results to the great variety of materials that characterise historic substrata: brick or stonework, regular or rubble, with infill or solid, the impact that these variables have on the bond capacity and failure modes of the strength-only part of the anchor still needs investigating. The database assembled in this work is a first step in this direction, collating the most recurring typologies of materials and their mechanical properties for the pull-out capacity of the anchors. Additional experimental campaigns can be carried out comparable to those described herein with the purpose of studying the influence of other typologies of parent material on the anchor response. Moreover, in case of very weak or damaged substrates, the possibility of using the dissipative anchors in parallel with other interventions, such as injections, could be investigated to improve the mechanical properties of the wall and ensure that the bonding capacity between anchor and parent material is greater than the device's activation load.

Regarding the device's optimization, further tests should be carried out to investigate the resistance of the device to longer periods of weathering exposure and its corrosion resistance with respect to saline environment.

Future work should also involve testing and numerical activities to investigate the use of the D-GAS as a dissipative system for support substructures such as retaining walls and bridge abutments. Building reinforced concrete testing samples of such substructures will also allow exploring the behaviour of the D-GAS as embedded in concrete.

The proposed anchoring solution does not provide a self centering action to the wall which would display a residual drift at the end of the seismic event. Additional elements, such as uniaxial springs, working in parallel to the device would be necessary to provide a force sufficiently large to bring the wall back to its vertical configuration but smaller than the bonding strength at the grout/masonry interface to prevent the anchor's pull-out. This would have increased the complexity of the system and its shape, thus compromising two key factors for the design of the system, namely its simple functioning and its reduced size to minimize its impact on the wall during its implementation. Conversely, the self-centering action could be attained for devices connected to metallic ties that relies on plates on the exterior façade of the masonry to transfer the tension of the bars to walls. In that case, combinations of Belleville flat washers could be used at the bolted connection of the plate to provide a restoring action, as this anchoring technology has a larger load capacity compared to its grouted counterpart. Future work involving further improvement to the design concept could implement a similar solution.

Similarly, the computational models developed in this study would also benefit from exploring further scenarios and investigating different modelling techniques, thus refining the methodology developed so far and complementing the design procedure. For instance, other types of failures, as well as the initial strength of the connection could be included in the numerical model of the rigid block to cover a broader range of case studies. Moreover, a sensitivity analysis can be performed to validate the DI approach over a range of wall's geometries, varying its height and thickness, materials, and for large set of ground motion sequences.

References

Abrams, Daniel P., Omar AlShawa, Paulo B. Lourenço, and Luigi Sorrentino. 2017. “Out-of-Plane Seismic Response of Unreinforced Masonry Walls: Conceptual Discussion, Research Needs, and Modeling Issues.” *International Journal of Architectural Heritage* 11 (1): 22–30. https://doi.org/10.1080/15583058.2016.1238977.

Aiken, I.D., D.K. Nims, and A.S. Whittaker. 1993. “Testing of Passive Energy Dissipation Systems.” *Earthquake Spectra: August 1993, Vol. 9, No. 3, Pp. 335-370*.

Aktas, Yasemin Didem, Dina D’Ayala, Nigel Blades, and Christopher Calnan. 2017. “An Assessment of Moisture Induced Damage in Blickling Hall in Norfolk, England, via Environmental Monitoring.” *Heritage Science* 5 (1). https://doi.org/10.1186/s40494-017-0119-4.

Algeri, Cristiano, Elena Poverello, Giovanni Plizzari, and Ezio Giuriani. 2010. “Experimental Study on the Injected Anchors Behaviour on Historical Masonry.” *Advanced Materials Research* 133–134 (October): 423–28. https://doi.org/10.4028/www.scientific.net/AMR.133-134.423.

Alshawa, Omar, Gianmarco Felice, Alberto Mauro, and Luigi Sorrentino. 2012. “Out-of-Plane Seismic Behaviour of Rocking Masonry Walls.” *Earthquake Engineering & Structural Dynamics* 41 (5): 949–68. https://doi.org/10.1002/eqe.1168.

AlShawa, Omar, Domenico Liberatore, and Luigi Sorrentino. 2019. “Dynamic One-Sided Out-Of-Plane Behavior of Unreinforced-Masonry Wall Restrained by Elasto-Plastic Tie-Rods.” *International Journal of Architectural Heritage* 13 (3): 340–57. https://doi.org/10.1080/15583058.2018.1563226.

AlShawa, Omar, Laura Liberatore, Domenico Liberatore, Fabrizio Mollaioli, and Luigi Sorrentino. 2019. “Seismic Demand on a Unreinforced Masonry Wall Restrained by Elasto-Plastic Tie-Rods Under Earthquake Sequences.” *International Journal of Architectural Heritage* 13 (7): 1124–41. https://doi.org/10.1080/15583058.2019.1645239.

American Society of Civil Engineers (ASCE). 2000. *FEMA 356 Prestandard and Commentary for the Seismic Rehabilitation of Building*. *Rehabilitation*.

Antimo, Marina D, Jean-françois Demonceau, Massimo Latour, and Gianvittorio Rizzano.

2017. “Experimental Investigation of the Creep Effect on Prestressed Bolts Used in Innovative Friction Connections,” no. June.

Araújo, Ana S., Daniel V. Oliveira, and Paulo B. Lourenço. 2014. “Numerical Study on the Performance of Improved Masonry-to-Timber Connections in Traditional Masonry Buildings.” *Engineering Structures* 80: 501–13. https://doi.org/10.1016/j.engstruct.2014.09.027.

Araya, Rodrigo, Marco Marivil, and Mir Cristóbal. 2008. “Temperature and Grain Size Effects on the Behavior of CuAlBe SMA Wires under Cyclic Loading.” *Materials Science and Engineering*.

Arifovic, Fedja, and Morgens Peter Neilsen. 2006. *Strength of Anchors in Masonry*.

Baiguera, Marco, George Vasdravellis, and Theodore L Karavasilis. 2019. “Ultralow Cycle Fatigue Tests and Fracture Prediction Models for Duplex Stainless-Steel Devices of High Seismic Performance Braced Frames” 145 (1): 1–18. https://doi.org/10.1061/(ASCE)ST.1943-541X.0002243.

Bayraktar, Alemdar, Emin Hökelekli, F. Meral Halifeoğlu, Ayman Mosallam, and Halil Karadeniz. 2018. “Vertical Strong Ground Motion Effects on Seismic Damage Propagations of Historical Masonry Rectangular Minarets.” *Engineering Failure Analysis* 91 (November 2017): 115–28. https://doi.org/10.1016/j.engfailanal.2018.04.029.

Benedetti, D., P. Carydis, and P. Pezzoli. 1998. “Shaking Table Tests on 24 Simple Masonry Buildings.” *Earthquake Engineering and Structural Dynamics* 27: 67—90. https://doi.org/10.1111/j.1752-7325.1960.tb00316.x.

Bolhassani, Mohammad, Ahmad A. Hamid, Alan C.W. Lau, and Franklin Moon. 2015. “Simplified Micro Modeling of Partially Grouted Masonry Assemblages.” *Construction and Building Materials* 83: 159–73. https://doi.org/10.1016/j.conbuildmat.2015.03.021.

Bolis, Valentino, Marco Preti, Alessandra Marini, and Ezio Giuriani. 2017. “Experimental Cyclic and Dynamic In-Plane Rocking Response of a Masonry Transverse Arch Typical of Historical Churches.” *Engineering Structures* 147 (October): 285–96. https://doi.org/10.1016/j.engstruct.2017.05.058.

Bonci, A, G Carluccio, M G Castellano, G Croci, S Infanti, and A Viskovic. 2000. “Use of Shock Transmission Units and Shape Memory Alloy Devices for the Seismic Protection

of Monuments: The Case of the Upper Basilica of San Francesco at Assisi." *Archi 2000 International Congress: Overview, Program and Selected Papers from the UNESCO-ICOMOS Millennium Congress Held September 10-12, 2001 at UNESCO Headquarters*.

Borri, A., G. Castori, M. Corradi, and E. Speranzini. 2011. "Shear Behavior of Unreinforced and Reinforced Masonry Panels Subjected to in Situ Diagonal Compression Tests." *Construction and Building Materials* 25 (12): 4403–14. https://doi.org/10.1016/j.conbuildmat.2011.01.009.

BS EN 1881:2006. 2006. "Products and Systems for the Protection and Repair of Concrete Structures. Test Methods. Testing of Anchoring Products by the Pull-out Method."

Cacciola, P., Agathoklis Giaralis, and Alessandro Tombari. 2020. "An Inerter-Equipped Vibrating Barrier for Noninvasive Motion Control of Seismically Excited Structures." *Structural Control and Health Monitoring* 27 (3): 1–21. https://doi.org/10.1002/stc.2474.

Cacciola, P., and A. Tombari. 2015. "Vibrating Barrier: A Novel Device for the Passive Control of Structures under Ground Motion." *Proceedings of the Royal Society A: Mathematical, Physical and Engineering Sciences* 471 (2179). https://doi.org/10.1098/rspa.2015.0075.

Calvi, GM, MJN Priestley, and MJ Kowalsky. 2008. "Displacement-Based Seismic Design of Structures."

Candela, Michele, Antonio Borri, and Luca Righetti. 2016. "Effect of Transversal Steel Connectors on the Behavior of Rubble Stone- Masonry Walls : Two Case Studies in Italy." *Brick and Block Masonry: Proceedings of the 16th International Brick and Block Masonry Conference*, no. June: 2029–37.

Casapulla, Claudia, Alessandra Maione, and Luca Umberto Argiento. 2019. "Performance-Based Seismic Analysis of Rocking Masonry Façades Using Non-Linear Kinematics with Frictional Resistances: A Case Study." *International Journal of Architectural Heritage* 00 (00): 1–15. https://doi.org/10.1080/15583058.2019.1674944.

Casciati, Fabio, and Lucia Faravelli. 2009. "A Passive Control Device with SMA Components : From the Prototype to the Model," no. June 2008: 751–65. https://doi.org/10.1002/stc.

Casciati, Fabio, Lucia Faravelli, and Karim Hamdaoui. 2007. "Performance of a Base Isolator with Shape Memory Alloy Bars." *Earthquake Engineering and Engineering Vibration* 6 (4): 401–8. https://doi.org/10.1007/s11803-007-0787-2.

CEB. 1994. “CEB, Comité Euro-International Du Béton, Fastenings to Concrete and Masonry Structures. State-of-the-Art Report, Thomas Telford, London.”

Ceroni, Francesca, Roberto Cuzzilla, and Marisa Pecce. 2016. “Assessment of Performance of Steel and GFRP Bars as Injected Anchors in Masonry Walls.” *Construction and Building Materials* 123: 78–98. https://doi.org/10.1016/j.conbuildmat.2016.06.124.

Ceroni, Francesca, and Marco Di Ludovico. 2020. “Traditional and Innovative Systems for Injected Anchors in Masonry Elements : Experimental Behavior and Theoretical Formulations.” *Construction and Building Materials* 254: 119178. https://doi.org/10.1016/j.conbuildmat.2020.119178.

Cho, Chang Geun, and Minho Kwon. 2004. “Development and Modeling of a Frictional Wall Damper and Its Applications in Reinforced Concrete Frame Structures.” *Earthquake Engineering and Structural Dynamics* 33 (7): 821–38. https://doi.org/10.1002/eqe.379.

Christopoulos, C, R Tremblay, H Kim, and M Lacerte. 2008. “Self-Centering Energy Dissipative Bracing System for the Seismic Resistance of Structures : Development and Validation” 134 (January): 96–107.

Ciampi, V., M. De Angelis, and F. Paolacci. 1995. “Design of Yielding or Friction-Based Dissipative Bracings for Seismic Protection of Buildings.” *Engineering Structures* 17 (5): 381–91. https://doi.org/10.1016/0141-0296(95)00021-X.

Cintec International. 2019. “Reinforcement Systems and Masonry Anchoring - Material Safety Data Sheet.” https://cintec.com/wp-content/uploads/2021/06/Contractor-Notes-CAN.pdf.

Clemente, P., and A. De Stefano. 2011. “Application of Seismic Isolation in the Retrofit of Historical Buildings.” *WIT Transactions on the Built Environment* 120: 41–52. https://doi.org/10.2495/ERES110041.

Clemente, P, A De Stefano, and R Zago. 2012. “Seismic Isolation in Existing Complex Structures.” *15th World Conf. on Earth. Eng., 15WCEE,(Lisbon, 24-28 Sept.), Paper*, no. 0712.

CMIT. 2009. *Ministero Delle Infrastrutture e Dei Trasporti. Circolare 2 Febbraio 2009 , n. 617, Contenente Le Istruzioni per L’applicazione Delle “Nuove Norme Tecniche per Le Costruzioni” Di Cui Al DM 14 Gennaio 2008. Gazzetta Ufficiale Della Repubblica Italiana n. 4*.

Constantinou, M. C., A. M. Reinhorn, and R. Watson. 1988. “Teflon Bearings in Aseismic Base Isolation: Experimental Studies.” *American Society of Mechanical Engineers, Pressure Vessels and Piping Division (Publication) PVP* 147 (January): 9–13.

Constantinou, M C, T T Soong, and G F Dargush. 1998. *Passive Energy Dissipation Systems for Structural Design and Retrofit*.

Constantinou, Michalakis, Anoop Mokha, and Andrei Reinhorn. 1990. “Teflon Bearings in Base Isolation. II: Modeling.” *Journal of Structural Engineering,* 116 (2): 455–74.

Contrafatto, Loredana, and Renato Cosenza. 2014. “Behaviour of Post-Installed Adhesive Anchors in Natural Stone.” *Construction and Building Materials* 68: 355–69. https://doi.org/10.1016/j.conbuildmat.2014.05.099.

Cook, R.A. 1993. “Behaviour of Chemically Bonded Anchors.” *Journal of Structural Engineering* 119(9):274.

Costa, Alexandre A., António Arêde, Andrea Penna, and Aníbal Costa. 2013. “Free Rocking Response of a Regular Stone Masonry Wall with Equivalent Block Approach: Experimental and Analytical Evaluation.” *Pacific Conference on Earthquake Engineering,* no. 056: 1–6. https://doi.org/10.1002/eqe.2327.

Costigan, Adrian, and Sara Pavía. 2013. “Influence of the Mechanical Properties of Lime Mortar on the Strength of Brick Masonry.” *RILEM Bookseries* 7: 359–72. https://doi.org/10.1007/978-94-007-4635-0_28.

D’Amato, Michele, Rosario Gigliotti, and Raffaele Laguardia. 2019. “Seismic Isolation for Protecting Historical Buildings: A Case Study.” *Frontiers in Built Environment* 5 (July): 1–16. https://doi.org/10.3389/fbuil.2019.00087.

D’Antimo, Marina, Massimo Latour, Giovanni Ferrante Cavallaro, Jean Pierre Jaspart, Shahab Ramhormozian, and Jean François Demonceau. 2020. “Short- and Long- Term Loss of Preloading in Slotted Bolted Connections.” *Journal of Constructional Steel Research* 167: 105956. https://doi.org/10.1016/j.jcsr.2020.105956.

D’ayala, Dina. 2005. “Force and Displacement Based Vulnerability Assessment for Traditional Buildings.” *Bulletin of Earthquake Engineering* 3 (3): 235–65. https://doi.org/10.1007/s10518-005-1239-x.

D’Ayala, Dina. 2013. *Assessing the Seismic Vulnerability of Masonry Buildings*. *Handbook of*

Seismic Risk Analysis and Management of Civil Infrastructure Systems. https://doi.org/10.1533/9780857098986.3.334.

———. 2014. “Conservation Principles and Performance Based Strengthening of Heritage Buildings in Post-Event Reconstruction.” *Geotechnical, Geological and Earthquake Engineering* 34: Chapter 15-179-194. https://doi.org/10.1007/978-3-319-07118-3_5.

D’Ayala, Dina, and Yasemin Didem Aktas. 2016. “Moisture Dynamics in the Masonry Fabric of Historic Buildings Subjected to Wind-Driven Rain and Flooding.” *Building and Environment* 104 (May): 208–20. https://doi.org/10.1016/j.buildenv.2016.05.015.

D’Ayala, Dina, and Michael Forsyth. 2008. “What Is Conservation Engineering?” *Structures & Construction in Historic Building Conservation*, no. April: 1–11. https://doi.org/10.1002/9780470691816.ch1.

D’Ayala, Dina, and Sara Paganoni. 2011. “Assessment and Analysis of Damage in L’Aquila Historic City Centre after 6th April 2009.” *Bulletin of Earthquake Engineering* 9 (1): 81–104. https://doi.org/10.1007/s10518-010-9224-4.

———. 2014. “Testing and Design Protocol of Dissipative Devices for Out-of-Plane Damage.” *Proceedings of the Institution of Civil Engineers: Structures and Buildings* 167 (1): 26–40. https://doi.org/10.1680/stbu.12.00087.

D’Ayala, Dina, and Yanan Shi. 2011. “Modeling Masonry Historic Buildings by Multi-Body Dynamics.” *International Journal of Architectural Heritage* 5 (4–5): 483–512. https://doi.org/10.1080/15583058.2011.557138.

D’Ayala, Dina, and Elena Speranza. 2003. “Definition of Collapse Mechanisms and Seismic Vulnerability of Historic Masonry Buildings.” *Earthquake Spectra* 19 (3): 479–509. https://doi.org/10.1193/1.1599896.

Dassault Systems. 2019. “Abaqus Cae, v.19.”

Derakhshan, Hossein, Dmytro Dizhur, Michael C. Griffith, and Jason M. Ingham. 2014. “In Situ Out-of-Plane Testing of As-Built and Retrofitted Unreinforced Masonry Walls.” *Journal of Structural Engineering* 140 (6): 04014022. https://doi.org/10.1061/(asce)st.1943-541x.0000960.

Dizhur, Dmytro, Arturo Schultz, and Jason Ingham. 2016. “Pull-out Behavior of Adhesive Connections in Unreinforced Masonry Walls.” *Earthquake Spectra* 32 (4): 2357–75.

https://doi.org/10.1193/011115EQS006M.

Doerr, G T, and R E Klingner. 1989. “Adhesive Anchors: Behaviour and Spacing Requirements.” *Res. Rep. No. 1126-2*, no. 2.

Doherty, K., M. C. Griffith, N. Lam, and J. Wilson. 2002. “Displacement-Based Seismic Analysis for out-of-Plane Bending of Unreinforced Masonry Walls.” *Earthquake Engineering and Structural Dynamics* 31 (4): 833–50. https://doi.org/10.1002/eqe.126.

Dolce, M., and R. Marnetto. 1999. “Passive Seismic Devices Based on Shape Memory Alloys.” *12th World Conference on Earthquake Engineering*, no. January: 1–8.

Dolce, M, F C Ponzo, M Di Croce, C Moroni, F Giordano, D Nigro, R Marnetto, and Federico M Mazzolani. 2009. “Experimental Assessment of the CAM and DIS-CAM Systems for the Seismic Upgrading of Monumental Masonry Buildings.” *International Conference on Protection of Historical Buildings*, 1021–27.

Dolce, Mauro, Donatello Cardone, and Domenico Nigro. n.d. “EXPERIMENTAL TESTS ON SEISMIC DEVICES BASED ON SHAPE MEMORY,” 1–8.

Dolšek, Matjaž, and Peter Fajfar. 2008. “The Effect of Masonry Infills on the Seismic Response of a Four-Storey Reinforced Concrete Frame - a Deterministic Assessment.” *Engineering Structures* 30 (7): 1991–2001. https://doi.org/10.1016/j.engstruct.2008.01.001.

DPCM 2011. 2011. “Linee Guida per La Valutazione e La Riduzione Del Rischio Sismico Del Patrimonio Culturale Con Riferimento Alle Norme Tecniche per Le Costruzioni Di Cui Al Decreto Del Ministero Delle Infrastrutture e Dei Trasporti Del 14 Gennaio 2008 (09/02/2011)” 1 (c): 1–83.

ElGawady, M., P. Lestuzzi, and M. Badoux. 2004. “A REVIEW OF CONVENTIONAL SEISMIC RETROFITTING TECHNIQUES FOR URM.” *Journal of Bridge Engineering* 7 (1): 31–38. https://doi.org/10.1061/(ASCE)1084-0702(2002)7:1(31).

Eligehausen, R., E. P. Popov, and V. V. Bertero. 1982. “Local Bond Stress-Slip Relationships of Deformed Bars Under Generalized Excitations.” 4 (January 1982): 69–80.

EN 1015:1999. 1999. “Methods of Test for Mortar for Masonry.”

EN 1052:1999. 1999. “Methods of Test for Masonry.”

EN 1090-2:2008. 2008. *Execution of Steel Structures and Aluminium Structures*.

EN 15129. 2006. “CEN/TC 340 Anti-Seismic Devices.”

EN 1881:2006. 2006. “Products and Systems for the Protection and Repair of Concrete Structures – Test Methods – Testing of Anchoring Products by Pull-out Method.”

EN 1998-1:2004. 2004. *Design of Structures for Earthquake Resistance*. Vol. 1. London.

EN 1998-3:2005. 2005. “Eurocode 8: Design of Structures for Earthquake Resistance - Part 3: Assessment and Retrofitting of Buildings.” Vol. 1.

EN 1998:2005. 2011a. “Eurocode 8: Design of Structures for Earthquake Resistance. Part 1 : General Rules, Seismic Actions and Rules for Buildings.” Vol. 1.

———. 2011b. “Eurocode 8: Design of Structures for Earthquake Resistance.” Vol. 1.

EN 6 -1996-1-1. 2005. *Eurocode 6 - Design of Masonry Structures - Part 1-1: General Rules for Reinforced and Unreinforced Masonry Structures*. Vol. 2.

EN 772:2000. 2000. “Methods of Test for Masonry Units.”

EN 846-2:2000. 2000. “Methods of Test for Ancillary Components for Masonry. Part 2: Determination of Bond Strength of Prefabricated Bed Joint Reinforcement in Mortar Joints.”

Fajfar, Peter. 2000. “A Nonlinear Analysis Method for Performance-Based Seismic Design.” *Earthquake Spectra* 16 (3): 573–92. https://doi.org/10.1193/1.1586128.

Felice, Gianmarco De, and Renato Giannini. 2001. “Out-of-Plane Seismic Resistance of Masonry Walls.” *Journal of Earthquake Engineering* 5 (2): 253–71. https://doi.org/10.1080/13632460109350394.

FEMA 273. 1997. “FEMA 273: NEHRP Guidelines for the Seismic Rehabilitation of Buildings (FEMA Publication 273),” no. October: 435. https://doi.org/10.1074/jbc.274.12.7958.

FEMA 547. 2006. “Techniques for the Seismic Rehabilitation of Existing Buildings.”

Ferrante Cavallaro, Giovanni, Massimo Latour, Antonella Bianca Francavilla, Vincenzo Piluso, and Gianvittorio Rizzano. 2018. “Standardised Friction Damper Bolt Assemblies Time-Related Relaxation and Installed Tension Variability.” *Journal of Constructional Steel Research* 141: 145–55. https://doi.org/10.1016/j.jcsr.2017.10.029.

Ferreira, Fernando, Carlos Moutinho, Álvaro Cunha, and Elsa Caetano. 2020. “An Artificial

Accelerogram Generator Code Written in Matlab." *Engineering Reports* 2 (3): 1–17. https://doi.org/10.1002/eng2.12129.

Ferretti, Elena. 2020. "Recent Advances in the Straps/Strips Technique for out-of-Plane Strengthening of Load-Bearing Masonry Walls." *Procedia Structural Integrity* 25 (2019): 33–46. https://doi.org/10.1016/j.prostr.2020.04.007.

Freddi, Fabio, Christoforos A. Dimopoulos, and Theodore L. Karavasilis. 2017. "Rocking Damage-Free Steel Column Base with Friction Devices: Design Procedure and Numerical Evaluation." *Earthquake Engineering and Structural Dynamics* 46 (14): 2281–2300. https://doi.org/10.1002/eqe.2904.

Gigla, Birger. 2004. "Bond Strength of Injection Anchors as Supplementary Reinforcement Inside Historic Masonry." In *13th International Brick and Block Conference*, 119–28.

———. 2012. "Structural Design of Supplementary Injection Anchors inside Masory." In *15th International Brick and Block Masonry Conference*.

Gigla, Birger, and F. Wenzel. 2000. "Design Recommendations for Injection Anchors as Supplementary Reinforcement of Historic Masonry." *12th International Brick/Block Masonry Conference*, 691–706.

Giresini, Linda, Massimo Fragiacomo, and Paulo B. Lourenço. 2015. "Comparison between Rocking Analysis and Kinematic Analysis for the Dynamic Out-of-Plane Behavior of Masonry Walls." *Earthquake Engineering & Structural Dynamics* 44:2359–23. https://doi.org/10.1002/eqe.2592.

Giresini, Linda, Mario Lucio Puppio, and Francesca Taddei. 2020. "Experimental Pull-out Tests and Design Indications for Strength Anchors Installed in Masonry Walls." *Materials and Structures/Materiaux et Constructions* 53 (4): 1–16. https://doi.org/10.1617/s11527-020-01536-2.

Giresini, Linda, Mauro Sassu, and Luigi Sorrentino. 2018. "In Situ Free-Vibration Tests on Unrestrained and Restrained Rocking Masonry Walls." *Earthquake Engineering and Structural Dynamics* 47 (15): 3006–25. https://doi.org/10.1002/eqe.3119.

Giresini, Linda, Fabio Solarino, Francesca Taddei, and Gerhard Mueller. 2021. "Experimental Estimation of Energy Dissipation in Rocking Masonry Walls Restrained by an Innovative Seismic Dissipator (LICORD)." *Bulletin of Earthquake Engineering* 19 (5): 2265–89.

https://doi.org/10.1007/s10518-021-01056-6.

Giuliani, Domenico, and Fernando Antenucci. 2017. “Valori Medi Climatici Dal 1951 Al 2000 Nella Regione Abruzzo.”

Giuriani, Ezio, and Alessandra Marini. 2008. “Experiences from the Northern Italy 2004 Earthquake: Vulnerability Assessment and Strengthening of Historic Churches.” *Structural Analysis of Historic Construction: Preserving Safety and Significance - Proceedings of the 6th International Conference on Structural Analysis of Historic Construction, SAHC08* 1: 13–24.

Gostič, S, V Bosiljkov, and M Jarc. 2012. “In-Situ Testing of Brick Masonry Walls Strengthened with CFRP Fabric.” *15th International Brick and Block Masonry Conference*. https://doi.org/10.1093/cercor/bht174.

Green-Warren, Robert. 2018. “An Experimental Investigation of Torque Loss in a Die Cast Aluminum Threaded Fastener Joint.” *McNair Scholars Research Journal* 11 (1): 6.

Grigorian, C.E., T.S. Yang, and E.P. Popoc. 1993. “Slotted Bolted Connection Energy Dissipators.” *Earthquake Spectra* 9 (3): 491–504.

Heistermann, Christine. 2014. *Resistance of Friction Connections with Open Slotted Holes in Towers for Wind Turbines*. http://urn.kb.se/resolve?urn=urn:nbn:se:ltu:diva-18533.

Housner, George. 1963. “The Behaviour of Inverted Pendulum Structures during Earthquakes” 53 (2): 403–17.

I. Schmidt, R. Lammering. 2004. “The Damping Behaviour of Superelastic NiTi Components.” *Material Science*.

ICOMOS/ISCARSAH. 2021. “Recommendations for the Analysis , Conservation and Structural Restoration of Architectural Heritage Part II,” 1–28.

ICOMOS. 2003. *Icomos Charter- Principles for the Analysis , Conservation and Structural Restoration of Architectural Heritage (2003). Architectural Heritage*.

Indirli, M., M. G. Castellano, A. Viskovic, A. Bonci, M. Biritognolo, G Croci, S. Infanti, and A. Martelli. 2001. “Out-of-Plane Seismic Behaviour of Masonry Walls With Shape Memory Alloy Ties,” no. September 2001.

Indirli, M., and Maria Gabriella Castellano. 2008. “Shape Memory Alloy Devices for the

Structural Improvement of Masonry Heritage Structures." *International Journal of Architectural Heritage* 2 (2): 93–119. https://doi.org/10.1080/15583050701636258.

James, Peter, Dennis Lee, Sara Paganoni, and Dina D'ayala. 2011. Improvements In and Relating To Building Anchor Systems, issued 2011.

James, Peter, Dennis Lee, Sara Paganoni, and Dina D'Ayala. 2014. Building Anchoring System, issued 2014.

Johnson, Jerod. 2005. "Modern Solutions to Historic Problems: The Utah State Capitol Building Seismic Retrofit Poject." *Utah Preservation*.

Kaushik, Hemant, Durgesh Rai, and Sudir Jain. 2007. "Stress-Strain Characteristics of Clay Brick Masonry under Uniaxial Compression." *Journal of Materials in Civil Engineering* 1561 (September): 454–61. https://doi.org/10.1061/_ASCE0899-1561_200719:9_728.

Keightley, W. O. 1977. "Dry Friction Damping of Multistory Structures." *7th WCEE*.

Kodur, Venkatesh, Sonali Kand, and Wasim Khaliq. 2012. "Effect of Temperature on Thermal and Mechanical Properties of Steel Bolts." *Journal of Materials in Civil Engineering* 24 (6): 765–74. https://doi.org/10.1061/(ASCE)MT.1943-5533.0000445.

Lagomarsino, Sergio. 2015. "Seismic Assessment of Rocking Masonry Structures." *Bulletin of Earthquake Engineering* 13 (1): 97–128. https://doi.org/10.1007/s10518-014-9609-x.

Lagomarsino, Sergio, and Serena Cattari. 2015. "PERPETUATE Guidelines for Seismic Performance-Based Assessment of Cultural Heritage Masonry Structures," 13–47. https://doi.org/10.1007/s10518-014-9674-1.

Latour, M., M. D'Aniello, M. Zimbru, G. Rizzano, V. Piluso, and R. Landolfo. 2018. "Removable Friction Dampers for Low-Damage Steel Beam-to-Column Joints." *Soil Dynamics and Earthquake Engineering* 115 (July): 66–81. https://doi.org/10.1016/j.soildyn.2018.08.002.

Latour, M., V. Piluso, and G. Rizzano. 2014. "Experimental Analysis on Friction Materials for Supplemental Damping Devices." *Construction and Building Materials* 65: 159–76. https://doi.org/10.1016/j.conbuildmat.2014.04.092.

Latour, Massimo. 2014. "Experimental Analysis on Friction Materials for Supplemental Damping Devices." *Construction and Building Materials* 65 (August): 159–76.

https://doi.org/10.1016/j.conbuildmat.2014.04.092.

Latour, Massimo, Vincenzo Piluso, and Gianvittorio Rizzano. 2015. “Free from Damage Beam-to-Column Joints: Testing and Design of DST Connections with Friction Pads.” *Engineering Structures* 85: 219–33. https://doi.org/10.1016/j.engstruct.2014.12.019.

———. 2018. “Experimental Analysis of Beam-to-Column Joints Equipped with Sprayed Aluminium Friction Dampers.” *Journal of Constructional Steel Research* 146: 33–48. https://doi.org/10.1016/j.jcsr.2018.03.014.

Lee, Chang Hwan, Jaeho Ryu, Jintak Oh, Chang Hee Yoo, and Young K. Ju. 2016. “Friction between a New Low-Steel Composite Material and Milled Steel for SAFE Dampers.” *Engineering Structures* 122 (September): 279–95. https://doi.org/10.1016/j.engstruct.2016.04.056.

Li1, Hui, Chen-Xi Mao, and Jin-Ping Ou. 2014. “Experimental and Theoretical Study on Two Types of Shape Memory Alloy Devices,” no. September 2007: 407–26. https://doi.org/10.1002/eqe.

Lim, S C, and M F Ashby. 1987. “Wear-Mechanism Maps.” *Acta Metallurgica* 35 (I): 1–24.

LL.GG. 2011. “Linee Guida per La Valutazione e La Riduzione Del Rischio Sismico Del Patrimonio Culturale Con Riferimento Alle Norme Tecniche per Le Costruzioni Di Cui Al Decreto Del Ministero Delle Infrastrutture e Dei Trasporti Del 14 Gennaio 2008 (09/02/2011)” 1 (c): 1–83.

Longana, Marco Luigi. 2014. “Intermediate Strain Rate Testing Methodologies and Full-Field Optical Strain Measurement Techniques for Composite Materials Characterisation.” *University of Southampton*.

Luca, Antonello De, Elena Mele, Javier Molina, Guido Verzeletti, and Artur V. Pinto. 2001. “Base Isolation for Retrofitting Historic Buildings: Evaluation of Seismic Performance through Experimental Investigation.” *Earthquake Engineering and Structural Dynamics* 30 (8): 1125–45. https://doi.org/10.1002/eqe.54.

Luca, Antonello De, Elena Mele, Javier Molina, Guido Verzeletti, and Artur V Pinto. 2001. “Base Isolation for Retroÿtting Historic Buildings : Evaluation of Seismic Performance through Experimental Investigation” 1145 (98): 1125–45. https://doi.org/10.1002/eqe.54.

Maddaloni, G., M. Di Ludovico, A. Balsamo, Giuseppe Maddaloni, and A. Prota. 2018.

"Dynamic Assessment of Innovative Retrofit Techniques for Masonry Buildings." *Composites Part B: Engineering*.

Maddaloni, G., M. Di Ludovico, A. Balsamo, and A. Prota. 2016. "Out-of-Plane Experimental Behaviour of T-Shaped Full Scale Masonry Wall Strengthened with Composite Connections." *Composites Part B: Engineering* 93: 328–43. https://doi.org/10.1016/j.compositesb.2016.03.026.

Maddaloni, Gennaro. 2016. "Analisi Sperimentale Del Comportamento Di Edifici in Muratura Rinforzati Con Tecniche e Materiali Innovativi." *PhD Thesis*.

Maddaloni, Gennaro, M. Di Ludovico, A. Balsamo, Giuseppe Maddaloni, and A. Prota. 2018. "Dynamic Assessment of Innovative Retrofit Techniques for Masonry Buildings." *Composites Part B: Engineering* 147 (March): 147–61. https://doi.org/10.1016/j.compositesb.2018.04.038.

Magenes, Guido, Andrea Penna, and Alessandro Galasco. 2010. "A Full-Scale Shaking Table Test on a Two-Storey Stone Masonry Building." *14th European Conference on Earthquake Engineering*, no. August: 384.

Mahmoud, Hussam, Santiago Rodriguez Lopez, and Guillermo A. Riveros. 2016. "Causes of Pretension Loss in High-Strength Bolts." *The U.S. Army Engineer Research and Development Center*, no. April 2017. https://doi.org/10.13140/RG.2.2.21852.80000.

Mainstone, Rowland. 1969. "Justinian's Church of St Sophia, Istambul: Recent Studies of Its Contruction and First Partial Reconstruction." *Architectural History* 12: 39–49. https://doi.org/https://doi.org/10.2307/1568335.

Maione, A, C Casapulla, M Di Ludovico, A Prota, and F Ceroni. 2021. "Efficiency of Injected Anchors in Connecting T – Shaped Masonry Walls : A Modelling Approach." *Construction and Building Materials* 301: 124051. https://doi.org/10.1016/j.conbuildmat.2021.124051.

Makris, Nicos, and Jian Zhang. 1999. "Rocking Response and Overturning of Anchored Equipment under Seismic Excitations." *Pacific Earthquake Engineering Research Center*, no. November: 1–82.

MATLAB (R2019b). 2018. "9.7.0.1190202 (R2019b). Natick, Massachusetts: The MathWorks Inc."

Mayes, R. L., and N. A. Mowbray. 1975. “The Effect of Coulomb Damping on Multidegree of Freedom Elastic Structures.” *Earthquake Engineering & Structural Dynamics* 3 (3): 275–86. https://doi.org/10.1002/eqe.4290030306.

Mazzolani, F. 2001. “Passive Control Technologies for Seismic-Resistant Buildings in Europe.” *Progress in Structural Engineering and Materials* 3 (3): 277–87. https://doi.org/10.1002/pse.83.

Mehrotra, Anjali, and Matthew J. DeJong. 2018. “The Influence of Interface Geometry, Stiffness, and Crushing on the Dynamic Response of Masonry Collapse Mechanisms.” *Earthquake Engineering and Structural Dynamics* 47 (13): 2661–81. https://doi.org/10.1002/eqe.3103.

Melatti, Victor, and Dina D’Ayala. 2020. “Methodology for the Assessment and Refinement of Friction-Based Dissipative Devices.” *Engineering Structures* 229 (October 2020): 111666. https://doi.org/10.1016/j.engstruct.2020.111666.

———. 2021. “Displacement-Based Design Procedure of Grouted Anchoring Systems for the Seismic Upgrade of Heritage Buildings.” *Construction and Building Materials*.

Melatti, Victor, Dina D’Ayala, and Erica Modolo. 2019. “Computational Validation of Dissipative Device for the Seismic Upgrade of Historic Buildings.” *COMPDYN Proceedings* 3 (June): 5135–52. https://doi.org/10.7712/120119.7293.19538.

Mendes, N., P. Lourenco, and A. Campos-Costa. 2014. “Shaking Table Testing of an Existing Masonry Building: Assessment and Improvement of the Seismic Performance.” *Earthquake Engineering and Structural Dynamics*, no. 056: 1–6. https://doi.org/10.1002/eqe.2342.

Mercuri, Micaela, Madura Pathirage, Amedeo Gregori, and Gianluca Cusatis. 2020. “Computational Modeling of the Out-of-Plane Behavior of Unreinforced Irregular Masonry.” *Engineering Structures* 223 (July): 111181. https://doi.org/10.1016/j.engstruct.2020.111181.

Mohsenian, Vahid, and Alireza Mortezaei. 2019. “A New Energy-Absorbing System for Seismic Retrofitting of Frame Structures with Slender Braces.” *Bulletin of Earthquake Engineering* 17 (5): 2715–39. https://doi.org/10.1007/s10518-018-00543-7.

Mokha, Anoop S ., Navinchandra Amin, Michael C. Constantinou, and Victor Zayas. 1996.

"Seismic Isolation Retrofit of Large Historic Building Anoop S . Mokha ; Navinchandra Amin / Michael C . Constantinou /" 122 (3): 298–308.

Mokha, By Anoop, Michalakis Constantinou, Associate Member, and Andrei Reinhorn. 1990. "Teflon Bearings in Base Isolation. I: Testing." *Journal of Structural Engineering* 116 (2): 438–54.

Moon, Lisa, Dmytro Dizhur, Ilaria Senaldi, Hossein Derakhshan, Michael Griffith, Guido Magenes, and Jason Ingham. 2014. "The Demise of the URM Building Stock in Christchurch during the 2010-2011 Canterbury Earthquake Sequence." *Earthquake Spectra* 30 (1): 253–76. https://doi.org/10.1193/022113EQS044M.

Moreira, Susana, Luís F. Ramos, Daniel V. Oliveira, and Paulo B. Lourenço. 2014. "Experimental Behavior of Masonry Wall-to-Timber Elements Connections Strengthened with Injection Anchors." *Engineering Structures* 81: 98–109. https://doi.org/10.1016/j.engstruct.2014.09.034.

MSJC, Masonry Standard Joint Committee's. 2013. "Building Code Requirements for Masonry Structures, (TMS 402-13/ACI, 530-13/ASCE)."

Mualla, Imad H, and Borislav Belev. 2002. "Performance of Steel Frames with a New Friction Damper Device under Earthquake Excitation" 24: 365–71. https://doi.org/10.1016/S0141-0296(01)00102-X.

Muñoz, Rosana, Paulo B. Lourenço, and Susana Moreira. 2018. "Experimental Results on Mechanical Behaviour of Metal Anchors in Historic Stone Masonry." *Construction and Building Materials* 163: 643–55. https://doi.org/10.1016/j.conbuildmat.2017.12.090.

Nabid, Neda, Iman Hajirasouliha, and Mihail Petkovski. 2017. "A Practical Method for Optimum Seismic Design of Friction Wall Dampers." *Earthquake Spectra* 33 (3): 1033–52. https://doi.org/10.1193/110316EQS190M.

Nakamura, Yutaka, and Keiichi Okada. 2019. "Review on Seismic Isolation and Response Control Methods of Buildings in Japan." *Geoenvironmental Disasters* 6 (1). https://doi.org/10.1186/s40677-019-0123-y.

Nastri, Elide, Mario D'Aniello, Mariana Zimbru, Simona Streppone, Raffaele Landolfo, Rosario Montuori, and Vincenzo Piluso. 2019. "Seismic Response of Steel Moment Resisting Frames Equipped with Friction Beam-to-Column Joints." *Soil Dynamics and*

Earthquake Engineering 119 (January): 144–57. https://doi.org/10.1016/j.soildyn.2019.01.009.

NIKER. 2012. *Guidelines for Assessment and Improvement of Connections in Buildings, Final Reports D10.2 – New Integrated Knowledge Based Approaches to the Protection of Cultural Heritage from Earthquake Induced Risk, NIKER, Contract FP7-ENV-2009-1, n. 244123*.

Niker Project. 2010. "Critical Review of Retrofitting and Reinforcement Techniques Related to Possible Failure Mechanisms and Requirements," 113. www.niker.eu.

Nims, D., P. Richter, and R. Bachman. 1993. "The Use of the Energy Dissipating Restrain for Seismic Hazard Mitigation."

Paganoni, Sara. 2015. "Dissipative Anchor Devices for the Seismic Retrofit of Heritage Buildings." *Ph.D. Thesis, University of Bath, Department of Architecture and Civil Engineering* 1.

Paganoni, Sara, and Dina D'Ayala. 2010. "Experimental and Computational Validation of Dissipative Prototype for the Seismic Protection of Heritage Buildings." *Advanced Materials Research* 133–134: 831–36. https://doi.org/10.4028/www.scientific.net/AMR.133-134.831.

Paganoni, Sara, and Dina D'Ayala. 2014. "Testing and Design Procedure for Corner Connections of Masonry Heritage Buildings Strengthened by Metallic Grouted Anchors." *Engineering Structures* 70: 278–93. https://doi.org/10.1016/j.engstruct.2014.03.014.

Palermo, Antonio, Sebastian Krödel, Alessandro Marzani, and Chiara Daraio. 2016. "Engineered Metabarrier as Shield from Seismic Surface Waves." *Scientific Reports* 6: 1–10. https://doi.org/10.1038/srep39356.

Pall, A., and C. Marsh. 1982. "Response of Friction Damped." *International Association of Geodesy Symposia* 133 (June): 701–7. https://doi.org/10.1007/978-3-540-85426-5_80.

Pall, Avtar.S., Cedric Marsh, and Paul Fazio. 1980. "Friction Joints for Seismic Control of Large Panel Structures." *PCI Journal* 25 (6): 38–61.

Pall, Avtar, and R Tina Pall. 2004. "Performance-Based Design Using Pall Friction Dampers - An Economical Design Solution." *13th World Conference on Earthquake Engineering Vancouver*.

Pantò, B., F. Cannizzaro, I. Caliò, and P. B. Lourenço. 2017. “Numerical and Experimental Validation of a 3D Macro-Model for the In-Plane and Out-Of-Plane Behavior of Unreinforced Masonry Walls.” *International Journal of Architectural Heritage* 11 (7): 946–64. https://doi.org/10.1080/15583058.2017.1325539.

Park, R. 1989. “Evaluation of Ductility of Structures and Structural Assemblages from Laboratory Testing” 22 (3): 155–66.

Patil, SJ, and GR Reddy. 2012. “State Of Art Review - Base Isolation Systems for Structures.” *International Journal of Emerging Technology and Advanced Engineering* 2 (7): 438–53.

Petrini, Francesco, Agathoklis Giaralis, and Zixiao Wang. 2020. “Optimal Tuned Mass-Damper-Inerter (TMDI) Design in Wind-Excited Tall Buildings for Occupants’ Comfort Serviceability Performance and Energy Harvesting.” *Engineering Structures* 204 (March 2019): 109904. https://doi.org/10.1016/j.engstruct.2019.109904.

Prajapati, Sanjeev, Omar Alshawa, and Luigi Sorrentino. 2015. “Out-of-Plane Behaviour of Single-Body Unreinforced-Masonry Wall Restrained By a Flexible Diaphragm.” *Proceedings of the 5th International Conference on Computational Methods in Structural Dynamics and Earthquake Engineering (COMPDYN 2015)*, no. May: 3127–38. https://doi.org/10.7712/120115.3607.1552.

Preti, Marco, Sara Loda, Valentino Bolis, Stefania Cominelli, Alessandra Marini, and Ezio Giuriani. 2019. “Dissipative Roof Diaphragm for the Seismic Retrofit of Listed Masonry Churches.” *Journal of Earthquake Engineering* 23 (8): 1241–61. https://doi.org/10.1080/13632469.2017.1360223.

Putrino, Valentina, and Dina D’Ayala. 2018. “Cumulative Damage Assessment and Strengthening Efficacy of Masonry Buildings in Norcia Affected by the 2016 Seismic Events in Central Italy.” *2017 EEFIT Research Award*. https://www.istructe.org/IStructE/media/Public/Resources/report-eefit-grant-cumulative-damage-20181001.pdf.

Putrino, Valentina, and Dina D’Ayala. 2019. “Effectiveness of Seismic Strengthening to Repeated Earthquakes in Historic Urban Contexts: Norcia 2016.” *Disaster Prevention and Management: An International Journal* 29 (1): 47–64. https://doi.org/10.1108/DPM-07-2018-0230.

Python Software Foundation. n.d. “Python Programming Language, Version 3.6. Available at

Http://Www.Python.Org."

Rockside Export. 2019. "Properties of Grade 8.8 Bolt & Nut (Iso)."

Rojas, P, J. M. Ricles, and R Sause. 2005. "Seismic Performance of Post-Tensioned Steel Moment Resisting Frames With Friction Devices." *Journal of Structural Engineering* 131 (4): 529–40. https://doi.org/10.1061/(ASCE)0733-9445(2005)131:4(529).

S. Zhu and Y. Zhang. 2014. "Seismic Behaviour of Self-Centring Braced Frame Buildings with Reusable Hysteretic Damping Brace," no. February: 1329–46. https://doi.org/10.1002/eqe.

Saha, S, S Srimani, S Hajra, A Bhattacharya, and Santanu Das. 2007. "On the Anti-Loosening Property of Different Fasteners." In *13th National Conference on Mechanisms and Machines (NaCoMM07), IISc, Bangalore, India, December 12-13, 2007*, NaCoMM-200:229–32.

Sarangapani, G., B. V. Venkatarama Reddy, and K. S. Jagadish. 2005. "Brick-Mortar Bond and Masonry Compressive Strength." *Journal of Materials in Civil Engineering* 17 (2): 229–37. https://doi.org/10.1061/(asce)0899-1561(2005)17:2(229).

Sarno, Luigi Di, and Giovanni Manfredi. 2012. "Experimental Tests on Full-Scale RC Unretrofitted Frame and Retrofitted with Buckling-Restrained Braces." *Earthquake Engineering & Structural Dynamics*, no. 056: 1–6. https://doi.org/10.1002/eqe.1131.

Shadlou, M, P Cacciola, A Ayoub, Y F Rashed, and A Tombari. 2019. "Non-Invasive Vibrating Control of the Zoser Pyramid."

Shahverdi, Moslem, Christoph Czaderski, and Masoud Motavalli. 2016. "Iron-Based Shape Memory Alloys for Prestressed near-Surface Mounted Strengthening of Reinforced Concrete Beams." *Construction and Building Materials* 112: 28–38. https://doi.org/10.1016/j.conbuildmat.2016.02.174.

Shawa, Omar Al. 2011. "Dinamica Non Lineare Fuori Piano Di Pareti Murarie. Stato Dell'arte, Sperimentazione e Modellazione." Roma, Sapienza.

Shawa, Omar Al, de Felice Gianmarco, Alberto Mauro, and Luigi Sorrentino. 2012. "Out-of-Plane Seismic Behaviour of Rocking Masonry Walls Omar." *Earthquake Engineering and Structural Dynamics*, no. 056: 1–6. https://doi.org/10.1002/eqe.1168.

Shi, Ya-Nan. 2016. “Dynamic Behaviour of Masonry Strucutres.”

Silveri, Francesca, Paolo Riva, Giacomo Profeta, Elena Poverello, and Christiano Algeri. 2016. “Experimental Study on Injected Anchors for the Seismic Retrofit of Historical Masonry Buildings.” *International Journal of Architectural Heritage* 10 (2–3): 182–203. https://doi.org/10.1080/15583058.2015.1113333.

Sisti, Romina, Marco Corradi, and Antonio Borri. 2016. “An Experimental Study on the Influence of Composite Materials Used to Reinforce Masonry Ring Beams.” *Construction and Building Materials* 122: 231–41. https://doi.org/10.1016/j.conbuildmat.2016.06.120.

Söderlund, Anders. 2017. “Influence of Surface Flatness on Bolted Flanges.” Karlstad University.

Soong, T. T., and B. F. Spencer. 2002. “Supplemental Energy Dissipation: State-of-the-Art and State-of-the-Practice.” *Engineering Structures* 24 (3): 243–59. https://doi.org/10.1016/S0141-0296(01)00092-X.

Sorrentino, Luigi, Omar AlShawa, and Luis D. Decanini. 2011. “The Relevance of Energy Damping in Unreinforced Masonry Rocking Mechanisms. Experimental and Analytic Investigations.” *Bulletin of Earthquake Engineering* 9 (5): 1617–42. https://doi.org/10.1007/s10518-011-9291-1.

Sorrentino, Luigi, Dina D’Ayala, Gianmarco de Felice, Michael C. Griffith, Sergio Lagomarsino, and Guido Magenes. 2017. “Review of Out-of-Plane Seismic Assessment Techniques Applied To Existing Masonry Buildings.” *International Journal of Architectural Heritage* 11 (1): 2–21. https://doi.org/10.1080/15583058.2016.1237586.

Sorrentino, Luigi, Renato Masiani, and Michael C. Griffith. 2008. “The Vertical Spanning Strip Wall as a Coupled Rocking Rigid Body Assembly.” *Structural Engineering and Mechanics* 29 (4): 433–53. https://doi.org/10.12989/sem.2008.29.4.433.

The European Stainless Steel Development Association. 2009. “Stainless Steel in Contact with Other Metallic Materials.” *Materials and Applications Series* 10: 1–24.

Thomaidis, Ioannis M., Alfredo Camara, and Andreas J. Kappos. 2017. “Simulating the Response of Free-Standing Rocking Rigid Blocks Using Abaqus / Standard.” *2017 SIMULIA UK Regional User Meeting*, no. March 2018.

Tomaževič, Miha. 1999. *Earthquake-Resistant Design of Masonry Buildings*. Edited by

Imperial College Press.

Tomaževič, Miha, Marjana Lutman, and Polona Weiss. 1996. “Seismic Upgrading of Old Brick-Masonry Urban Houses: Tying of Walls with Steel Ties.” *Earthquake Spectra*. https://doi.org/10.1193/1.1585898.

Totoev, Yuri. 2015. “Design Procedure for Semi Interlocking Masonry.” *Journal of Civil Engineering and Architecture* 9 (5): 517–25. https://doi.org/10.17265/1934-7359/2015.05.003.

UNESCO. 1989. “Draft Medium-Term Plan (1990-1995).”

Uni En. 2005. “BS EN 1993-1-8:2005 - Eurocode 3: Design of Steel Structures - Part 1-8: Design of Joints.” *Eurocode 3* 8 (2005): 135.

Valente, Marco, and Gabriele Milani. 2016. “Seismic Assessment of Historical Masonry Towers by Means of Simplified Approaches and Standard FEM.” *Construction and Building Materials* 108: 74–104. https://doi.org/10.1016/j.conbuildmat.2016.01.025.

Vasdravellis, George, Theodore L. Karavasilis, and Brian Uy. 2014. “Design Rules, Experimental Evaluation, and Fracture Models for High-Strength and Stainless-Steel Hourglass Shape Energy Dissipation Devices.” *Journal of Structural Engineering* 140 (11): 04014087. https://doi.org/10.1061/(asce)st.1943-541x.0001014.

Wang, Bin, and Songye Zhu. 2018. “Cyclic Tension – Compression Behavior of Superelastic Shape Memory Alloy Bars with Buckling-Restrained Devices” 186: 103–13.

Wilkinson, Sean, Damian Grant, Elizabeth Williams, Sara Paganoni, Stuart Fraser, David Boon, Anna Mason, and Matthew Free. 2013. “Observations and Implications of Damage from the Magnitude Mw 6.3 Christchurch, New Zealand Earthquake of 22 February 2011.” *Bulletin of Earthquake Engineering* 11 (1): 107–40. https://doi.org/10.1007/s10518-012-9384-5.

Woods, Richard. 1968. “Screening of Surface Wave in Soils.” *Journal of the Soil Mechanics and Foundations Division*. https://doi.org/https://doi.org/10.1061/JSFEAQ.0001180.

Zahrai, Seyed Mehdi, and Maryam Yazdani. 2014. “Behavior of Base Isolated Structures in the Christchurch Earthquake Behavior of Base Isolated Structures in the Christchurch Earthquake,” no. November.

Zheng, H., D. F. Liu, C. F. Lee, and L. G. Tham. 2005. “Displacement-Controlled Method and Its Applications to Material Non-Linearity.” *International Journal for Numerical and Analytical Methods in Geomechanics* 29 (3): 209–26. https://doi.org/10.1002/nag.410.